The University of Manchester

Regional modelling of air quality and aerosol–cloud interactions over southern Africa

Impact of aerosols and regional-scale meteorology

A thesis submitted to the

The University of Manchester

for the Degree of Doctor of Philosophy (PhD)

in the Faculty of Engineering and Physical Sciences

by

Modise Wiston

School of Earth, Atmospheric and Environmental Science,

Supervisors: Prof. Gordon McFiggans and Prof. David M. Schultz

2016

Table of Contents

List of figures

List of tables

Abbreviations

ACI: aerosol cloud interaction
AMMA: African Multidisciplinary Monsoon Analysis
ARI: aerosol radiative interaction
AOD: aerosol optical depth
APINA: Air Pollution Information Network for Africa
AQ: air quality
ARI: aerosol-radiation interactions
ARW: Advanced WRF post-processing
ASTEM: Adaptive Stem Time-Split Euler Method
BB: biomass burning
BBA: biomass burning aerosol
BC: black carbon
BVOC: biogenic volatile organic compounds
CAB: Congo Air Boundary
CBM-Z: Carbon-Bond Mechanism version-Z
CCN: cloud condensation nuclei
CDNC: cloud droplet number concentration
DMS: dimethylesulphide
DRC: Democratic Republic of Congo (Congo-Kinshasa)
ECMWF: European Centre for Medium-range Weather Forecasts
EDGAR: Emission Database for Global Atmospheric Research
ENSO: El Niño Southern Oscillation
EOS: Earth Observing System
EU: European Union
F-TUV: fast Tropospheric Ultraviolet-Visible
GCM: global climate model
GFS: Global Forecast System
GHG: greenhouse gas
GOCART: GOddard Chemistry Aerosol Radiative and Transport model
IPCC: Intergovernmental Panel on Climate Change
ITCZ: intertropical convergence zone
MEGAN: Model of Emissions of Gases and Aerosols
MESA: Multicomponent Equilibrium Solver for Aerosols
MODIS: Moderate Resolution Imaging Spectroradiometer
MOSAIC: Model for Simulating Aerosol Interactions and Chemistry
MOZART: Model for Ozone and Related Chemical Tracers
MSA: methane sulfonic acid
MTEM: Multicomponent Taylor Expansion Method
NASA: National Aeronautics and Space Administration
NCAR: National Centre for Atmospheric Research
NCEP: National Centre for Environmental Prediction
NCL: NCAR Command Language

NILU: Norwegian Institute for Air Research
NMHC: nonmethane hydrocarbon
NMVOC: non-methane volatile organic compound
NOAA: National Oceanic and Atmospheric Administration
NO_x: oxides of nitrogen (nitrogen dioxide [NO_2] + Nitric oxide [NO])
NWP: numerical weather prediction
PBL: planetary boundary layer
PM: particulate matter
POM: primary organic matter
RADM: Regional Acid Deposition Model
RCM: regional climate model
RETRO: REanalysis of the TROpospheric
RF: radiative forcing
SADC: Southern African Development Community
SAFARI: Southern African Regional Science Initiative
SAPRC: State-wide Air Pollution Research Centre
SOA: secondary organic aerosol
SSA: single scattering albedo
SST: sea surface temperature
SVP: supersaturation vapor pressure
TKE: turbulent kinetic energy
TOA: top of the atmosphere
VOC: volatile organic compound
WHO: World Health Organisation
WPS: WRF Pre-processing System
WRF: Weather Research and Forecasting model
WRF-Chem: Weather Research and Forecasting with Chemistry
YSU: Yonsei University PBL scheme
3BEM: Brazilian Biomass Burning Emission Model

Abstract

Atmospheric trace components play a critical role in the earth–atmosphere system through their interaction and perturbation to global atmospheric chemistry. They perturb the climate through scattering and absorbing of solar radiation (direct effects), thereby impacting on the heat energy balance of the atmosphere, and alter cloud microphysical properties affecting cloud formation, cloud lifetime and precipitation formation (indirect effects). These trace components can also have adverse effects on human health, visibility and air quality (AQ) composition, including various feedback processes on the state of the atmosphere. As well as their direct and indirect effects, aerosols are important for cloud formation. They serve as cloud condensation and ice nuclei (CCN and IN) during cloud droplet and ice crystal formations. Although many connections between clouds and aerosol effects have been established in cloud physics and climate modelling, aerosol–cloud interaction (ACI) is still one of the areas of large uncertainties in modern climate and weather projections. Different models have been developed placing much emphasis on ACIs, to have robust and more consistent description processes within the meteorological and chemical variables to account for ACIs and feedback processes. Because pollutant distributions are controlled by a specific meteorology that promotes residence times and vertical mixing in the atmosphere, reliable chemical composition measurements are required to understand the changes occurring in the earth–atmosphere system. Also, because atmospheric pollution is a combination of both natural and man-made (anthropogenic) sources, to direct controlled and/or mitigation procedures efficiently, contributions of different sources need to be considered. Occasionally these are explored from a particular region or global environment, depending on a specific area of interest.

A fully coupled online meteorology–chemistry model framework (WRF-Chem) is used to investigate atmospheric ACIs over southern Africa –a region characterized by a strong and intense seasonal biomass burning (BB) cycle. The large transport of aerosol plumes originating from the seasonal burning from agriculture, land-use management and various activities give rise to a unique situation warranting special scrutiny. Simulations are conducted for the 2008 dry season BB episode, implementing a chemical dataset from various emission sources (anthropogenic, BB, biogenic, dust and sea salt) with the meteorological conditions. A base line (CNTRL) simulation was conducted with all emission sources from 26 August to 10 September 2008. To probe the contribution of BB on the regional pollution and influence on ACIs, a sensitivity (TEST) simulation was conducted without BB emissions and compared to the base line. The impact of natural and anthropogenic aerosol particles is studied and quantified for the two simulations, focusing on aerosol concentration and cloud responses under different model resolutions. A statistical analysis of pollutant concentration of major regulated species and cloud variables is conducted and the percentage difference used to assess the contribution due to BB emissions. Results confirm the high variability of spatial and temporal patterns of chemical species, with the greatest discrepancies occurring in the tropical forests whereas the subtropics show more urban/industrial related emissions. Whilst CO and O_3 show statistically significant increases over a number of cities/towns, the trend and spatial variability is much less uniform with NO_2 and PM in most urban and populous cities. Statistical analysis of major chemical pollutants was mainly influenced by BB emissions. O_3, NO_x, CO and PM increase by 24%, 76%, 51%, 46% and 41% over the main source regions, whereas in the less affected regions concentrations increased by 5%, 5%, 5%, 3% and 2% when BB emissions are included. This study sheds new light on the response of cloud processes to changing aerosol concentrations and different model resolutions. In the parameterised case (dx = 20 km), clouds become more cellular, correlated with high supersaturations, whereas in the resolved case (dx = 4 km), they become more faint with relatively lower supersaturations. Aerosol effects on cloud properties were further studied and statistical analysis conducted on CCN, cloud droplet number concentration (CDNC), supersaturation and aerosol optical depth (AOD) at two different grid spacings. Most clouds occur to the west of the domain coincident with increase in aerosol concentration and AOD, while single scattering albedo (SSA) decreases. A considerable cloud 'burn-off' occurs in tropical west Africa, where aerosols can also be lofted up to 500-hPa level when

BB emissions are included in the simulation. Due to BB, absorbing aerosol increased by 76% and 23% over tropical west and subtropical southeast, while tropical east shows no change. The study shows that tropical central Africa is characterized by an increased build-up in biomass burning aerosols (BBAs), forming a regional haze with high AOD; this becomes stronger near active burning areas with a significant proportion occurring to the west. AOD enhancement increases up to 38%, 31% and 11% in the west, east and south respectively. Although CDNC increased in areas with high aerosol concentration, supersaturation decreases (in the small domains) since increase in aerosol number concentration decreases maximum supersaturation S_{max}. Changes in absorbed radiation increased by +56 Wm^{-2}, +23 Wm^{-2} and +14 Wm^{-2} in the west, east and southeast. To further evaluate the model sensitivity and its skill, an analysis was conducted by comparing the model performance with measurement data. Simulated AOD, surface concentrations of CO and O_3, ozonesondes and liquid water path (LWP) were compared with measured data from MODIS satellite, SAFARI2000 field study and Cape Point WMO. The model shows a good skill in capturing and reproducing the trends as that measured. However, a severe lack of measurement data over southern Africa makes it more difficult to effectively evaluate WRF-Chem over southern Africa. There is a need for increased availability of measurements to adequately compare with models. This study is one of the first WRF-Chem studies conducted over southern Africa to simulate the weather and pollution interaction. The novelty of the present study is the combined analysis of ACI sensitivity to aerosol loading and cloud response in a regime-based approach. Consideration of different emission sources and aerosol feedbacks allows for a comprehensive investigation of aerosols on clouds and precipitation. The study concludes with a brief discusssion of future directions for work on AQ and modelling interactions between pollution and weather over southern Africa.

Declaration

The University of Manchester

Candidate name: Modise Wiston

Faculty: Engineering and Physical Sciences

Thesis title: Regional modelling of air quality and aerosol-cloud interactions over southern Africa: Impact of aerosols and regional-scale meteorology

I declare that no portion of the work referred to in this thesis has been submitted in support of an application for another degree or qualification to any other university or institute of learning.

Copyright

Acknowledgements

This thesis is a culmination of research performed over the past four years I endured in the project. Firstly, I would like to thank my advisors Profs. Gordon McFiggans and David M. Schultz, for supporting me from the beginning of my research work and tiring journey. The continuous support and encouragement they gave me throughout the study and the timely discussions and indispensible suggestions helped strengthen the science presented in this report. The meetings and conversations we had have been fruitful and were the source of great insight into cloud microphysics. Appreciation also goes to Professor Hugh Coe, for I greatly benefited from the discussions that also helped me in the approach used to analyse and understand the processes in the model. I acknowledge the contribution of other members in our research group –particularly Scott Archer-Nicholls and Douglas Lowe for their assistance in the development and update of the WRF-Chem model and constructive remarks in the project. Most of the skills I learnt in numerical modelling are through working with them –whether it was showing me the ropes of research skills, inner workings of the model tool itself, or just taking time to "break the model." I am especially grateful when they offered assistance even during their busy schedules. Beyond scientific thought, my success as a graduate student stemmed directly from the support team.

I also wish to thank Mrs E. Sephatla (from Morupule Power Station), for her valuable time she spent with me when I was in need of data concerning my research proposal. She found it fit to schedule a time slot in her busy time and offer assistance to me where she could. Extended gratitude also go to Miss Peggy Ndaba (from the Department of Meteorological Services) and her colleagues, who also didn't rest in sharing with me some information about the meteorology and climate research findings from their department. She has always been updating me with information relevant to my research; her continuous encouragement coupled with inspiring scriptural words. My remembrance also goes to all my mentors at undergraduate level, who introduced and moulded me into the field of climate and atmospheric research, most notably Prof. Akintayo Adedoyin.

Last but not least, I had unending support from my family. Special regards to my mother Obaeditse Moepedi, for raising me to a smart young man intrigued by science and passionate about teaching and sharing the knowledge I get with others. I am indebted to auntie Tabuya Moyaga, whom words alone cannot describe. She was, and will always be my 'surrogate mother' throughout my personal life in this era both socially and academically. I also want to thank my fiancé Dipeo for taking care of our kids. Truly it has not been an easy path to traverse through, but with all the courage and support, I managed to overcome some obstacles and challenges in the way. Indeed there's a long way to go in life, especially in the field of a research educationist and more challenges still lie ahead. I look forward to see where my next adventure takes me!

P. M. Wiston
Center for Atmospheric Science (CAS)
The Unviversity of Manchester, UK

Dedication

This is dedicated to:

- My late father: Wiston Nkgata
- My two beautiful daughters: Tshephang Tessie and Leatile Lucia

To God be glory….

Chapter 1

Introduction

1.0 Atmospheric Composition

The troposphere is comprised of the major gases (nitrogen and oxygen) and many trace components, and it is part of the atmosphere where the majority of bio-geochemical cycling and physical processes take place. The atmosphere is a major reservoir through which compounds ascend from the surface at their emission sources to the sites of deposition or dispersal and is a medium through which different products undergo chemical and physical transformations into other substances. Tropospheric air is never perfectly "clean" of trace constituents; there are always both natural and man-made trace components (both gaseous and particulate) in the atmosphere. Although some would be fresh or recently emitted, others will have been resident for a long time and have been interacting with other components within the atmosphere.

Trace components provide a number of challenges of direct societal relevance, depending on the source distribution and atmospheric lifetimes of both physical and chemical processes, as well as consequential effects. For example, quantities of airborne particles in industrialised regions have increased markedly since Industrial Revolution. These particles can affect climate and have been implicated in human morbidity and mortality (Seinfeld and Pandis, 2006). Their role in climate arises from their ability to reflect or absorb solar radiation and to serve as cloud condensation nuclei (CCN). Some particles are sufficiently small so as to be respirable, and are sometimes even absorbed into the bloodstream. At certain concentration levels and exposure time, pollutants can endanger human health (World Health Organisation, (WHO)). As well as particulate matter (PM), some gases can be toxic, increase mortality or serious illness or threaten human health.

Air quality (AQ) is a condition relating the standard of ambient air to the concentration of species in the atmosphere. Although there has been considerable progress in controlling and managing air pollution, AQ problems remain a serious public concern: humankind and natural activities add and promote unpleasant conditions that affect ambient air (e.g. Heintzenberg and Charlson, 2009). Global rapid industrial and population growth have led to enhanced emissions of a wide range of pollutant gases and particles (Horowitz, 2006), leading to impacts on the climate system and human society (IPCC, 2013). Emissions come from human-induced activities (e.g. burning fossil fuels, chemical solvents, agricultural and manufacturing). Recent rapid increase in urban populations has been a major driving force behind the increase in air pollution in many developing regions, leading to increased energy demand, industrial activity and road traffic.

Weather and pollution are bidirectionally linked. First, the weather influences the dispersion and transport of pollutants; changes in meteorological parameters (e.g. wind speed, humidity, temperature, precipitation) can directly affect pollution concentration, distribution and removal, including the occurrence and rate of chemical reactions. Second, air pollution can also affect the weather and climate. Increases in trace components may influence climate change by causing adjustments to the radiative forcing (RF) and aerosol–cloud interactions (ACIs).

The science of air pollution is mainly concerned with determining, tracking and predicting chemical concentrations. Four key areas include emissions, transport, chemical interactions, and deposition (e.g. Zhang et al., 2010). Although understanding trace components is still evolving, there have some developments in understanding their formation mechanisms and changes in the atmosphere. Also, knowledge about their roles and consequent impacts in the atmosphere is growing. The following sections highlight the major trace components responsible for the effects highlighted above –the main focus of this study. The rest of this chapter is organised as follows: section 1.1 introduces trace composition in the troposphere, section 1.2 deals with trace gas chemistry, whereas section 1.3 focuses on aerosol properties and processes. Section 1.4 deals with particle interactions with clouds while section 1.5 focuses on meteorological controls on atmospheric composition and section 1.6 deals with impacts of trace components. Section 1.7 focuses on the representation of AQ and dynamical interactions at regional scale, section 1.8 discusses atmospheric composition and its interaction with the meteorology over southern Africa; section 1.9 discusses the scope of the study, and lastly section 1.10 gives an outline of the study.

1.1 Trace components in the atmosphere

Some of the trace species in atmosphere occur naturally, whereas others are from human-related activities. Although there is still some uncertainty in the formation of secondary organic components (Kroll and Seinfeld, 2008; Hallquist et al., 2009) from oxidation of volatile organic compounds (VOCs), Goldstein and Galbally (2007) estimate that about 10^4–10^5 different types of organic compounds have been measured in the atmosphere, mostly biogenic in origin. Biogenic VOCs (BVOCs) are probably the largest source globally, of gaseous emissions oxidized by the hydroxyl radical (OH) and ozone (O_3), giving rise to thousands of other compounds. However, the uncertainty is compounded by the fact that VOCs undergo various atmospheric degradation processes to produce a wide range of other species that may or may not contribute to the formation and evolution of secondary components from oxidation (Hallquist et al., 2009). Formation products evolve rapidly after primary emissions such that the chemical and physical properties change rapidly (Li et al., 2003), and the processes controlling evolution of species are different (Hallquist et al., 2009). BVOCs, together

with anthropogenic VOCs, can participate in reaction cycles with other trace components (e.g. NO_x, where $NO_x = NO + NO_2$) giving rise to a huge complexity of secondary components. The relative importance of the competing reactions (either by oxidants or photolysis) depends on the structure of the compounds, as well as ambient conditions (Atkinson and Arey, 2003). This section focuses on the main trace gaseous and particle phase components.

1.1.1 Trace gas composition

The main constituents in the air are nitrogen (N_2: 78%) and oxygen (O_2: 21%), while the remaining 1% is made up of trace gases, including noble gases and greenhouse gases (GHGs) such as carbon dioxide (CO_2), methane (CH_4), water vapour (H_2O) and ozone. The major natural sources of gases are biogenic, solid earth, oceans as well as human-induced or anthropogenic sources. Despite being in low concentration, these trace gases can have profound effects in the atmosphere (Williams, 2004), depending on their chemical and physical properties. Variations in gas concentrations are controlled by factors such as reactivity, lifetime and rate of production from different sources (e.g. geologic, anthropogenic, biological and chemical processes). The major carbon-containing gases (CO_2 and CH_4) have increased rapidly in the atmosphere and are major contributors to the anthropogenic-enhanced greenhouse effect. Although biomass burning (BB) is globally a much smaller source of trace gases (compared to biogenic and other natural emissions), it is one of the major sources of atmospheric pollutants (Li et al., 2003; Freitas et al., 2007) and climate altering species (Cristofanelli et al., 2009, and references therein). Fires contribute a considerable amount of primary gases such as carbon monoxide (CO) and nitrogen oxides (NO_x), which also lead to production of secondary gas components such as CO_2 and O_3. Also, anthropogenic processes (e.g. industrial combustion, automobiles, chemical reactors) constitute a substantial amount of pollutant species such as CO, NO_x, O_3 and sulphur dioxide (SO_2) in the atmosphere. A substantial amount of VOCs is generated from both anthropogenic and biological sources (section 1.2.3); the earth's natural vegetation releases huge amounts of organic compounds into the air (Guenther et al., 2000; Williams, 2004; Atkinson, 2008, and references therein). These trace gases play a crucial role in the Earth's radiative balance and atmospheric chemistry. Tropospheric species' concentrations attributed to human activities have increased markedly since Industrial Revolution era (Seinfeld and Pandis, 2006; Horowitz, 2006, and references therein). These changes affect the overall chemical processes in the atmosphere and influence the radiative adjustments. However, it is widely expected that global emissions will decrease strongly throughout the remainder of the 21st Century as a result of emission reduction policies enacted to protect human health (e.g. Westervelt et al., 2015).

1.1.2 Particulate matter (PM)

Airborne particulate matter (when suspended in air, species are collectively referred to as aerosols) can be highly variable in chemical and physical properties and vary across several orders of magnitude in sizes. Aerosols are of special interest to humankind because they affect the atmospheric branch of the hydrological cycle (cloud dynamics) and influence the chemical composition of the atmosphere. They play key roles in many environmental processes: scattering and absorption of solar radiation, influencing cloud formation (Torres et al., 1998; Pöschl, et al., 2010), participating in heterogeneous chemical reactions and affecting the abundance and distribution of trace gases (Hobbs, 2000; Hallquist et al., 2009). Likewise, PM can have profound effects both on human health and AQ (e.g. coughing, shortness of breath, lung damage, premature deaths), chemical composition and formation of photo-oxidants (Saud et al., 2011). For regulatory purposes and AQ monitoring, PM is classified in two groups ($PM_{2.5}$ and PM_{10}), each defining a range of particle sizes (section 1.3), although the types of aerosols not specified.

Different types of aerosols are directly emitted into the atmosphere (primary aerosols), whereas some are formed in the atmosphere (secondary aerosols) from chemical transformations and multiphase reactions of primary gaseous species. Examples of aerosols from the categories described above include desert dust, volcanic eruptions, pollen grains and marine sprays (natural); combustion products, construction site dust, industrial and automobile particulates (anthropogenic). Because of different production mechanisms and chemical properties, atmospheric particulates play different roles in the atmosphere. For example, particulates such as black carbon (BC) are good absorbers of solar radiation while some (e.g. sulphates) reflect solar radiation. PM sources, properties and processes fates are described further in section 1.3.

1.2 Photochemistry and gas reactions in the atmosphere

Tropospheric gaseous processes are driven largely by daytime photochemistry, with the energy from the sun interacting with trace molecular absorbers (as well as being attenuated by clouds and aerosols). The gas-phase oxidation initiated by reaction with OH and nitrate (NO_3) radicals and O_3, or via photolysis is the primary process through which most species evolve in the atmosphere (e.g. Monks, 2005). These reactions can alter the chemical or physical properties of most species and lead to the formation of other species or transformation of primary components.

Photochemistry is the underlying mechanism concerned with the chemical effects of light and reactions in the atmosphere, initiated by photons absorbed by molecules. It is the main driver of the atmospheric chemistry. When molecules absorb light photons they get into ‘excited state’ because of the excess energy. Consequently, the bonds between the atoms can be altered as the molecule wants to

get rid of excess energy absorbed, whereby it may either remain in the same or different state at the end. This results in energy loss to the environment in the form of heat or reduced light energy, leading to one or more chemical transformations via the formation of excited states (Brown, 1999). The process is driven by two basic principles: (i) light of a particular wavelength must be absorbed by a compound for the reaction to take place, and (ii) for each photon absorbed, only one molecule will be activated per subsequent reaction (Bailey et al., 1978). All subsequent physical and chemical reactions then follow from the excited species. Overall, the absorbed light energy acts to 'break' or reorganize the bonds within the compound molecules.

Tropospheric chemical reactions depend greatly on NO_x (Brown et al., 2007). NO_x is an important primary pollutant produced from anthropogenic and natural sources (e.g. fossil fuel combustion, BB, soil bacteria, lightning, oxidation of ammonia, mobile transport and other heavy machinery. Precisely, NO_x dominates the tropospheric O_3 budget, the abundance of OH and the nitrate aerosol (NO_3^-) formation (Miyazaki et al., 2012). It is emitted into the troposphere during the day, mainly as nitric oxide (NO) and later establishes a rapid equilibrium state with nitrogen dioxide (NO_2). At night, NO_2 is oxidized by O_3 into NO_3 –a photochemically unstable state, but one of the most chemically important atmospheric species (Brown and Stutz, 2012). The reaction influences the vertical profiles of O_3 and NO_2, which are precursor species of the NO_3 radical. Consequently NO_3 becomes a major oxidant during the night at the expense of the OH radical (when there is no photolysis), usually accompanied by the presence of dinitrogen pentoxide (N_2O_5) produced from the reaction between NO_3 and NO_2. NO_x can also be oxidized in the atmosphere to form nitric acid (HNO_3). Similarly, N_2O_5 can react with water molecules (H_2O) to form HNO_3 –a reaction responsible for depleting NO_x from the stratosphere, especially in Polar Regions. The OH radical, because of its short lifetime (~1s), is only present during the day, whereas the NO_3 radical plays a major role in nocturnal chemistry. The reaction of NO_2 with O_3 is perhaps the largest source of NO_3 in the atmosphere.

1.2.1 Daytime chemistry

Tropospheric daytime chemistry is driven by photolytic reactions. During the day, NO_2 is efficiently photolysed by solar radiation ($\lambda \leq 420$ nm) into O_3 and NO. The resulting O_3 can react with NO to form NO_2. The NO_x photostationary state process can be described through the following reactions (Monks, 2005; Atkinson et al., 2004):

$$NO_2 + h\nu \rightarrow NO + O(^3P) \quad [1.1]$$

$$O(^3P) + O_2 + M \rightarrow O_3 + M \quad [1.2]$$

$$NO + O_3 \xrightarrow{k} O_2 + NO_2 \quad [1.3]$$

where $k = 1.4 \times 10^{12} \exp[1310/T]$ (cm^{-3} $molecule^{-1}$ s^{-1}) is the rate constant at temperature T (Atkinson et al., 2004), M could be the sum of all abundant third molecules (e.g. N_2 and O_2) at a given pressure height. The photo-stationary state for O_3 equilibrium concentration is defined by:

$$[O_3] = \frac{J_{NO_2}[NO_2]}{k[NO]} \qquad [1.4]$$

where J_{NO2} is the photolysis rate of NO_2. Reaction [1.4] controls the partitioning between the NO_x family. Because O_3 reacts quickly with NO, the reaction leads to O_3 destruction. Therefore, the overall reactions result in no net formation or loss of O_3, unless VOCs are present to consume NO or convert it back to NO_2 (Al Razi and Hiroshi, 2012; Gacek, 2014). Because NO is consumed, it would no longer be available to react with O_3, but if more VOCs are added into the atmosphere, more NO will be oxidized to NO_2 and increase O_3. However, O_3 can be photolysed (λ = 290–320 nm) in the presence of water, which is the main source of OH in the troposphere:

$$O_3 + h\nu \rightarrow O_2 + O(^1D) \qquad [1.5]$$

$$O(^1D) + H_2O \rightarrow 2OH \qquad [1.6]$$

Once OH exists, it can oxidise VOCs and initiate the formation of the intermediate HO_x and RO_x radicals. Within the oxidation chain, O_3 is produced from the reactions of the peroxy radicals (RO_2 and HO_2) with NO. These radicals can convert NO to NO_2, which would later photolyse to produce the ground-state oxygen atoms $O(^3P)$ for the net ozone production (Atkinson, 2000), as illustrated in Fig. 1.1:

$$HO_2 + NO \rightarrow OH + NO_2 \qquad [1.7a]$$

$$H\dot{O}_2 + NO \rightarrow R\dot{O} + NO_2 \qquad [1.7b]$$

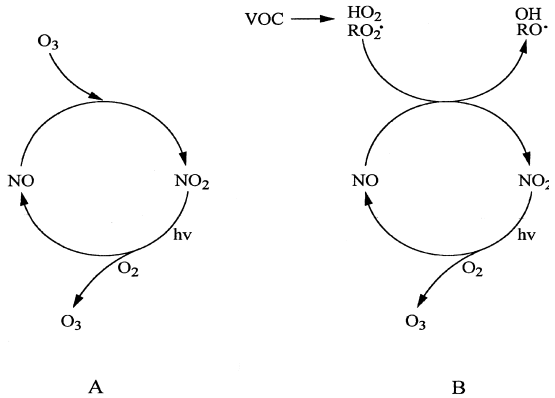

Fig. 1.1: Schematic reactions involving NO-to-NO_2 conversion and O_3 formation, (A): NO-NO_2-O_3 systems without VOCs and (B): NO-NO_2-O_3 systems in the presence of VOCs. (Adapted from Atkinson, 2000).

The influence of varying VOCs and NO_x concentrations on the O_3 production strongly depends on the ambient conditions (i.e. relative concentrations of NO_x and VOC). As shown in the ozone isopleth (Fig. 1.2), O_3 concentrations are sensitive to both VOC-limited and NO_x-limited regimes. A reduction

in O_3 positively correlates with a decrease in both VOC and NO_x concentrations (Jenkin and Clemitshaw, 2000; Monks et al., 2014). The isopleth is a useful regulatory control for O_3. For example, in highly polluted areas, the VOC : NO_x ratio is lower than 8:1, indicating that limiting VOC emissions is the most effective method for controlling O_3 (Jacobson, 2005). However, this conclusion does not always stand out because O_3 mixing ratios depend on other factors (e.g. meteorology, gas-to-particle partitioning), in addition to the chemical processes. Consequently high NO_2 leads to depletion of O_3. Thus, the reaction between NO_2 and OH is favoured leading to production of HNO_3 (the most active removal pathway for NO_x in the atmosphere during the day). The reaction is given by:

$$NO_2 + OH \rightarrow HNO_3 \qquad [1.8]$$

The nitric acid produced is a direct gas-phase precursor of ammonium nitrate aerosols (NH_4NO_3), removed mostly through wet or dry deposition rather than photolysing back to its products. Reaction [1.8] also provides an important OH loss mechanism under polluted conditions. The reaction terminates the cyclic chain reactions shown in Figure 1.1 and removes both NO_x and HO_x (HO_x = OH + HO_2) from the system (Seinfeld and Pandis, 2006). OH (daytime oxidant) is the most primary cleansing agent in the lower troposphere produced from O_3 photolysis, followed by the reaction of excited O_2 atoms with H_2O molecules. Its atmospheric abundance is controlled by the presence of species such as NO_x, CO, O_3, CH_4 and other high-order hydrocarbons, including UV solar radiation.

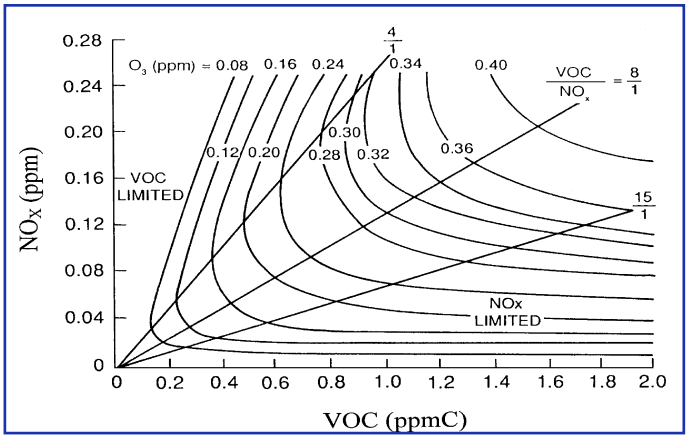

Fig. 1.2: Daily maximum O_3 concentrations [in ppmv] (curved lines) generated from various NO_x and VOC mixtures. O_3 shows an equal sensitivity to the VOC/NO_x ratio at a proportion of 8 to 1 (diagonal line through the origin). (Jenkin and Clemitshaw, 2000).

1.2.2 Night-time chemistry

Eventually, either lack of sunlight, NO or VOCs limits O_3 production. O_3 remaining at dusk can produce NO_3, the main active night-time chemistry driver. NO_3 is readily photolysed (Dentener and Crutzen, 1993; Monks, 2005), and so cannot persist during daytime:

$$NO_3 + h\nu \rightarrow NO + O_2 \qquad [1.9a]$$

$$NO_3 + h\nu \rightarrow NO_2 + O(^3P) \quad [1.9b]$$

The nitrate radical can oxidise a number of nonmethane hydrocarbons (NMHCs), including sulphur-containing compounds, and nitrate provides a route for the conversion of NO_x to nitric acid (Allan et al., 2000). The gas-phase oxidation of NO_2 by O_3 produces N_2O_5. This is also followed by the reaction of NO_3 with NO_2, one of the most important reactions in the formation of N_2O_5:

$$NO_2 + O_3 \rightarrow NO_3 + O_2 \quad [1.10]$$

$$NO_3 + NO_2 \leftrightarrow N_2O_5 \quad [1.11]$$

Reaction [1.11] indicates that N_2O_5 is thermally unstable and can dissociate back to NO_3 and NO_2 respectively. The forward reaction is pressure-dependent, whereas the reverse is temperature dependant thermal decomposition (Jacobson, 2005). Concentrations of NO_3 and N_2O_5 depend on the changes in meteorological conditions as well as NO_x variations (Brown et al., 2003). One of the dominant reactions at the surface at night, is the reaction between NO_3 and NO:

$$NO_3 + NO \rightarrow 2NO_2 \quad [1.12]$$

Although the above reaction leads to low NO_3 and N_2O_5 daytime concentrations, the latter concentrations can be sustained in polluted urban and agricultural conditions. But it is often assumed that for areas with large NO emissions, NO_3 chemistry is relatively less important because of its shorter lifetime (Stutz et al., 2004). Other major loss pathways for NO_3 include reactions with dimethyl sulphide (CH_3SCH_3 or DMS) and hydrocarbons (Allan et al., 2000) or heterogeneous uptake. The reaction between NO_3 and DMS is mostly important in marine environments:

$$NO_3 + CH_3SCH_3 \rightarrow CH_3SCH_2 + HNO_3 \quad [1.13]$$

$$CH_3 + SCH_2O_2 + NO_3 \rightarrow CH_3S + CH_2O + NO_2 + O_2 \quad [1.14]$$

At night (in the absence of NO), reaction [1.13] leads to NO_3 removal and consequently affects the turnover of NO_3 lifetime, but not the rate of NO_x removal (Allan et al., 2000). Because NO_3 is water-soluble and has a high dry deposition velocity, it is easily removed from the atmosphere through wet or dry deposition. At steady state, the nitrate radical lifetime is given (Allan et al., 2000; Brown et al., 2003; 2007) by:

$$\tau[NO_3] = \frac{[NO_3]_{SS}}{k_1[NO_2][O_3]} \quad [1.15]$$

where $[NO_3]_{ss}$ is the steady state nitrate concentration, and k_1 is the first-order rate coefficient. Also, because N_2O_5 is only produced at night and decomposes within a short time, it becomes unimportant during daytime (Jacobson, 2005). Daytime N_2O_5 loss by photolysis (λ = 385 nm) occurs slowly, given by:

$$N_2O_5 + h\nu \rightarrow NO_2 + NO_3 \quad [1.16]$$

The NO_3 starts building up after sunset and reaches its maximum concentration around midnight; its abundance or destruction is determined by the rate at which NO_2 is oxidized by O_3. Production ceases once all NO_2 has been consumed by O_3. Because high O_3 mixing ratios exist during daytime within the residual layer and are constant with height, the NO_3 profile would likely resemble that of NO_2, but production slows down at night due to decreases in O_3 concentration according to reaction [1.3]. Under many tropospheric conditions, NO_2, NO_3 and N_2O_5 can reach an equilibrium (Brown and Stutz, 2012) given by:

$$[N_2O_5] = k_{eq}[NO_2][NO_3] \qquad [1.17]$$

where k_{eq} (cm^3 $molecule^{-1}$ s^{-1}) is a temperature-dependent equilibrium constant. The rate of N_2O_5 uptake by particles depends on aerosol composition and meteorology (e.g. relative humidity [RH] and temperature) however, is still not fully understood (Chang et al., 2011, and references therein). Its loss pathways occur through direct (hydrolysis reaction) and indirect (any reaction that can act to limit NO_3 radical production) reactions. One of the main loss of N_2O_5 is the heterogeneous reaction with H_2O leading to nitrate aerosol production through reaction:

$$N_2O_{5(g)} + H_2O_{(l)} \rightarrow 2HNO_{3(aq)} \qquad [1.18]$$

The above reaction is thought to be a dominant pathway for N_2O_5 loss (Dentener and Crutzen, 1993), whereas the HNO_3 produced contributes to the nitrate burden in the atmosphere (Lowe et al., 2015). Because HNO_3 is a longer-lived reservoir than N_2O_5, conversion of N_2O_5 to HNO_3 slows down the regeneration of NO_x and decreases its ratio. From reaction [1.17], the mixing ratio of NO_2 can be determined (Brown et al., 2007) from the ratio of N_2O_5 to NO_3 and the ambient temperature:

$$[NO_2]_{cal} = \frac{[N_2O_5]}{K_{eq}[T] \times [NO_3]} \qquad [1.19]$$

where $K_{eq}(T)$ is a temperature-dependent equilibrium constant for the reversible association of NO_2 with NO_3 to form N_2O_5. Figure 1.3 highlights the chain reactions between NO_x and other species, including the radicals in the atmosphere.

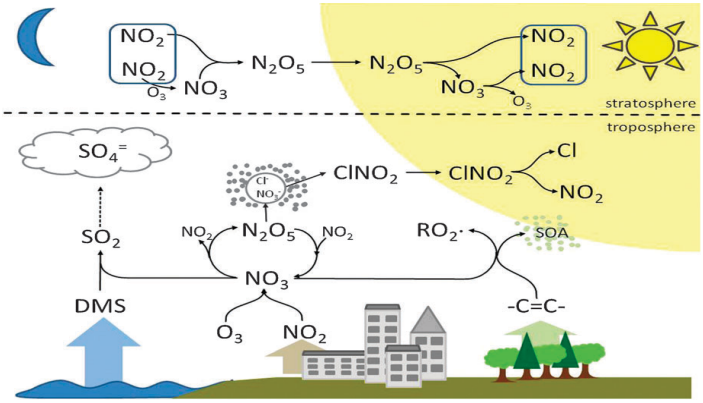

Fig. 1.3: Schematic diagram of the nitrogen cycle and the atmospheric aerosol uptake (Brown and Stutz, 2012).

1.2.3 Volatile Organic Compounds and their oxidation

Major anthropogenic VOC classes include alkanes, alkenes aromatic hydrocarbons, whereas biogenic VOCs (mainly from vegetation) are alkenes: isoprene, monoterpenes, sesquiterpenes and other oxygenated VOCs (Atkinson, 2008, and references therein). VOCs are highly reactive species (Guenther et al., 2000; Atkinson and Arey, 2003; Seinfeld and Pandis, 2006), which once entering the atmosphere are transformed by photolysis reactions ($\lambda \geq 290$ nm) and oxidation by the OH radical during daytime, whereas at night transformations occur due to reactions with the NO_3 radical. Reactions with O_3 occur in certain locations and times, whereas reactions with chloride (Cl) atoms can occur during daylight hours (Atkinson and Arey, 2003) in the marine environment (Hallquist et al., 2009). Oxygenated VOCs and organic nitrates are, to a large extent, similar to alkanes, alkenes and aromatics in their reactivity (Atkinson, 2008). BVOCs influence the atmospheric O_3 chemistry in many ways and play dominant roles in the chemistry of the lower troposphere and atmospheric boundary layer (Fuentes et al., 2000). For example, isoprene can compete with O_3, acting as a direct sink for oxidants such as NO_x, and can contribute to the sequestration of N_2 and oxidation products (Guenther et al., 2000). The double carbon bonds (C=C) react significantly with NO_3 and O_3 radicals, whereas those containing carbonyl (>C=O) or nitrate (ONO_2) groups absorb radiation ($\lambda \geq 290$ nm) and undergo photolysis.

The double bonds within these molecules make them liable to abstraction by the O_3 or the NO_3 radical, in addition to the OH radical. However, there are cases other than those mentioned above, which occur for alkenes, alkanes and aromatics (Atkinson, 2008) such as the formation of alcoxy and peroxy radicals. On a global and regional scale, the emissions of BVOCs exceed those from anthropogenic compounds by a factor of ~10 worldwide, but they tend to have shorter lifetimes because of their high atmospheric reactivity (Woods and Hall, 1994). Table 1.1 shows tropospheric lifetimes of some VOCs calculated at 298 K rate constants (Atkinson and Arey, 2003, Atkinson, 2008).

VOC	OH	NO_3	O_3	Photolysis
Propane	11 days	>1.8 years	>4,500 years	
n-decane	1.0 days	165 days	>4,500 years	
Propene	5 h	5 days	1.6 days	
Isoprene	1.4 h	50 min	1.3 days	
α-pinene	2.7 h	5 min	5 h	
Benzene	9 days	>4 year	>4.5 years	
m-xylene	6 h	180 days	>4.5 years	
Formaldehyde	1.3 days	80 days	>4.5 years	4 h
Acetone	60 days	>4 years	>4.5 years	60 days
Ethanol	4 days	>0.6 years	>4.5 years	

Table 1.1: Calculated lower tropospheric lifetimes (at 298 K) for selected VOCs. All VOCs react with the OH radical and may also react with NO_3 and O_3. Contrastingly, only alkenes and other VOCs with double carbon bonds (C=C) react significantly with NO_3 and O_3, while only compounds containing carbonyl (>C=O) groups and nitrate (-ONO_2) undergo significant photolysis. (Adapted from Atkinson, 2008).

In the continental boundary layer, several VOCs (particularly monoterpenes and isoprene) react rapidly with NO_3. The reactions constitute a major sink of the nitrate in rural environments where monoterpenes are usually the most important reaction species (Geyer et al., 2001). The lifetime of a VOC with respect to a reaction with a compound X can be expressed (Atkinson, 2008) as:

$$\tau_X = \left(k_X[X]\right)^{-1} \quad [1.20]$$

where k_X is a VOC rate constant for reaction with X, and for photolysis:

$$\tau_{photolysis} = \left(k_{photolysis}\right)^{-1} \quad [1.21]$$

The overall VOC lifetime is given by:

$$\frac{1}{\tau_{overall}} = \sum\left(\frac{1}{\tau_i}\right) \quad [1.22]$$

1.3 Atmospheric particulate matter

Particulate matter (PM) comprises a range of chemically and physically diverse solid or liquid components suspended in the atmosphere. The particles can span 5 or 6 orders of magnitude in size and are made up of thousands of different substances entering the atmosphere from both anthropogenic and natural sources (Querol et al., 2004). Some particles are small enough to be easily blown around by wind, or inhaled into the human body system through the lungs (Holland et al., 2001). PM is sometimes referred to as totally suspended particles (TSPs). A complete description of particulates must account for their chemical composition, morphology, particle size distributions and different types in nature.

1.3.1 Sources

Because atmospheric particulates are formed from different sources (anthropogenic and natural), and production mechanisms (primary and secondary), they exhibit wide heterogeneity and a range of physical, chemical and thermodynamic properties. Their concentrations vary in the atmosphere as many of them continuously undergo mechanical and chemical transformations and have widely varying lifetimes.

1.3.1.1 Anthropogenic and biogenic sources

Two categories of aerosol production mechanisms include anthropogenic (or man-made) and biogenic (natural). Anthropogenic sources include fossil fuel and human-induced BB, industries and power

plants, automobiles (including marine transport and aircrafts), construction site dust, mining, textiles or milling industries and agricultural activities. These are sources in which aerosol generation occurs as a result of human influence or involvement in the process. Since the beginning of the Industrial Revolution, population has also grown and more urbanization increased, leading to enhancement of particles in the atmosphere. On the other hand, biogenic sources are natural aerosol-producing processes. Biogenic sources depend on environmental and ecological parameters and are prone to global change influence (Andreae and Crutzen, 1997). The sources include aeolian or wind-blown dust, volcanic eruptions, natural wild fires, plant emissions (VOCs), ocean sprays, microbes/soil bacteria, etc.

Anthropogenic and biogenic sources can be further classified into production mechanism or process of pollution generation. For example, anthropogenic sources can be described into point sources (e.g. blast or combustion furnace, chimneys), mobile sources (e.g. automobiles) where emissions are driven by fuel burning engines; area sources (e.g. livestock operations such as piggery), controlled burning (agricultural activities, fuel production, clay heating), waste disposal and landfill. Similarly, biogenic sources can also be classified in terms of deserts and open land, oceans (marine biology), volcanic eruptions, radioactivity, termites (microbes and soil bacteria) vegetation, natural/veld fires (e.g. lightning).

1.3.1.2 Primary and secondary particulates

Atmospheric particulates may be divided into two classes according to their originating processes: primary and secondary. Primary aerosols (PAs) comprise particles that enter the atmosphere directly from the sources as liquid or solid particles, and may either be natural or anthropogenic (e.g. volcanic, sea sprays, pollen grains, biogenic plants debris, microbes, combustion products, construction site dust, automobiles, biomass- and fossil fuel burning etc.). Aeolian dust is a major natural contributor to primary aerosols, although mineral dust contribution can sometimes be attributed to human influence (e.g. construction and mining).

Secondary aerosols (SAs) are formed in the atmosphere from chemical reactions and physical transformations of primary particulates, under different conditions (temperature, RH and sunlight or photo energy), from different precursors of both biogenic and anthropogenic VOCs, or by oxidation reactions followed by gas-to-particle conversion (Kroll and Seinfeld, 2008; Crippa et al., 2013). Their formation processes such as coagulation, aggregation outgassing and gas-to-particle conversion evolve rapidly after emission of primary products. As a result their chemical, physical and optical properties can change dramatically during aging (Li et al., 2003, and references therein). Also, condensation of gas phase material -most notably water vapour, on existing particles can add secondary PM to the

aerosol (Heintzenberg, 2003). Formation may also be initiated by chemical reactions of primary emitted organics in the particle phase (Robinson et al., 2007). Meanwhile, the most uncertainty about secondary aerosols is their formation and evolution processes from the chemical transformation of atmospheric organic compounds (Kroll and Seinfeld, 2008; Hallquist et al., 2009).

Primary and secondary aerosols differ from one another in terms of their emission sources, formation, particle sizes and to some extent, atmospheric residence times and transport mechanisms. For example, SAs make up most of the fine particle mode whereas PAs make up most of the coarse mode. Fine particulates can be transported over longer distances from the sources and have longer residence times in the atmosphere than coarse particulates. Their formation is dominated by a few classes of VOCs that form aerosols with yields readily measured in laboratory chamber studies (Kroll and Seinfeld, 2008). Also, PAs can have higher concentrations near the sources than SAs and tend to have relatively shorter lifetimes because of their large particle sizes and they are quickly deposited or transported over short distances.

1.3.2 Particle sizes

Atmospheric particulates can range in size from a few nanometers to a few hundred micrometers. They are classified and described in modes describing particle size ranges and production sources. Although particulates are referred to as having a diameter (implying that they are spherical), this assumption is necessarily idealised for simplification of mathematical problems or representation of aerosol behaviour. There are various diameter definitions used in describing aerosols: projected area, aerodynamic (Yurteri, 2010) geometric, stokes and mobility. The aerodynamic equivalent diameter d_a is one of the commonly used (Hinds 1999; Yurteri, 2010). As such, for the purpose of the current modelling study we assume equivalence.

Particle size distributions are classified in terms of magnitudes of diameter range (function of diameter, D_p). However, because of different instruments and methods used in aerosol technology, different sizes will be reported for different measures of diameter in the literature. Generally, particles are classified in terms of ‘fine’ or ‘coarse’ modes (Fig. 1.4). Furthermore, sizes are roughly divided into sub-modes or ranges. The nucleation (or nuclei) mode comprises of particles up to 0.01μm in diameter, whereas the *Aitken* mode or fine particles spans roughly 0.01–0.1 μm in diameter. Particles in this mode form interstitial aerosols scavenged by cloud droplets (Binkowski and Roselle, 2003). Nucleation is one of the processes leading to the formation of new particles through gas-to-particle phase change, especially in the Aitken mode (Hussein et al., 2004; Kukkonen et al., 2011), though close to source the nucleation mode is frequently present as an even finer discrete mode.

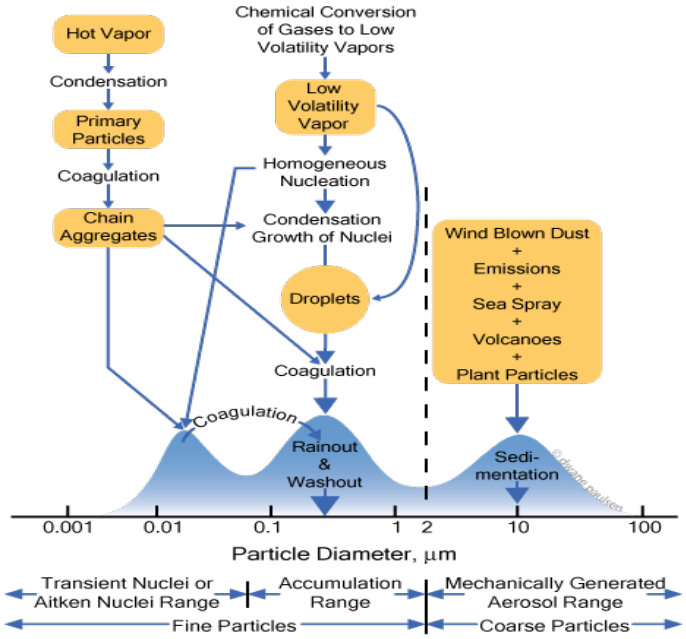

Fig. 1.4: Schematic particle size distribution of atmospheric aerosols showing principal modes. (www.dwanepaulsen.net/blog/category/aerosols/).

The next set of particles (*accumulation* mode) spans between 0.1–1 μm. This range represents particle growth mainly due to coagulation or from condensation of semi-volatile or involatile gases (e.g. sulphuric (H_2SO_4), nitric (HNO_3) and hydrochloric (HCl) acids, ammonia (NH_3) and organic compounds). CCN formed in this range will be distributed as aerosol within cloud water, where the mass, surface area and number may be lost through precipitation (Binkowski and Roselle, 2003). The last range (*coarse* mode) comprises particles larger than around 2.0 μm in diameter, includes particles produced from mechanical processes and introduced directly into the atmosphere. These are efficiently deposited to the ground mainly by sedimentation processes because of their particle mass.

PM is normally classified into two main groups for regulatory purposes. The particle mass of size range D_p < 10 μm is known as PM_{10}, whereas finer particles with D_p < 2.5 μm are commonly referred to as $PM_{2.5}$. The coarsest particles of D_p > 10 μm are included in the definition of TSP. The fine mode particles have longer residence times in the atmosphere than the coarse modes. They can be transported over longer distances (hundreds to thousands of kilometres) from their sources, whereas the coarse particles are quickly removed from the atmosphere within a short time. Carbonaceous compounds such black- and organic carbon (BC and OC) –which are the main components of PM, also are of small sizes, although they can be generated in large quantities. Both BC and OC lie in the submicron range and exhibit wider size distributions.

1.3.3 Particle composition

Atmospheric particulates exhibit large spatial and temporal variations, not only in terms of particle size distribution, but also in terms of chemical composition. Many of these species are mixtures of different chemical compounds; water-soluble inorganic and organic salts, mineral salts and other various types from the Earth's crust (Hobbs, 2000). They comprise sulphates, nitrates, ammonium, organic matter, crustal species, sea salt, metal oxides and hydrogen ions, including water droplets (Zhang et al., 2000; Seinfeld and Pandis, 2006). Sulphates, ammonium, organic and elemental carbon are found mostly in the fine particle mode, whereas crustal materials (including silica, SiO_2), Ca, Mg, NH_4^+ and other particles, occur in the coarse mode. However, not all particles contain all of the above species because some can be externally mixed, depending on the source formation and/or evolution (Haywood and Boucher, 2000; Zaveri, 2008).

One of the major components in atmospheric particulates is organic compounds (carbonaceous aerosols); the two main classification being BC and OC. Organic material accounts for a large fraction of atmospheric aerosols (Pöschl, 2005; Baltensperger, et al., 2005; Kroll and Seinfeld, 2008; Ram et al., 2012) and consists of a mixture of material with different radiative properties, both absorbing and non-absorbing (Torres et al., 1998). They are complex mixtures of chemical compounds containing carbon atoms, generated primarily from their sources or formed as secondary organic compounds (SOCs) during aggregation or nucleation of gaseous components in the atmosphere. Although VOCs are both anthropogenic and biogenic, they are mainly generated from biogenic sources.

1.4 The role of aerosols as cloud condensation nuclei and in cloud formation

Aerosols are fundamental to cloud formation because they serve as sites upon which clouds form when water vapour condenses to form liquid droplets (or freeze to form ice). Specifically, liquid droplet formation occurs when water vapour condenses on the surface of particles known as cloud condensation nuclei (CCN). By definition, CCN refers to a subset of aerosols that can nucleate into cloud droplets at a given supersaturation. The ability of aerosols to act as CCN depends on particle sizes and chemical composition (McFiggans et al., 2006; Andreae et al., 2009). Clouds form when the environmental supersaturation exhibits a transient maximum triggered by the rising air parcel, accompanied by expansion and adiabatic cooling and condensation onto the particles, permitting the activation of CCN into cloud droplets. Depending on the ambient temperature, cloud droplets will form, beginning a chain that may lead to large cloud droplets precipitating (Andreae et al., 2009).

During liquid droplet formation, an aerosol that grows to a size exceeding its critical radius r_c, is said to be 'activated.' This depends on the degree of supersaturation S, and updraft velocity w within the

air parcel. Evolution of droplets depends on the microphysical dynamics, including competition of CCN particles for water vapour. *Köhler theory* is an equilibrium description of droplet activation, describing the relationship between the chemical composition, size and supersaturation of an aqueous solute growth in thermodynamic equilibrium (Köhler, 1936). The relationship is expressed (McFiggans et al., 2006) as:

$$e'(r) = e_s(\infty)\alpha_\omega \exp K_e \qquad [1.23]$$

where $\alpha_\omega = \left\{1 = \frac{3v\Phi M_s m_w}{4\pi r^3 \rho_w m_s}\right\}$ and $K_e = \left(\frac{2\sigma}{rR_v T\rho_w}\right)$

In the expressions above, $e'(r)$ represents the vapour pressure of water, $e_s(\infty)$ represents the saturation vapour pressure of water, v is the number of ions in the solution, Φ is the molar osmotic coefficient, M_s is the solute molecular weight, m_w is the molecular weight of water, r is the solute radius, ρ_w is the water density, m_s is the mass of solute, σ is the surface tension, R_v is the universal gas constant, T is the temperature, α_ω is the water activity, and K_e is the Kelvin factor. Two opposing effects (the Kelvin and Raoult effects) normally act to modify the droplet growth within the solution. The Kelvin effect describes the change in supersaturation vapour pressure (SVP) due to a curved surface, whereas the Raoult effect describes the effect of a dissolved solute on the vapour pressure. Specifically, a dissolved solute dissociates, and SVP of the solvent is lowered by a factor known as the ionic dissociation (van Hoff's vector). Thus, Köhler theory can be viewed as the balance between the two effects. The Köhler equation given by [1.23] above combines the Kelvin and Raoult effects and governs the growth of solution droplets that originates from deliquescence of solutes. The Köhler curve (Fig. 1.5) depicts the combined effect of the two forces on the SVP of water vapour as a function of particle size (for droplets containing different amounts of salt). If RH becomes higher than the equilibrium humidity for the droplet radius and solute concentration, the droplet experiences condensation and grows; if RH becomes lower than the equilibrium humidity, then the droplet evaporates. Otherwise, it remains in stable equilibrium with its environment at S_c (critical saturation), corresponding to the peak of the Köhler curve at critical radius r_c. Any change in saturation ratio will result in the droplet either growing or evaporating. The region where $r < r_c$ is when the droplet is in a stable equilibrium and still growing towards the activation point, whereas $r > r_c$ is when the droplet is in an unstable equilibrium (condensation region). If the droplet radius becomes slightly larger than r_c, RH also reduces and the droplet grows further but deviating from its equilibrium point.

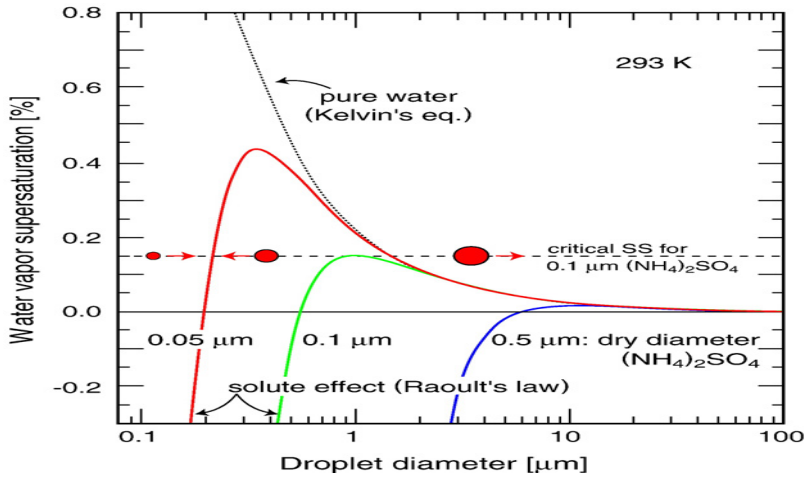

Fig. 1.5: Schematic diagram of Köhler curves showing equilibrium of water vapour saturation. Dotted curve indicate pure water whereas solid curves represent dissolved solute at different masses. When droplet radius is less than r_c, droplets are in stable equilibrium, whereas for $r > r_c$ then droplets are in unstable equilibrium. (Andreae and Rosenfeld, 2008).

1.4.1 Cloud formation

Cloud formation occurs due a combination of both thermodynamic and microphysical processes. As mentioned earlier, condensation of water vapour will not occur unless sufficient CCN are present to initiate the process. However, this is an atmospheric property that CCN are always present so that supersaturation rarely exceeds 1% during cloud formation. The presence of aerosols in the atmosphere facilitates water vapour condensation and initiates cloud droplet formation. Cloud droplets and ice particles do not form in the atmosphere by homogenous nucleation in the absence of foreign condensation nuclei (Andreae and Rosenfeld, 2008). Otherwise it would require initial formation of tiny embryonic water droplets with very tightly curved surfaces onto which water vapour will condense. This effect (described by the Kelvin effect) is such that the vapour pressure over the embryo is much greater than that over a flat surface. Survival of the droplets is determined by the balance between condensation and evaporation. On the other hand, heterogeneous nucleation is favoured because water vapour pressure over a solute is lower than that over pure water (Andreae and Rosenfeld, 2008). This is the opposing Raoult effect. Condensation of water vapour on soluble particles occurs because of the solute effect opposing the curvature term on the droplet. Once droplets become activated, they grow quickly at first. But because the rate of droplet growth is inversely proportional to droplet radius, growth slows as droplets grow bigger. This means cloud can take some time to reach the sizes at which they can precipitate (at $r \approx 1000$ μm). For clouds to initiate precipitation, droplets need to grow to the precipitable sizes as stated above. Cloud droplet growth can be facilitated by a series of mechanisms such as water vapour condensation, droplets coalescence, and ice processes (Seinfeld and Pandis, 2006).

Meanwhile, different processes can hinder droplet growth. For example, two or more particles can coagulate, especially when some droplets are much larger than the majority of the droplets. This can result in larger particles growing (bigger) at the expense of smaller nucleated ones –which can shrink. However a large population of small-nucleated particles increase the chance of coagulation between themselves. While this will make them increase in size, the number concentration consequently reduces as they merge. A cloud mass can exist in both warm phase (in which the ice phase does not play a significant role in either the thermodynamics or precipitation processes), and cold phase (where the ice phase plays a role). Generally, warm clouds have their top surface temperature above 0° C, although the physical processes can still be effective in cold or supercooled clouds (Cosgrove, 2010). Therefore, it is important to understand cloud dynamics from the underlying factors of cloud development and those that influence precipitation in cloud systems (Martins et al., 2011).

1.5 Meteorological influences on atmospheric composition

Even after chemical species are formed, further modifications and evolution can still take place, particularly as a result of fluctuation in meteorological conditions (Appraisal, 2013) that are effective mechanisms for pollution transport, distribution and removal from the atmosphere. The processes are driven by the meteorology which feedback to the chemistry and vice versa. Ambient pollutant concentrations are impacted by meteorology because sunlight affects the rate at which pollutants form, as well as other chemical properties (Garcia et al., 2008). Transport of chemical species and their distribution mechanisms are all important processes involved in pollution variation and interaction with the atmosphere. For example, the prevailing westerly and southwesterly flows (see Chapter 4) transport moisture from the Atlantic and Indian Oceans, as well as anthropogenic aerosols from the coastal areas into higher elevations. It is outside the scope of this thesis to provide an in-depth discussion of the range of weather patterns and meteorological features that can influence atmospheric components. However, this section outlines key factors dominating the distribution of atmospheric components.

1.5.1 Atmospheric stability, mixing and the planetary boundary layer height

The first stage of the effluents after their initial injection into the atmosphere is to enter the general atmospheric circulation. While in the atmosphere, circulation and exchange of species occurs through different layers, controlled by the local meteorological patterns that strongly affect the transport and mixing of both trace gas and particulates (Chapman, et al., 2009). Concentrations are controlled by several factors such as reactions with other substances (e.g. oxidation and photochemistry), rate (or flux) of emission from the sources, as well as the height of the planetary boundary layer (PBL) within which emissions are mixed in the troposphere.

During the day, the Earth absorbs solar radiation, which increases the surface temperature and facilitates turbulent mixing, whereas at night (because there is no sunlight and most chemical processes are dormant), the cooling of the surface air can create an inversion near the ground. A stable layer exists in the lower PBL at night, preventing the ventilation of the emissions (Seinfeld and Pandis, 2006). Consequently the PBL shrinks so that pollutants emitted at night are trapped within a shallow boundary layer and can reach relatively high concentrations. After sunrise, the surface heats up and the increasing turbulence transports pollutants within the PBL. As the day progresses, the heating of the atmosphere gradually erodes stable conditions developed at night until the unstable daytime profiles are re-established at some height above. This unstable layer in direct contact with the surface is known as the *mixing layer*, the top of which is known as the *mixing depth*. In low-wind conditions, temperature inversion develops near the surface, but if the winds are strong, cold air can still be forced upwards by mechanical turbulence and moderately stable conditions extend to some depth above, hence extending the boundary layer height. When the day ages, the surface temperature begins to cool again, increasing the stability; the upward transport of pollutants is then hindered by the stable conditions. Concentrations of pollutants are less dispersed within a deeper PBL than in a shallow PBL.

An analogue of the above diurnal variations can be explained through Fig. 1.6 below. Normally the lowest layer within the troposphere (about 1–2 km in depth) forms a layer with which the atmosphere is in contact with the ground surface or sea. Surface–air interaction occurs through two processes: mechanical (due to friction exerted by the wind against the ground surface causing wind shear and turbulence) and thermal (contact between the lower atmospheric layer and the ground surface through electromagnetic radiation). The vertical height, denoted z gives the thickness of the PBL. Radiative cooling at night is compensated by decrease in the vertical height known as the *nocturnal boundary layer* (NBL), in which mixing is caused by wind friction. The thickness of z_i at night depends on the prevailing wind fluctuations as well as the roughness of surface, and rarely exceeds 300 m. Above NBL, the air becomes slightly stratified due to heat loss at night. After sunrise, the atmosphere begins to heat up from below and convective motions overtake the wind shear-turbulence. The resulting penetrative convective processes gradually erode the stratified layers created at night and replace them with the new boundary layer height. Depending on the strength of the stratification above the NBL, penetrative convection may either be fast or slow. However, the wind-induced turbulence is much weaker than convection-induced turbulence, except near the base of the PBL created, where they might be of equal intensity. Subsidence inversion occurs when the PBL reaches its maximum.

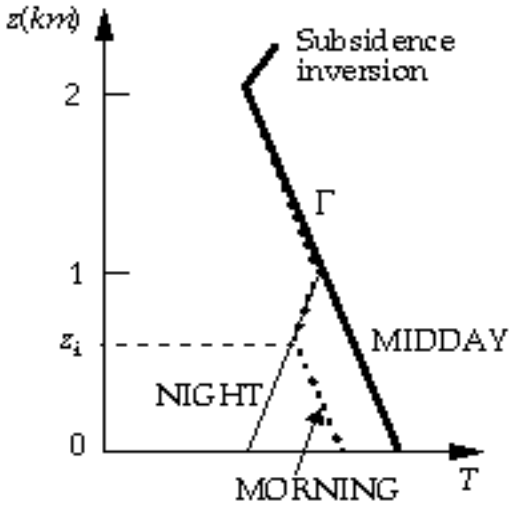

Fig. 1.6: Variation in the PBL between night-time and daytime. The PBL layer height varies due to the radiative solar heating (day) and cooling (night). (http://acmg.seas.havard.edu).

Pollution sources such as BB release a large amount of thermal energy (in the form of heat) in addition to the solid and gaseous substances emitted into the atmosphere. This thermal energy gives the smoke plume the buoyancy that generates strong updrafts above the fire (Labonne et al., 2007) and also determines the probable height through which emissions can rise before mixing into the atmosphere, depending on the buoyancy that the fires can maintain. However, the actual injection height depends on environmental factors (e.g. atmospheric stability, amount of water vapour, wind speed) prevailing at the time, heat flux and the intensity or fire size (Guan et al., 2007; Freitas et al., 2007; Rio et al., 2009; Williams et al., 2012). Emissions are well mixed by diurnal convection in the boundary layer, while those reaching the free troposphere can be transported over long distances (Labonne et al., 2007).

1.5.2 Lifetimes of atmospheric components

The production and rate of pollution distribution from the Earth's surface or sources, their subsequent dispersion and residence (i.e. lifetime) in the atmosphere are dependent upon the type of emission and the prevailing meteorology. During emission, pollutants become concentrated around the point source; concentrations decline with distance away from the source as dispersion and transport take place. Similarly, concentration can be high around a place of deposition, depending on the amount of pollution and mechanisms involved and the form of deposition taking place. Nevertheless, the lifetimes of pollutants are not only determined by species concentrations and removal processes in the atmosphere. Other factors such as the competing rates of chemical reactions and transformations also play a role (Husar and Husar, 1996). Collectively, pollution flux in the atmosphere is determined by their emission, transport and removal (Rind et al., 2009). The fine particles are easily blown by wind and can be transported over long distances; these are mainly removed by wet deposition. For the

coarse particles, the main form of deposition is sedimentation due to gravity. On the other hand, intermediate species can coagulate to form larger particles and be deposited in the same way. Particles that can be lifted higher into the atmosphere tend to have longer lifetimes.

The daily average distribution and mixing ratios of atmospheric compounds are strongly influenced by their dispersal into the atmosphere (Forkel et al., 2006). For example, the rate of reaction and oxidation products contribute to the diurnal variation in species concentration and are strongly influenced by the diurnal vertical mixing. Two main ways through which a variety of trace components are removed from the atmosphere are wet deposition (involving gas and particle scavenging in the air by clouds and precipitation), and dry deposition (direct collection of gases and particles in the air by vegetation and the earth's surface). Wet deposition involves multistage pathways including interactions between gas and particle phases. For example, various interactions such as absorption, solubility, reaction, nucleation, species capture and precipitation. Similarly, dry deposition can be accompanied by chemical processes such as oxidation reactions. These pathways also act as key determinants of residence times of trace components. Wet deposition and scavenging occurs through several ways such as:

Rainout: aerosols (CCN particles leading to rain drops) that will later be deposited into the ground surface during precipitation.

Washout: removal of aerosol by cloud droplets. This occurs when an aerosol is incorporated into an already existing cloud drop and then grows large enough to fall as rain.

Sweep out: occurs in aerosols entrained below cloud base, which then impact onto the falling raindrops. The impaction can result in particles incorporated into the raindrops and later deposited with the drops.

Occult deposition: (deposition by fog and cloud droplets). This is dependent on the impaction efficiency (likelihood) that a particle will strike a surface during the flow. It is a function of particle size where larger particles are more likely to impact on a surface feature such as raindrop than smaller particles.

1.6 Effects of atmospheric trace components

1.6.1 Air quality: The role of atmospheric trace components and human health

Air pollution is the main area of concern in human health affecting both developed and developing nations. It has been widely recognized that atmospheric pollutants can substantially degrade AQ, thereby presenting significant problems to human health and ecosystem. For many decades, air pollution has been associated with the export of pollutants from urban (e.g. large cities and industrial areas) to regional and global environment. This is one of the major concerns of AQ because of the wide-ranging potential consequences to human health, ecosystems, visibility, weather modification, RF and changes in the tropospheric oxidation capacity (Salam et al., 2008; Al Razi and Hiroshi, 2012).

The rapid development and increased urbanization has been a major environmental driving force regarding AQ degradation in all scales as a result of vehicular emissions, stack releases, construction dust and gaseous emissions, where humans are exposed to high levels of pollutants. Governments and other organisations put in place some governing standards and regulations to monitor the amount of emissions in the atmosphere. AQ guidelines provide an assessment on health effects due to air pollution; threshold limits are set to ensure that the total average concentrations of pollutants do not exceed certain range.

Depending on the duration of exposure and type of pollutant, effects can be severe or long lasting (e.g. respiratory diseases and disorders) and/or result in deaths (Garcia et al., 2008). For example, WHO estimate about 80% of outdoor pollution-related premature deaths due to heart disease and stroke, 14% due to chronic obstructive pulmonary disease or acute respiratory infections and 6% due to lung cancer (www.who.int/mediacentre/factsheets/fs313/en/). WHO also report that outdoor air pollution is carcinogenic to humans, with PM closely associated with increased cancer risk. For example, exposure to PM_{10} through ambient outdoor pollution in both rural and urban areas was estimated at 3.7 million premature deaths worldwide in 2012.

Although different countries and organisations have different set standards, global guidance is offered for threshold limits to key pollutants that pose health risks. The standards vary between countries and organisations for different pollutants, but are constantly reviewed to ensure that polluting sources do not exceed the limits. Different regulatory limits are provided by EU directives, UK legislative laws, SADC and NILU –all abiding to the set limits and apply worldwide, based on expert evaluation of current scientific evidence for key pollutants such as PM, NO_x, CO, SO_2 and O_3. These pollutants and their precursors may be of anthropogenic or natural and comprise of primary and secondary components. AQ guidelines provide the basis for protecting human health from adverse effects of air pollution by reducing or eliminating those contaminants known to be hazardous to human health and well-being. The standards support the establishment and implementation of ambient AQ objectives to protect humans and the environment (SADC report, 2008). Once they are adopted, they become legally binding and enforceable. The standards can be developed for 1-hour, 8-hour, 24-hour, monthly or yearly-averages. Air quality and pollution concentration is the key focus of chapter 5, and shall be discussed further in that chapter.

1.6.2 Influence of trace components on meteorology and climate

In addition to their influence on the AQ, trace components can influence atmospheric dynamics on both short- and long-term scales. Although increases in long-lived GHGs are responsible for most of global-scale perturbations in industrial era, the short-lived trace components also play crucial roles in

local contributions. For example, water vapour is a strong infrared absorber but is a locally, regionally and temporally variable component. On the other hand, O_3 is an important regional contributor to tropospheric warming. However, it has also been acknowledged that increased atmospheric aerosol concentrations have a substantial impact on the planetary RF process. The resulting perturbations due to these species are of fundamental importance for both short- and long-term changes. The sections below discuss the contributions and influence of aerosols on the climate.

1.6.2.1 Direct and indirect aerosol effects

Aerosols can absorb or scatter solar radiation, thereby impacting on the heat energy balance (Torres at al., 1998; Jacobson, 2002; Formenti et al., 2003; Gao et al., 2003; Zhang et al., 2010; IPCC, 2013). These effects (known as 'direct effects') can result in either increase in atmospheric heating or cooling at the surface. Scattering and absorption of solar radiation can produce radiative adjustments and changes to the planetary albedo (Haywood and Boucher, 2000; Haywood et al., 2004), as well as enhancing the greenhouse effect and consequently changing temperature profiles, RH and atmospheric stability. Similarly, aerosols can alter cloud microphysical properties (Torres et al., 1998; Abdul-Razzak et al., 1998; Haywood and Boucher, 2000; Edwards et al., 2004) influencing cloud formation, and hence precipitation and cloud reflective properties by serving as CCN and ice nuclei (IN) respectively (Zhang et al., 2010). These are described as aerosol 'indirect effects'.

Aerosols from all sources mainly affect radiation in the visible wavelength region of electromagnetic spectrum (Hodzic et al., 2013). The efficiency of absorption or scattering of radiation varies between aerosol properties. For example, BC and brown carbon (BrC) are good absorbers of solar radiation (Tuccella et al., 2015), absorbing both incoming and outgoing radiation of a wavelength, whereas sulphates reflect more radiation. The rate of absorption depends on properties such as aerosol single-scattering albedo (SSA), refractive index (RI), aerosol optical depth (AOD) and mass absorption coefficient (μ). However, effects tend to vary locally and regionally because of the relatively short aerosol lifetimes in the atmosphere.

The above terms (SSA, AOD, RI, μ) are key indicators of aerosol direct effects. AOD is a dimensionless quantity indicating a measure of the reduction intensity of light due to scattering and absorption of particles along a path length (vertical column). It is the degree to which aerosols prevent the transmission of light by absorption or scattering, and a key parameter for determining radiative effects (Rind et al., 2009). When AOD = 0, there is no aerosol effect, when AOD ~1, there is a larger aerosol effect and when AOD > 1, there is an extremely large effect. SSA defines the ratio of scattering to the total light attenuation. This quantity indicates the rate of absorption or scattering by aerosols (varying between 0 and 1). An SSA value of 0 means that particle extinction is due to

absorption, and an SSA of unity means particle extinction is due to scattering. RI describes how light propagates through a medium. Different components have different refractive indices and therefore refract light differently. For certain components, these are based on literature values derived from laboratory experiments and vary with wavelengths for some aerosol compositions (Hodzic et al., 2013). μ is a measure of radiation by a medium per unit mass (units: m^2 kg^{-1}). However, because aerosol sizes change due to water uptake (depending on their hygroscopicity), their optical properties depend strongly on RH (Zieger at al., 2011). SSA is given by the expression:

$$SSA = \frac{\sigma_{sca}}{\sigma_{ext}} = \frac{\sigma_{sca}}{\sigma_{sca} + \sigma_{abs}} \quad ; 0 \leq \text{SSA} \leq 1 \qquad [1.24]$$

where σ_{sca} is scattering coefficient, σ_{ext} is extinction coefficient and σ_{abs} is absorption coefficient. In the Weather Research and Forecasting model with chemistry (WRF-Chem) SSA is computed at four wavelengths (λ = 300, 400, 600 and 1000 nm respectively) used within the radiation scheme. The wavelength, AOD or τ and atmospheric turbidity are related through the expression:

$$\tau = \beta\lambda^{-\alpha} \qquad [1.25]$$

where β is the Ångstrom's turbidity coefficient and α is the Ångstrom exponent. Just like SSA, τ can be computed at the four wavelengths defined above. Meanwhile, in most analysis, τ is discussed at a peak intensity around 550 nm for normal visible light. Given two wavelengths (e.g. 400 and 600 nm) one needs to determine the intermediate wavelength at 550 nm. However, this wavelength can be output directly from the model (setting appropriate *namelist.input* options).

The refractive index is a function expressing the real part and an imaginary part of a material. For example, RI for BC equals 1.850 + 071i (Hodzic et al., 2013), where 1.850 is a real part and 0.71i is the imaginary part. A higher imaginary part indicates more absorption by the material. The mass absorption coefficient is related to the transmissions intensity through a material of density ρ (kg m^{-3}) and thickness or length d (m) through the expression (Gullikson, 2001):

$$I = I_0 e^{-\mu\rho d} \qquad [1.26]$$

where I is the number of photons absorbed. The above expression gives transmittance as:

$$\mu = \frac{-1}{\rho d}\ln\left(\frac{I}{I_0}\right) \qquad [1.27]$$

Indirect effects involve mechanisms through which aerosols modify the microphysical cloud properties, cloud lifetime and morphology (Haywood and Boucher, 2000). For example, these include the *first indirect*, albedo or Twomey effect (Twomey, 1974; 1977; Lohmann and Feichter, 2005) and the *second indirect*, cloud lifetime or Albrecht effect (Albrecht, 1989). The first indirect effect occurs when droplet concentration is enhanced at the expense of cloud particle size in polluted clouds with

increased CCN number, consequently increasing cloud albedo (Williams and Baltensperger, 2009). The second indirect effect involves microphysical-induced effects on cloud lifetime and precipitation formation, influencing cloud lifetime. Increase in aerosol concentration leads to an enhanced CCN number concentration and numerous cloud droplets, but negatively impact on the cloud droplet growth for a given liquid water content (LWC) with less coalescence. Aerosol-induced effects on cloud droplet number concentration have an impact on the cloud optical properties and efficiency of cloud microphysical processes such as precipitation formation by collisional growth of cloud droplets.

Aerosol indirect effects have been identified as large uncertainties in the modelling community. In the latest International Panel on Climate Change (IPCC) report, these are referred to as 'cloud adjustments' due to aerosols (IPCC, 2013). Cloud representation is one of the key challenges in climate modelling because accurate representation and prediction of cloud processes is not easily achieved even with current model simulations. Also, there is large variability in cloud albedo due to large variability in cloud types (Haywood and Boucher, 2000). Despite the uncertainties in representing ACIs, these have large impacts in the climate system, not only in the radiation balance, but also in precipitation formation and water re-distribution in the atmosphere.

Clouds play a major role in the climate system through their interaction with the solar radiation and hydrological cycle. They are multiphase systems in which gaseous compounds, aerosols and liquid droplets or solid crystals undergo complex physical and chemical interactions (Shrivastava et al., 2013). Also, precipitation is an important mechanism in the hydrological cycle linking aspects of climate, weather and the global chemistry. Therefore, any change in the amount or the spatial and temporal distribution of precipitation indirectly impacts on climate and life on Earth. Increases in atmospheric aerosols have been suggested to suppress precipitation in polluted regions as a result of increase in CCN number concentration leading to reduced cloud droplet size and collisions coalescence (Ramanathan et al., 2001). These changes can be manifested even at a global scale (Lin et al., 2006). Suppression can potentially lead to positive feedback in terms of drying of the land surface, strong susceptibility to fires and enhanced aerosol-induced suppression of rainfall. These perturbations in the hydrological cycle can have major consequences for fresh water supply (Lin et al., 2006, and references therein). The consequences can be evidenced through reduction in cloud droplet sizes and delays in precipitation onset within smoky clouds (Lin et al., et al., 2006).

1.6.2.2 Semi-direct effect

A further important aerosol influence on the radiative budget is provided through influences on changes in atmospheric stability and temperature profiles on cloud coverage, the so-called semi-direct effect. This involves mechanisms by which aerosols absorb shortwave radiation, leading to

tropospheric heating that alters the RH and atmospheric stability, ultimately affecting cloud cover or the probability of cloud formation (Johnson et al., 2004). The process is distinct from both direct and indirect effect. Semi-direct effects are caused by a change in cloud cover or liquid water path due to heat energy absorbed by aerosols (Skaeda et al., 2011). The heating can cause cloud 'burn-off' and evaporates clouds. The effect depends on factors such as aerosol type, relative position of the aerosols with respect to the clouds, as well as cloud types. For example, if aerosols are embedded within or near clouds, they promote cloud evaporation and eventually lead to a reduction in cloud cover. If aerosols are beneath clouds, they can enhance convection and cloud cover. If aerosols are above clouds, then they may stabilize the underlying cloud layer. Semi-direct mechanisms can, to a large extent, depend on the local meteorological conditions (Johnson et al., 2004).

Although the magnitude of the effects can vary, some studies indicate that the magnitude of semi-direct could exceed the direct forcing, and the atmospheric feedback processes arising from these effects could play an important role in explaining the total radiative effect (Skaeda et al., 2011, and references therein). Different studies also recognise the dependence of the vertical aerosol distribution on the radiative forcing. For example, Johnson et al. (2004) used the Met Office large-eddy model (LEM) to investigate the semi-direct effects on marine stratocumulus-capped boundary layer and found that aerosol layers advected above cloud layers led to a positive forcing than those below cloud layers. They found that the effect of semi-direct aerosol forcing was increased when aerosols were above the boundary layer (and above the clouds). The magnitude and sign of the semi-direct effect were dependent upon the aerosol concentration within or above clouds. Therefore, semi-direct effect can be significantly affected by vertical advection or mixing of aerosols within the boundary layer (Johnson et al., 2004).

1.6.2.3 Aerosol–Cloud Interactions (ACIs)

Aerosol–cloud effects are recognized as contributions from anthropogenic and natural effects on climate and the hydrological cycle. Interaction between aerosols and clouds is critical to understand the extent to which these particles affect solar energy budget, cloud dynamics and induce perturbations to the global climate. Although certain aspects in ACIs have been relatively studied and understood, others are not well known (Spichtinger and Cziczo, 2008). On other hand, although recent advances have lead to some understanding of ACIs, further progress is still hampered by limited observation capabilities and model resolutions (Rosenfeld et al., 2014). The latest IPCC report also account for some of the aerosol-cloud effects. The fourth IPCC report described aerosol radiative forcing (ARF) as a concept used in the quantitative comparison of the strength and effects of aerosols due to both

anthropogenic and natural factors resulting in global change (IPCC, 2007). However, this term is deprecated in the latest report; a new concept 'effective radiative forcing' is now used.

Two important terminologies used are: *Forcing* (associated with agents such as GHGs and aerosols act on global mean surface temperature through the global radiative energy budget), and *Rapid adjustments* (arising when forcing agents, by altering flows of energy internal to the system, affect cloud cover or other components of the climate system and alter global budget) (IPCC, 2013). While several model studies indicate that increase in aerosol loading leads to cloud invigoration (e.g. Ntelekos et al., 2009) due to increased CCN concentration, these particles can also enhance CCN concentrations and impact negatively on cloud droplet growth (Twomey, 1977; Haywood and Boucher, 2000). Small changes in the initial conditions can evolve largely in cloud size, shape and microphysical properties, and result in the modification of radiative properties and their ability to precipitate. Consequently, these modifications influence the environmental dynamics through changing the vertical latent heat distribution within clouds.

Clouds are important regulators of the earth radiative budget, covering earth's surface (Lohmann & Feichter, 2005), and they play key roles in the atmosphere: hydrological cycles, atmospheric cooling and precipitation formation. For example, persistent supersaturated conditions in the upper troposphere, the interplay of dynamics versus effects attributed to aerosols are some of the uncertainties. This topic will be discussed further in chapter 6.

1.7 Representing air quality and dynamical interactions on the regional scale

The complex nature of interactions between meteorological, chemical and microphysical processes leads to a number of challenges in predicting AQ. Until very recently, after the introduction of online models, atmospheric chemistry and weather forecasting have always been treated as separate disciplines (Baklanov et al., 2014) whereby meteorology and chemistry models were run separately and the output from the meteorology model used to drive the chemistry. Although this was attributed to lack of computational power (Baklanov et al., 2014), limited knowledge about the process interactions can also be a consequence (Prein et al., 2015). Most current models are integrated coupled models conducted at both regional and global scales, while on the other hand reducing the complexities in running them. Introduction of coupled meteorology–chemistry climate models have improved in recent years (Baklanov et al., 2014), although efforts still continue to improve the uncertainties. Improvement is credited to the availability of cost-effective high performance computers, advancement in high-resolution modelling and availability of real-time AQ monitoring (Schere et al., 2006). Online integrated models handle the meteorology and chemistry together, using

the same grid, both integrated in one time step (Grell et al., 2011a; Baklanov et al., 2014), allowing information to be exchanged between meteorology and chemistry.

Nevertheless, challenges still exist in the representation of chemical and physical processes, even by combining the two models. The modelling community strives to improve the understanding of the physical and chemical aerosols ranging from local to regional and global scales. For example, particle size, mass and number concentration are essential aspects of aerosol modelling which need to be taken into consideration, together with the meteorological condition that vary in time and significantly influence AQ (Appraisal, 2013).

One importance in regional modelling is the representation of pollutant distribution more accurately, especially in areas where it is important (e.g. urban locations) or near concentrated emission sources where there are strong gradients in the concentration fields (Mensink and de Ridder, 2000). Because they are designed for limited-area domains (as opposed to global domains), regional models can use smaller grid spacing, allowing more detailed predictions. Also, emission distribution between grid boxes is more efficient, compared to coarse grid simulations in global models. Their higher resolution (although still limited) allows for more process interactions on the appropriate grid scales.

Baklanov et al. (2014) outline four key areas critical for coupled modelling: (i) advection, convection and vertical diffusion, (ii) cloud microphysics, (iii) radiative transfer, and (iv) turbulence at the surface. These are important areas in chemical process simulations and AQ in climate models, especially where information at a local scale is important. One problem also arises from modelling secondary pollutants from complex chemical reactions, which involve VOCs, NO_x and other precursors (Hallquist et al., 2009; Caenevale et al., 2012). Secondary organic aerosols (SOA) represent a major atmospheric component affecting the global atmosphere, although their accurate prediction is still hampered by lack of detailed understanding of the formation processes. Although the formation and evolution of SOA is still one of the debatable subjects in AQ studies, SOA plays a central role in atmospheric composition, visibility, climate and the oxidative capacity (Crippa et al., 2013).

1.8 Atmospheric composition, air quality and its interactions with meteorology in southern Africa

1.8.1 General characteristics of the southern African climate

Southern Africa generally has a spatially varying arid climate in the west through semi-arid, temperate and sub-humid in the central region, to semi-arid in the far east (SADC report, 2010). The climate becomes largely humid towards the tropical rainforest of the Congo Basin. It is influenced to a large extent, by the prevailing air masses over the local atmosphere, which strongly influence the regional weather patterns (Tyson et al., 1996a) and the adjacent oceans on either side of the continent. Common

amongst these mechanisms include the Intertropical Convergence Zone (ITCZ), the Democratic Republic of Congo (formerly Zaïre) Air Boundary (CAB), El Niño Southern Oscillation (ENSO), and the monsoon systems. The long-term precipitation changes from both northern and southern regions of Africa are linked to the monsoon circulations and controlled by precessional variations in summer insolation (Schefub et al., 2005, and references therein).

Reports suggest that the sub-continent has experienced increasing inconsistent temperatures over the last decades since the 1970s. For example, global trends in temperature rise have increased by about 0.5° C over the last 100 years (IPCC, 2013), while sea surface temperatures (SSTs) have also risen by more than 1° C since the 1950s. Rainfall has decreased over the same period; below-normal rainfalls are characterized by recurrent droughts (sometimes more severe) where frequent increases and intensification of ENSO dry episodes (El Niño) have been observed in most areas. ENSO is a major driving force to climate variability in southern Africa, especially affecting the rainfall patterns (Nicholson and Entekhabi, 1987).

Recent research suggests that the regional climate will continue to change and temperatures expected to rise higher than they are today. For example, annual average temperatures are expected to rise by about 1.5–2.5° C by 2050 for countries in the south, and about 2.5–3.0° C in the north compared to the time before the 1990s (Ragab and Prudhomme, 2002). A report on southern Africa's drought prediction (http://www.scidev.net/en/news/decades-of-drought-predicted-for-southern-africa.html) states that 'model researches show the Indian Ocean with a very clear and dramatic warming into the future suggesting persistent droughts for southern Africa.' Comparing the model results with those from 1950–2000, researchers conclude that 'changes in the Indian and Atlantic Oceans are causing climate change in Africa, and findings indicate that the Indian Ocean warming is responsible for droughts in southern Africa, while temperature changes in the Atlantic have generated more rainfall in the Sahel.' They also suggest that GHG emissions from anthropogenic sources are responsible for the oceanic warming in the Indian Ocean, and by 2050 the monsoon winds bringing rainfall to sub-Saharan Africa are likely to be 10–20% drier than the period 1950–2000 in southern Africa. Model results suggest precipitation decrease in equatorial Indian Ocean in association with uniform SST increase, however not indicating intensified deep convection with higher precipitation to be more likely where SSTs are locally larger than their surroundings (Sherwood et al., 2013, and references therein). Overall, the subcontinent is characterized by a unique combination of natural climate zones, with loose soil cover and dense forests in some areas and abundance of sunny days. These factors set conditions for natural emissions (e.g. dust, VOCs) and human-induced (e.g. BB, industrial) emissions into the atmosphere. This section provides a contextual climatic background to the current study.

1.8.2 Transport patterns in southern Africa

The sub-continent has a unique set of meteorological and chemical characteristics influencing pollution transport and climate forcing (Garstang et al., 1996). For example, the anticyclonic nature of atmospheric circulation results in the formation of stable layers so that aerosol and trace gas recirculation occurs in a significant local, regional or sub-continental scale (Torres et al., 2002). A significant mass of air re-circulates over southern Africa (Tyson et al., 1996a; Tyson and D'Abreton, 1998) before exiting the sub-continent. As a result, large amounts of airborne particles can be trapped over the sub-continent for longer periods (Freiman and Piketh, 2003; Liousse et al., 2010).

Transboundary transport involves transport of particles over thousands of kilometers crossing regional and continental boundaries. A typical example is the so-called "river of smoke" outflow from the mainland into the Indian Ocean. Garstang et al. (1996) postulate five basic trajectories of aerosols and trace gas over southern Africa (Fig. 1.7): direct easterly or westerly transport, easterly or westerly advection out of an initially anticyclonic circulation, and anticyclonic recirculation. The easterly flow transports less pollution than the westerly flow. According to Garstang et al. (1996), on the southern periphery, wave perturbations from the trajectories occur at 18°S into the Atlantic Ocean, whereas the bulk of the transport into the Indian Ocean occurs at 35°E. Also, the general climatological conditions are such that the anticyclonic activities dominate and become favourable in specific locations where pollution accumulates and/or transported away. The pathways through which pollution from southern Africa is transported over the South Atlantic and Indian Oceans are described (Tyson et al., 1996a) as the "Angolan plume" and the "Natal plume" respectively.

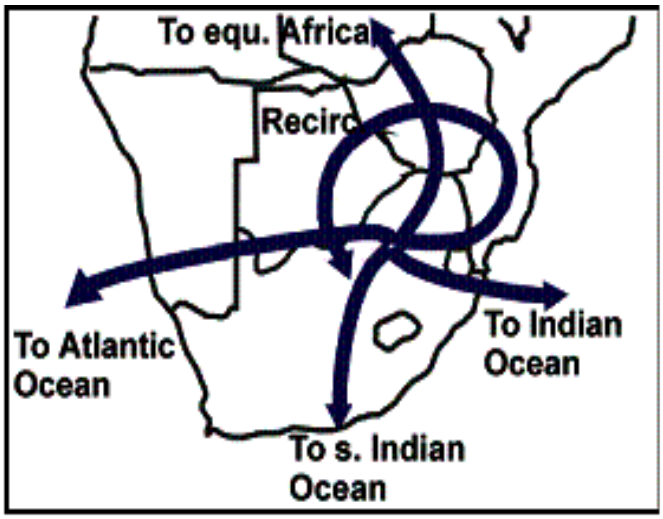

Fig. 1.7: Transport pathways of air over southern Africa. (http://www.sei-international.org.rapidc/atmtrans.htm).

There is a well-documented evidence for the regional and intercontinental transport of pollution within and outside southern Africa (e.g. Tyson et al., 1996a, Garstang et al., 1996; Piketh and Walton, 2004).

In-situ observations also document possible long-range transport of BB plumes and anthropogenic pollution across the Atlantic Ocean (Piketh et al., 1999; Piketh and Walton, 2004, Kaufman et al., 2005) and the Indian Ocean, although the greater transport occurs towards the Indian Ocean (Tyson et al., 1996a). Distribution is strongly influenced by the transport dynamics and air mass layers prevailing over the sub-continent (Kirkman et al., 2000). Circulation systems and transport pathways described above play vital roles for the local meteorology over southern Africa. For example, the frequent high-pressure systems are important to the regional atmosphere and act as 'accumulation' mechanisms for trace gas and aerosols associated with haze layers and the westerly wave passages responsible for the 'clean out' signatures. Overall, persistent occurrence of these layers effectively caps the horizontal transport and inhibits the vertical motion and mixing of air in the free troposphere. This leads to pollution accumulation between the layers, which can stay longer before being transported away or deposited with varying annual frequencies. This provides the contextual meteorological backdrop to the current study.

1.8.3 Southern Africa's contribution to pollution

The sub-continent bears an influx of aerosol and trace gas pollution from local sources and to some extent, external sources due to pollution of transport. Pollutants are generated from sources such as BB, domestic fires, fossil fuels, dust particulates, BVOCs and other anthropogenic emissions. There are few comprehensive studies of pollution over southern Africa, but these emissions could have a direct impact on the local, regional and global atmosphere, providing large quantities of gas- and particle phase species. Biomass burning aerosols (BBAs) comprise predominantly of organic particles in combination with other products such as BC and OC, the percentage of which depends on the burning efficiency of the fires. These are observed through the large plumes associated with the "river of smoke" over southern Africa (e.g. Swap et al., 2003). Although vast amounts of aerosols are said to be more abundant in the industrialized regions of the Northern Hemisphere (Andreae, 1996), a significant amount is also generated in the Southern Hemisphere, particularly southern Africa. Various authors in literature (e.g. Tyson, 1986; Tyson et al., 1996a,b; Tyson and D'Abreton, 1998; Freiman and Tyson, 2000; Tyson and Preston-Whyte, 2000; Piketh et al., 2002; Freiman and Piketh, 2003) have discussed the evidence of aerosol and trace gas emission in southern Africa.

1.8.3.1 Previous studies on southern African BB and other emissions

The problem of air pollution has been one of the major concerns about AQ degradation in the regional and global environment. Particulate and trace gas emissions over southern Africa has fallen under considerable scrutiny over the last few decades, leading to the establishment of several regional and international field campaigns, most notably the Southern Africa Fire–Atmosphere Initiative of 1992

and 2000 [SAFARI-92/2000] (Lindesay et al., 1996; Le Canut et al., 1996; Swap et al., 2002; 2003), a subcomponent of the International Global Atmospheric Chemistry Program/Biomass Burning Experiment project [IGAC/BIBEX], Southern Tropical Atlantic Region Experiment [STARE] (Le Canut et al., 1996), Southern Africa Atmosphere Research Initiative [SA'ARI] (Helas et al., 1995) and the Aerosol Recirculation and Rainfall Experiment [ARREX] (Terblanche et al., 2000). The overall objective of these campaigns was to characterize southern African recirculation of the aerosol burden and understand the relationships between the physical, chemical biological and anthropogenic processes underlying bio-geophysical and chemical system over southern Africa (e.g. Swap et al., 2002; 2003).

The campaigns offered an opportunity to study aerosols over southern Africa (e.g. Pósfai et al., 2003) and their impacts since different participants worked on different aerosol specialties. For example, the SAFARI campaign invited researchers to bring their own resources to the project, conceptualizing contributions broadly, including time and commitment, personnel, granting access to research sites and data and host scientists (Lahsen et al., 2013). Participants and researchers were able to study aerosol and trace gas influence on the radiative budget through their modifications of the cloud optical and microphysical properties (Swap et al., 2002; Pósfai et al., 2003). The studies proposed that stable atmospheric conditions prevail over southern Africa especially during winter, coinciding with the peak of BB.

Several other studies have also discussed aerosol and trace gaseous pollutants over southern Africa (either pre-BB or post-BB), looking at pollution build-up over the regional environment, carbonaceous properties of BBAs or effects on the regional climate due to BB. For example, Sinha et al. (2004) used a global model to quantify the eastward flux of BB emissions from southern Africa into the Indian Ocean during the dry season to determine the changes in the eastward flux during the meteorological events, and assess the contribution of southern African BB smoke to the subtropical global plume forming over the South Indian Ocean after the dry season. They reported, for example, that up to 60 Tg and 40 Tg of CO on average (between 1994-2000) was transported eastward and westward respectively. Costantino and Bréon (2010) used satellite remote-sensing observations from Moderate Resolution Imaging Spetroradiometer (MODIS) and Cloud-Aerosol Lidar and Infrared Pathfinder Satellite Observation (CALIPSO) retrievals to quantify the various ACI processes over the South East Atlantic Ocean. They reported that southern African BB results in large semi-permanent elevated aerosol layers advecting over the SE Atlantic stratocumulus cloud deck. Skaeda et al. (2011) used a global coupled model to assess the aerosol direct and semi-direct effects associated with carbonaceous aerosols emitted by southern African BB. Other studies include those of Scholes et al. (1996) (using

satellite techniques to quantify the amount of biome burnt, its types and locations as well as the time of burning over southern Africa); Liu et al. (2000) (characterisation of atmospheric aerosols and savanna fire samples during southern African BB); Abel et al. (2005) (using satellite and in-situ based measurements of BBAs into a multi-column radiative transfer code to assess their direct radiative effect during the transition period when anthropogenic induced burning activities are widespread over southern Africa), and Wai et al. (2014) (impact of BB on tropospheric composition in the tropics and seasonal variation, combining in-situ measurement with model simulation).

Other studies (e.g. Moxim and Levy II, 2000; Chatfield et al., 2004) also state that there is evidence of interhemispheric transport of pollutants between seasons, especially from the end-of-burning season toward the wet season. However, the duration and quantitative scales of the recirculation and frequency of the air circulation varies, depending on the season, height within the atmosphere, and the dominant circulation types, as well as changes in weather patterns. Chatfield et al. (2004) described seasonal and geographic O_3 distributions between the Atlantic and Indian Oceans and highlighted periods of maximum tropospheric O_3. They reported that BB and smog over adjacent continents were responsible for the O_3 discovered over the equatorial Atlantic Ocean. Phadnis and Carmichael (2000) indicate that the widespread BB in South America and southern Africa is the dominant source of precursor gases responsible for the high O_3 concentrations over the South Atlantic Ocean.

1.8.4 Air quality in southern Africa

Air pollution in southern Africa is still faced with continued and widespread exceedances, particularly the major regulated pollutants (e.g. PM, CO and O_3). Although there might not be national AQ problems on record over the sub-continent, a number of air pollution conditions exist (ESA, 2005) where severe AQ problems are likely to occur, for example, locations within active BB region and high anthropogenic emissions. The regional organisation Southern African Development Community (SADC) also recognise pollution as an environmental problem. For example, the Air Pollution Information Network for Africa (APINA) was established to address issues related to pollution and coordinate key processes related to AQ (www.sacd.int; Simukanga et al., 2003). However, performance evaluation is still limited in the current AQ modelling/studies. Health impact assessment is still a subject of concern in most areas or source factors and/or stakeholders involved. The only evaluation in place is on abatement strategy based on the compliance to limit concentration values and does not consider computing the input on health. Also, there is currently not enough (or virtually none) scientific evidence to warrant the use of threshold values below which health effects could be impacted. Also, a couple of model studies so far conducted over southern Africa have been focusing

mainly on meteorology (Crétat et al., 2012); only a few being coupled, with the exception of field studies discussed above.

Generally, research in AQ and health effects in Africa is less comprehensive compared to Europe and America, and there is a need for region-specific information to influence policy makers. For example, studies on dose-response relationships, indoor air pollution, particulate concentrations and practical examples of emission controls are required (Ivertfeldt, 2002). AQ modelling and monitoring are essential components of assessment. Increasing activity in key economic source sectors contribute substantially to air pollution over southern Africa (UNEP, 2004). Unsustainable patterns of consumptions and energy production such as industry, transport and household sectors are the leading sources of key indoor pollution. On the other hand, gaseous and particulate emissions from Africa's growing industry are an increasing nuisance. A combination of vehicular emissions, dust and smoke from domestic fires is a potential AQ concern over southern Africa (Kgabi, 2012). For example, South Africa alone emits 306.3 million metric tons of CO_2 from the coal consumption only; this accounts to 90.6% of Africa's energy-related carbon emissions and 3.4% of the world's energy from CO_2 emissions (UNEP, 2004). About 1.8 million tons of SO_2 are emitted annually from electrical generation; the levels have increased in the past few years due to industrial activity. On average, annual ambient SO_2 concentration from South Africa now approach 20 ppb guideline (WHO; Kgabi, 2012).

Some studies demonstrate a strong seasonal trend in indoor air pollution over southern Africa because of increased reliance on solid fuels for space heating (Barmes et al., 2009), energy production and fuel use. This is common in low-income groups –mostly reliant on wood and low-grade coal, with high morning peaks in average CO and NO_x concentrations (Barmes et al., 2009, and references therein). For example, APINA identified some AQ gaps such as: lack of reliable emissions inventory, modelling experience as well as data on measured impacts (Kgabi, 2012, and references therein). Most countries do not regulate monitoring methods for specific pollutants, with the exception of South Africa with the evidence of identification of high priority areas and a centrally coordinated monitoring and reporting system. However, there are several acts and/or laws enacted to govern and protect citizens and their environmental health. In 2003, a 'Regional Dialogue on Air Pollution' was drafted, drawing heavily on the use of scientific observation from the SAFARI 2000, involving SADC government officials (SADC Draft report, 2008), the major outcome of which was a policy entitled "The Maputo Declaration on the Prevention and Control of Air Pollution in southern Africa and its Likely Transboundary Effects" (Lahsen et al., 2013). A legislation (National Environmental Management: Air Quality Act of 2004) was implemented in 2005 to provide reasonable measures for the prevention of

pollution and ecological degradation and securing ecological sustainable development and promoting justifiable economic and social development; providing national norms and standards regulating AQ monitoring, management and control by all government sectors for specific AQ measures (Government Gazette, 2005).

The SADC regional policy framework signed in Lusaka, 2008 also indicated some of the major concerns on AQ in the region including air pollution standards, increased emissions from industrial, power stations and BB impacting on human health as well as road standards. The framework proposed some objectives amongst others to: promote and establish regional training centers on AQ management and related issues, supporting inclusion of air pollution in environmental impact studies and socio-economic assessment, collaboration with local and international institutions/organisations and regional networks as well as regional dialogue on transboundary transport of air pollution through APINA.

1.9 Scope of the study

There is great need to improve the understanding of AQ predictions and the feedbacks between air pollution and weather interactions over southern Africa. Understanding the interactions is important in order to relate and describe the roles airborne substances play in the atmosphere. This study is envisaged at determining aerosol contribution and influence on the regional pollution and interaction with the meteorology. The work is formulated on the basis of assessing a regional simulation from a potentially high-pollution event resulting from vigorous BB, taking into account the contribution from other pollution sources, changes in AQ, and the weather to perform an analysis (through a modelling experiment) of the tropospheric chemical composition and weather patterns over southern Africa. The analysis is conducted (chapters 4, 5 and 6) through testing the hypotheses from the simulations and model comparison with measurements. This modelling study is aimed at addressing the following objectives:

- evaluate the role of air pollution and to better understand interactions between meteorology, chemistry and aerosols.
- simulate pollution distribution throughout the regional troposphere and evaluate model performance over southern Africa.
- understand the contribution of various pollutant sources within southern Africa, including transportation, concentrations and effects within targeted sub-regions.
- study the influence on the regional pollution and feedback mechanisms due to aerosols from anthropogenic and natural sources through perturbations in cloud microphysical properties.

To address these objectives, the investigation is carried out using a fully coupled online numerical mesoscale model called Weather Research and Forecasting model coupled with chemistry [WRF-Chem] (Grell et al., 2005a). The simulation is conducted during the southern African dry season.

1.10 Outline of the study

This study utilizes the WRF-Chem model, including particle and gas phases from natural and anthropogenic processes and distinct emissions in and around southern Africa. The novelty of the present study is the combined analysis of ACI sensitivity to aerosol loading and cloud response in a regime-based approach, enabling a profound view into the aerosol chemistry meteorology system. The study complements earlier studies on regional transport over southern Africa (e.g. Tyson et al., 1996a,b; Freiman and Tyson, 2000; Swap et al., 2002; 2003; Piketh and Walton, 2004) and adds to the understanding of the regional–scale modelling of trace substances through the atmosphere. The main objective is to demonstrate that aerosols can result in observed changes in the individual weather conditions. Key importance is to identify linkages among the physical and chemical processes underpinning the functioning of the bio-geochemical and atmospheric systems over southern Africa leading to significant perturbations over considerable parts of the region. The present chapter introduces the subject area to the study conducted with WRF-Chem over southern Africa. It serves as a background to the study described in the subsequent chapters. The rest of the thesis is structured as follows: chapter 2 gives an overview of regional modelling, various components and data preparation carried out to setup the model system. The utilised data and methodological approach are outlined in chapter 3. Chapter 4 characterises the regional pollution from the WRF-Chem simulation; typical regional aerosol and weather conditions are also described to lay the foundations of this work. Chapter 5 addresses regional pollution and AQ, whereas chapter 6 focuses on ACIs and RF over southern Africa. A summary of the thesis and outlook is given in chapter 7. Supplementary material is also presented in the appendices at the end.

Chapter 2

Coupled regional-scale models: climate modelling with the Weather Research and Forecasting model with chemistry (WRF-Chem)

2.1 Introduction

Air quality and precipitation are of fundamental societal importance, and therefore their realistic predictions are important to atmospheric scientists. Yet the interactions between poor air quality (AQ) and cloud processes remain poorly understood. Climate scientists and weather researchers strive to understand the behaviour of such processes. Numerical weather prediction (NWP) models that couple atmospheric dynamics with atmospheric chemistry are well suited to investigate effects of these interactions that are otherwise difficult to observe (SACOS, 2003). Coupled limited-area models have become highly sophisticated numerical tools embodying detailed descriptions of physical processes.

There has been rapid recent advancement in the model capability with consequent improvement in forecasting and atmospheric understanding. Also, the aerosol and chemistry community have developed models placing more emphasis on the dynamics between aerosol composition and cloud microphysics (Feingold et al., 2009). Many of the subgrid processes important to meteorology are equally important to chemistry (Gustafson et al., 2011). Although there has been a great advancement in the area of modelling, the field of cloud-aerosol and their dynamical interactions remain at the core of uncertainties about atmospheric aspects of climate modifications (e.g. Sherwood et al., 2013) and continue to be one of the challenges in model predictions. Model resolution is key importance to the representation of geographical variations, regional/global weather events and the underlying processes in the atmosphere. Proper representation of cloud physical and chemical processes is important for model prediction skill and accuracy.

2.2 Nested modelling

Limited-area modelling requires boundary conditions (BCs) from global datasets to the smaller nested domain (Fig. 2.1). There are two ways of nesting: one-way and two-way nesting. One-way nesting is whereby the parent domain provides the information to the nested domain, with no feedback from the nest to the parent domain. Usually, the parent domain is run first, after which the output is used to provide the BCs to the nest. In a two-way nesting, information flows in both directions and simulations from two different domains are run simultaneously and the nest also feeds back to the parent domain. Nesting can comprise of several model grids of different resolutions used in conjunction with one another or the same model run at different resolutions.

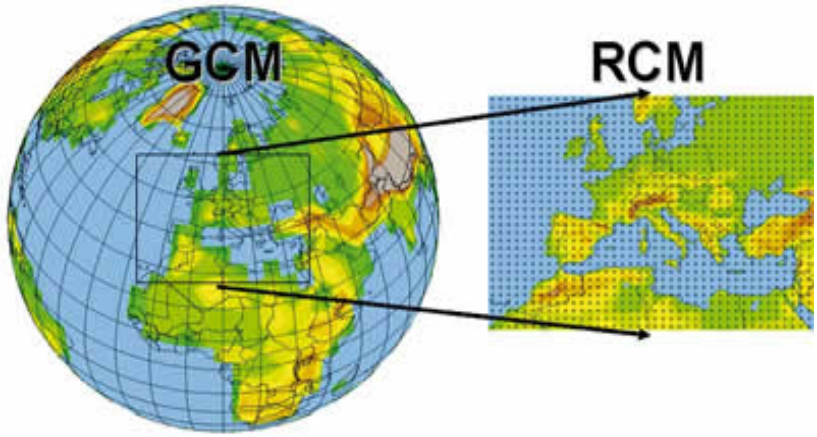

Fig. 2.1: A limited-area model (listed here as a regional climate model, (RCM)) nested within a global circulation model (GCM). (Giorgi, 2006).

Outputs from the large (parent) domain are used as initial and boundary conditions to drive the smaller domain (Mearns et al., 2003). In cases where fine-scale and process forcings are necessary for the simulations of synoptic drivers, nested limited-area models are necessary to produce simulations at regional and local scale. They are flexible tools (order of 5–20 km), where multiple simulations can be done. The basic strategic approach in this technique is that because the global model resolution is too coarse to capture regional or local climate processes, coupling with a limited-area model is employed to give a better representation. Information from the sub-grid cells of the global model is better represented in a small-scale model.

2.3 The Weather Research and Forecasting model with chemistry (WRF-Chem)

WRF-Chem is an advanced community regional meteorological and fully coupled "online" atmospheric chemical transport model (Grell et al., 2005a; 2011a,b; Fast et al., 2006) developed from the WRF model (Skamarock et al., 2005; 2008). It is based on state-of-the-art components of the description of the meteorology, chemistry and aerosols, featuring an integrated approach to couple them. The chemistry component consists of several internal drivers, such as those for anthropogenic and biogenic emissions, photolysis, dry and wet deposition, convective transport parameterisation, chemical mechanism and the aerosol chemistry mechanisms, including the aqueous-phase chemistry and the gas-phase chemical reaction mechanism coupled with microphysics parameterisation of the WRF model. WRF-Chem enables scientific questions related to the aerosol chemistry and meteorological feedbacks to be addressed (Gustafson et al., 2005; Zhang et al., 2010). These include the gas-phase chemistry mechanisms, particle phase modules, aerosol and radiation feedbacks. Because interactions and transport of meteorological and chemical variables are calculated using the same physical parameterisations, there is no need to interpolate in time and/or space (Grell et al., 2004a; 2005b).

WRF-Chem requires meteorology and emissions (section 2.5) as input data through each grid point to predict concentrations and depositions of different chemical species. The primary physical and chemical processes included in the model are the emissions of chemical species, advection and dispersion to transport species emitted, cloud and precipitation processes leading to chemical reactions of both gas and particle phases, interaction between meteorological parameters, mixing and wet deposition, inflow and outflow of chemicals across domain boundaries. The WRF Pre-processing System (WPS) is used to provide meteorological initial conditions: the chemical initialisations are provided by an external model simulation. Various input parameters are defined in the *namelist.input* file –a template defining a set of variables and parameters for input/output operation in the model. Data declared in the namelist is transferred to different model components and programs for job execution during the simulation. The figure below illustrates the structure of the WRF-Chem model, showing different components and data flow in the model.

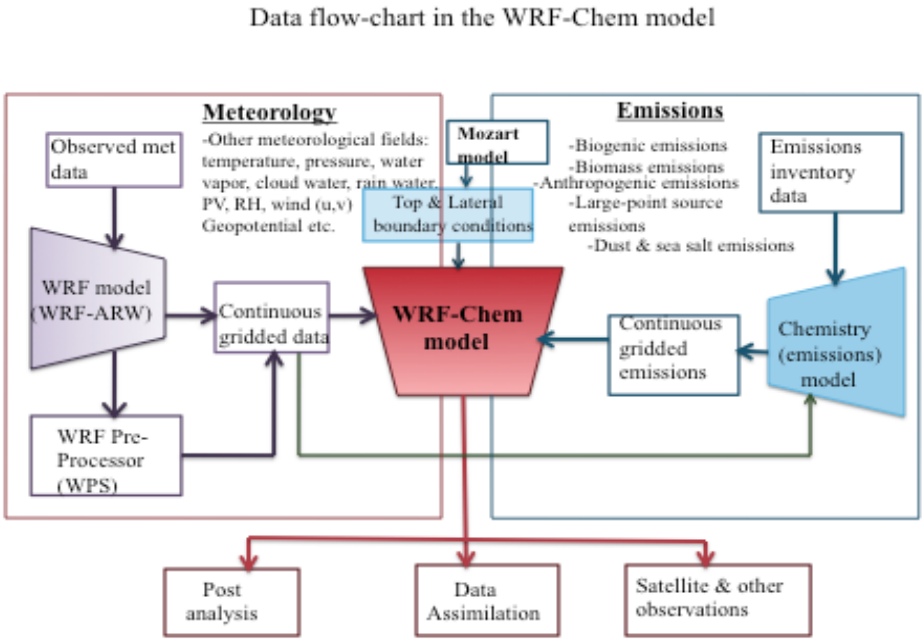

Fig. 2.2: The WRF-Chem modelling system. The model incorporates both the chemical and meteorological components in the same framework. Initial boundary conditions for meteorology are provided by the WPS, whereas the chemistry module prepares initial chemical BCs.

2.4 Parameterisations in the meteorological part of the WRF model

Although limited-area models have a better representation of atmospheric processes (because of the resolutions at which they are run), it is still not possible to perfectly resolve many processes. This is a challenge at any scale of modelling. In order to account for small-scale unresolved perturbations on the larger scales that can be explicitly resolved by the model, their effects are parameterised by including terms in the fundamental equations to give a simplified description of the phenomena.

Parameterisation is a way of representing physical processes that cannot be resolved by models even at fine resolutions. Several parameterisation categories are available for the WRF model: microphysics, radiation, cumulus parameterisation, land surface model (LSM) and planetary boundary layer (PBL). These schemes are important aspects that strongly influence model forecasts (Stensrud, 2007) and interact with each other indirectly through the changes to the model variables (Fig. 2.3). The physics section is incorporated in the Advanced Research WRF (ARW) solver, insulated from the rest of the dynamic section responsible for filling arrays in the model code with the required physics variables. All the physics categories in the ARW solver (with the exception of cloud microphysics) are computed in the first Runge–Kutta time step (Skamarock et al., 2008; Ma et al., 2014). Microphysics is computed after the last step to maintain proper saturation conditions at the end (Skamarock et al., 2008). This section describes the various physical parameterisation incorporated in the WRF-Chem model.

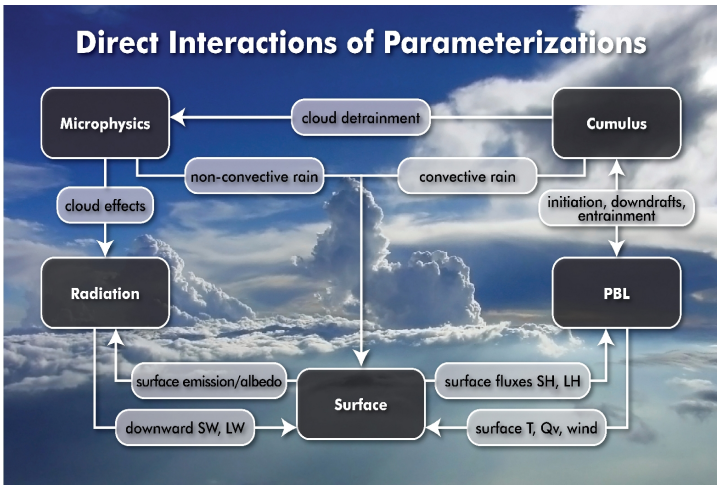

Fig. 2.3: Model parameterisations and the basic interactions within the atmosphere. Interactions are influenced by changes in atmospheric variables.
(http://www.ncep.noaa.gov/newsletter/october2011).

2.4.1 Cloud microphysics

Clouds exist in different forms and structures, but the primary basic processes leading to their formation can be described through the evolution of their constituent particles. Cloud microphysics parameterisation is concerned with the representation of the physics of ice and liquid droplets and their interactions (Sen and Roos, 1994). The parameterisation accounts for processes and interactions involving conversions and/or transfer rates between the hydrometeors (Fig. 2.4). The parameterisation also accounts for the condensation of water vapour in cloud droplet growth, droplet evaporation, autoconversion of cloud droplets to rain, accretion and collection of cloud droplets into rain, as well as evaporation of rain droplets (cloud droplet formation is treated by the separate activation parameterisations (see section 2.8)). Parameterisation also involves explicit resolving of water vapour, cloud, precipitation and the mixing ratios of the processes.

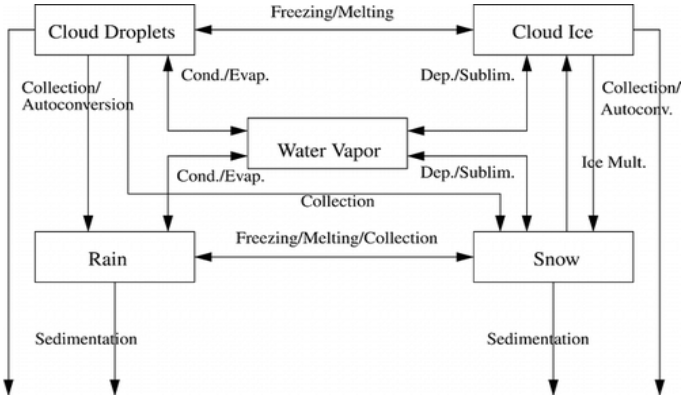

Fig. 2.4: Box diagram of the microphysics scheme (Morrison et al., 2005).

The microphysics scheme used in this study is the Morrison-double moment scheme (Morrison et al., 2005; 2009). The Morrison's parameterisation scheme is developed from the two-bulk microphysics schemes (Morrison et al., 2005; Morrison and Pinto, 2006) to predict the number concentration and mixing ratios for different hydrometeors. This scheme carries six hydrometeors: cloud water, water vapour, rainwater, cloud ice, snow and graupel, with a set of prognostic equations for diagnosis. While the single-moment schemes only predict the mixing ratios of hydrometeors, double-moment schemes include additional prognostic variables related to size distribution such as number concentration. Moreover, several liquid, ice and mixed-phase processes are included (Baró et al., 2015). Because of its characteristic features (e.g. treat both number concentration and mixing ratios), it essentially allows for more robust treatment of particle size distributions, the key to calculating microphysical process rates and cloud/precipitation (Skamarock et al., 2008).

2.4.2 Cumulus parameterisation

Cumulus parameterisation redistributes moisture and heat distribution in response to unresolved convective clouds. The parameterisation resolves updrafts within the model grid cells to determine the upscale effect of convection. The cumulus physics routine determines if the sub-grid convective clouds are present within the model grid column and the physical properties of the cumulus clouds used in the cumulus effects (Berg et al., 2014). The choice of cumulus scheme is determined by the size of grid spacing and/or type of simulation. Although parameterisations were designed to reduce model instability, proper parameterisation of convective processes is still a challenging problem in NWP (Grell and Dévényi, 2002). This is due to the fact that cloud processes occur at microscopic scales, many of which are not captured by models even at finer resolutions. The parameterisations are highly regime selective because they are based fundamentally on different assumptions and parameters (Pei et al., 2014, and references therein). In this study, we use the Grell 3D scheme; an improved version and effective in generating an ensemble with significant spread suitable for use on high-resolution simulation, especially when subsidence spreading is turned on (Grell et al., 2011a).

The Grell 3D scheme (Grell and Dévényi, 2002) was developed to offer an approach to a large number of ensembles of assumptions and parameters leading to uncertainties in 3D models. It has explicit downdrafts/updrafts and includes cloud and ice detrainment with mean feedback of ensembles. Also, ensemble simulations using multiple cumulus parameterisations have demonstrated to provide better climate predictions (Niu et al., 2011, and references therein). Several other schemes available to the WRF model are given in the WRF user guide at: http://www2.mmm.ucar.edu/wrf/users/docs/user_guide_V3/ARWUsersGuideV3.pdf.

2.4.3 Radiation

Radiation parameterisation accounts for the longwave and shortwave processes associated with clouds. It handles the integration of solar flux, cloud albedo, cloud optical depth and absorption due to aerosols and gases. The parameterisation provides the net surface radiation for the land-surface schemes, partitioned into the total available energy for sensible, latent, and ground heat fluxes, and the vertical radiative flux divergence used to calculate the radiative heating and cooling rates for a given atmospheric volume (Stensrud, 2007). Absorption and emission from aerosols and clouds are included in the longwave, whereas shortwave treats extinction from aerosols, clouds and Rayleigh scattering (Iacono et al., 2008; Spyrou et al., 2013). The radiative effects are treated through the specification of their optical properties within each spectral interval. Clouds play an important role in the radiative field of the earth-atmosphere system and significantly affect the atmospheric thermal structure (Gu et al., 2011). The Rapid Radiative Transfer Model for Global [RRTMG] (Mlawer et al., 1997; Iacono et al., 2008) parameterisation scheme is employed in this study. This is a more accurate scheme and accounts for multiple cloud bands, trace gases, and microphysics species and commonly used in most simulations. See the WRF user guide for other schemes used in WRF.

2.4.4 Land surface

The land-surface parameterisation accounts for sub-grid scale fluxes and coupling between the Earth surface and the first few model layers. This parameterisation is responsible for the computation of friction velocities and exchange coefficients to enable the calculation of surface heat, moisture and momentum fluxes in the model. The fluxes provide a lower boundary condition for the vertical transport processed in the planetary boundary layer scheme. Land-surface parameterisation interacts with other parameterisations such as radiation, cumulus convection and the planetary boundary layer schemes. It also provides quantities such as surface sensible and surface latent heat fluxes, upward longwave and reflected shortwave radiation (including skin temperature and surface emissivity) and surface albedo (Chang, 2007). In this study, we employ the Noah land surface model (LSM) scheme (Cheng and Dudhia, 2001). Noah LSM is widely used in climate model simulations, and is a

physically based LSM scheme allowing soil moisture nudging and easily incorporates new time-varying input data and physics (Tong et al., 2013), as well as identification of optimal scheme combinations and critical processes controlling the coupling strength (Park et al., 2015, and references therein). It has multiple key options for key land-atmosphere interaction processes (Niu et al., 2011) and has its soil moisture predictions more accurate than most other schemes (Ferreira et al., 2005).

2.4.5 Planetary boundary layer (PBL)

PBL schemes are used to parameterise unresolved turbulent vertical heat fluxes, momentum, and constituents such as moisture within the PBL (Hu et al., 2010). Turbulent fluxes are computed at each model grid point from the mean atmospheric variables and/or their gradients. As highlighted above, various properties of the land surface can influence the energy fluxes that occur in the atmospheric surface layer and hence influence the evolution of the atmosphere. These influences first occur within the PBL (Stensrud, 2007). The land surface and PBL are intimately tied together such that response to surface forcing occurs within a short time period (typically a few hours or less). In this study, we use the Yonsei University PBL scheme (YSU) (Hong et al., 2006). Although the schemes have the strongest effect on temperature, humidity vertical distribution and precipitation, the YSU takes into account momentum and mass transfer from large eddies and has an explicit treatment for entrainment (Flaounas et al., 2010). This scheme is widely used in meteorological and atmospheric chemistry simulations because it realistically captures the vertical structure of the meteorological variables (Hu et al., 2013). Several other PBL schemes used in WRF are given in the user guide.

2.5 Gas- and aerosol-phase mechanisms and modules in WRF-Chem

The growing realisations of the importance of aerosol microphysical processes have led to the implementation of different schemes in models (Mann et al., 2012). These are of varying levels of complexity, depending on chemical speciation, process representation and mapping. The requirements are developed to improve the accuracy of simulated atmospheric processes such as climate forcing and aerosol–cloud interactions (ACIs). Two main approaches commonly used in chemical simulations are the modal and sectional schemes. Several aerosol and gas modules are available for use in chemical models. Similarly, there are several types of aerosol schemes implemented in WRF-Chem, either as modal or sectional -depending on the simulation performed.

Although the schemes are developed and implemented for use in different model simulations, precisions differ between the schemes and/or process representation. Modal approaches tend to be favoured over sectional approaches because of the computational efficiency and limited number of modes. These are less detailed and represent the size distribution of particles by several overlapping intervals, assuming a log-normal distribution within each mode (Mann et al., 2012; Zhao et al., 2013).

For example, aerosol spectra are assumed as a continuum, averaged over a scale (Cotton et al., 2010). Only mass of compounds is prognostic. However, simplifications in the parameterised approach can be biased to process rate and particle-size distributions (Kokkola et al., 2009; Mann et al., 2012, and references therein). The sectional approach is more detailed, whereby particle-size distributions are represented according a discrete set of size sections or bins (each bin representing particle size and number). This approach allows for a more nuanced representation of particle variation across the bins as opposed to the modal approach. Both approaches represent the entire particle spectra. To enable the complex interactions of various atmospheric processes, the aerosol representation is coupled with gas-phase chemistry (section 2.5.2) and clouds treatment.

2.5.1 Aerosol modules

There are three aerosol schemes available for WRF-Chem:

- MADE/SORGAM (Modal Aerosol Dynamic Model for Europe/Secondary ORGanic Aerosol Model) –modal aerosol scheme
- GOCART (GOddard Chemistry Aerosol Radiative and Transport model) –bulk aerosol scheme
- MOSAIC (Model for Simulating Aerosol Interactions and Chemistry) –bin aerosol scheme.

The MADE aerosol module is developed from the modified Regional Particulate Model and is incorporated with the SORGAM (Grell et al., 2005a, and references therein). MADE can predict aerosol mass components (e.g. SO_4^{2-}, NO_3^-, NH_3, sea salt, OC, BC, dust) and SOA. MADE/SORGAM is a modal representation and predicts particle growth (expressed in log-normal distributions) within the Aitken and accumulation modes. SORGAM can also treat anthropogenic and biogenic precursors.

The GOCART scheme is a bulk representation of the aerosol and works with the Regional Atmospheric Chemistry Mechanism Kinetic Pre-Processor (RACM-KPP) gas-phase chemical scheme. The use of KPP makes it easier to add/modify any chemical reaction (Kazil, 2009). GOCART contains several aerosol modules, enabling it to simulate emissions (e.g. sulphur, BC, OC, sea salt) and other chemical species (OH, H_2O_2, NH_3), advection, turbulent mixing, moist convection, dry and wet deposition for major tropospheric aerosols (Chin et al., 2002). Although GOCART can predict aerosol mass components quite efficiently, it cannot be used to determine aerosol size and interaction with radiation since it is a bulk scheme. There is also no coupling with cloud processes (neither aqueous chemistry nor indirect effects).

The MOSAIC sectional aerosol scheme (Zaveri et al., 2008) currently used in WRF-Chem has been implemented in the model to study aerosol evolution and direct radiative forcing (Grell et al., 2005a). This is an advanced module that allows for the coupling between various chemical and microphysical processes and is able to treat most aerosol species commonly found in regional or global scales, as well as within populated urban areas, including sulphate compounds (SO_4^{2-} and H_2SO_4), methanesulfonate

(CH_3SO_3), nitrate (NO_3^-), chloride (Cl), carbonate (CO_3^{2-}), ammonium (NO_4^+), sodium (Na^+), calcium (Ca^{2+}), black carbon (BC), primary organic matter (POM) and liquid water (H_2O). Other types of unspecified species are grouped together as "other inorganic mass" (OIN), largely to account for dust particles. Reactive inorganic species such as potassium (K^+) and magnesium (Mg^{2+}) are not explicitly modelled in MOSAIC because of their low atmospheric abundance compared to other aerosols; they are represented by equivalent amounts of Na because of their similar soluble sea salt components (sulfate, nitrate and chloride) in water. However, because of the simulation time constraints and computer memory, it would not be feasible to represent all species explicitly in the model, hence the user need to choose species based on accuracy for a given application (Zaveri et al., 2008).

2.5.1.1 Particle representation in MOSAIC

MOSAIC is a sectional aerosol framework designed to explicitly simulate aerosol particle evolution in terms of number, mass and mixing ratios. Aerosol particles are divided into bin size (defined in terms of their upper and lower bounds of dry-particle size limits). The sectional approach can be implemented in 4 or 8 bins. Each bin is assumed to be of internally mixed so that all particles are of the same chemical composition (Zaveri et al., 2008; Chapman et al., 2009), whereas particles in different bins are externally mixed. The same particle-size distribution is assigned to all PM emissions, including sulphate, nitrate, organic mass and OIN (Shrivastava et al., 2013) and all components in a single size section are assumed to be internally mixed. However, the user has the flexibility to select the number of bins. MOSAIC includes treatments of nucleation, coagulation, and condensation as described by Chapman et al. (2009) and Fast et al. (2009b). The mass and number are simulated for each bin and particle growth or shrinking resulting from the gas-to-particle partitioning (from gases H_2SO_4, CH_3SO_4H, HNO_3, HCl, NH_3) is calculated in a Lagrangian manner. Aerosol coagulation is determined with a Brownian coagulation kernel (Zaveri et al., 2008; Chapman et al., 2009, and references therein). Currently, MOSAIC uses the Wexler parameterisation for H_3SO_4–H_2O homogeneous nucleation.

At the core of the thermodynamic module is another sub-module to estimate the activity coefficients of various electrolytes in multicomponent aqueous aerosols. Activity coefficients are repeatedly required in solid–liquid phase equilibrium and gas–particle partitioning calculations (Zaveri et al., 2008). The thermodynamic module is repeatedly called for each size bin during the integration. The module consists of the components (Multicomponent Taylor Expansion Method [MTEM] and Multicomponent Equilibrium Solver for Aerosols [MESA]) for calculating the activity coefficients on aqueous atmospheric aerosols and the intraparticle solid–liquid phase equilibrium, respectively. MTEM estimates the mean activity coefficient of an electrolyte in a multicomponent solution on the basis of

its values in binary solution of all electrolytes present in the mixture at the solution water activity (a_w), assuming that it is equal to the ambient RH. This is determined using the Zdanoskii-Stokes-Robinson (ZSR) method. For self-consistence, most MTEM parameters are derived using the Pitzer-Simonson-Clegg model (PSC) (Zaveri et al., 2008, and references therein). MESA is used to solve the multicomplex solid–liquid equilibria within each aerosol bin, using a modified pseudotransient continuation technique in which equilibrium reactions are formulated as pseudotransient precipitation and dissociation reactions resulting in a set of equations, as described below.

Aerosol chemistry requires more reliable and accurate thermodynamic modules able to predict particle deliquescence, water content and solid–liquid phase equilibrium in aerosol speciation at any given RH and temperature. This requires a module that can compute the mass transfer driving forces for dynamic gas-to-particle partitioning of various semi-volatile species (Zaveri et al., 2008). As highlighted above, the MESA sub module is a thermodynamic solver for solid, liquid and mixed-phase state of aerosols. The MOSAIC aerosol thermodynamic module is specifically designed to be coupled to MOSAIC for use in dynamic gas-to-particle partitioning because it is reliably accurate and computationally efficient.

2.5.1.2 Gas–particle partitioning

Gas–particle partitioning of some semi-volatile species (e.g. HNO_3, HCl, NH_3) is reversible and depends on gas–particle mass transfer kinetics, thermodynamic conditions and multiphase chemical reactions. These factors are very sensitive and respond directly to changes in meteorological controls (e.g. temperature, RH), as well as gas-phase changes, particle size and distribution. The MOSAIC module determines the mass transfer rate for semi-volatile gases over aerosol bin sizes (from gas to aerosol phase) at equilibrium. The approach is described by a system of nonlinear ordinary differential equations (ODEs) of the form:

$$\frac{dC_{a,i,m}}{dt} = k_{i,m}\left(C_{g,i} - C^*_{a,i,m}\right) \qquad [2.1]$$

$$\frac{dC_{g,i}}{dt} = -\sum_m k_{i,m}\left(C_{g,i} - C^*_{a,i,m}\right) \qquad [2.2]$$

where $C_{a,i,m}$ (mol m^{-3}) is particle-phase concentration of the i^{th} species in aerosol bin m, $C^*_{a,i,m}$ denotes equilibrium gas-phase concentration of species i with the particle-phase of bin m; $C_{g,i}$ is the bulk gas-phase concentration of the same species i. The term $\left(C_{g,i} - C^*_{a,i,m}\right)$ drives the mass transfer, where $k_{i,m}\left(C_{g,i} - C^*_{a,i,m}\right)$ (mol cm^{-3} s^{-1}) is called the *instantaneous flux* of species i to or from bin m, $k_{i,m}$ (s^{-1}) is the first order mass transfer coefficient, defined by:

$$k_{i,m} = 4\pi \bar{R}_{p,m} D_{g,i} N_m f\left(Kn_{i,m}, \alpha_i\right) \qquad [2.3]$$

where $D_{g,i}$ ($cm^2\ s^{-1}$) is gas diffusivity of species i, N_m (cm^{-3}) is the number concentration of particles in bin m, and $f(Kn_{i,m},\alpha_i)$ is the transition regime correction factor to the Maxwellian flux as a function of the Knudsen Number $Kn_{i,m} = \lambda_i / \overline{R}_{p,m}$ (where λ_i is the mean free path):

$$f\left(Kn_{i,m},\alpha_i\right) = \frac{0.75\alpha_i(1+Kn_{i,m})}{Kn_{i,m}(1+Kn_{i,m}) + 0.283\alpha_i Kn_{i,m} + 0.75\alpha_i} \qquad [2.4]$$

The above correction factor also accounts for interfacial mass transport limitation characterized by the mass accommodation coefficient α_i, assumed to be very small equal to 0.1 for all condensing species (Zaveri et al., 2008, and references therein).

In order to successfully partition the gas–particle described above, the coupled nonlinear ODEs must be solved to obtain unique-dependent solutions. But this gives rise to a stiffness problem due to different characteristic times required by the semi-volatile species in different aerosol bins to reach their equilibrium condition. ASTEM is designed to accommodate prominent characteristics of gas–particle partitioning while at the same time reducing the stiffness involved in separating the non-volatile gases from the semi-volatile ones. ASTEM uses a time-split solver by analytically integrating the condensation of non-volatile gases (H_2SO_4 and methane sulfonic acid [MSA]) for all the bins, solution of which is independent from the gas-phase state of the particles in the bins with a more complex solution for the semi-volatile gases (HNO_3, HCl and NH_3). A full account of the mass transfer algorithm is given in Zaveri et al. (2008).

2.5.2 Gas-phase modules

In addition to the aerosol schemes, there are several gas-phase chemistry mechanisms available for WRF-Chem, including Regional Acid Deposition Model [RADM], Regional Atmospheric Chemistry Mechanism [RACM] (Stockwell et al., 1990; 1997), Carbon Bond Mechanism -version 4 [CB-4], Carbon Bond Mechanism-Z [CBM-Z] (Zaveri and Peters, 1999), State-wide Air Pollution Research Center mechanism of 1999 [SAPRC99] (Cater, 2000). The Regional Acid Deposition Model v2 (RADM2) mechanism comprises of detailed chemistry and accurate chemical predictions and is widely used in atmospheric models to predict the concentrations of oxidants and other air pollutants. RADM2 includes 14 stable species, 4 reactive intermediates and 3 abundant stable ones (O, N and H_2O), 26 stable species and 16 peroxy radicals representing organic species. RADM represents organic chemistry species through reactivity aggregated molecular approach, commonly used with MADE/SORGAM (sometimes with aqueous reactions) or RADM2-Kinetic Pre-Processor (RADM2-KPP).

The Kinetic Pre-Processor software tool is designed to facilitate the numerical solution of chemical reaction network (Damian et al., 2002). The tool is used in the model code to read chemical reactions

and rate constant in ASCII input files and automatically generates the code for the chemistry integration (Sulzman and Lawrence, 2006). The code computes the time-evolution of chemical species based on the specifications on the user-defined chemical mechanism. The user need to describe the application in terms of logical modules within the model and specify a set of equations, initial chemical concentration values and the integration algorithm (Damian et al., 2002). Addition of the chemical mechanisms is done in the WRF-Chem Registry (Registry.EM_CHEM). To enable the KPP library in the model, one has to switch "ON" the code in the *chemistry directory* by setting "SETENV WRF_KPP 1" (to include KPP) or 0 (if KPP is not included). This process is advantageous in that it is less time consuming, numerically efficient and less error prone. There is also the flexibility of updating mechanism with additional species and equations (Ahmadov, 2012). The KPP is compiled automatically when the model is compiled and the KPP input files for the chemistry mechanisms implemented are located in the subdirectories of the chem/KPP/mechanisms with the corresponding packages declared in the Registry containing their names.

Trace gas chemistry for urban and global scales for use with MOSAIC is presented in a "lumped-structure" photochemical scheme CBM-Z (Zaveri and Peters, 1999), based on the widely used Carbon Bond Mechanism (CBM-IV) developed by Gery et al. (1989). CBM-Z was developed by extending the original CBM-IV framework to function at larger spatial and longer timescales. This is a condensed mechanism capable of describing tropospheric hydrocarbon chemistry with reasonable accuracy and sensitivity at various scales. Individual particles can be explicitly resolved in a complex aerosol composition within a small air volume representing a large well-mixed air mass (Zaveri et al., 2010). For example, a large number of organics are grouped together into a concise set of VOC categories based on similarity in oxidation reactivity, emission magnitudes, molecular weights and types of bonds. CBM-Z has a better accuracy than most other gas phase modules, with less computational demand, making it better than its precursor mechanisms and does well at regional to global spatial scales and longer time periods. It also includes a condensed dimethylesulphide (DMS) photo-oxidation mechanism for simulating temperature dependence on the formation of sulphur compounds (SO_2, H_2SO_4 and MSA) in marine environments.

2.5.3 Photolysis scheme

The photolysis gas-phase chemical mechanisms encompass photolysis reactions calculated using the Fast-J scheme (Wild et al., 2000; Fast et al., 2006). The photolysis driver computes frequencies at each grid point (Grell et al., 2005a) using an online treatment of molecular and aerosol absorption and scattering. The actinic flux profiles are calculated at each grid point using temperature, ozone and cloud profiles from the meteorological model. Hygroscopic aerosol growth is taken into account using

the simultaneous water vapour mixing ratios. Actinic flux is calculated using the Rayleigh scattering, absorption and reflection by aerosols and clouds. The calculation starts with the incident solar radiation at the top of the atmosphere (TOA), including absorption and scattering of light at the surface (Madronich, 1987). Photolysis frequencies for the 20 photochemical reactions are computed as the integral of the product of the actinic flux $I_A(\lambda)$, absorption cross-section $\sigma(\lambda)$ and quantum yield $\Phi(\lambda)$ over a range of wavelengths λ. The basic photolysis equation for the i^{th} species in WRF-Chem (Grell et al., 2005a; Lo and Hung, 2012) is expressed as:

$$J_i = \int_0^{\lambda} I_A(\tau,\lambda)\sigma_i(\lambda)\Phi_i(\lambda)d\lambda \qquad [2.5]$$

where J_i (molecules cm^{-3} s^{-1}) is the frequency of gas-phase photochemical reaction of species i at each wavelength. The actinic flux is affected by several factors (Collins et al., 1997). For example, the solar flux incident on the atmosphere is attenuated by ozone and molecular oxygen absorption, whereas the remaining flux reaching the troposphere is scattered by aerosols, clouds and atmospheric molecules and reflected by the earth surface. There are some photolysis schemes used in WRF-Chem (e.g. Madronich, F-TUV (Madronich, 1987; Tie et al., 2003) and Fast-J (Wild et al., 2000; Fast et al., 2006)). The Fast-J scheme is used in this study. This scheme has demonstrated to be a flexible and accurate, compared to its other alternatives and efficient to be incorporated in 3D chemical transport models. Also, it has its photolysis rates updated hourly, hence computationally efficient (Wild et al., 2000). Because photolysis rates are computed online, the influence of aerosols on photolysis rates are taken into account (Emmons et al., 2010; Zhao et al., 2013). Fast-J directly uses the physical properties of the scattering and absorbing particles in the atmosphere as calculated by the model or specified in a climatology (Wild et al., 2000).

2.6 Boundary conditions, emissions, aerosols and gas phase modules in WRF-Chem

Boundary conditions are important aspects in any model environment because they constrain the overall model performance to pre-defined values at the extent of the domain. These are provided at every grid cell at the physical boundary of the model domain throughout the simulation. They can either be kept constant or varied during the course of the simulation. For this study, model configuration, setup and simulation are described in chapters 3 and 4. Configuration options and preparation for emission data used are provided in Appendix A.

2.6.1 Meteorological boundary conditions

Meteorological input data are provided at hourly intervals consisting of layer-averaged 3D gridded fields of wind, temperature, humidity, density and 2D gridded fields of mixing height, boundary layer and surface variables, precipitation rate and cloud cover. This data can be obtained from several

datasets such as the operational European Centre for Medium-Range Weather Forecasts (ECMWF), Global Forecast System (GFS), National Centre for Environmental Prediction (NCEP) etc., to produce initial BCs for the model simulation.

2.6.2 Chemical boundary conditions

Although the importance of lateral BCs in atmospheric and numerical prediction models has been well established in the meteorological community, increasing attention has been drawn to consideration of the chemical lateral BCs in regional chemical transport models, AQ simulations and inflow of pollution (Pfister et al., 2011). However, because there is no single tool to construct emission dataset for any particular domain and chemistry mechanism, the task lies upon the user to construct chemical input data for the desired domain (Peckham et al., 2012). Care must be taken to ensure that correct emission data files are chosen for the desired simulation. For this study, a set of chemical BCs were obtained through the downscaling of output from the MOZART-4 (Model for Ozone and Related chemical Tracers, version 4) global chemical transport model.

2.6.2.1 The MOZART module

The archived global 6-hr MOZART described by Emmons et al. (2010) is developed from the update of its precursor versions (MOZART-2 and MOZART-3), built from the framework of the Model of Atmospheric Transport and Chemistry (MATCH) including several other modifications from various parameterisation schemes and options included in the new source pack. The module can be driven by any meteorological dataset and emission inventory at any resolution (provided it matches with the meteorological input fields); the highest resolution so far has been run with the full chemistry at $0.7^{o} \times 0.7^{o}$ grid spacing (Emmons et al., 2010). Global MOZART data is available at: http://web3acd.ucar.edu/wrfchem/mozart.stml/ and is able to operate on most common map projections (e.g. Lambert conformal, Mercator, polar). The free-to-download source code "mozbc" is then compiled to generate the chemical BCs. The source code is controlled in the *namelist.input* file defining specific mappings for the chemical modules such as RADM, RACM, CBMZ, MADE/SORGAM, MOSAIC, and GOCART (section 2.5). Building on from the previous module MOZART-2, the chemical mechanism in MOZART-3 was expanded to incorporate the representation of non-methane hydrocarbon and allow for online aerosol calculation, including wet deposition. An online photolysis scheme takes into account the impact of aerosol and cloud photolysis rates. MOZART-3 also includes a scheme for determining albedo.

The standard MOZART model has about 85 gas-phase species, 12 bulk aerosol components, 39 photolysis reactions and 157 gas-phase reactions. The reaction set include the updated isoprene oxidation scheme and VOC treatment, with three lumped species representing alkanes and alkenes,

about four or more carbon and aromatic compounds (BIGALK, BIGENE and TOLUENE) and their oxidation products. A full list of speciation for gas-phase, particle-phase and photolysis reactions is given by Emmons et al. (2010).

For our simulations, Prep-chem was used to map the MOZART components at the boundaries onto the species in the chosen CBM-Z scheme. PREP-CHEM-SRC (Freitas et al., 2011) was designed to provide emissions made with RADM2, RACM and GOCART gas-phase and aerosol mechanisms. The chemical mechanism is determined by providing the corresponding chemistry files during the code compiling (Freitas et al., 2011), whereby interpolation routines for creating emission fields are used by the model grid, either nearest-neighbour interpolation (fine grid) or averaging (coarser grid). Both options are mass conservative. Mapping emissions onto the model grids was done following the methodology described by Archer-Nicholls et al. (2014). For the gas-phase anthropogenic reactions, the same mapping used for RADM2 speciations are adapted to CBM-Z within WRF-Chem. Long-chained hydrocarbons were added to the CBM-Z species paraffin carbon (PAR), terminal olifin and internal olefin carbons (OLET and OLEI) (Zaveri and Peters, 1999). Because the code produces particle values for BC, OC and PM ($PM_{2.5}$ and PM_{10}), based on factors defined by Andreae and Merlet (2001), BB emissions of OC were converted to particulate organic matter (POM), to account for the non-carbon fraction of the organic matter, multiplying by factor of 1.5 whereas those for anthropogenic were multiplied by factor of 1.6. All particulates (other than BC or POM), assumed to be unreactive are mapped to OIN. Prep-chem also provides data for the model to drive and distribute the smoke plumes within the model columns, accounting for plume buoyancy based on the fire size. This is achieved using the plume-rise parameterisation (Freitas et al., 2007) to determine the injection height of the plumes during the flaming phase.

2.7 Emissions in the model

2.7.1 Prep-chem source

The use of global emission data is commonly used in most WRF-Chem simulations and available to WRF-Chem users. Annual emissions dataset obtained from global databases was used to generate the emission data files to run the model. These were prepared by running a simple grid-mapping program called the Prep-Chem_source code (Freitas et al., 2011). The code is written in FORTRAN-90 and C program languages and requires HDF and netCDF libraries for visualisation. It can use several map projections (Polar-Stereographic, Gaussian, Lambert conformal, Mercator and FIM model grid) at regional and global grid resolutions. The desired grid configuration and emission inventories are set and defined in a FORTRAN *namelist.input* template called *prep_chem_sources.inp*. Detailed description of the use of the script is given by Freitas et al. (2011) and the WRF-Chem user Guide

(http://ruc.noaa.gov/wrf/WG11/Users_Guide). Successful running of the source code creates raw emissions data in binary form. Because the model only read data in a netCDF format, the binary files must be converted into a readable format for the WRF-Chem model and mapped into a 3D simulation. This is done through a program called *convert_emiss.exe.* The source code and its implementation in WRF-Chem is also discribed in the Appendix at the end.

2.7.2 Anthropogenic emissions

Anthropogenic emissions comprise mainly of emissions from fossil and biofuel combustions and chemical use from industries and other machinery or traffic, including ships and aircraft. These also include emissions from solvent usage and a large portion coming from urban sources (Seinfeld and Pandis, 2006). Anthropogenic emissions were obtained from various datasets based on global emission inventories, including Emission Database for Global Atmospheric Research [EDGARv4.2] (http://edgar.jrc.ec.europa.eu) available in two formats: ASCII (0.1° × 0.1°) per year and netCDF (0.1° × 0.1°) per year in kg (N) m^{-2} s^{-1} for the period 2000–2005; REanalysis of the TROpospheric [RETRO] chemical composition over the past 40 years (http://retro.enes.org) provided at 0.5° × 0.5° grid spacing for 2004; Studies of Emissions, Atmospheric Composition, Clouds and Climate Coupling by Regional Surveys [SEAC^{4}RS]; GOddard Chemistry Aerosol Radiative and Transport model [GOCART] and the fourth dataset based on "an assessment study on biofuel use and agricultural waste burning [bawb] in developing world since 1985" (Yevich and Logan, 2003). The databases provide global emissions of various gas phases and particulates. Data calculation is based on factors such as location of energy, manufacturing facilities, road network, shipping routes (coastal areas), human and animal population density and agricultural land use and industry.

EDGAR emissions were favoured because of consistency between different sectors and completeness over the sectors. The database has a better representation at high resolution for most of the emission distributions. They were selected (except where some could not be obtained or a particular species being better represented from a different database). For example, the *bawb* data was considered for some of the emissions (e.g. NH_3, wood fuels and other burning residues) missing or unavailable from some source sectors.

2.7.3 Biogenic emissions

WRF-Chem has four choices for biogenic emissions: Guenther emission (which treats emissions of isoprene, monoterpenes, other BVOCs and nitrogen emission from the soil) has two options with- and without biogenic emission; the EPA Biogenic Emissions Inventory System [BEIS v3.13] data (http://ruc.noaa.gov/wrf/WG11/biogenic.htm) and the Model of Emissions of Gases and Aerosols from Nature (MEGAN), described by Guenther et al. (2006; 2012) and Jiang et al. (2012). MEGAN is a

model system capable of estimating the net gas and aerosol emissions from terrestrial systems into the atmosphere, with its driving variables such as land cover, weather and atmospheric chemical composition. It is available as an offline code, but has also been coupled into land surface and atmospheric chemistry models (Guenther et al., 2012). The module provides a method by which normalized biogenic emissions for standard light and temperature conditions can be brought into simulations. Parameterisation of biogenic emissions in the *namelist* template (*bio_emiss_opt*) is set depending on the domain of simulation and emission data used. MEGAN uses the land use data to estimate the biogenic emissions (km^{-2} h^{-1}) based upon the vegetation type (e.g. deciduous, coniferous, mixed forests and croplands), weather conditions and shortwave radiation. It has a horizontal grid spacing of about 1 km, enabling it to be used in almost all WRF-Chem simulations. Acquisition of data is upon the user to obtain and compile a full utility of the data from the NCAR web sites (http://cdp.ucar.edu) or (http://www.acd.ucar.edu/wrf-chem) and prepare biogenic input files (*wrfbiochemi*) for use in the model (Peckham et al., 2012), while assimilation of the module is also dependent upon the correct settings in the *namelist.input* file. For the present study, these emissions were built on runtime using an online MEGAN module.

2.7.4 Biomass burning (fire) emissions

Open biomass burning (wildfires, agricultural burning and managed burns) make up one of the important parts of the total global emissions of both trace gases and particulate matter (Wiedinmyer et al., 2011). According to the authors, current emissions inventories estimate that open biomass burning (BB) emits about 26–73% of global emissions for primary PM and 33–42% of fine BC emissions. For example, Andreae and Merlet (2001) reported emission factors (EF) for conversion from carbon emissions to other species such as CO, CH_4, NMHC, NO_x, NH_3, SO_2, $PM_{2.5}$, TPM, OC and BC in terms of land use types: tropical forest, extra-tropical, agricultural residues, savanna and grassland areas. Gas phase components from the fire plumes (e.g. VOCs and NO_x) can react downwind of the fire locations and contribute to the chemical reactions (forming secondary aerosols), which may have important implications for the chemical cycles in the atmosphere. Depending upon the interaction between chemical kinetics and physical dynamics in the flame, intermediate products of flame radical chemistry such as CO, CH_4, H_2, C_2H_4, PAH and soot particles are released during combustion (Andreae and Merlet, 2001).

Although some inventories are created from in-situ measurements and observations, others are created from a combination of satellite-derived datasets. Regional emission estimates and inventories are created for specific time periods while other predictions can also be created for longer time periods. Several global scale emission inventories also exist, e.g. Logan and Yevich (2003) (biofuel use and

agricultural waste burning in developing world), Andreae and Merlet (2001) (total global gaseous and particulate emissions in the late 90s). The importance of these emissions is critical for characterising AQ problems, in-situ measurements and/or estimates and simulating the chemistry in climate models (Wiedinmyer et al., 2011). However, the nature of these emissions (being episodic and highly variable) makes them difficult to measure or predict. Different mechanisms used to detect the fire emissions include satellite remote-sensing techniques. The techniques monitor fire activities over a range of scales at high resolutions (Qian et al., 2009) and represent heterogeneity within biomes (van der Werf et al., 2006, and references therein).

There are two products of fire data used in WRF-Chem: the Fire INventory from NCAR (FINN) model (Wiedinmyer et al., 2011) and the Brazilian Biomass Burning Emission Model [3BEM] (Longo et al., 2010). Both methods use the "bottom-up" approach to estimate the quantity of biomes consumed during combustion, and are designed to use any available fire detection data. The location and timing for the fires can be identified and picked globally by satellite observations (e.g. MODIS) to generate monthly burnt area estimates. However, detection of burnt areas can represent a greater challenge (van der Werf et al., 2006), especially in tropical deforestation areas because of consistent cloud cover and, to some extent, human manipulation of fire processes. FINN uses satellite observations of active fires and land cover, together with emission factors and estimated fuel loadings, to provide daily, high-resolved open burning emissions estimates for use in regional and global chemical transport models (Wiedinmyer et al., 2011). Emissions are estimated using the expression:

$$E_i = A(x,t) \times B(x) \bullet FB \times ef_i \qquad [2.6]$$

where E is the mass of emitted species i, A is the burnt area at location x and time t, B is the amount of biome burnt (biomass loading), FB is the fraction of burnt biome in the fire, and ef_i is the emission factor of species i emitted/burnt. All terms in the equation are on a dry weight basis.

The 3BEM parameterisation scheme (Longo et al., 2010) is based on the approach of Freitas et al. (2005), which uses a different approach to calculate the mass of emitted tracer calculated for each fire pixel detected. Fire emissions are updated once they become available, spatially and temporally distributed according to the fire count location obtained by remote-sensing techniques (e.g. Advanced Very High Resolution Radiometer [AVHRR] or MODIS). Using the satellite data, 3BEM employs a hybrid remote-sensing fire product to minimise the adverse impact of missing remote-sensing observations (Grell et al., 2011a). The fire product may be combined using a filter algorithm to avoid double fire counting, by eliminating additional fires within a 1-km radius circle. The emitted tracer is calculated (Longo et al., 2010) from the expression:

$$M^{[\eta]} = \alpha_{veg} \bullet \beta_{veg} EF_{veg}^{[\eta]} \bullet a_{fire} \qquad [2.7]$$

where M is mass of tracer for species η, α is amount of above-ground biome available for burning, β is combustion factor, EF is emission factor from appropriate vegetation type and a_{fire} is burning area for each event. Taking into account all the possible observed sub-grid fires burning different types of vegetation, the total emission per species for each grid box is given by:

$$Q^{[\eta]}(t) = \frac{r(t)}{\rho_0 \Delta V} \sum_{\substack{fires\_\in \\ Grid\_Box}} M^{[\eta]} \qquad [2.8]$$

where $r(t)$ is the Gaussian function centred at the time of maximum fire activity, ρ_0 is the basic-state air density, ΔV is the grid cell volume, and $M^{[,]}$ is as defined in equation [2.7] above. Assuming the area burnt to be proportional to the fire pixel counts (Giglio et al., 2006), the number of fire pixels observed within the same region during the same time period N_f, for the i^{th} species at time t can be expressed as:

$$N_f(x,t) = \frac{A(x,t)}{\alpha} \qquad [2.9]$$

where $A(x,t)$ and α are defined in equations [2.6] and [2.7] above. Emissions are normally calculated as a product of burnt area, fuel load, and combustion completeness integrated over time and space scales of interest (van der Werf et al., 2006). However, the burnt area is usually considered the most uncertain parameter in emissions estimates. This uncertainty arises due to the potentially high spatial and interannual variability at continental to global scales (Giglio et al., 2006). Therefore, accurate, spatially explicit, multi-year estimates of burnt areas should be available when using these relationships. BB emissions are then mapped onto the WRF-Chem domain to generate the fire emissions using the model-supported Prep_chem_source code package, depending the user-supplied geographic coordinates for each wildfire and emission species.

The MODIS is a key instrument aboard the Terra (EOS AM) and Aqua (EOS PM) satellites acquiring data in 36 spectral bands (http://modis.gsfc.nasa.gov/about/). The satellite, launched by the National Aeronautics and Space Administration (NASA) on the polar-orbiting Earth Observatory System (EOS) is calibrated and processed using cloud screening, geo-location and atmospheric correction is available at: http://modis-atmos.gsfc.nasa.gov. The instrument has two channels (21 and 22) at wavelength 4 μm used for global fire detection (Kaufman et al., 1998). Channel 22 is saturated at 331 K, less noisy than channel 21 and used whenever possible, whereas channel 21 is saturated at 500 K and not affected by gas absorption or water vapour. It is used when there is data missing from channel 22 (Giglio et al., 2003). MODIS detects a threshold of potentially active fires using brightness temperatures derived between 4 μm and 11 μm channels at varying spatial resolutions to differentiate fire pixels from the non-fire background.

Active fire products fall within the suite of terrestrial products and provide information about actively burning fires, including the location, timing, instantaneous radiative power and smouldering ratio (Giglio et al., 2003, and references therein). The algorithm examines each of the MODIS swath-based fire masks (i.e. list of fire pixel locations and dates) and assigns it to different categories: missing data, cloud, water, non-fire and unknown (where mixing data are pixels lacking valid data). There are two logical paths through which fire pixels are identified: a single absolute threshold test (set sufficiently high so that it is triggered only by very unambiguous fire pixels) and the one consisting of a series of contextual tests designed to identify the majority of active fire pixels. However, false alarms and clouds can be detected using the brightness temperatures for the 250-m red (ρ0.65) and near-infrared (ρ0.86) channels, whereas water-induced false alarms can be detected by the 500-m 2.1 μm band (ρ2.1) (Giglio et al., 2003). Observations are often summarised at coarse horizontal grid spacings (e.g. 0.5° × 0.5°) for daily or monthly time periods, yielding data products containing gridded fire counts (Giglio et al., 2006). Although the two methods for the fire products discussed above are both used in WRF-Chem, the fire emissions used in the present study were generated with the Prep-Chem_source code using fire products from 3BEM, based on MODIS satellite retrievals archived at (http://ftp-supercomputacao.inpe.br/public/rodrigo.braz/).

2.7.5 Sea salt

Sea-salt aerosol is emitted from the oceans and produced primarily from the bursting of air bubbles resulting from the entrained ocean whitecaps and the ocean crests torn off by the wind over the water surface (Blanchard, 1989; Kuhns and Vukovich, 1997; Piketh et al., 2002). Sea-salt aerosols are produced when the wind (typical 9 m s^{-1} or above) blows over the ocean, breaking the waves and entrain air bubbles on the water forming small patches of cloud-like structure. When injected to the atmosphere, the bubbles burst and yield small film jets or spumes known as sea sprays composed of both inorganic sea-salt and organic matter. Their release from the oceans occurs through two ways (Andreae et al., 1994): (i) shattering of the film caps generates small droplets (of varying size ranges) into the surface and, (ii) a jet directly projected upward from the collapsing bubble cavity which breaks into small droplets in the air. Their production rate is strongly dependent on meteorological conditions on the water surface (Kuhns and Vukovich, 1997). In our WRF-Chem simulations, sea-salt is considered to comprise solely of sodium (Na^+) and chlorine (Cl^-). However, it must be acknowledged that we don't know the biological activity in the ocean and hence organic content of seawater. These emissions were prepared through online parameterisation in the model.

2.8 Aerosol–cloud interactions in WRF-Chem

Cloud microphysical and cumulus parameterisations are treated within the WRF part of the model. However, because WRF does not treat aerosols on its own, ACIs are treated within the WRF-Chem modules. Simulations of the influences of aerosol dynamics require a model capable of handling the coupling of aerosol interactions, meteorology and radiation in a fully interactive manner. WRF-Chem is such a model that allows for the investigation of feedbacks amongst the various atmospheric processes (Grell et al., 2006; Chapman et al., 2009; Yerramilli et al., 2010).

2.8.1 Parameterisation of aerosol particle activation into cloud droplets

Aerosol activation in WRF-Chem is determined by the Ghan et al. (1997) and Abdul-Razzak and Ghan (2000; 2002) (herein, ARG) scheme. Activation and droplet nucleation is based on a maximum supersaturation S_{max}, determined from a Gaussian spectrum of updraft velocities and internally mixed aerosols within each size bin (ARG, 2002). CCN particles are tightly coupled with *chemistry-physics* portions in the code within the dynamical framework, adiabatically with a prescribed updraft velocity (w) to compute S_{max} achieved by the ascending air parcel (Meskhidze et al., 2005). Aerosol–cloud processes require a microphysics scheme with prognostic capability because the prognostic droplet number depends upon advection, loss due to evaporation and droplet source due to nucleation (Grell et al., 2011a). A prognostic cloud droplet option is used by the microphysics scheme to compute cloud droplet number. The scheme uses the subgrid w calculated from the turbulent kinetic energies (TKE) for all layers above the grid surface. Activation of particles is calculated simultaneously with turbulent vertical mixing (Chapman et al., 2009). Only CCN particles satisfying the criteria $S_c \leq S_{max}$ activate into cloud droplets.

The number and mass mixing ratios for both interstitial and cloud-borne particles are treated separately as fully prognostic species (Grell et al., 2011a), and cloud-borne particles transported into non-cloudy grid cells are re-evaporated to interstitial aerosols (Shrivastava et al., 2013). The bulk hygroscopicity κ for each size bin is based on the volume of the weighted-average of the hygroscopicity for each aerosol component (Grell et al., 2011a; Tuccella et al., 2015). κ is used in the calculation of aerosol activation to cloud droplets. Following Ghan et al. (1997), droplet-number concentration is predicted by accounting for transition processes (e.g. autoconversion, nucleation, evaporation/condensation, collision/coalescence). Although cloud-borne particles are treated separately, the cloud-chemistry module provides the fraction of each trace gas that is cloud-borne or dissolved in cloud water. In the event of cloud formation, particulates and gases that become associated with precipitation are deposited immediately to the surface.

Cloud-droplet number is an essential parameter in investigating aerosol effects on cloud radiation and lifetime, whereas particle size is one of the essential properties in determining its ability to form clouds. A series of stages exist through which aerosols activate into cloud droplets. First, the aerosol population is defined in terms of chemical composition and size distribution. Because it is computationally expensive to track particles individually, various mathematical attempts have been made to describe aerosols in terms of number-size distributions. The activation of a single or multiple distribution of particles can be described by a distribution function, where the number of aerosol particles per logarithmic bin width $\frac{dN}{d\ln D_p}$ is described by the expression (Simpson et al., 2014):

$$\frac{dN}{d\ln D_p} = \frac{N}{\ln\sigma\sqrt{2\pi}}\exp\left[\frac{\ln^2\left(\frac{D_p}{d_m}\right)}{2\ln\sigma^2}\right] \qquad [2.10]$$

where D_p and N are the particle diameter and particle-number concentration, σ is the geometric standard deviation and d_m is the median diameter.

The ARG parameterisation uses the Junge power law distribution to predict S_{max} of the rising air parcels, number and mass activated for each size section, assuming particles to grow from their initial equilibrium size $r_i = r$ to the size at which they activate ($r = r_c$) at critical supersaturation $S = S_c$. The scheme is applied by calculating an effective critical supersaturation of all sections from which S_{max} is determined (ARG, 2002). The smallest activation dry radius $r_{act,i}$ for each mode (ARG, 2000) is given by:

$$r_{act,i} = r_{m,i}\left(\frac{S_m}{S_{\max}}\right)^{\frac{2}{3}} \qquad [2.11]$$

and critical supersaturation $S_{m,i}$ and ambient maximum saturation S_{max} (ARG 2000; 2002) given by:

$$S_{\max} = S_m\left[f(\sigma)\left(\frac{\varsigma}{\eta}\right)^{\frac{3}{2}} + g(\sigma)\left(\frac{S_m^2}{\eta+3\varsigma}\right)^{\frac{3}{4}}\right]^{\frac{-1}{2}} \qquad [2.12]$$

$$\text{and} \quad S_m = \frac{2}{\sqrt{B}}\left(\frac{A}{3r_m}\right)^{\frac{3}{2}} \qquad [2.13]$$

The terms $f(\sigma)$ and $g(\sigma)$ are functions of the standard deviation σ_w of the log-normal size distribution for the critical saturation S_m of the particle with a dry radius equal to the geometric mean dry radius r_m of the distribution. A and B are the coefficients of curvature (Kelvin term) and hygroscopic parameter (Raoult term) as defined in the Köhler equation (chapter 1), given by:

$$A = \frac{2\sigma_w M_w}{\rho_w RT} \quad \text{and} \quad B = \frac{v\Phi M_w \rho_a}{M_a \rho_w} \qquad [2.14]$$

Once the droplet number concentrations are computed for each perturbation value of temperature and RH, they are averaged to provide a single value of cloud droplet number for each grid cell. Distribution is centred on the grid box vertical velocity *w*, whereas standard deviation σ is calculated from:

$$\sigma_w = \frac{\sqrt{2\pi}K}{\Delta z} \qquad [2.15]$$

where *K* is the vertical eddy diffusion, and *Δz* is the model layer thickness. The number of cloud droplets forming depends on S_{max}, within an air parcel containing an aerosol population, determined by atmospheric conditions (e.g. adiabatic cooling, condensation of water vapour) and aerosol distribution. In order for aerosols to serve as cloud nuclei, they must have an affinity for water (hygroscopic) so that water vapour can condense onto them. The number of activated CCN spectra is determined beneath S_{max} for each model grid to give the total cloud droplet number concentration N_d, given by:

$$N_d = CCN(S_{\max}) \qquad [2.16]$$

Activation occurs when the environmental supersaturation in the air entering cloud exceeds S_c of the particles. During cloud formation, the environmental supersaturation for a given air parcel exhibits a short transient maximum, triggered by initial adiabatic cooling and quenched by condensation of water vapour onto the newly formed cloud droplets, which serve as sinks for water vapour. Consequently, the process results in a decrease in supersaturation as aerosols compete with the already-activated droplets for available water vapour. Under such conditions, the mass balance of each particle and the rate of supersaturation change of the air parcel can be expressed (Abdul-Razzak et al., 1998; Ghan et el., 2011) as:

$$\frac{dS}{dt} = \alpha v - \gamma \frac{dW}{dt} \qquad [2.17]$$

where *v* is the vertical updraft velocity of the particle, *W* is liquid water mass mixing ratio, α and γ are size invariant coefficients (Abdul-Razzak et al., 1998; Pruppacher and Klett, 1998, Seinfeld and Pandis, 2006) defined by:

$$\alpha \equiv \frac{gM_wL}{c_pRT^2} - \frac{gM_a}{RT} \text{ and } \lambda \equiv \frac{pM_a}{e_sM_w} + \frac{M_wL^2}{c_pRT^2} \qquad [2.18]$$

Based on assumptions by Ghan et al. (2011), S_{max} is obtained when $\frac{dS}{dt} = 0$ and the rate of condensation can be expressed in terms of size distribution:

$$\frac{dW}{dt} = 4\pi\rho_w \int_0^S r^2 \frac{dr}{dt} n(S')dS' \qquad [2.19]$$

where ρ_w is water density, r is droplet radius and $n(S')dS'$ denotes the number concentration of particles activating between supersaturation boundaries S' and $(S'+dS')$. The droplet growth rate can be expressed (Abdul-Razzak et al., 1998) as:

$$\frac{dr}{dt} = \frac{G}{t}\left\{S - \frac{A}{r} + \frac{Br_a^3}{r^3}\right\} \qquad [2.20]$$

where the growth coefficient G is defined (Abdul-Razzak et al., 1998; Pruppacher and Klett, 1998; Seinfeld and Pandis, 2006) by:

$$G \equiv \left\{\frac{\rho_w RT}{e_s(\infty)D_v' M_w} + \frac{L\rho_w}{K_v' T}\left(\frac{LM_w}{RT} - 1\right)\right\}^{-1} \qquad [2.21]$$

In the above expression, e_s is the saturation vapour pressure of water, L is the latent heat of vaporization, D_v is the modified water vapor diffusivity, and K_v is the modified thermal conductivity of air (expressions given by Pruppacher and Klett (1998), Seinfeld and Pandis (2006) and Ghan et al. (2011)). Substituting terms into equation [2.20] and integrating from the particle activation time t_{act} to the time at maximum supersaturation t_{max} gives droplet radius as:

$$r^2(t_{\max}) = r^2(t_{act}) + 2G\int_{t_{act}}^{t_{\max}} S(t')dt' \qquad [2.22]$$

Equation [2.21] can be substituted into equation [2.19] to give the rate of condensation as:

$$\frac{dW}{dt} = 4\pi\rho_w G S_{\max}\int_0^{S_{\max}}\left\{r^2(t_{act}) + 2G\int_{t_{act}}^{t_{\max}} S(t')dt'\right\}^{\frac{1}{2}} n(S')dS' \qquad [2.23]$$

The expression given by equation [2.23] can be considered by splitting aerosol population into two parts: particles with S_c near S_{max} and particle with S_c much less than S_{max} (Ghan et al., 2011, and references therein). Substituting back into equation [2.19] (where $\frac{dS}{dt} = 0$), the general solution reduces to:

$$\frac{\alpha v}{\gamma^*} = GS_{\max}\int_0^{S_{part}}\left(2G\int_{t_{act}}^{t_{\max}} S(t')dt'\right)n(S')dS' + \int_{S_{part}}^{S_{\max}} r(t_{act})n(S')dS' \qquad [2.24]$$

where $\gamma^* = \frac{4\pi\rho_w\gamma}{\rho_a}$ and S_{part} is a partitioning supersaturation distinguishing particles that grow substantially between t_{act} and t_{max} and those that do not. Because the above expression cannot be solved analytically (Ghan et al., 2011), numerical simulations for a single lognormal distribution can be used (Abdul-Razzak et al., 1998; ARG, 2000) to find the ratio S_m/S_{max} to the function S_m (S_m = critical supersaturation for the mode of radius r) and dimensionless parameters from equation [2.12]:

$$\eta_m \equiv \frac{2(\alpha V/G)^{\frac{3}{2}}}{\gamma^* N_m} \quad \text{and} \quad \varsigma_m \equiv \frac{2A}{3}\left(\frac{\alpha V}{G}\right)^{\frac{1}{2}} \qquad [2.25]$$

The multiple log-normal case (ARG, 2000) has a solution of the form:

$$S_m^2 = \left\{ \sum_m \frac{1}{S_m^2} \left[f_m \left(\frac{\varsigma}{\eta_m} \right)^{\frac{3}{2}} + g_m \left(\frac{S_m^2}{\eta_m + 3\varsigma} \right)^{\frac{3}{4}} \right] \right\}^{-1} \quad [2.26]$$

where

$$f_m = 0.5 \exp(2.5 \ln^2 \sigma_m) \text{ and } g_m = 1 + 0.25 \ln \sigma_m \quad [2.27]$$

2.9 Summary

This chapter described the modelling tool and different modules employed in the study. It gives a description of the processes undertaken in preparing data for the simulation, including data acquisition as well as different mechanisms and programs used. Key components of the WRF-Chem model such as boundary conditions, (section 2.6) and emissions (section 2.7) that interact with the clouds through parameterisations (section 2.4) driven by the meteorology leading to aerosol–cloud feedbacks, are briefly described. To drive the model, initial chemical and meteorological conditions are prepared. Although anthropogenic and fire emissions were prepared with Prep-chem_source, biogenic, dust and sea salt were calculated directly online and linked to the WRF-Chem directory. However, the user has the flexibility to use one or some of the emissions in the simulation, depending on the type of simulation to be performed by switching ON/OFF the appropriate control options in the *namelist.input* file.

Chapter 3

Methodology: An illustrative application of the modelling tool

3.1 Introduction

This chapter describes an approach employed for the case-study analysis of the model simulation that combines meteorological and chemical-process dynamics to simulate effects of aerosol–cloud interactions. The study focuses on a biomass burning (BB) case study conducted with the WRF-Chem model. The approach illustrates the technique used to evaluate impacts of aerosols from the WRF-Chem predictions that will be employed in the subsequent chapters of this thesis. The nomenclature illustrated in Fig. 3.1 is employed to simplify the process analysis, with six key areas highlighted through which the diagnosis will be conducted. An evaluation of the performance will be done (in subsequent chapters) to assess the adequacy and suitability of WRF-Chem for use in a regional coupled modelling system over southern Africa. Output plots from the model and observation data are generated and discussed to demonstrate the model performance and its sensitivity. Comparisons are made using time series plots (e.g. domain-average plots and box-and-whiskers) for quantitative analysis. I also use the plots generated for qualitative evaluation of the model's capability and suitability in simulating the chemistry and meteorology. Plotted fields generated from the model output are inspected visually against reanalysis data, whereas statistical summaries for the simulated variables are calculated and inspected through the plots.

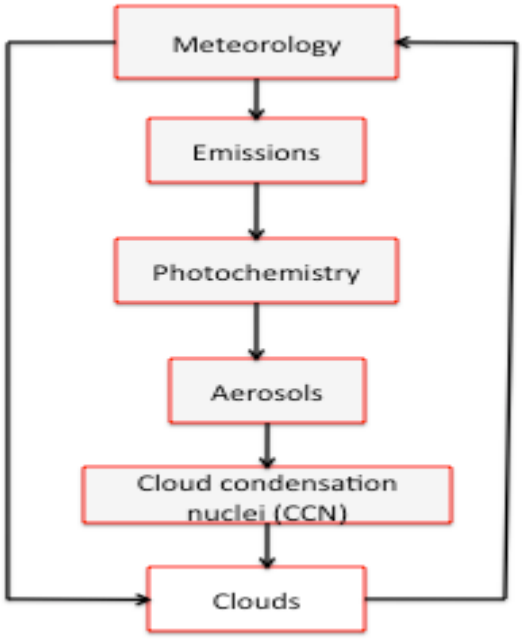

Fig. 3.1: Illustration of the various components of the simulation. Arrows indicate dependencies between the processes.

3.2 Model setup

The simulation is performed on 20-km horizontal grid spacing over a large domain covering southern Africa. This is performed on a single coarse grid (Fig. 3.2) to test the model performance. The setup is built over a domain with 321 × 251 points centered at 20°S and 30°E, configured with 41 vertical sigma levels, spaced to give a better resolution in the atmospheric boundary layer. The coarse grid was set to cover reasonable geographical space enough to accommodate the flow of emissions within the domain and to simulate the long-range transport of smoke from the fires over land into the oceans. Topography, land use and land water data are interpolated from the United States Geological Survey (USGS) at 1-km grid spacing to the appropriate spatial grid spacing of the domain. A quad grid simulation will be conducted in the next chapter, including the small nests numbered d02, d03 and d04.

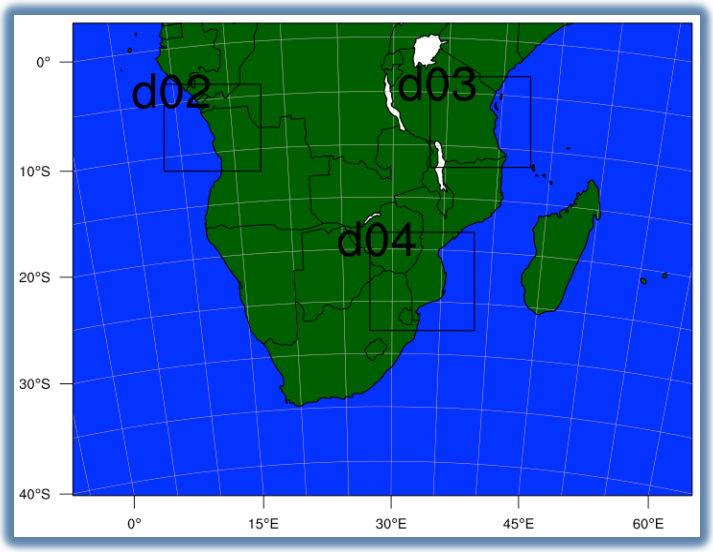

Fig. 3.2: Model simulation domain and locations of sub-domains (numbered). Domains d02, d03 and d04 at 4-km grid horizontal spacing each, whereas the parent domain is at 20-km grid spacing.

The model was initialized at 0000 UTC 23 August 2008 with meteorological boundary conditions every 6-hr from the European Centre for Medium-Range Weather Forecasting (ECMWF) ERA–Interim, and with constant background concentrations of aerosol and precursor gases for idealized simulations from the Model for Ozone and Related chemical Tracers (MOZART) module (Emmons et al., 2010). Emissions were input daily into the model domain through 0000 UTC 10 September 2008, derived from three sources including (i) ambient aerosol and gas anthropogenic emissions from Emissions Database for Global Atmospheric Research (EDGAR) v4.2, (ii) fire products from the Brazilian Biomass Burning Emission Model (3BEM) (Longo et al., 2010) identified with Moderate Imaging Spectroradiometer (MODIS) and (iii) biogenic emissions from the Model of Emissions of Gases and Aerosols from Nature (MEGAN). EDGAR emissions are available at 0.1° × 0.1° grid spacing per year in kg (N) m^{-2} s^{-1} during 2000–2005, with primary black carbon (BC) and organic

carbon (OC) from the Goddard Chemistry Aerosol Radiation and Transport (GOCART) model (Freitas et al., 2011) at 1° × 1° grid spacing. Emissions for burning of residues in fields, dung used in biofuels, wood and charcoal burning are included using the Yevich and Logan (2003) inventory at 1° × 1° grid spacing. Gas-phase emissions are specified in units of mol km^{-2}, whereas aerosol emissions are given in μg m^{-2} s^{-1}. Fire emissions from MODIS are identified for daily averages of burnt areas and fire pixels at 1-km grid spacing. Biogenic emissions (0.5° × 0.5° grid spacing) are calculated online using the MEGAN v2 module (Guenther et al., 2006; 2012) that uses WRF-predicted temperature and downward radiation for its calculations. Similarly, dust and sea-salt emissions are also calculated using an online parameterisation in the model.

WRF-Chem is run for a two-week period described above with simulations restarted every three days with new initial conditions to limit the size of synoptic-scale errors. The period is selected because of the amount of observational data available and also that it occurred during the peak of the dry season. The simulation was conducted by re-initializing the meteorological boundary conditions at the end of every three-day simulation interval, while carrying the chemistry from the previous run, but without using the subsequent forecast as the first-guess fields for the next cycle. To prevent the model from diverting further away from the initial conditions, reinitializing helps to ensure the simulation remains relatively faithful to the meteorological analyses used in each initialisation, while continuing with the chemistry from the previous simulation. The first three days of the simulation are discarded as the model spin-up period. Detailed description of model parameterisations, chemical and meteorological boundary conditions is given in Chapter 2, whilst model setting and configuration options are given in the appendix section (Appendix A) at the end.

3.3 Meteorology

Meteorological models provide four-dimensional predicted data, which is not available from observations. The models are not perfect and therefore require validation. In a complex chemistry transport model such as WRF-Chem that handles many processes simultaneously, it is important to ensure that results and data used for the initialization and boundary conditions are checked and verified against observations where available (e.g. reanalysis, satellite imagery or measurement) to ensure that the model is a reasonable representation of the real atmosphere. The observational data are gridded and incorporate observation and numerical weather prediction model output.

BB is one of the potentially episodic cases of potentially large concentration of air pollution. It is a source of atmospheric aerosols that play a crucial role in the radiative budget, cloud formation, precipitation and climate variability. These events usually result in a large pollution scenario with significant chemical interaction with the meteorology. For example, the period between late August to

early September 2008 had the sub-continent ablaze with fires where huge tracks of land were destroyed by 'out-of-control fires' as reported by the BBC news (http://news.bbc.co.uk/1/hi/world/africa/7591950.stm). The news bulletin also reported that at least 20 people were killed in South Africa as of 2 September 2008; the number doubled the following day. By 5 September 2008, 32 people were also reported killed in Mozambique, and thousands others left homeless –with more than 16 000 hectares of agricultural land destroyed (http://news.bbc.co.uk/1/hi/world/africa/7601114.stm). In Botswana, the fires were reported within the Central Kalahari Game Reserve (CKGR), beginning late August until late September of the same year (earthobservatory.nasa.gov/IOTD/view.php?id=35403), scorching nearly 80% of the park. By late September, nearly 40 000 km^2 of the CKGR had been burnt by the fires. Officials in the Ministry of Environment described the fires as 'the worst fires in years' (www.theguardian.com/world/2008/sep/21/3). Before analyzing the chemical fields, we first need to ensure that the meteorology is well represented in the model.

To allow for a comparison with widely available data, three fields were chosen for verification: sea-level pressure (SLP), 925-mb wind and cloud cover. A visual comparison of these three fields was performed for each 66-hr simulation. The variables were chosen because (i) SLP represents the integrated mass distribution of the atmosphere and so provides an initial look at how well the model is simulating the real atmosphere. However, even if SLP is verified, it does not necessarily mean the rest of the model adequately represents the real atmosphere. Therefore, other fields such as winds and clouds also need verification. (ii) Winds are particularly important in chemical modelling because of their direct influence on transport, atmospheric stability and mixing of pollution. This is important for my simulations because, by knowing the wind fields over the simulation areas, I will be able to describe transport patterns and possible influence of pollution in areas downwind. For example, wind speed determines how quickly pollutants mix with the surrounding air and how fast they move away from their sources. (iii) To better understand aerosol–cloud effects, whether there are clouds over the domain and where they are located needs to be known. Satellites provide estimates of area coverage of clouds by the cloud-top temperature and the column-integrated optical thickness.

3.3.1 Verification of meteorology

Modelled fields are compared against reanalysis from the National Centre for Environmental Prediction (NCEP) (http://www.esrl.noaa.gov/psd/data/composites/hour/) and satellite images from NERC Earth Observation Data Acquisition and Analysis Service (NEODAAS) (http://www.sat.dundee.ac.uk) and National Oceanic and Atmospheric Administration (NOAA) (http://www.ncdc.noaa.gov/) datasets. Figures 3.3–3.4 below show model outputs and observation

plots for the three variables at 1800 UTC 29 August 2008. Results indicate that broad trends of the fields are well represented in the model. SLP is adequately represented in the model (Fig. 3.3), even though the observations have few contours over land. The contours are of the same magnitude between model and observation. The model predicts a low below Port Elizabeth on the south coast, but is still able to capture the low-pressure systems in the southern part of the domain. The wind field (Fig. 3.4) is also well represented, although the model misses predictions over Democratic Republic of Congo (DRC), Uganda, Zambia, eastern Zimbabwe and some parts of South Africa. High wind speed (>20 m/s) is predicted near the south coast at the same location where a low is predicted in Fig. 3.3.

The purpose is to check the presence and spatial coverage of clouds over the domain predicted by the model, and how it compares with satellite. Figure 3.5 shows modelled cloud- and ice-water content compared with satellite imagery. Model output is the sum of column-integrated cloud-water and ice-water content over each grid cell. Some cloud water is predicted over Angola, DRC and Tanzania (between 0.6 and 2 g m^{-2}) while more ice water is predicted over the landmass, largely in the upper half of the domain. Also, there are more clouds around the low in Fig. 3.3, suggesting high winds as predicted in Fig. 3.4. Note the high cloud water content offshore near Angola. The same strategy will be repeated for the whole period to ensure the accuracy of forecasts. The resulting differences between observation and model prediction might be due to the model coarse resolution. Given this limitation in the model for example, fine details cannot be fully represented or resolved within the model grid cells. To summarize, the majority of the simulations produced reasonably realistic features of relevance to this research. The 20-km grid spacing simulated variables indicate the model's capability to capture the active weather systems. These simulations will make reasonable surrogates for understanding the effects of BB emissions on the clouds and precipitation in south-central Africa.

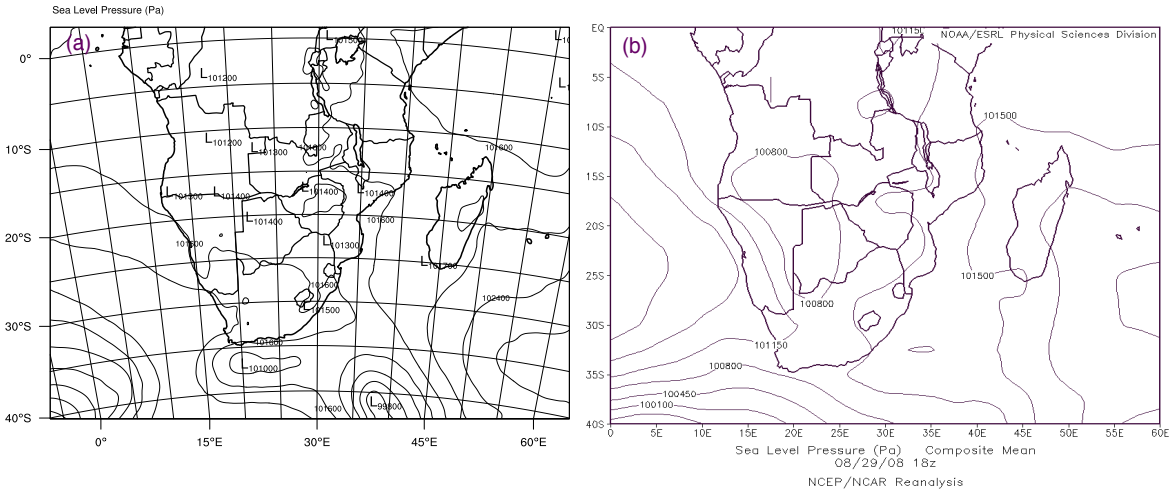

Fig. 3.3: (a) WRF-Chem modelled sea level pressure and (b) NCEP/NCAR reanalysis observation at 1800 UTC 29 August 2008. Contours indicate pressure. Although Fig. 3.3(b) has fewer labeled contours than Fig. 3.3(a), it is the only figure available from the web.

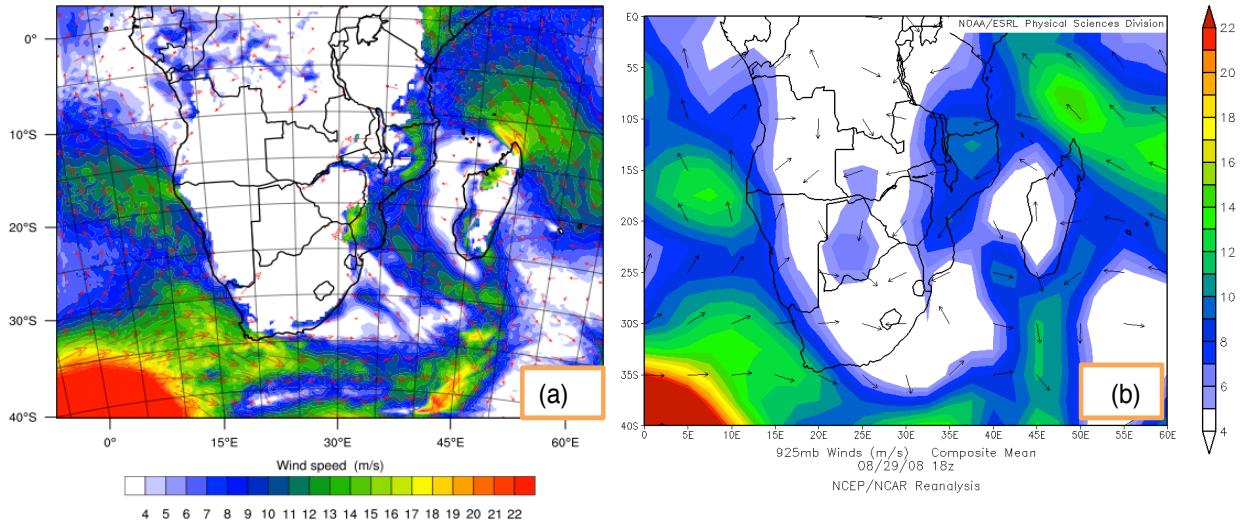

Fig. 3.4: (a) WRF-Chem modelled 925-mb wind and (b) NCEP/NCAR reanalysis observation (units: m/s) at 1800 UTC 29 August 2008. Arrows indicate wind direction in both figures and scales are colour-coded in terms of wind speed.

Acknowledgements
Satellite imagery (Figs. 3.3(b) and 3.4(b)) were provided by the NOAA/ESRL Physical Sciences Division. Boulder Co. website: htpp://esrl.noaa.gov/psd/.

Figure 3.6 shows temporal variations for cloud- and ice water quantities described above. I shall also compare and discuss in the subsequent chapters, predictions for some quantities against measurements (e.g. satellites and/or field studies) over southern Africa where available. The objective being to demonstrate if the model is fit for purpose and the relevance of results to the real world. The time series shown below is for the entire simulation period described above. Brown curves represent cloud water whereas blue curves represent ice water.

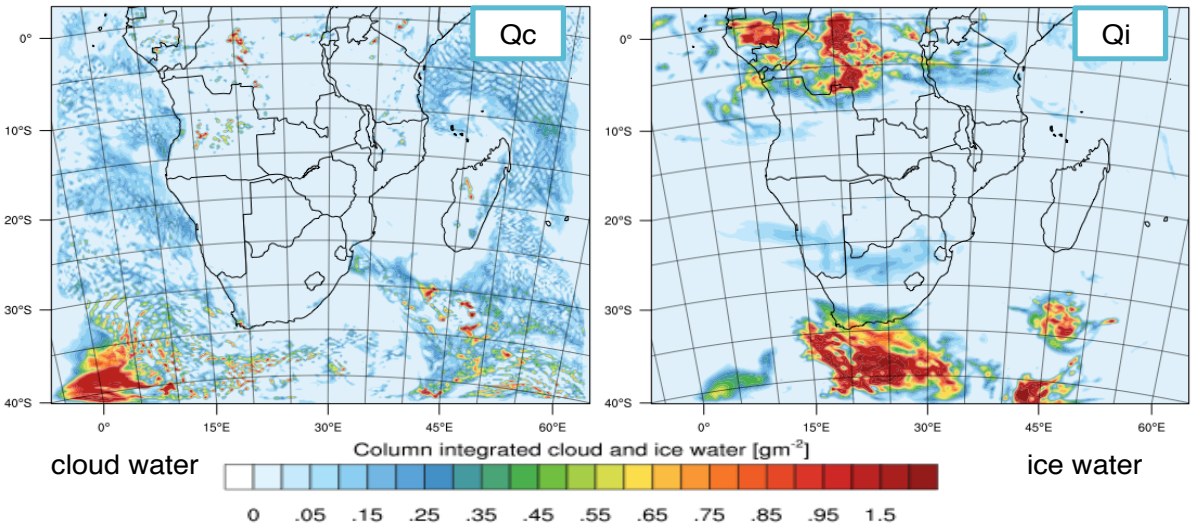

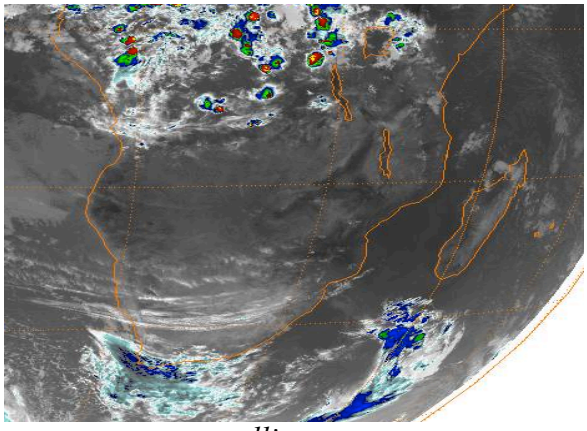

satellite

Fig. 3.5: Top: Column integrated cloud (Qc) and ice (Qi) water content and, below: Meteosat 9 satellite (NOAA Environmental Satellite and Information Service) image at 1800 UTC 29 August 2008.

The model predicts more cloud liquid water than cloud ice water (both quantities increase in the afternoons) and the average cloud water is more than that for the cloud ice water. Cloud water has two maxima (morning and afternoon) and the midday minima. On the other hand, ice water increased from morning towards the afternoons, although a decrease occurs in some days. Maximum average cloud water is 0.75 g m^{-2} whereas for the ice water it is 0.15 g m^{-2}. Whilst Fig 3.5 is an output at a single time, Fig. 3.6 shows daily averages for the entire simulation. In the comparison to be discussed later (chapters 5 and 6), I will also discuss impacts and contribution of BB emissions and their interactions with clouds in different geographical locations. This will also compare prediction of liquid water path (LWP) with measurement.

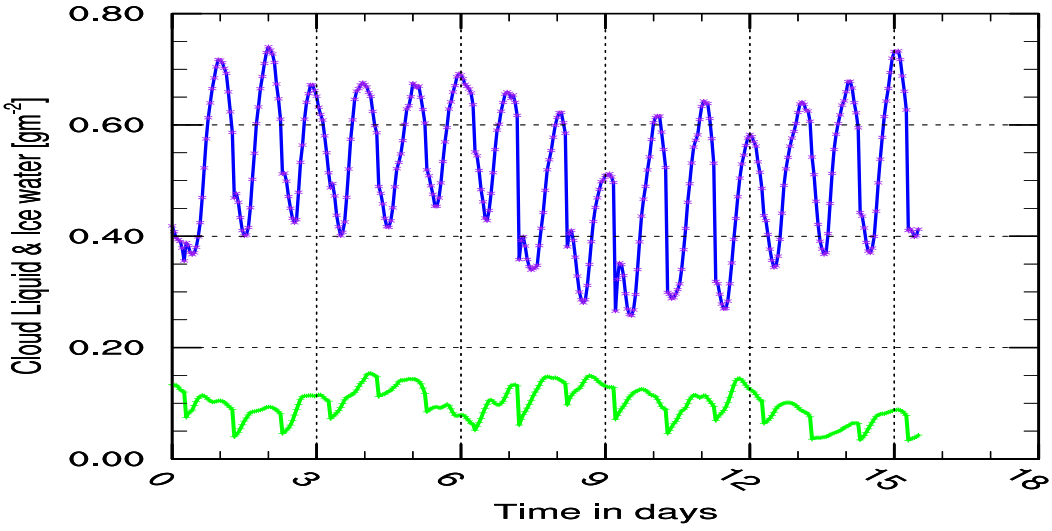

Fig. 3.6: Temporal variations of simulated cloud liquid and ice water content. Blue- and green curves represent cloud liquid and ice water respectively. Model output beginning 0000 UTC 26 August to 1200 UTC 10 September 2008.

3.4 Emissions

Air quality and atmospheric chemistry in southern Africa are frequently affected by open BB (a significant source of trace gas and aerosol emissions) around tropical central and savanna regions during winter. The burning activities have long been used for hundreds of years mainly as agricultural and land management tool; majority of which are thought to be anthropogenic set for various purposes such as forest clearing, bush and litter accumulation to preserve pastureland, game hunting, pest/weeds control and various religious reasons. Numerous fires give rise to regional smoke patches in the dry season, while the wet season is usually preceded by widespread of fires across the continent. Vegetation is also composed of various categories (e.g. deciduous, shrubland, grass, savanaas) from which volatile organic compound (VOC) emissions occur. These emissions exhibit large quantities of gas and aerosol pollutants. Although BB is the predominant source of chemical pollutants, emissions also come from other sources including anthropogenic (e.g. urban, industrial and automobiles), natural (e.g. desert dust, sea salt and biogenic).

Figures 3.7 and 3.8 show emissions from anthropogenic (in units of $\mu g\ m^{-2}\ s^{-1}$) and BB (in units of $mol\ km^{-2}\ hr^{-1}$) sources of some primary species (e.g. BC, OC, CO, NO), prepared with PREP-CHEM-SRC. The figures show the spatial distribution of different emissions over southern Africa and their associated sources (e.g. industrial, power generation, ship operation). As shown, some species are more spread whilst others are least spread from the sources. Anthropogenic emissions are the sum of all sectors (energy, industrial processes, agriculture, land use change and forestry burning, waste, road transport, residential, and other anthropogenic sources) from EDGAR, whereas biomass products are from the 3BEM –captured with MODIS satellite fire counter. Emissions were prepared with PREP-CHEM-SRC after modification of the original source code to map anthropogenic species (Archer-Nichols et al., 2014) onto the Carbon Bond Mechanism (CBM-Z) gas phase (Zaveri and Peters, 1999).

Anthropogenic emissions tend to have more spatial coverage than biomass emissions due to the spread of settlements, towns/cities and industries –including automobiles over land and marine transport. These are generally treated as surface fluxes in the model (Grell at al., 2011a). On the other hand, biomass emissions occur only in some areas (e.g. forests and savanna). The fire emissions are injected into the upper-most levels and transported upward due to positive buoyancy generated by the fire. They can loop through the entire columns to distribute emissions higher upwards. For example, spatial variation of emissions in Fig. 3.7 cover the entire landmass, whereas those in Fig. 3.8 are concentrated around the burning areas.

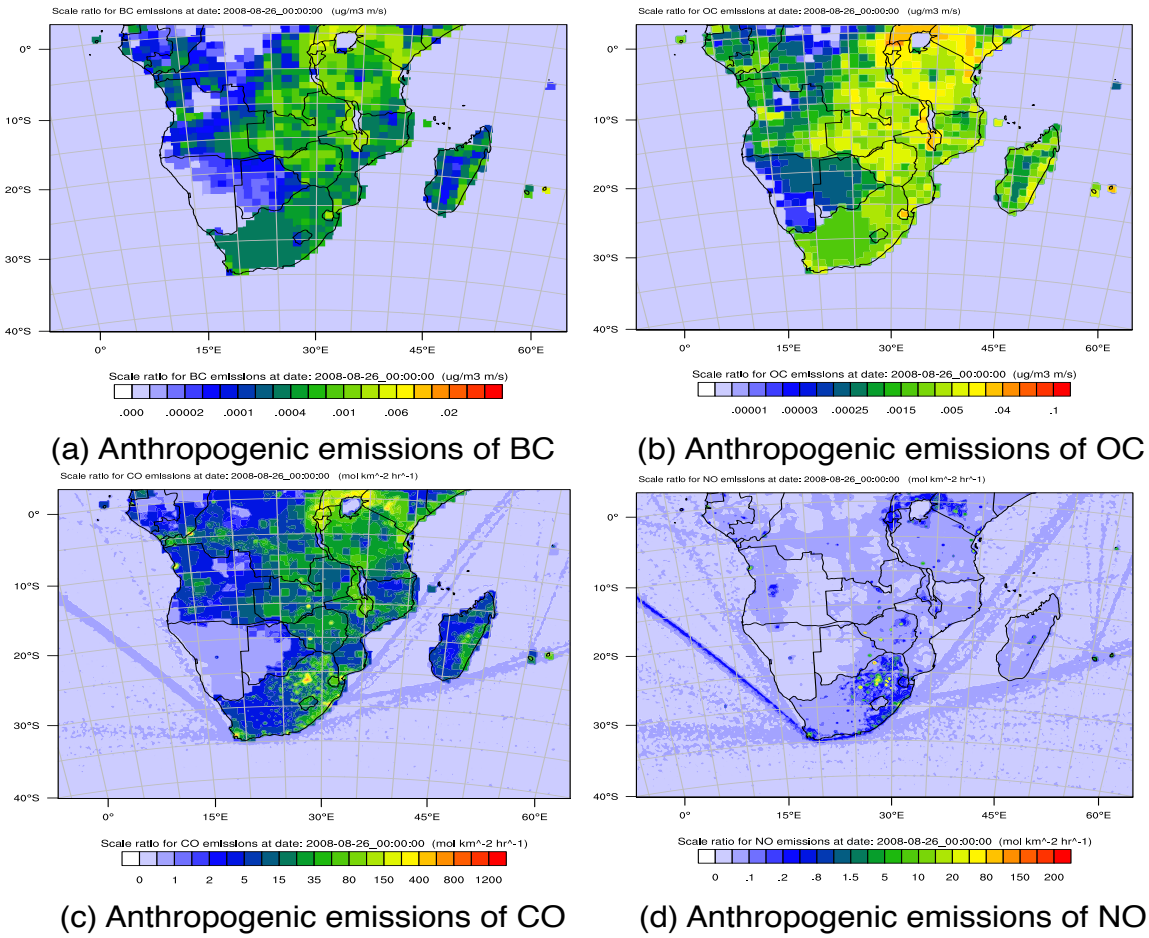

Fig. 3.7: Anthropogenic emissions over the domain, valid at 0000 UTC 26 August 2008. Emissions spread over the domain due to settlements, industries and transport.

3.5 Photochemistry

Photochemistry is the main process in the troposphere involving various chemical reactions in the atmosphere (oxidation reactions, photolysis and transformation of various chemical pollutants). Oxidants control daytime and night-time chemical processes. Figure 3.9 shows the daytime concentrations of photochemical and night-time species (OH, O_3, NO_3 and N_2O_5). These are plotted to illustrate the change in photochemical species' concentration in the atmosphere during the course of the day. Although some species (e.g. O_3) are daytime species, their concentration still persist at night because of longer lifetimes. Species such as OH are very reactive and have shorter lifetimes (~1s), and so the concentration declines at night because they are used up during the day. On the other hand, species such as NO_3 have their maximum concentration at midnight and are very active in nocturnal chemistry.

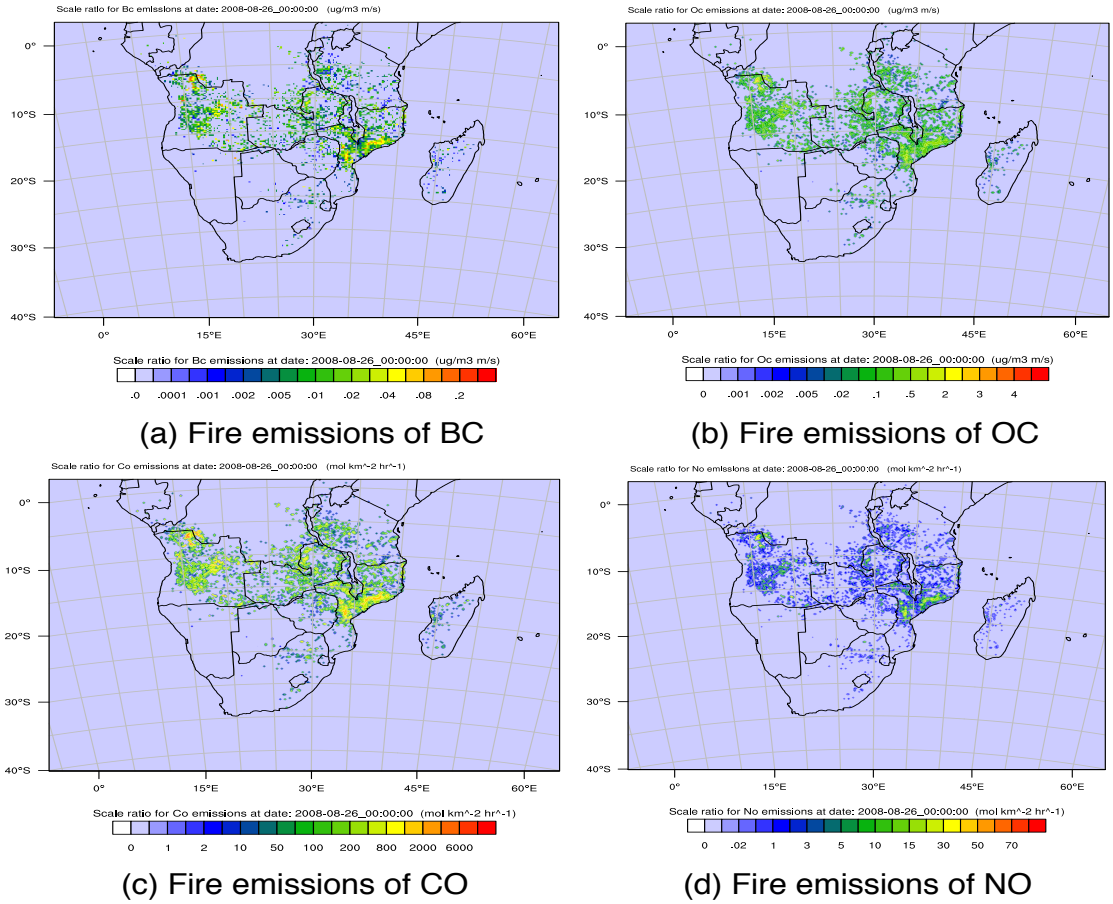

Fig. 3.8: Biomass burning emissions over the domain, valid at 0000 UTC 26 August 2008. Emissions primarily concentrated around burning areas only.

The surface plots in Fig. 3.9 also show locations over the domain where concentration increases, especially tropical central Africa (dominated by BB), including the ship routes along the coast from anthropogenic. Figure 3.10 shows vertical profile concentrations of the same species, plotted from the maps of Fig. 3.9. These are cross-sections plotted along the west-east direction. The figures are plotted at mid-afternoon so as to coincide with the peak of ignition times over land. Again these show how species' concentrations vary with respect to height. For example, high O_3 concentration is predicted above 16 km showing the clear stratospheric dominance over tropospheric ozone with its photolysis leading to enhanced OH at the same altitude, whereas high NO_3 and N_2O_5 concentrations are predicted within 8 km with the dominance of surface sources of NO_x. Figures 3.11 and 3.12 show the statistical variations as a function of time and height from 0000 UTC 26 August to 1800 UTC 31 August 2008.

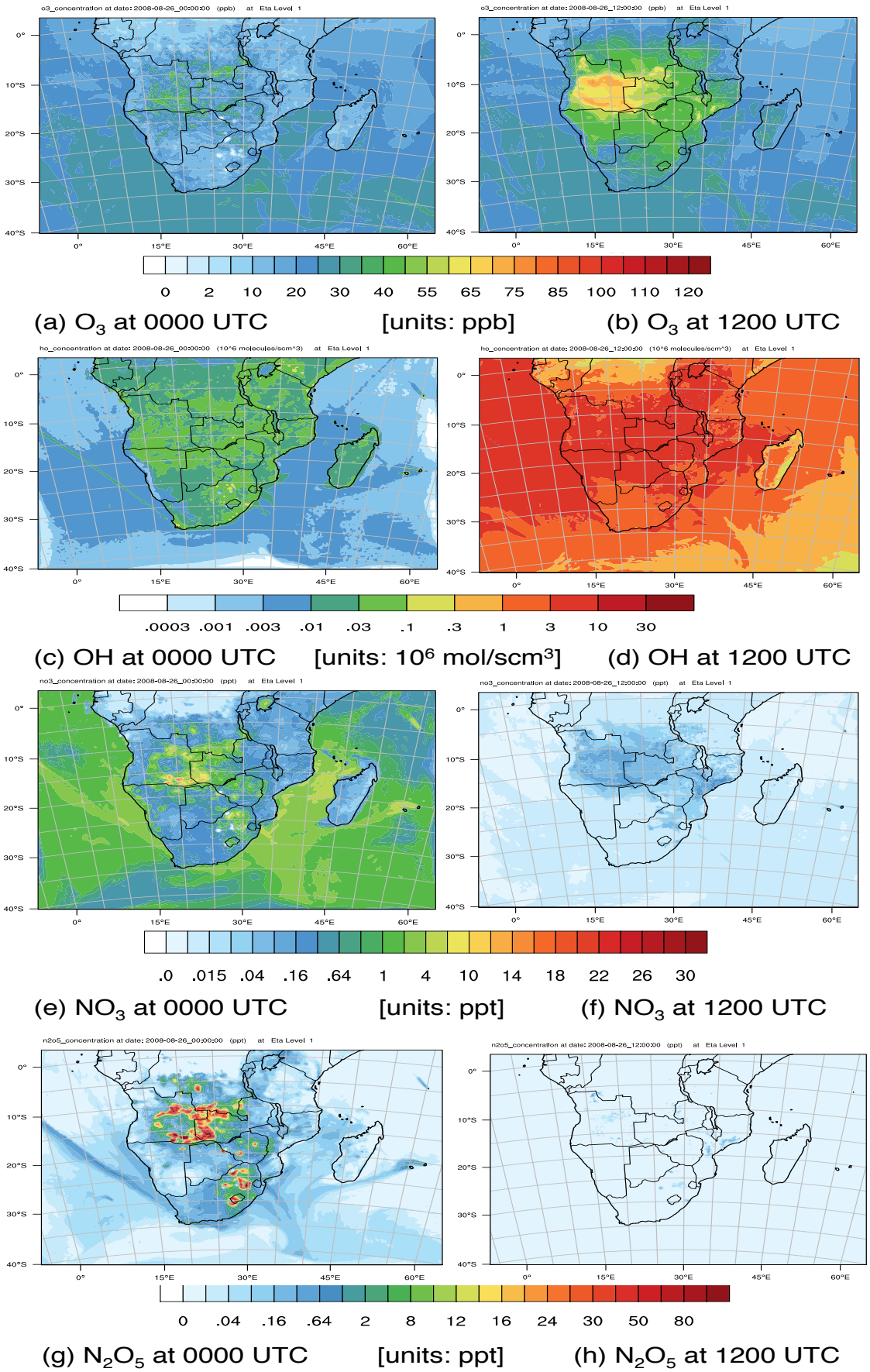

Fig. 3.9: Predicted concentrations of photochemical species. Model output night time ((a), (c), (e) and (g)) and daytime ((b), (d), (f) and (h)) concentrations on 26 August 2008.

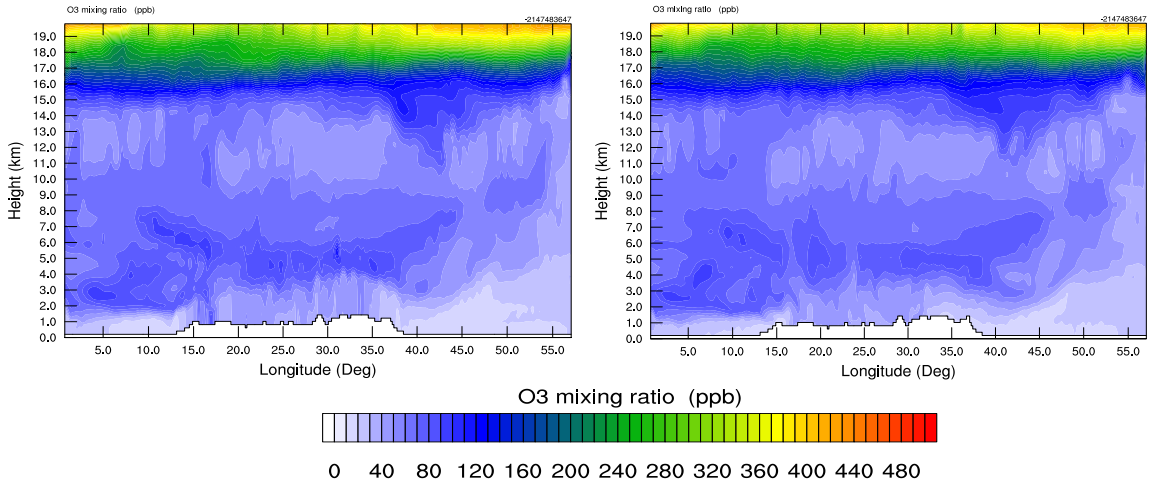

(a) O_3 at 1500 UTC (b) O_3 at 0000 UTC

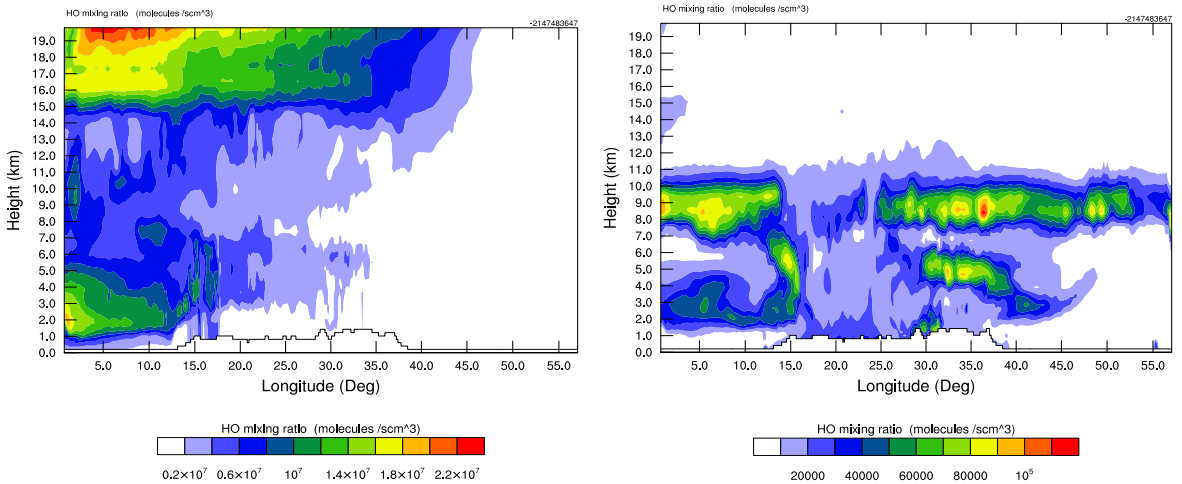

(c) OH at 1500 UTC (d) OH at 0000 UTC

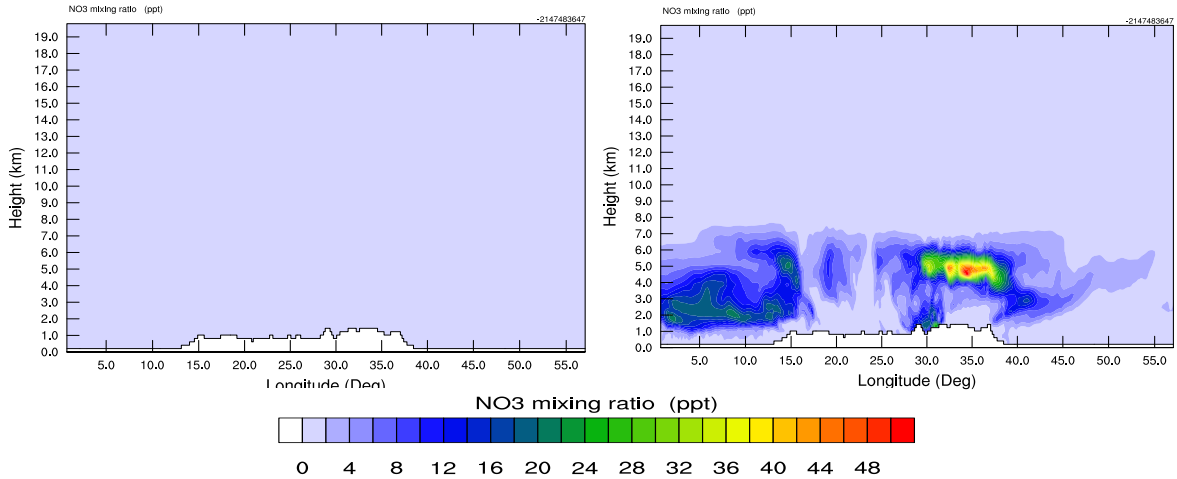

(e) NO_3 at 1500 UTC (f) NO_3 at 0000 UTC

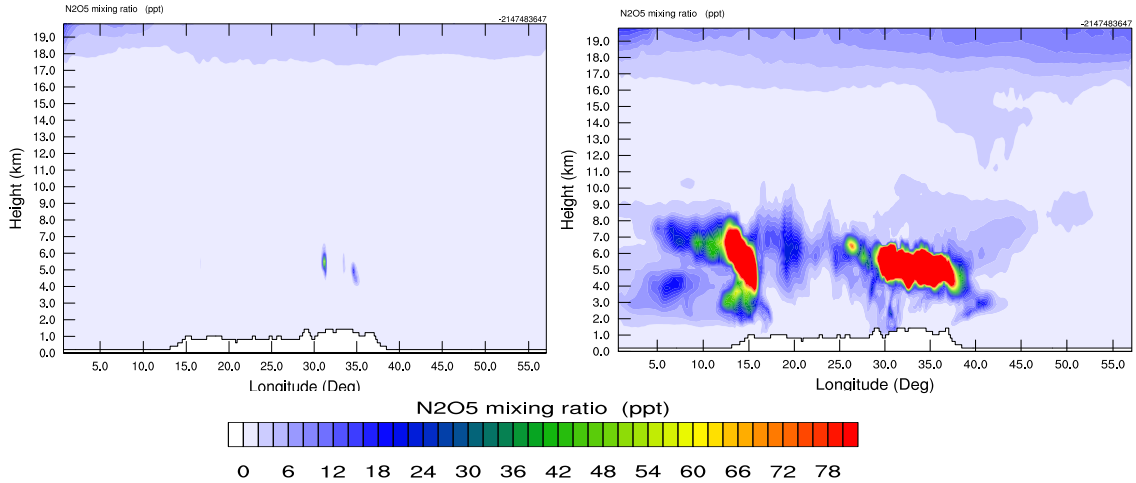

(g) N_2O_5 at 1500 UTC (h) N_2O_5 at 0000 UTC

Fig. 3.10: Vertical profile distribution in east-west cross section, fixed at 8° S latitude. ((a), (c), (e), (g)) daytime at 1500 UTC, 26 August 2008 and ((b), (d), (f), (h)) night-time at 0000 UTC, 27 August 2008.

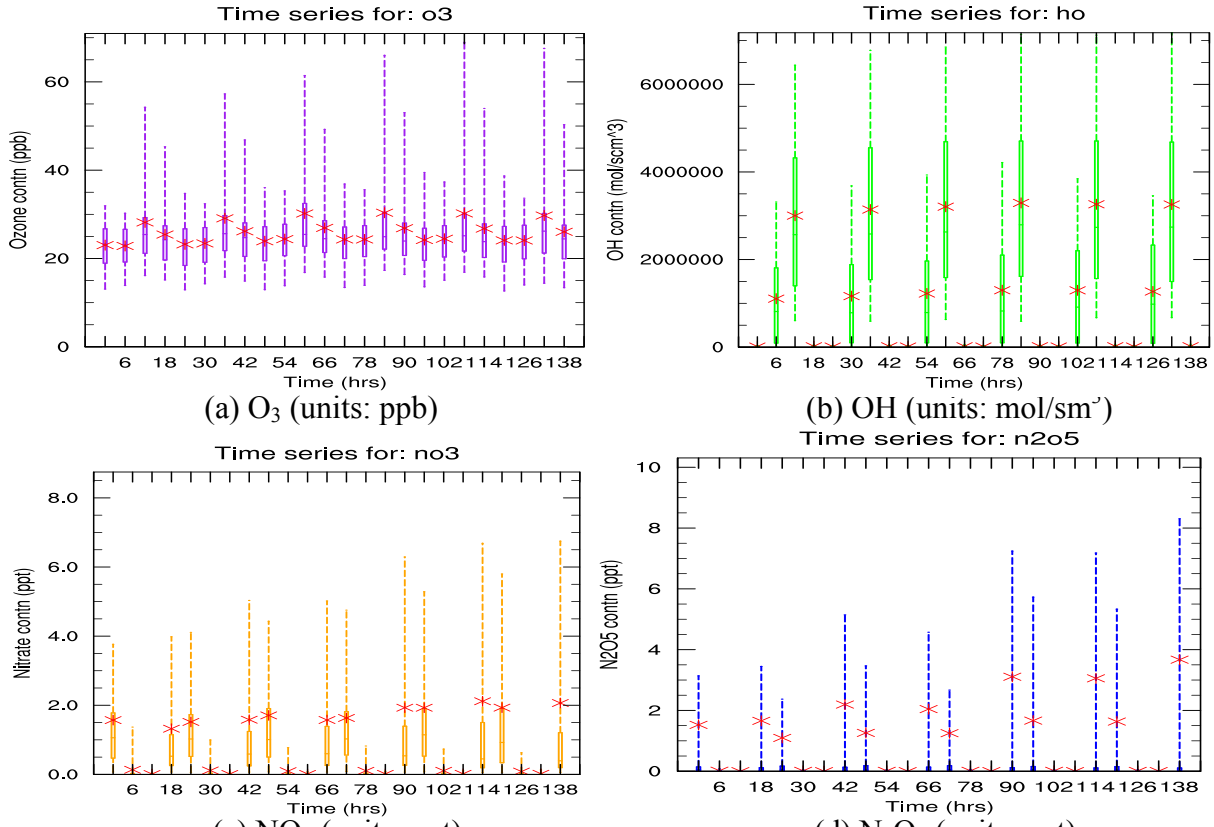

(a) O_3 (units: ppb) (b) OH (units: mol/sm^3)

(c) NO_3 (units: ppt) (d) N_2O_5 (units: ppt)

Fig. 3.11: Simulated time series, starting 0000 UTC 26 August to 1800 UTC 31 August 2008. The box-and-whisker plots help to show where the distribution is centered. Asterisks indicate the mean concentration. The plots show the interquartile range of the calculated statistics, with the median response (shown by the horizontal lines dividing the box), the 25th to 75th percentiles (shown by the box) and 5th and 95th percentiles (shown by the whiskers).

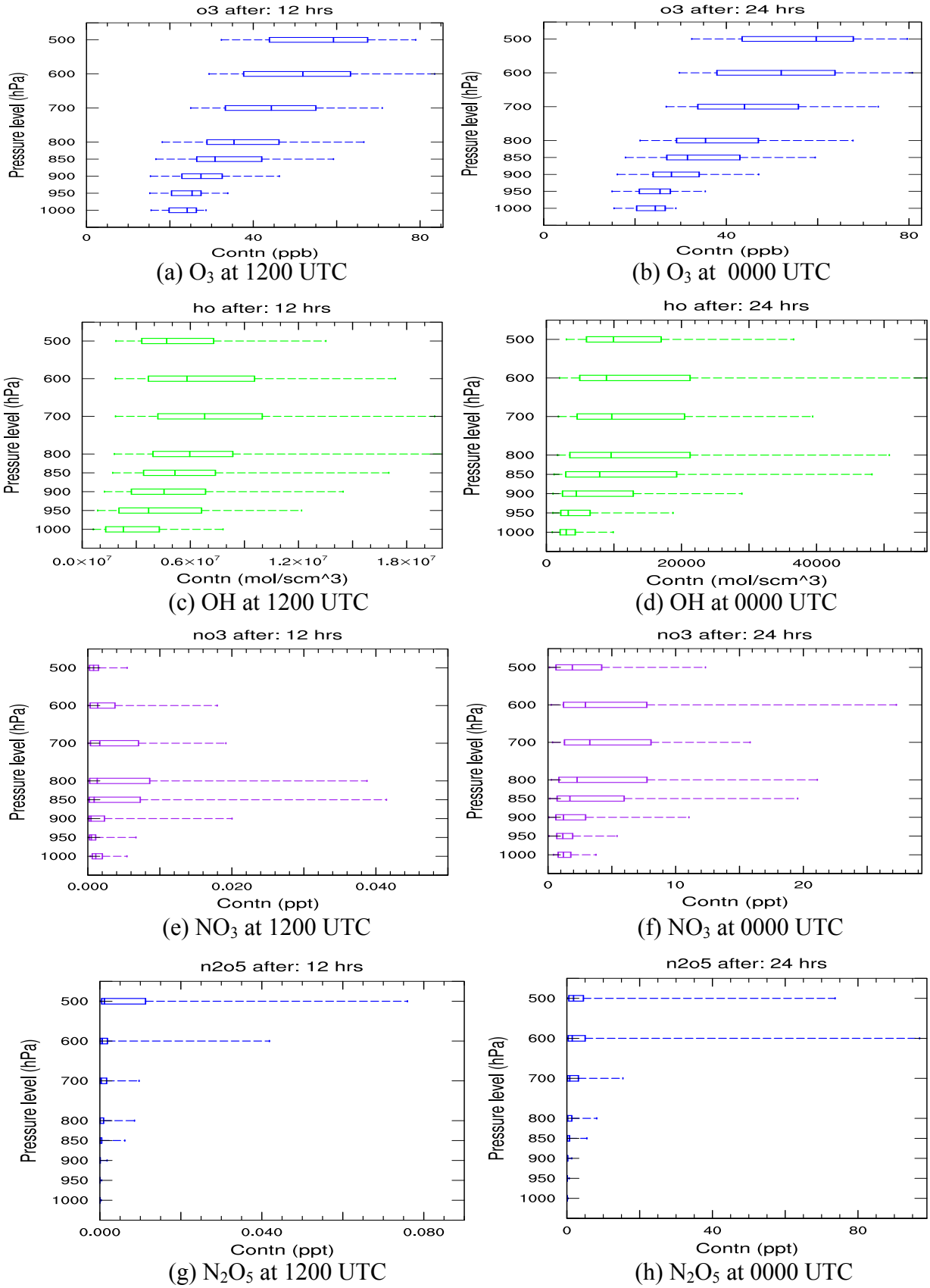

Fig. 3.12: Simulated vertical profiles for species concentration. Panels (a, c, e, g) at 1200 UTC on 26 August 2008; panels (b, d, f, h) at 0000 UTC, 27 August 2008. Box-and-whiskers show the interquartile range of the calculated statistics; with the median (vertical lines dividing the box), the 25th to 75th percentiles (shown by the box) and 5th and 95th percentiles (shown by the whiskers).

The above figures show photochemical species concentrations in the horizontal (Fig. 3.11) and vertical (Fig. 3.12) planes as a function of time. For example, O_3 and OH concentrations peak mostly during daytime than night-time, although the O_3 concentration is nearly constant compared to that of OH. OH peaks much higher at daytime and decrease during night-time, becoming almost zero. O_3 still persists at night for longer period than OH because of its longer lifetime than OH. On the other hand, NO_3 peaks late afternoon reaching its maxima at midnight, and minima during daytime. N_2O_5 behaves similarly to NO_3. For example, one can see (e.g. Fig. 3.12) that NO_3 and N_2O_5 concentrations are almost zero at daytime. These are night-time species, whereas the previous two are daytime species.

3.6 Aerosols

Aerosols directly emitted from the sources (primary) and those produced through chemical reactions (secondary) can be represented in the model. In a similar way to the representation of gaseous primary and secondary components, spatial distributions and statistical variations of particles at a given time or location can be presented. As shown for photochemical species (Fig. 3.9), model predictions for the surface concentrations of some primary and secondary aerosols are shown in Fig. 3.13 (however, noting that MOSAIC representation assume internal mixing of components), whereas vertical distributions are shown in Fig. 3.14. The figures show aerosol surface concentrations over the domain as function of height as shown in figures 3.9 and 3.10 above.

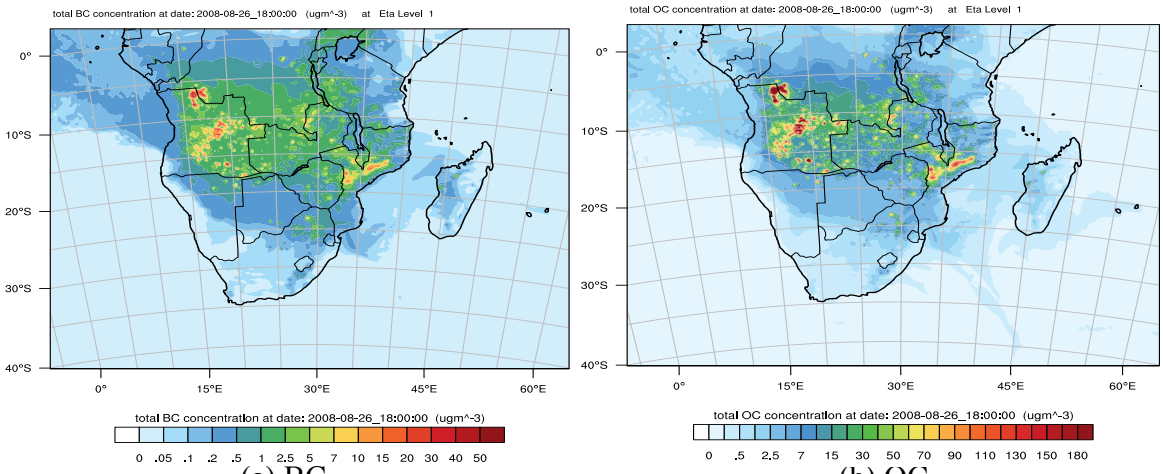

(a) BC (b) OC

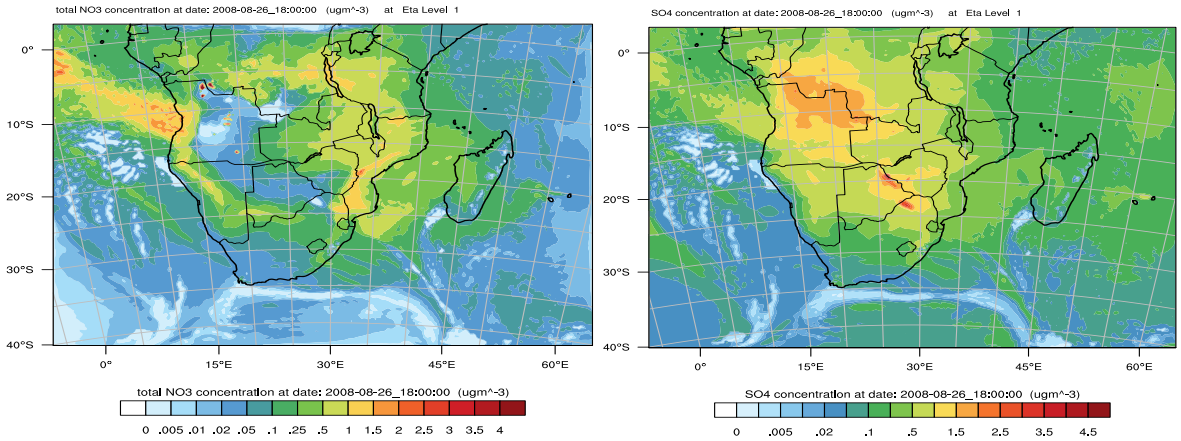

(c) NO_3^- (d) SO_4^{2-}

Fig. 3.13: Predicted surface aerosol concentrations. Model output at 1800 UTC 26 August 2008.

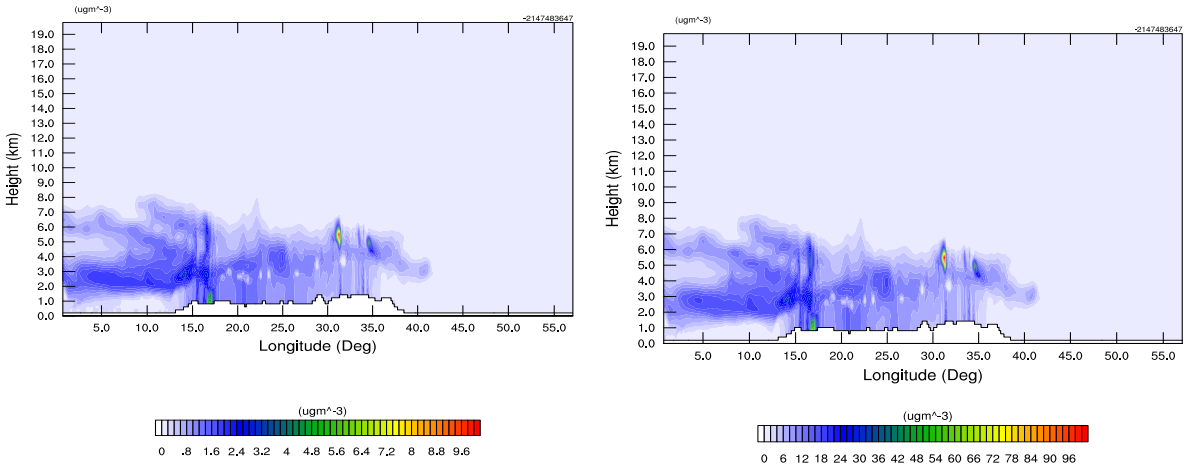

(a) BC (b) OC

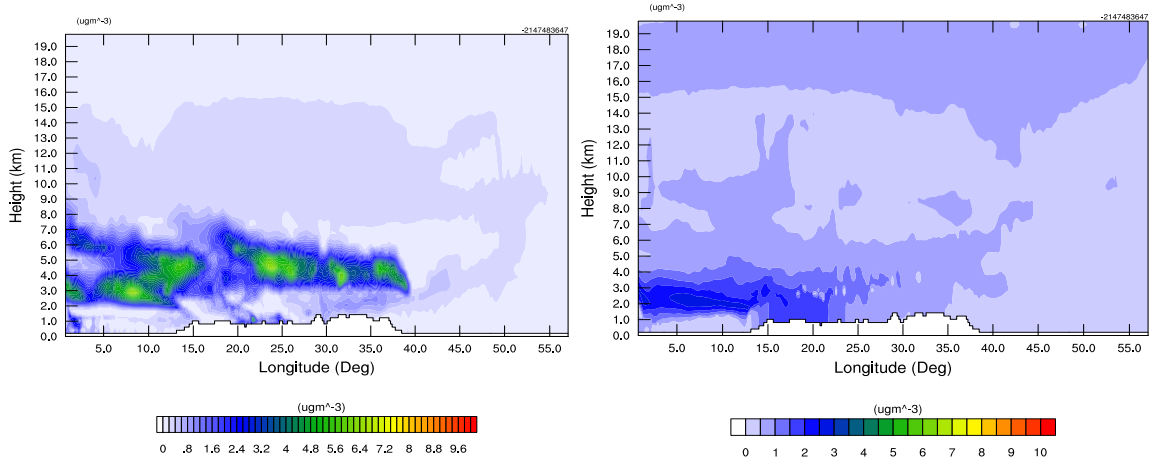

(c) NO_3^- (d) SO_4^{2-}

Fig. 3.14: Vertical distribution in east-west cross section at fixed 8° S latitude. Model output at 1500 UTC 26 August 2008.

To examine pollutant distribution across the entire domain, the temporal variation is shown in Fig. 3.15. Quantitative and qualitative modelled results can be compared with measurements where available and/or other model studies to assess the magnitude and spatial extent of the fields. Vertical profiles of aerosols are shown in Fig. 3.16.

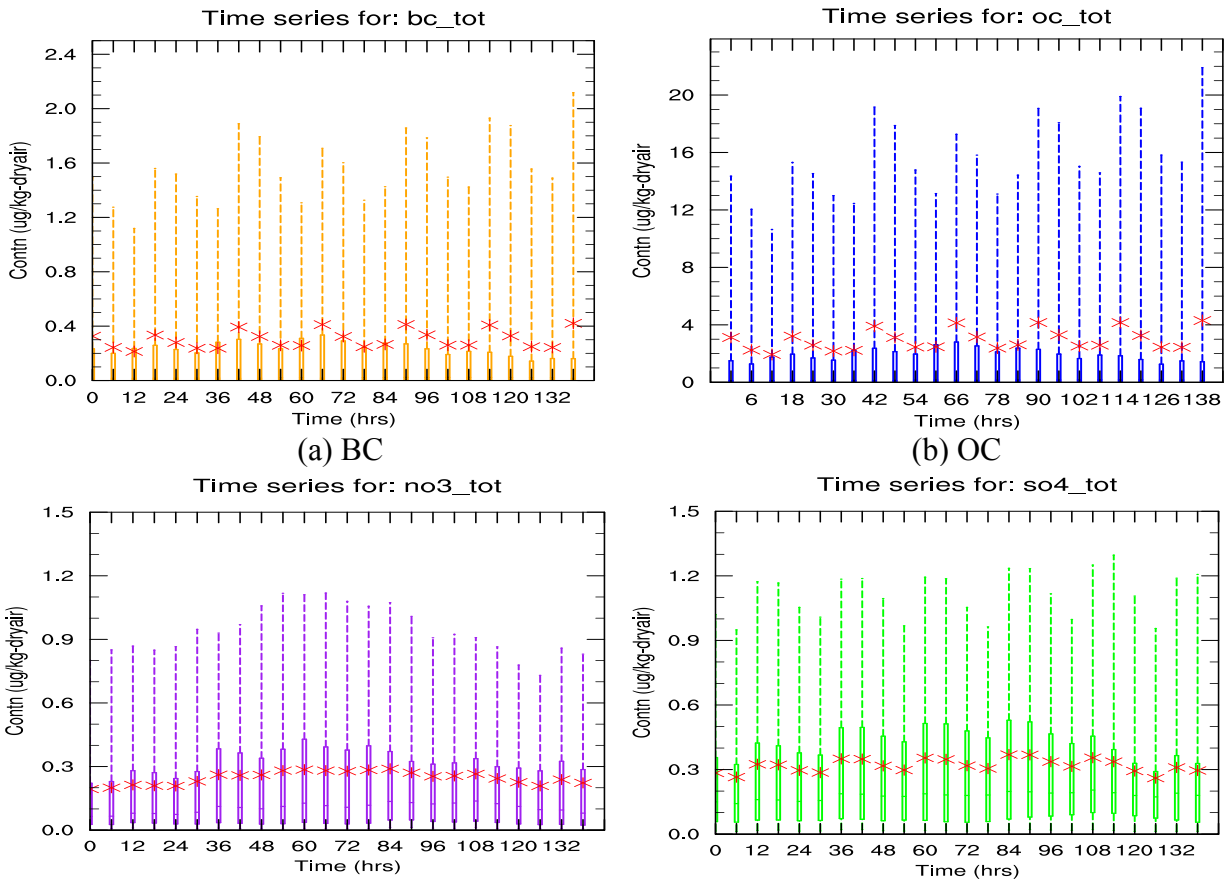

(a) BC (b) OC

(c) NO_3^- (d) SO_4^{2-}

Fig. 3.15: Temporal variations of simulated aerosols. Model output beginning 0000 UTC 26 August to 1800 UTC 31 August 2008. The box-and-whisker plots show the interquartile range of the calculated statistics; the median response (horizontal lines dividing the box), the 25th to 75th percentiles (length of the box) and 5th and 95th percentiles (shown by the whiskers) and the mean (shown by the asterisks).

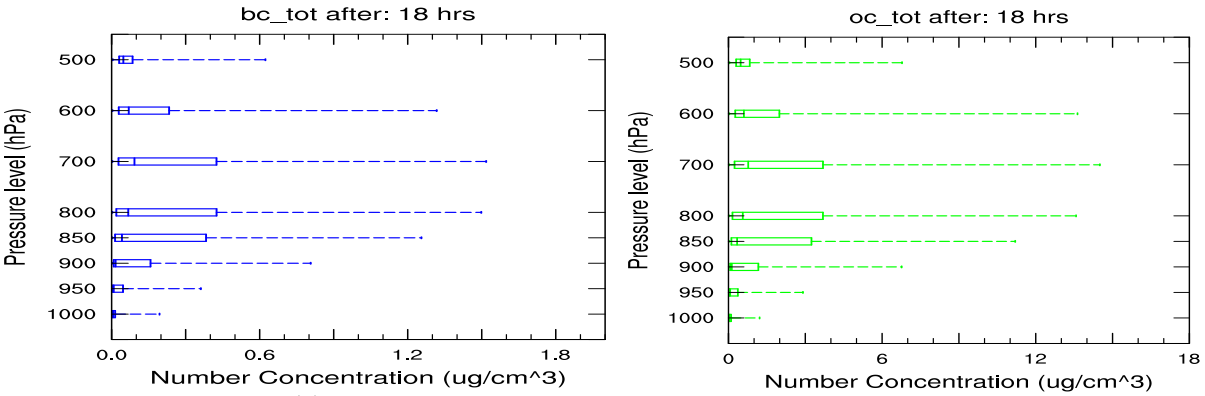

(a) BC (b) OC

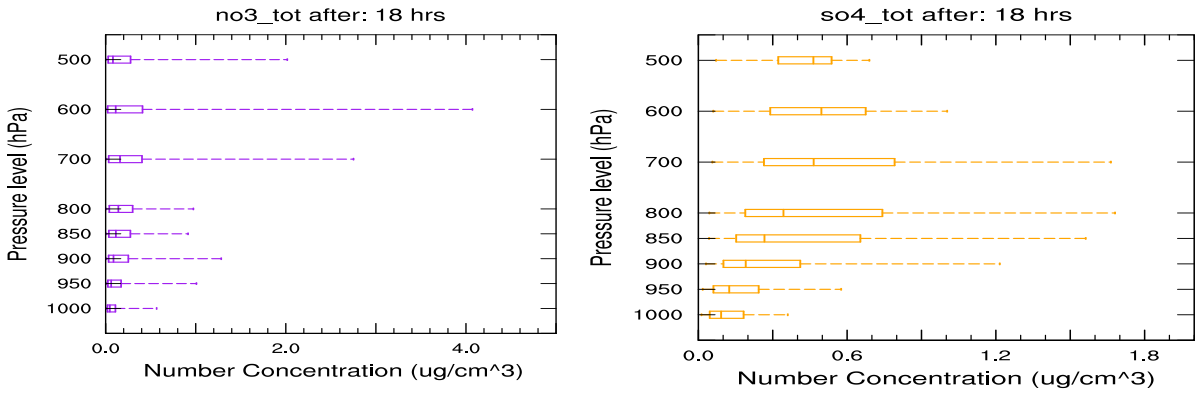

(c) NO_3^- (d) SO_4^{2-}

Fig. 3.16: Vertical profiles of modelled aerosols at 1800 UTC, 26 August 2008. Box-and-whiskers show the interquartile range of the calculated statistics; the median (vertical lines dividing the box), the 25th to 75th percentiles (shown by the box) and 5th and 95th percentiles (shown by the whiskers).

3.6.1 Size representation of aerosols in the model

The model is implemented with MOSAIC sectional aerosol scheme (Zaveri et al., 2008), and run with the 8-bin sectional representation. Discrete bins are defined in terms of their upper and lower dry-particle size limits (Table. 3.1). The size bins are based on the dry physical diameter D_p, whereby the widths of the bins increase geometrically from the smallest bin up to the largest (Barnard et al., 2010).

Diameter ranges (μm)							
Bin 1	Bin 2	Bin 3	Bin 4	Bin 5	Bin 6	Bin 7	Bin 8
0.0390625 –0.078125	0.78125– 0.15625	0.15625– 0.3125	0.3125 –0.625	0.625– 1.25	1.25– 2.5	2.5– 5.0	5.0– 10.0

Table 3.1: Particle sizes within an 8-sectional MOSAIC scheme

The diagnosed aerosols can also be quantified in terms of the particle number in a given bin size. In general, as a result of the size dependent source and sinks affecting the size distributions, the lower size bins have more particles than the upper bins. For example, shown below are vertical profiles of the sum of aerosols in the bins (number of particles added from each pair of bins). Profiles of the sum of all the eight bins are shown in Fig. 3.18. Similarly, the figures show aerosol concentrations in the bins as function of height (in terms of pressure levels).

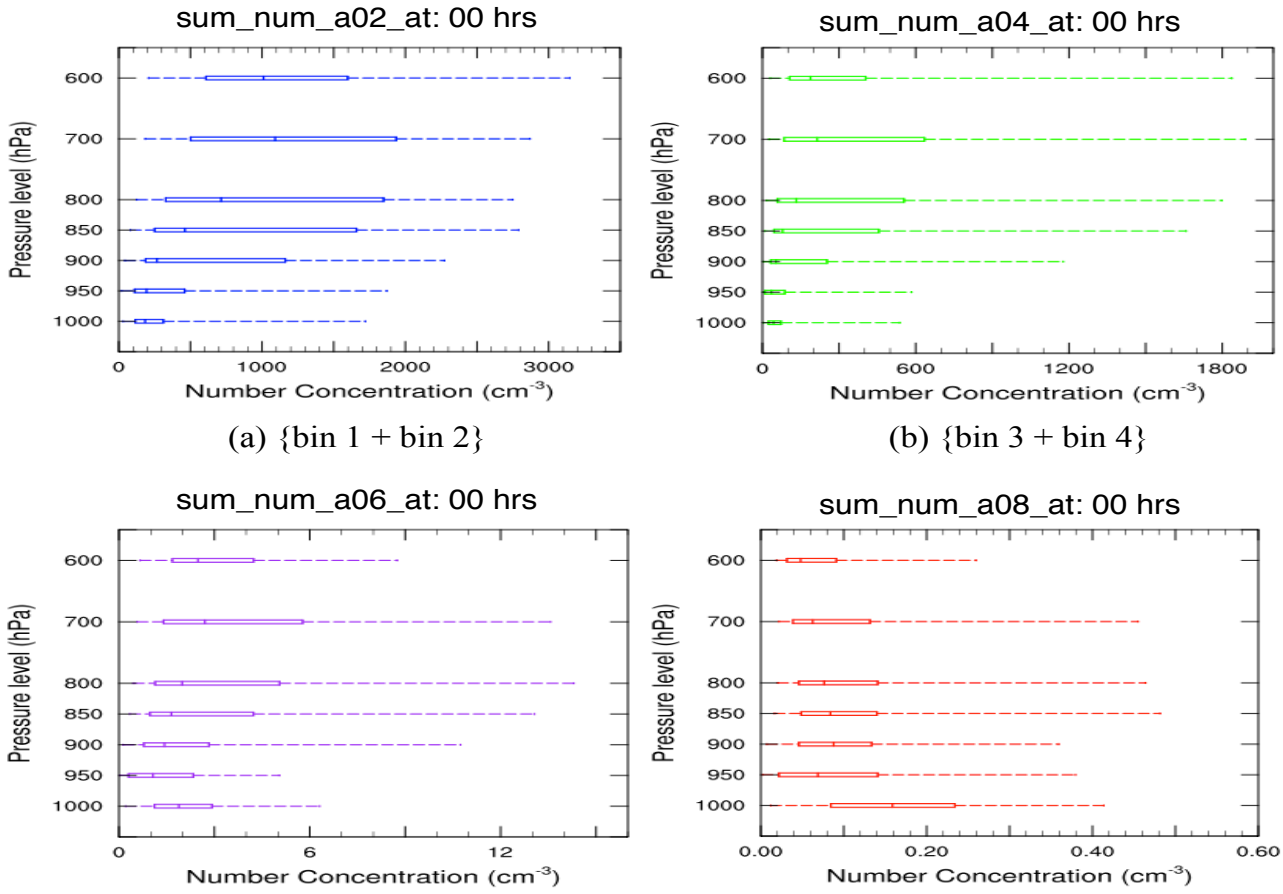

(a) {bin 1 + bin 2}

(b) {bin 3 + bin 4}

(c) {bin 5 + bin 6}

(d) {bin 7 + bin 8}

Fig. 3.17: Vertical profiles of particle number concentration in the bins. Output at 0000 UTC, 26 August 2008. Each plot is the sum of the two bins indicated below. Box-and-whiskers plots show the interquartile range of the calculated statistics; the median (vertical lines dividing the box), the 25th to 75th percentiles (shown by the box) and 5th and 95th percentiles (shown by the whiskers).

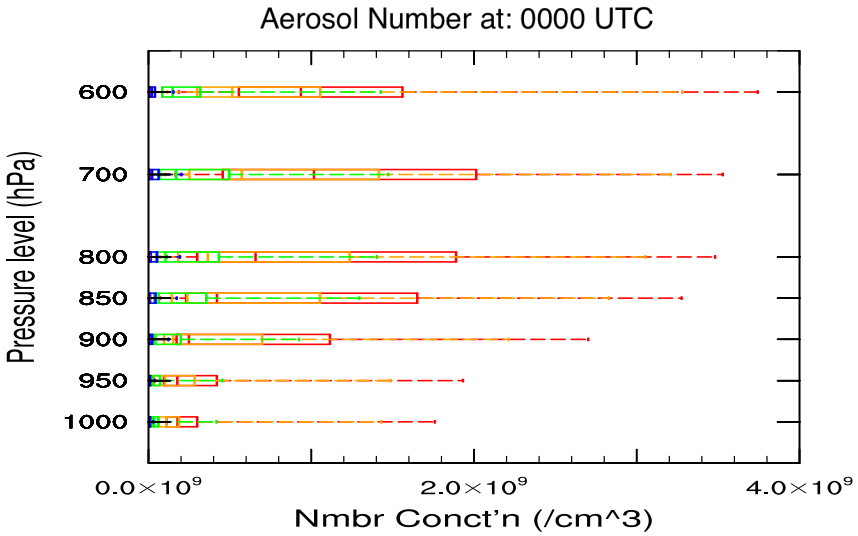

Fig. 3.18: Aerosol number concentrations as a function of height. Colour scale: black = bin8, brown = bin7, yellow = bin6, purple =bin5, blue = bin4, green =bin3, orange = bin2, red = bin1. The bin sizes are as defined in Table 3.1 above. Output at 0000 UTC 26 August 2008.

3.7 Cloud–aerosol feedbacks

WRF-Chem can be run with- or without aerosol feedbacks. The presence of clouds and aerosols in the atmosphere alters the photolysis rates that drive atmospheric chemistry. For example, the Fast-J photolysis scheme (Wild et al., 2000; Banard et al., 2004) determines the feedbacks to the chemistry. The scheme calculates photolysis rates from the predicted ozone, aerosol and photolysis rates (Fast et al., 2006), directly using the physical properties of the scattering and absorbing particles in the atmosphere as determined by the model or specified in a climatology (Wild et al., 2000). Evolution of atmospheric aerosols is strongly affected by meteorological parameters such as radiation, temperature and wind speed (Zhang et al., 2015). For example, the downward shortwave flux at the ground is strongly influenced by the existence of aerosols that can absorb or scatter the radiation. Fast-J can also calculate the divergence of the total flux throughout the atmosphere, it can be used to accurately determine the shortwave heating rates in the presence of clouds and aerosols (Wild et al., 2000). Size distribution of cloud droplets and other hydrometeors (e.g. snow, ice- and rain water) are determined and represented by a gamma distribution function, with the Morrison-double moment (Morrison et al., 2005; Morrison and Pinto, 2005; Morrison et al., 2009).

Interaction with the shortwave and longwave radiation for the hydrometeors predicted with the microphysics are represented by linking with the Rapid Radiative Transfer Model for Global (RRTMG) parameterisation (Mlawer et al., 1997) that calculates direct radiative forcing that influences the in-situ temperature profiles. Through wavelength-dependent attenuation of incoming shortwave radiation, aerosols have a strong effect on the photolysis frequency of molecular absorbers. Indirect effects are thereby handled by the microphysics scheme where aerosol properties can affect cloud droplet nucleation, cloud lifetime and precipitation (Shrivastava et al., 2013). For indirect aerosol feedbacks, the Abdul-Razzak and Ghan scheme (2000; 2002) determines the number of activated CCN, from which the Morrison microphysics scheme is used to predict the mass and number of prognostic variables (e.g. cloud water, rain water and water vapour). Finally, the processes are passed onto the radiation scheme to give aerosol–cloud indirect effects.

3.7.1 Cloud condensation nuclei (CCN)

Because aerosols act as embryos from which clouds form, the number or proportion of cloud-water droplets forming is a function of concentration and size of aerosol particles. Aerosol activation depends largely on the degree of supersaturation, which itself is related to the updraft velocity w (Pruppacher and Klett, 1998; Lance et al., 2004; Hoose et al., 2010). Aerosols activate at different supersaturation levels to form cloud particles. Higher updraft velocities can reach higher maximum supersaturation S_{max}, where more particles are activated. The S_{max} is in turn, affected by the

competition between activating particles for the available water vapour. S_{max} is diagnosed within the activation parameterisation (see equation 2.12 in section 2.8, Chapter 2). WRF-Chem carries about 6 diagnostic CCN variables (CCN1, CCN2, CCN3, CCN4, CCN5, and CCN6 respectively) corresponding to supersaturation levels (0.02%, 0.05%, 0.1%, 0.2%, 0.5% and 1.0%) at which aerosols activate, calculated by summing the particle number in each size bin that would activate at each supersaturation.

Figure 3.19 shows modelled CCN number concentration at different supersaturation levels, plotted only where there are clouds over the domain. These figures only show the CCN concentration (at each given supersaturation) available to activate into cloud droplets where there is sufficient water vapour to do so. Because the number of activated CCN is the sum of all particles of sufficient size that will activate at the specified supersaturation level, it is clear that CCN number increases with S and consequently droplet number will increase with increasing S_{max}. The number and composition of CCN particles depend on the type of aerosols at a location. Normally, continental air masses have higher CCN concentrations than maritime air masses (Pruppacher and Klett, 1998), mainly because of higher anthropogenic emissions over land. Also, CCN concentrations are enhanced around industrial urbanised and combustion areas (e.g. BB) releasing large plumes of particulates and gases into the atmosphere. Figure 3.20 shows the time series of average CCN number concentration at corresponding supersaturation levels.

3.7.2 The linkage between Aerosols and Clouds

CCN concentration is key to cloud droplet number (QNDROP), and hence a convenient means of characterizing cloud-nucleating ability (Schwartz and Slingo, 1995). However, CCN number concentration does not necessarily give the same droplet number concentration because not all particles activate into cloud droplets; some can reach activation levels and grow into cloud droplets, whereas some fail to activate and remain interstitial. The competition for water vapour is handled within the activation parameterisation. Although cloud droplet number concentration is key to numerical weather prediction, accurate prediction of this quantity is still a formidable challenge in cloud-resolving models. The parameterisation described in chapter 2 determines the number spectrum of activated CCN from S_{max} for each model grid cell, when $QNDROP = CCN[S_{max}]$ such that new droplets are formed from all CCN that have a critical supersaturation S_c less than the diagnosed maximum environmental supersaturation.

Figure 3.21 shows simulated clouds (in terms of droplet number concentration) and effective supersaturation (S_{eff}) levels over the domain. An NCL (NCAR Command Language) code was written

to calculate the maximum cloud droplet number (Nd_{max}) over the model grid cells. The quantities are determined within the lowest cloud bands in each column only.

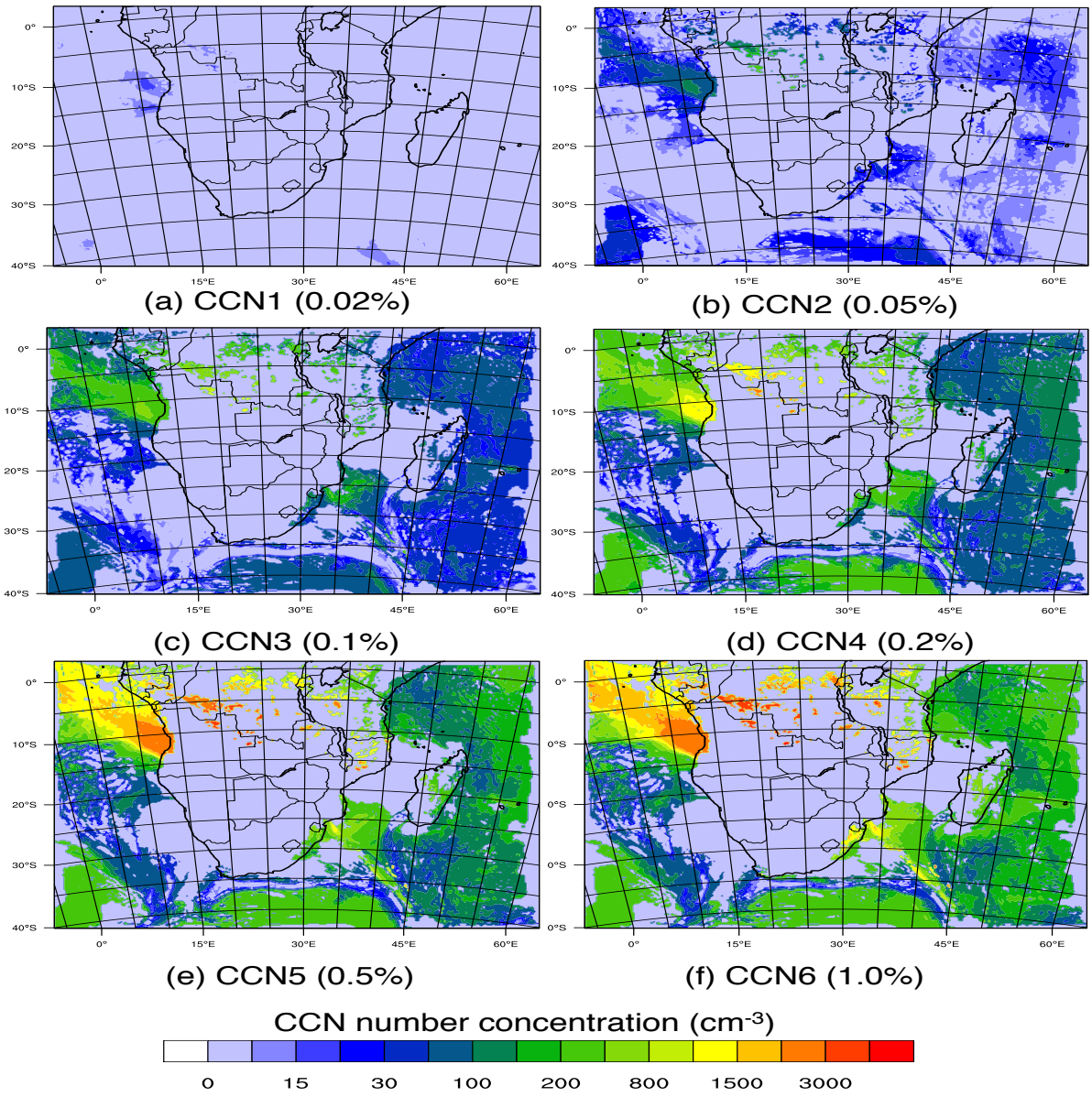

Fig. 3.19: CCN number concentrations at the layer below cloud_base, plotted only where there are clouds in the grid cell. Model output at 1800 UTC 26 August 2008.

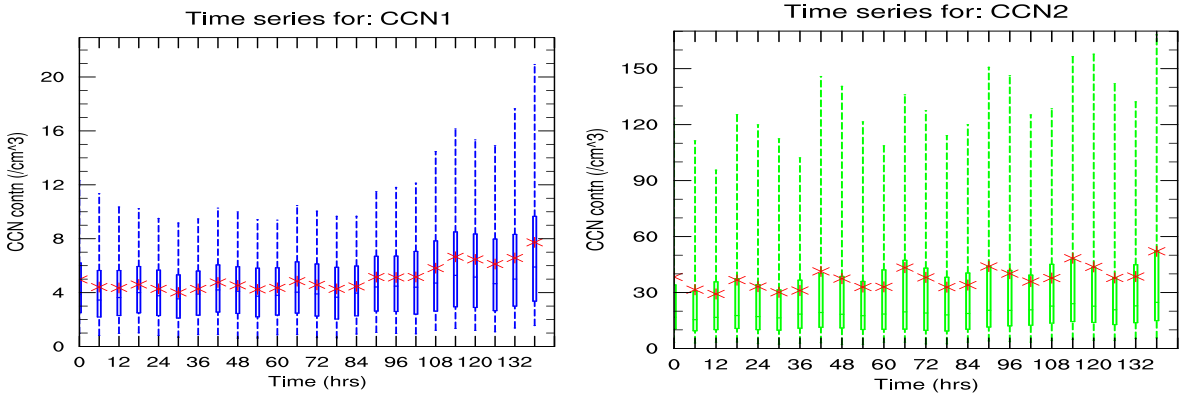

(a) CCN1 (b) CCN2

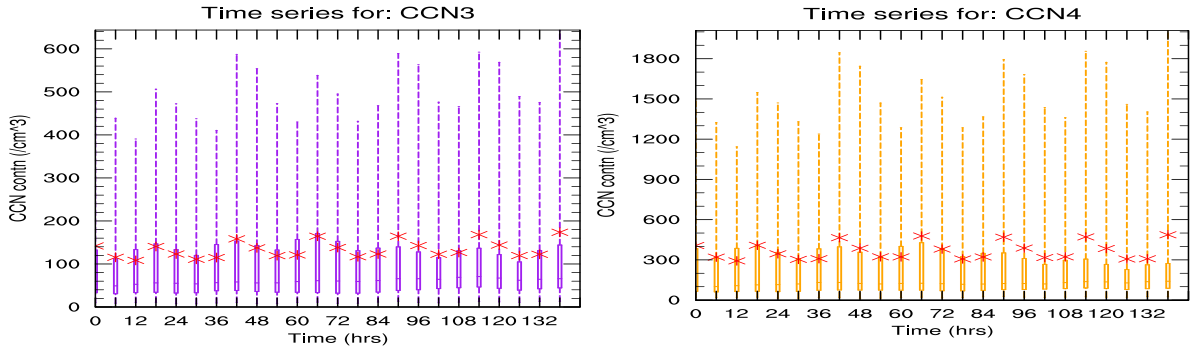

(c) CCN3 (d) CCN4

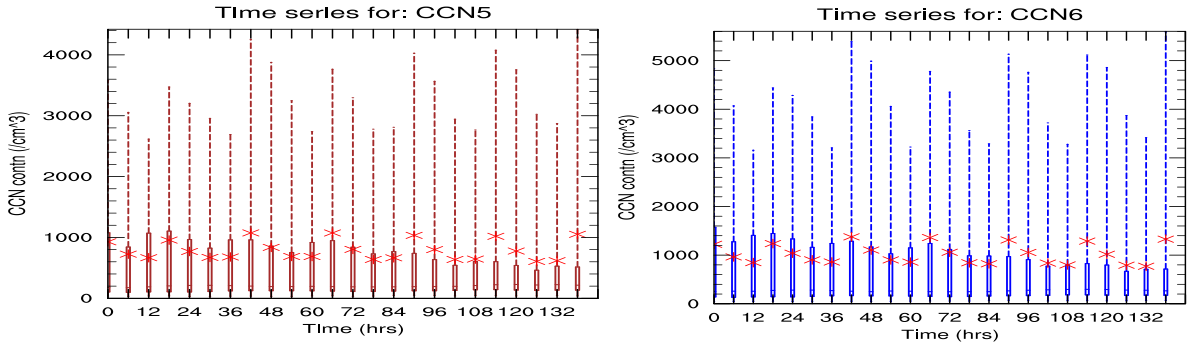

(e) CCN5 (f) CCN6

Fig. 3.20: Temporal variations of simulated CCN particles. Output starting 0000 UTC 26 August to 1800 UTC 31 August 2008.

The plots in Fig. 3.19 were also generated from the same script, where each of the CCN variables was predicted from the cloud base. CCN is determined from the cloud base and S_{eff} calculated in the location immediately above where CCN is diagnosed, whereas Nd_{max} is calculated within the cloud band. To understand how the changes in CCN due to BB affect the clouds in this simulation, the model-predicted Nd_{max} and S_{eff} are plotted (Fig. 3.21). In these examples, changes in CCN (aerosol concentration) within areas of polluted clouds can potentially change cloud optical properties through the first indirect effect.

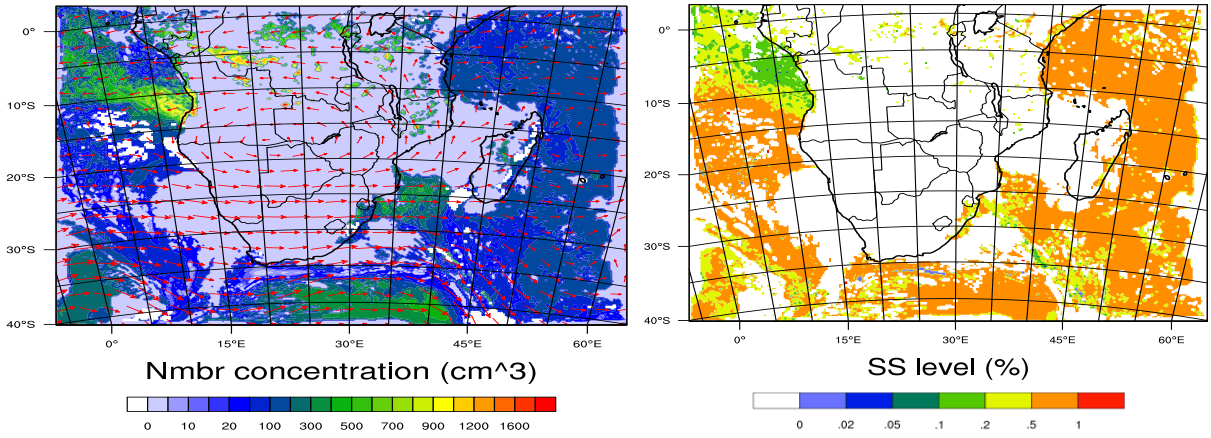

(a) Cloud droplet number concentration (b) Supersaturation

Fig. 3.21: Model predictions for maximum cloud droplet number and effective supersaturation, plotted only where there are clouds in the grid cell. S_{eff} is determined above where CCN concentration is diagnosed. Output at 1800 UTC 26 August 2008.

In addition, the second indirect effect will impact the cloud droplet number and likely affect cloud water over the areas downstream of the emissions. By following this procedure, I will be able to show (later in the thesis) how aerosols affect clouds through the changes in CCN and the common cloud types forming from BB aerosols. Fig. 3.22 show the vertical profile of the clouds over the domain. This is a slice fixed at 8° latitude from Fig. 3.21(a). Average droplet number concentration is shown in Fig. 3.23(a), whereas Fig. 3.23(b) shows the vertical profile of cloud droplet number concentration.

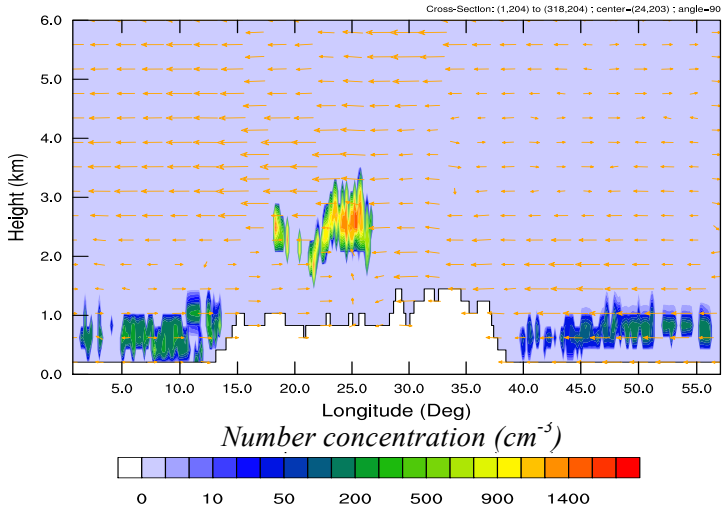

Fig. 3.22: Vertical profiles of cloud droplet number [units: cm^{-3}] at 8° S. Model output at 1200 UTC, 28 August 2008. Arrows indicate wind direction.

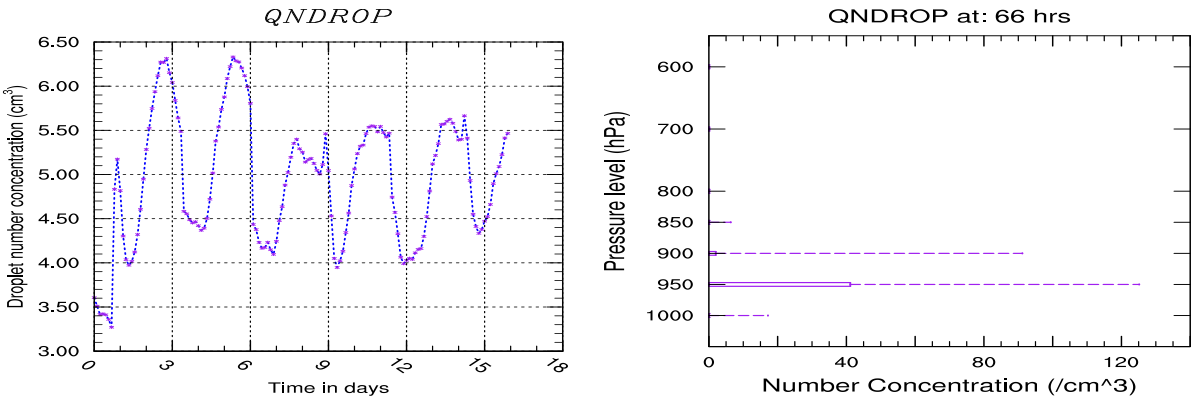

(a) (b)

Fig. 3.23: (a) Domain-averaged QNDROP, and (b) vertical profile of droplet number concentration. Left panel: output starting 0000 UTC 26 August to 1800 UTC 31 August. Asterisks indicate average points. Right panel: droplet number concentration at 1800 UTC, 29 August 2008.

A summary of the strategy to be employed in this thesis is given in Fig. 3.24, consisting of the characterization of the process simulation from the operational tool to simulate the effects of cloud-aerosol coupling. Since many of the environmental challenges in weather and air quality changes are strongly coupled, a modelling system such as WRF-Chem offers an opportunity to include these coupled-process interactions (Grell et al., 2006). The graphical outputs clearly indicate that the model

captures the processes suitably, responds to the linkages and makes testable predictions of the couplings across the domain.

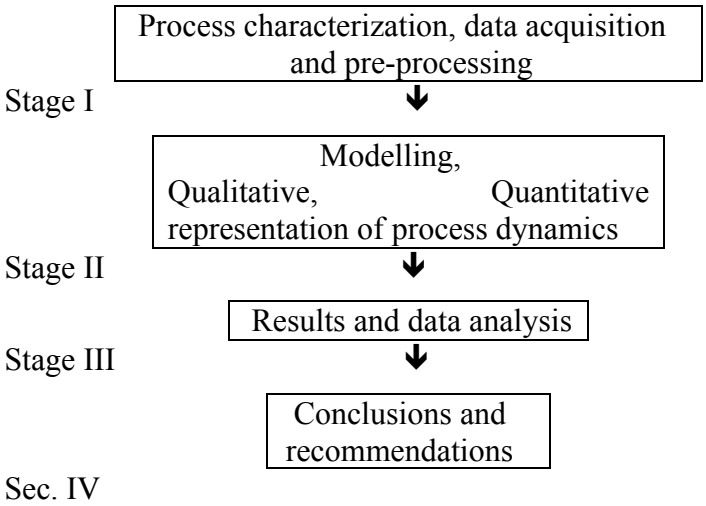

Fig. 3.24: Generic project flow chart

This chapter provides a template for the model diagnostics that will be developed in the subsequent chapters. The basis of this chapter is that it: (i) facilitates evaluation with meteorological, chemical and aerosol quantities in space and time, and (ii) encourages a process-oriented evaluation of the model simulation by examining variability that is characteristic of aerosol-cloud processes. An illustrative application of the WRF-Chem simulation to the aerosol-cloud interactions is demonstrated by the model outputs (figures) for different sections shown in Fig. 3.1. Although results for the simulation provided here give an understanding of the performance of the system during BB, they can still help demonstrate WRF-Chem performance in a more representative realistic environment.

Chapter 4

Characterisation of southern African regional pollution with the WRF-Chem model

4.1 Introduction

This chapter presents an atmospheric characterisation of the regional atmosphere over southern Africa, and evaluates the model behaviour based on the simulation of the biomass-burning (BB) episode in the dry season of 2008. With the model application described in Chapter 3, the present chapter provides an overview of the horizontal and vertical distribution of the regional haze and meteorological patterns. This chapter gives insight to how aerosols and clouds behave at different model resolutions. Emissions over southern Africa exhibit a mixture of large quantities of aerosols and gases from combustion processes such as BB, domestic fires [fire wood, waste burning, charcoal], fossil fuel sources [automobiles and industries], construction, manufacturing and aeolian dust. Vegetation is composed of various categories (e.g. deciduous, shrubland, grass, savannas etc.) from which volatile organic compound (VOC) emissions occur, especially during summer after the wet spells. Since the late 20th Century, the subcontinent has transformed from a rural to a complex society and has made great strides towards industrialization, urbanisation, and economic development (Simukanga et al., 2003). As a result, these changes –compounded with population growth brought about environmental problems (virtually non-existent in the past century) over the subcontinent.

Recently, the subcontinent has experienced a growing industrial infrastructure (most of which is coal powered), releasing large amounts of gas pollutants into the atmosphere. The most industrial trace gas emissions include sulphur compounds (SO_x [SO_2 + SO_3]), nitrogen oxides (NO_x), carbon monoxide (CO) and other combustion products from major pollution areas such as the Mpumalanga industrial area in South Africa and the Copperbelt Province in Zambia (Piketh and Walton, 2004). Near-point source emissions have also been reported in some areas (e.g. sulphur dioxide (SO_2) emissions in Selebi Phikwe mine, Botswana) exceeding health guidelines, thus affecting people downwind (Simukanga et al., 2003). Piketh and Walton (2004) also reported that about 2.24 Mt y^{-1} of sulphur was emitted from southern Africa's industrial areas, especially South Africa, Zambia and Botswana respectively, with Botswana contributing nearly 10% of the emissions. These emissions consist of important components in the photochemical production and destruction of other species (Ward et al., 2012) such as ozone (O_3), hydroxyl (OH) and nitrate (NO_3) radicals. On the other hand, sub-Saharan Africa burns more biomass per unit area of their land annually than most other regions in the world (Ichoku, 2008). A lot of burning occurs in tropical central, Africa decreasing southwards. The burning increases during the dry season (May–August) and decreases towards summer (September–October), marking the

beginning of the wet season (Piketh et al., 2002; Tummon et al., 2010, and references therein). Although BB can cause episodic high air-pollution events, it is mainly limited to the dry season, compared to anthropogenic and other emissions such as dust and sea salt, which are continuous throughout the year.

The purpose of this chapter is to provide an overview of the state of the regional atmosphere during the simulation period and highlight the appropriate dispersion package to study the peculiarities of meteorological and chemical process interactions of pollutants and climate perturbations in southern Africa. Special attention is given to the existence, transport and distribution of chemical pollutants over land and the relative importance of both natural and anthropogenic emissions.

4.2 Model application over southern Africa

Although development and occurrence of chemical pollution episodes have been studied using air quality models (AQMs) incorporating the contributing atmospheric physical and chemical processes, WRF-Chem is the next generation model currently used by many researchers for AQ studies (Al Razi and Hiroshi, 2012, and references therein). It has been applied in different parts of the world and has demonstrated its ability to simulate AQ and weather impacts under different conditions. Of particular interest are those studies investigating aerosol–cloud impacts. For example, there have been studies in Europe (Tuccella et al., 2012; Forkel et al., 2014), North America (Zhang et al., 2010; Grell et al., 2011a), South America (Archer-Nichols et al., 2014) and Asia (Tie et al., 2009; Kumar et al., 2012; Lin et al., 2014). Although many investigations on atmospheric pollution and air-quality studies have been conducted in many other parts of the world, only a handful of such studies have been reported for Africa, particularly sub-Saharan Africa.

There are very few regional coupled model studies focusing mainly on meteorology (Crétat et al., 2012), and none have particularly investigated aerosol–cloud interactions (ACIs), except those using satellite observations to evaluate model results (e.g. Constantino and Bréon, 2010; de Graaf et al., 2012; Yi et al., 2012; Tesfaye et al., 2013). Inadequate measurement data and poorly developed emission inventories have been identified as some of the main hindrances to aerosol modelling in southern Africa (Kuik et al., 2015). On the other hand, although projects such the AMMA (African Multidisciplinary Monsoon Analysis) were designed to address these gaps, they focused particularly on other parts of Africa (especially west Africa).

Recent WRF-Chem modelling studies in Africa include those of Yang et al. (2013), Zhang et al. (2014) and Kuik et al. (2015). Although these studies also investigated various aerosol impacts, they differ from this study. Both Yang et al. and Zhang et al. studies focused over the northern African equatorial region. For example, Yang et al. investigated smoke from fire emissions and mineral dust

transport, but their study did not include other emission sources. Similarly, Zhang et al. examined the sensitivity of smoke loading and direct radiative effect in the atmosphere to uncertainties in emission estimates. They only focused on BC and OC emissions, implementing only fire emission and excluding emissions from other sources (anthropogenic, biogenic, sea salt and dust emissions). On the other hand, although the Kuik et al. study was conducted over southern Africa, they only investigated the anthropogenic contribution in 2010 due to BC aerosols, focusing specifically on South Africa.

4.3 Meteorology

This section focuses on assessing the WRF-Chem model's skill in simulating the southern African weather following its application and testing described in the previous chapter. The main objective is to demonstrate that the model is a faithful representation of the real atmosphere. Because air-quality modelling relies strongly on the meteorology, errors in the meteorology may lead to under/over prediction of chemical species in the model. Accurate representation of meteorology and aerosol concentration in the model provides the foundations for quantifying aerosol feedbacks (Zhang et al., 2015). Therefore, it is vital to first understand the meteorological context in order to describe the chemical evolution and cloud processes. We first look at the broad meteorological features for the entire simulation period. Figure 4.1 shows model output at the start of the simulation plotted for the large domain.

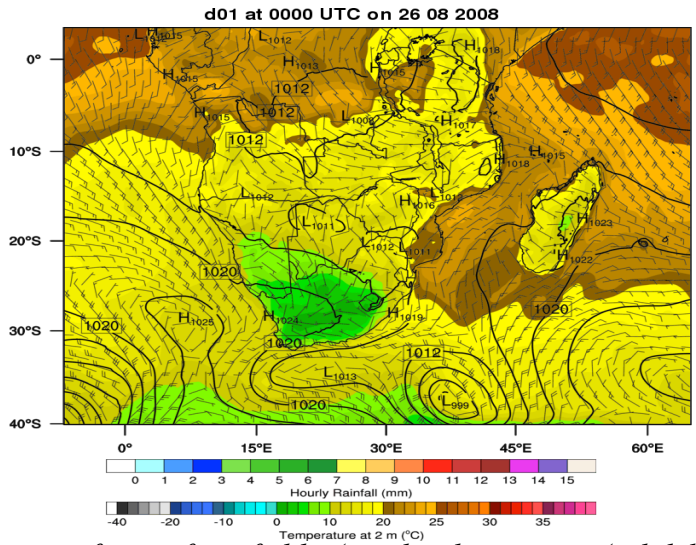

Fig. 4.1: Model initialization for surface fields (sea level pressure (solid lines every 4-hPa), 2-m temperature (in ℃, shaded according to scale) and wind barbs [pennant, full barb, and half-barb denote 25, 5, 2.5 m s^{-1} respectively; separation between displayed wind vectors is 20 km] at the start of the simulation (0000 UTC 26 August 2008).

A large part of the domain was relatively warm at the start of the simulation, except over the southwest where temperatures were below 10°C. Nearly half of the domain had temperatures up to 20°C, with the northern part being warmer (20–25°C). The wind was blowing southwesterly in the western part of

Africa, while in the east it was northwesterly and southwesterly towards the mainland, becoming slack over land. There were some extratropical pressure systems south of Africa moving eastwards. For example, a 1025-hPa high was situated south of 25°S in the west and a 999-hPa low was located to the east, just below south of Africa around 35°S. From 26 August to 31 August, the model predicts a seasonal change over southern Africa. Most noteworthy are the precipitation locations and surface air temperature differences. Temperature increased from the west to the east (e.g. over 35°C over Zimbabwe–Mozambique) Fig. 4.2(b), whereas over Madagascar it was warmer in the west than in the east. Convection occurred more often in the upper half of the domain, with precipitation occurring in the late afternoon around 1800 UTC (Fig. 4.2(a)).

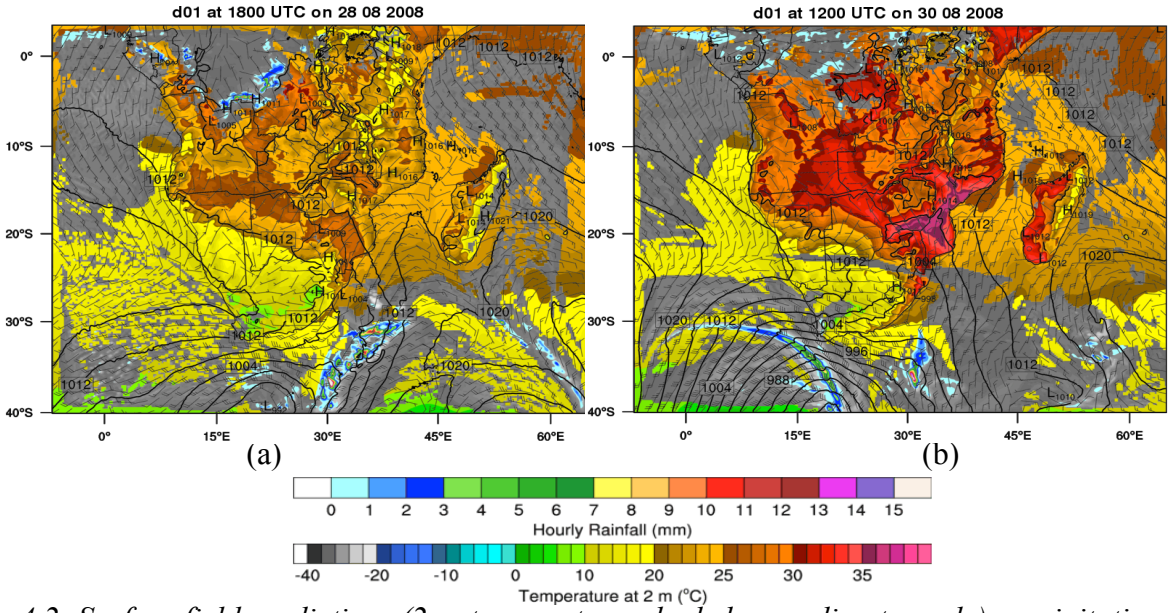

Fig. 4.2: Surface field predictions (2-m temperature, shaded according to scale) precipitation (mm/hr), simulated satellite, sea level pressure (solid lines every 4-hPa) and wind barbs (denoting 25, 5, 2.5 m s^{-1} respectively). Model output at (a) 1800 UTC 28 August and (b) 1200 UTC 30 August 2008, for the outermost domain.

At 1200 UTC 30 August, the subtropics (about 10–30°S) were relatively warm and dry, whereas precipitation occurred over the ocean in the south as frontal rains. The troughs in the mid-latitudes continued moving eastwards, passing below the mainland and Madagascar. For consecutive days, highs and lows passed, causing cyclogenesis in the mid-latitudes yielding frontal precipitation and westerly winds. However, pressure systems appear to be perturbed upon passing south of Madagascar, probably due to the wind direction (north-westerly), which resulted in increased precipitation (Fig. 4.4). An examination of mean sea level pressure also confirms this, as pressure increased over the southeast. The pattern suggests the presence of jet streams in the mid-latitudes accompanied by westerly extra-tropical cyclones influencing weather over the south of the mainland. On the other hand, convective cells are predicted over the tropics to the west of the mainland. The subcontinent

remained dry and warm for quite some time, with small precipitation totals in the tropics and the mid-latitudes.

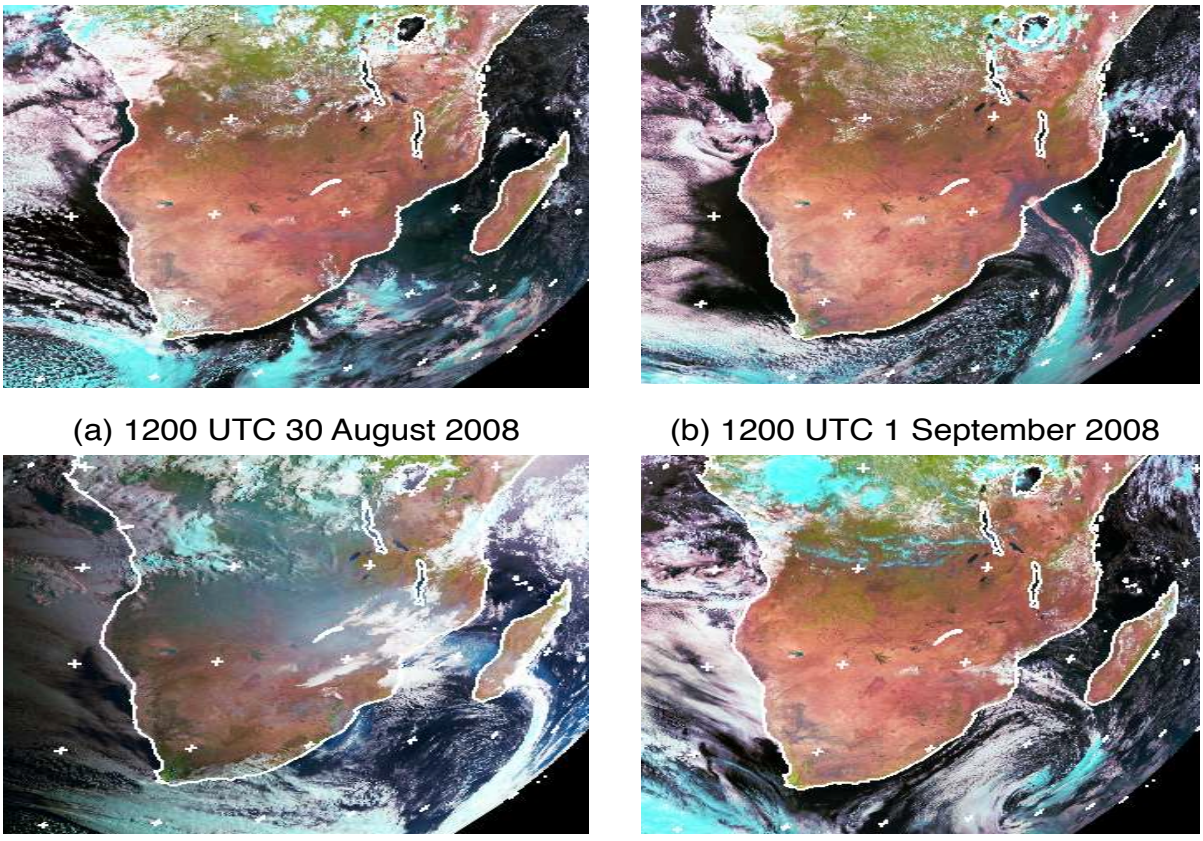

(a) 1200 UTC 30 August 2008 (b) 1200 UTC 1 September 2008

(c) 0600 UTC 2 September 2008 (d) 0600 UTC 6 September 2008

Fig. 4.3: Satellite images over southern Africa. Images show locations and structure of cloud cover over the domain. (http://www.sat.dundee.ac.uk).

To demonstrate that the model simulation is realistic, I compare results with satellite imagery (Fig. 4.3) for a selected period of the simulation. The figure shows satellite images between 30 August and 6 September 2008 over southern Africa. Although the satellite imagery does not show pressure and wind patterns, clouds are within areas where the model predicts precipitation. Also, the locations and structures of the storms in the model are similar to those in the satellite imagery. There are more precipitation regions over the central and eastern regions in the model than there are over western regions. However, model-predicted precipitation lies within cloudy areas on the satellite imagery. Between 1 and 6 September, the model predicts precipitation in the northern part of the domain, as shown in Figs. 4.4 and 4.5(a), while the southern part was still under the influence of eastward-moving storms. The wind in the east was southwesterly, becoming more easterly in southern Africa and southwesterly to the north. A 1026-hPa high developed off the coast of Mozambique–South Africa, south of Madagascar on 2 September (Fig. 4.4(b)), with a precipitation band located to the east of the high.

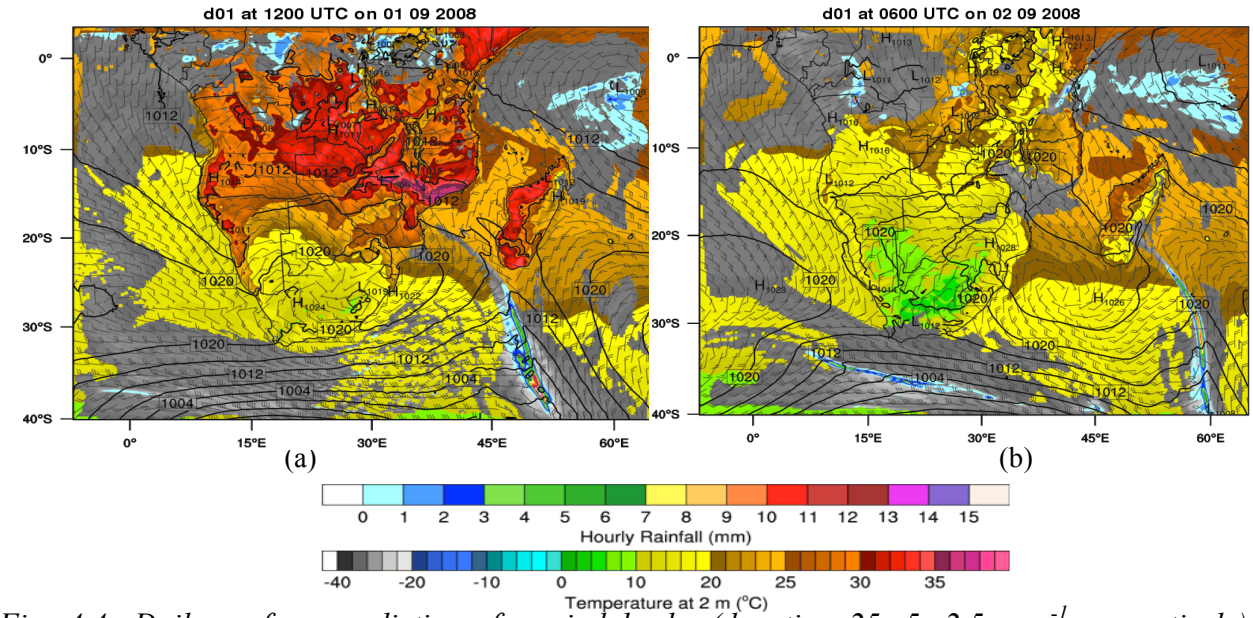

Fig. 4.4: Daily surface predictions for wind barbs (denoting 25, 5, 2.5 m s^{-1} respectively), 2-m temperature (°C, shaded according to scale) and mean sea level pressure (solid lines every 4-hPa) and precipitation (mm/hr). Model output at (a) 1200 UTC 01 September and (b) 0600 UTC 02 September 2008 on the outermost domain.

The southwest part of the mainland was colder (temperatures dropped below 10°C) than the upper part of the landmass. The southwest is usually subject to the cold fronts during winter, rolling in from the Atlantic Ocean. This part of the domain receives its winter rainfall due to these fronts (Hudson and Jones, 2002) when they are embedded in the westerly wind regimes (Obasi, 2001). The fronts passed immediately south of the mainland along the passage of the storms. As shown in the panels above, the landmass was fairly warm in the central part, with convective precipitation in some parts over the tropics (Fig. 4.4(b)), such as over Angola and Tanzania and stretching along the east coast towards Kenya (see also supplementary material, B1 in Appendix B).

Storms described above moved eastward throughout the simulation, whereas temperature changed, for example, the west was more warmer than the east (Fig. 4.5 (a)). Figure 4.5 shows the model prediction at midday on 6 September and the morning of 10 September, respectively. In Figure 4.5(a), the west tends to be warmer than the east (compared to Figs. 4.2(b) and 4.4(a)). A storm is predicted south of Madagascar (Fig. 4.5(a)) (see also Fig. 4.3(d)), followed by consecutive ones along the same path through 10 September (Fig. 4.5(b)). Although WRF-Chem predicts precipitation over most parts of the domain (albeit underestimating clouds), it tends to be slightly different in this case compared to predictions in Chapter 3 (e.g. Fig. 3.5) for cloud water content, especially in the west and south. Compared to the satellite imagery (Fig. 4.3), most parts of the subcontinent were entirely cloud-free (e.g. Fig. 4.4 and 4.5(b)). Meanwhile, persistent pressure systems and storms in the south are fairly well predicted in the model throughout the simulation. Low cloud cover over large areas where there is

precipitation may be related to a reduction in cloud lifetime with the more rapid cycling of water over the mainland, especially due to the surface temperatures and boundary layer winds being higher. This will be revisited in the next chapters, to investigate if it is due to the aerosol contribution, focusing more on ACIs at different model resolutions.

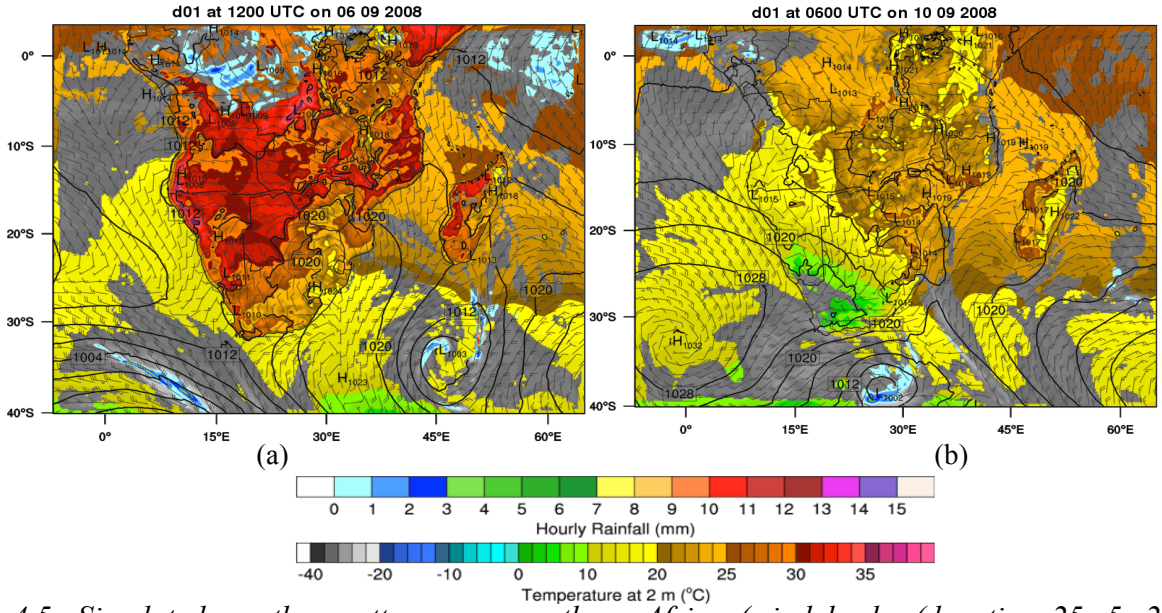

Fig. 4.5: Simulated weather pattern over southern Africa (wind barbs (denoting 25, 5, 2.5 m s^{-1} respectively), 2-m temperature (°C, shaded according to scale), mean sea level pressure (solid lines every 4-hPa) and precipitation (mm/hr)). Note the extra-tropical storms in the mid-latitudes associated with frontal precipitation. Model output at (a) 1200 UTC 06 September and (b) 0600 UTC 10 September 2008, on the outermost domain.

4.3.1 Resolving more process detail in the sub-domains

The purpose of this section is to focus mainly on the weather within the fine grids on the coarse grid. Locations of these sub-domains (see Fig. 3.2, Chapter 3) are chosen so as to match roughly with meteorological conditions over these regions. The nested grids have points as follows, d02: 241 × 241 grid points, d03: 281 × 251 grid points and d04: 291 × 281 grid points. An objective of this section is to assess to what extent the sub-domain data compares with the parent domain and how consistent are they with each other. The other reason also is to have a better understanding of the local information when comparing results from the fine grids with the coarse domain. Apart from grid resolution, the only other difference between the parent grid and the nests is convective parameterisation, which is turned off in the nests. Specifically, grid spacing in the sub-domains is small enough to resolve explicit convective processes. No other sub-grid parameterisations differ between the nests.

(a) West sub-domain (d02)

This region is dominated by high biomass burning aerosols (BBAs) that are transported southward (Constantino and Bréon, 2013). Tropical central-west Africa is the source region of smoke from

burning, although the sparse Namibian vegetation does not support much burning (Swap et al., 2003). Quite often, coastal areas of southwest Africa are characterized by a persistent deck of stratocumulus clouds influencing aerosol deposition into the Atlantic Ocean from nearby land regions (Ben-Weiss et al., 2014; Peers et al., 2014). During winter, strong easterly transport is established from the mainland toward the ocean. Transport from the landmass through the tropical Atlantic Ocean is favoured by easterly wave conditions (Kirkman et al., 2000), where transient mid-latitude anticyclones result in maximum transport from the mid-latitudes flowing towards the South Atlantic Ocean.

(b) East sub-domain (d03)

The region adjacent to the Indian Ocean is quite often characterized by cyclonic and monsoon conditions observed over east Africa. Most of the storms that hit Africa occur from the Indian Ocean, although much of the impacts occur further south. Synoptic features controlling airflow and precipitation include convergence zones superimposed upon regional factors (e.g. topography, maritime air). Common weather phenomena include the northeast and southeast monsoons and the southwesterly humid air from the Congo (Nicholson, 1996). Compared to the west sub-domain d02, BB is not as intense in east Africa except over areas farther inland. Although equatorial east Africa is considered one of the meteorologically complex parts in Africa (Nicholson, 1996; Okoola, 2000), there is comparatively less research in the region on AQ and climate studies.

(c) Southeast sub-domain (d04)

Stein et al. (2003) and Swap et al. (2003) give a synopsis of the meteorological and chemical conditions for coastal regions during BB events in southern Africa. Swap et al. (2003) described the regional haze and trace gas within the notional gyre, indicating that the eastern part of the subcontinent south of Mozambique is the main atmospheric corridor for continental air masses. The horizontal distribution of aerosols and haze layers observed during the anomalous wet conditions are consistent with the hypothesis by Garstang et al. (1996) that there is greater frequency of optically impacted days off the eastern coast during the wet ENSO episode, associated with shifts towards the equator along the exit path. According to Stein et al. (2003), the impact synoptic patterns exert on aerosol transport throughout the eastern coastal region can be described through the westerly wave passage. The synoptic mechanisms include an increased number of westerly wave passages, cutoff lows and a decrease in the strength and frequency of high-pressure systems.

4.4 Emissions

Emissions were prepared for each grid and were input into the model daily throughout the simulation period, as described in chapter 3. To prevent synoptic-scale error growth, meteorological boundary conditions were re-initialized every 24 hours, and the chemistry carried from the previous simulation.

Figure 4.6 shows the spatial distribution of emissions over southern Africa, plotted on the large domain (see supplementary, B2 in Appendix B for other emissions). Emissions shown are anthropogenic gas species (CO and NO), biomass-burning aerosol (BC) and biogenic (isoprene). However, all emission sources have both gas- and particle-phase species.

Anthropogenic emissions are clustered over the domain; the spread of these emissions follows human settlements, land use and industrial/urban areas, including marine operations and transport. There are fewer regions of high concentrations of anthropogenic emissions in the upper half of the domain than in the bottom half. Major pollutant sources are concentrated in the south, mainly around the Highveld region in South Africa (e.g. Fig. 4.6(b)) –a zone of high population density and industrial activity, including mining and power-generating areas around the Gauteng province (Winkler et al., 2008). Emissions include those from metallurgical industries such as within the Johannesburg–Pretoria megacity, the Vaal Triangle and the Mpumalanga Highveld (Kuik et al., 2015). Meanwhile, because there is no comprehensive regional inventory available, emission data for southern Africa is entirely based on emissions from the EDGAR database.

On the other hand, BB, dust and to some extent, biogenic emissions are seasonal, changing in intensity and shifting geographically throughout the year. As shown in Fig. 4.6(c), fire emissions are concentrated over the central part of southern Africa (between 5 and 20°S) where there is high biome density and abundant rainfall to foster prolific vegetative growth.

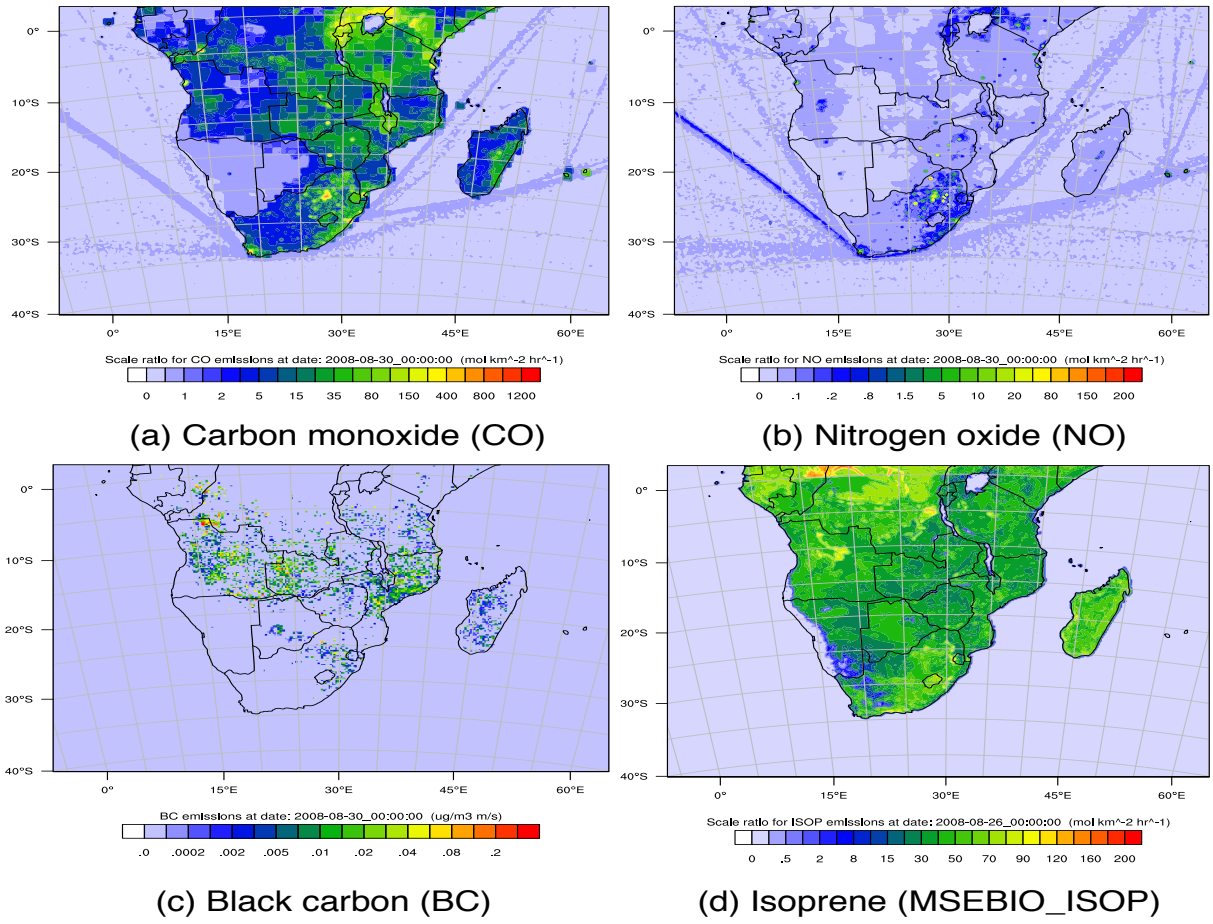

Fig. 4.6: Spatial distribution of emissions over southern Africa for anthropogenic, Biomass burning and biogenic emissions. All emissions valid at 0000 UTC 30 August 2008.

Calculating and processing of the fire emission data is based on daily satellite observations of fires and land cover, combined with emission factors and estimated fuel loadings. The MODIS instrument onboard the satellite identifies the fire location and size for each fire pixel (non-saturated and non-cloudy fire). The fire area is defined from the mean of the instantaneous size estimated by the satellite data for all the fires detected. Each fire pixel is then cross-referenced against 1-km grid spacing of vegetation- and land-use maps, and the fire is assigned to different biomes (or vegetation categories). For each biome, different carbon density (α) and combustion factors (β) are used and multiplied to determine the total biome burnt. Each biome type has an associated emission factor (EF_{veg}) (Andreae and Merlet, 2001) used to convert from burnt biome to quantify emitted species (i), which are then scaled to cover an estimated total burnt area (A_{fire}). Emissions are then scaled by an enhancement factor (f_x) to account for uncertainties in the calculated quantities (see section 2.7.4 in Chapter 2 for mathematical expressions). In the present study, we use default settings for fire emissions in PREP-CHEM-SRC, with average fire sizes of 22.8 ha for all vegetation types and an f_x = 1.3 (Longo et al., 2010). The source code was modified to convert OC into primary organic matter (POM) for all anthropogenic and to include NH_3 emissions (Archer-Nicholls et al., 2014).

Biogenic emissions of aerosol and precursor gases are dependent on atmospheric conditions and vary frequently. For example, isoprene emissions (connected to the process of photosynthesis) are dependent of solar radiation. These emissions generally increase with increasing temperature (Seinfeld and Pandis, 2006) and changes in ambient conditions such as relative humidity (RH) and wind speed. MEGAN uses a simple method to compute emission rates of biogenic emissions (Guenther et al., 2006). The rate of emissions for the standard environmental conditions, compounds and vegetation types is extracted from the emissions inventory and adjusted for deviations and model profiling. Emissions are then scaled by a canopy factor that accounts for the complexity of interactions between emitted species and biome type.

WRF-Chem uses an algorithm (plume-rise parameterisation) that computes the appropriate plume buoyancy for emission of effluents depending on biome density and ambient environmental conditions along the model columns. The algorithm applies a 1-D cloud-parcel model to each grid column within the domain containing fire (Freitas et al., 2007), superimposed with the time variations so that concentrations reflect the peak times in pollutants. For a full set of equations and description of the parameterisation, see Freitas et al. (2007).

4.5 Input data resolution and grid spacing: effect on model performance

This section highlights the importance of effects of grid resolution on model performance (i.e. resolution of input data vs. model grid resolution). Although it is important that model results be as close as possible to reality, model performance is often affected by several factors such as grid spacing, boundary conditions and parameterisations. For example, if a simulation is performed at two different resolutions, results can be biased towards one grid spacing depending on the resolution at which data (e.g. emissions) is input into the model. In this study, the simulation was performed at two different resolutions highlighted earlier. Although the simulation was run simultaneously, the coarse domain provides the boundary conditions to the fine grids. For chemical analysis, emissions are averaged for the coarse grid, whereas we interpolate for the fine grids.

However, the meteorology also needs to be correctly simulated/predicted in the model in order to describe the chemical evolution as highlighted in section 4.3. Although the coarse-grid simulation fairly captures the regional background concentrations and surface fields, fine-scale variations and local changes of emissions maxima and distinct point sources are captured better at high resolutions. This is demonstrated in the fine grids (depending on where emissions are concentrated) and emission ensembles, indicating less variability. I show this in the results section below and in the succeeding chapters. Meanwhile, a high resolution-simulation should be run with emissions at equally high resolution (Ammuaylojaroen et al., 2014) to improve regional-scale simulations of AQ.

Stroud et al. (2011) highlight three possibilities through which simulations may be affected by model grid spacing: (i) significant artificial diffusion occurring when emissions from compact sources are injected into a larger model grid cell; (ii) representation of transport processes affected by grid spacing when small-scale circulations are not well resolved at coarse grid spacing, and (iii) the chemistry being affected by grid spacing because chemical reactions in sub-grid scale plumes may less likely be accurately represented, given that chemical species within a single-cell plume will at least be partially isolated from the ambient chemical environment of the grid cell and that reacting species may overlap or remain separated. High resolution is important to improve simulations going at small grid spacing or more local scales. This also helps reduce sub-grid inhomogeneity and better resolving of aerosol plumes (Ma et al., 2014, and references therein). The sections below present and discuss results from the simulation. Other results are provided in the supplementary material (B3 in the Appendix).

4.6 Photochemistry and gases

4.6.1 Primary pollutants

Emissions from anthropogenic and natural sources consist of primary emitted species capable of impacting AQ and/or inducing radiative forcing in the atmosphere. These species can be precursors to both photochemical and other complex compounds. In this section I present results for the primary gas pollutants. Figures 4.7 and 4.8 show primary gas species concentrations for carbon monoxide (CO) and nitric oxide (NO) plotted in each domain at 1800 UTC 30 August 2008. The fine grids are plotted at 4-km and 20-km resolutions to compare with the coarse grid.

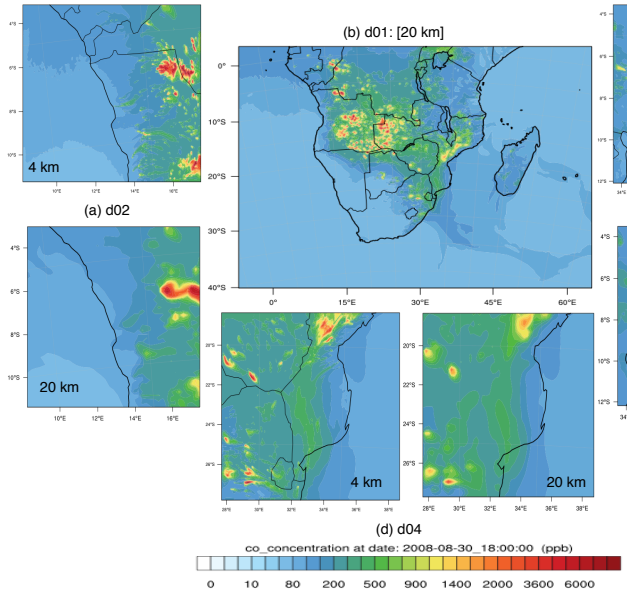

(a)

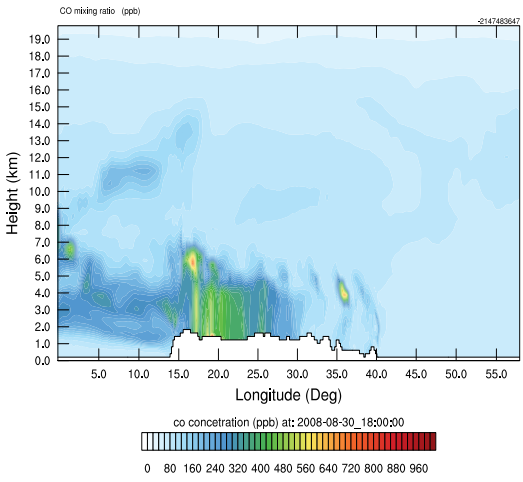

(b)

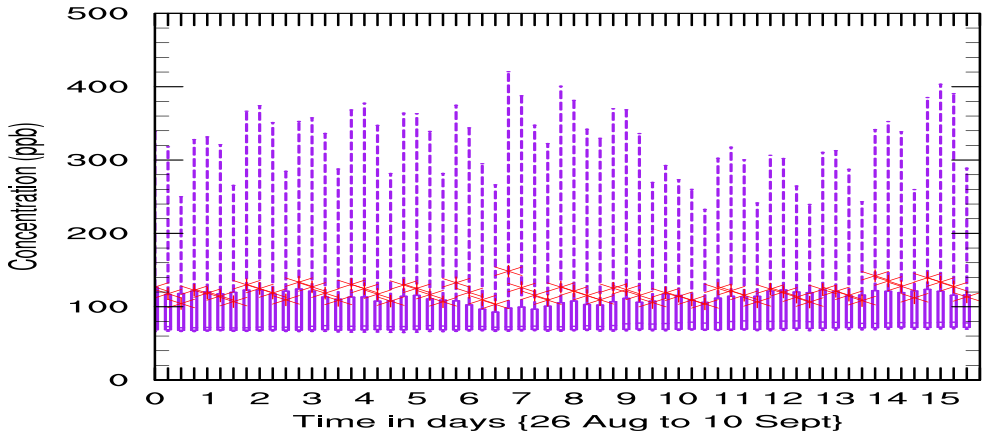

(c)

Fig. 4.7: (a) Carbon monoxide (CO) concentrations over southern Africa, plotted at the surface. Concentrations for the sub-domains are plotted at 4 km and 20 km resolutions respectively. Low-resolutions for the nests are plotted by extracting data from the parent grid (d01), considering only sizes/locations for each grid. Model output at 1800 UTC 30 August 2008. (b) Vertical profile for CO in the east-west direction, fixed at 10°S latitude. (c) Domain averaged CO concentration, averaged over d01.

Figure 4.7(a) shows the CO surface concentration for all the four grids between high and low resolutions, Fig. 4.7(b) shows the vertical profile across the domain (a slice plotted at 10°S) and Fig. 4.7(c) is the average concentration for the whole campaign, averaged over d01. High concentrations of CO are predicted mainly in the central and northwest of the mainland. The southwest part of the landmass has low concentrations compared to the southeast part, where pollution often exits the subcontinent into the Indian Ocean. The sub-domains have higher concentrations, especially d02 with high CO concentration (order of 3000 ppb) over Angola and some parts of Democratic Republic of Congo (DRC), followed by d04 (over eastern South Africa, southern Zimbabwe and Mozambique), whereas for d03, the CO concentration is below 2000 ppb (bottom corner).

Although the fine grids (at 20 km) are comparable to the coarse grid, the concentrations are higher for the same grids plotted at 4 km. Resolution dependence will be investigated further in chapter 5. This will aim to demonstrate whether the grid resolution dependence merely shows that we can resolve more details or whether there are systematic differences between resolutions for different pollutants. Pollution contours are more defined with high concentration areas (in the northwest, decreasing to the southeast). The latitude–height cross-section shows that CO is confined within 6 km above the surface, much of this towards the west. However, some CO is lofted up to 10–15 km between 5° and 25°E. The time series shown by the box-and-whiskers plot indicate that, on average, CO concentration increased between days 1–8, dropping after day 9 (4 September) and peaking a day after.

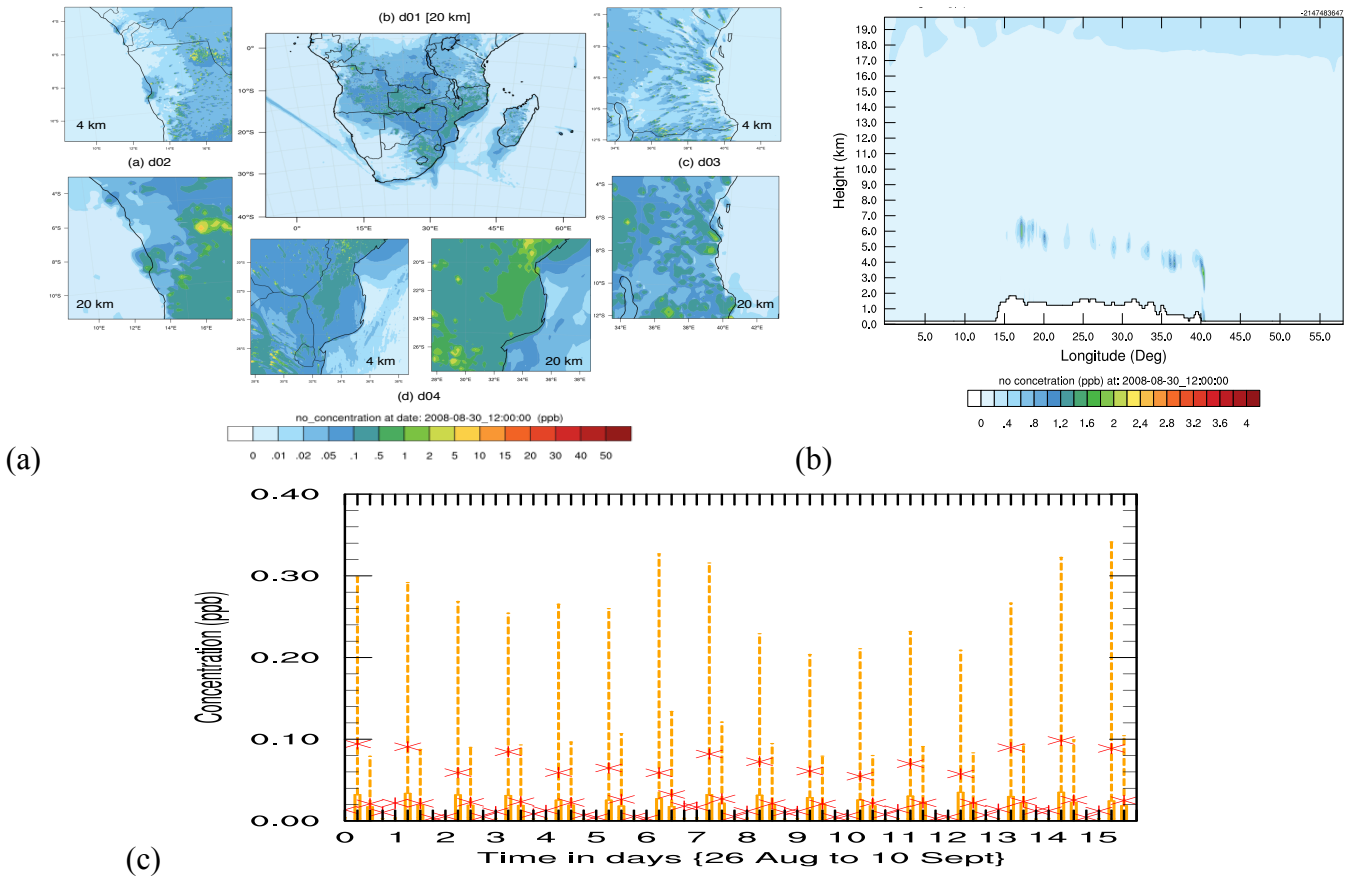

Fig. 4.8: (a) Nitric oxide (NO) concentrations over southern Africa, plotted at the surface. Sub-domains are plotted at 4 km and 20 km resolutions respectively. Low-resolutions for the nests are plotted by extracting data from the parent grid (d01). Model output at 1200 UTC 30 August 2008. (b) Vertical profile in the east-west direction, fixed at 10°S latitude. (c) Domain-averaged NO concentration, averaged over d01.

Figure 4.8 shows: (a) NO surface concentration, (b) vertical profile at 10°S latitude, and (c) temporal variation, averaged over d01. Surface NO concentrations in the fine grids are similar to the same locations on the coarse grid, although the concentrations in the 4-km grid spacing have higher concentrations than those in the 20-km grid output. Higher NO concentrations are confined over land than over the water. However, predictions differ from the CO concentrations whereby higher concentrations are confined around the fire areas, especially over the central part of the domain. Also, as in the case of CO, maximum concentrations are predicted in certain areas, whereas NO does not show the same pattern. This indicates that a significant amount of CO is attributed to BB, where such points could imply the fire locations. The height profile (Fig. 4.8(b)) shows that although emissions can be lofted above 5 km or higher, high-NO_x emissions remain near surface sources. Whilst CO does not show much variation (with time), NO peaks during the day, especially in the mornings and drops in the afternoons towards evenings as shown by the box-and-whisker plot (Fig. 4.8(c)). A reduction in NO_x concentration between days 8–12 either indicates reduction in emissions or wash-out of pollution.

It would be important to determine or have an understanding of the pollution scenario on these days, as discussed in the next chapter.

4.6.2 Secondary gas pollutants

Here I present results for secondary gas pollutants (e.g. O_3 –a photochemical gas pollutant). Figure 4.9 shows O_3 concentration and temporal variation from the simulation. The top panels show (a) surface O_3 concentration and (b) vertical profile, whereas the bottom panel (c) shows temporal variation. High O_3 concentrations are predicted mainly in the central part of the mainland near active burning regions, especially over Angola, Zambia and northeastern parts of Botswana. O_3 enhancement in these regions reaches up to 90–100 ppb. Although surface concentration increases in space more over land (in line with the precursor species), concentrations also increase over the oceans. One other difference between O_3, CO and NO noticed here is that there is not much difference between the high and low resolution in O_3 concentration, and its (O_3) dispersion also increases over the oceans than that for the primary species shown above. Because O_3 is an active daytime oxidant, the concentration peaks more during the day as shown in the temporal plot (Fig. 4.9(c)). Average concentration varies between 20–30 ppb. The longitude height profile shows that tropospheric O_3 increases above 16 km above mean sea level.

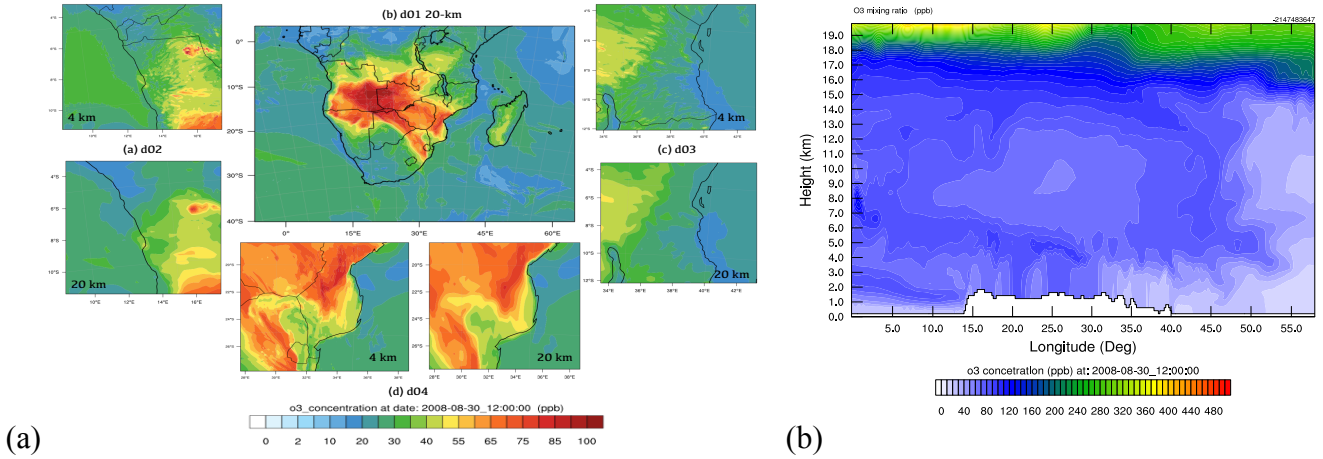

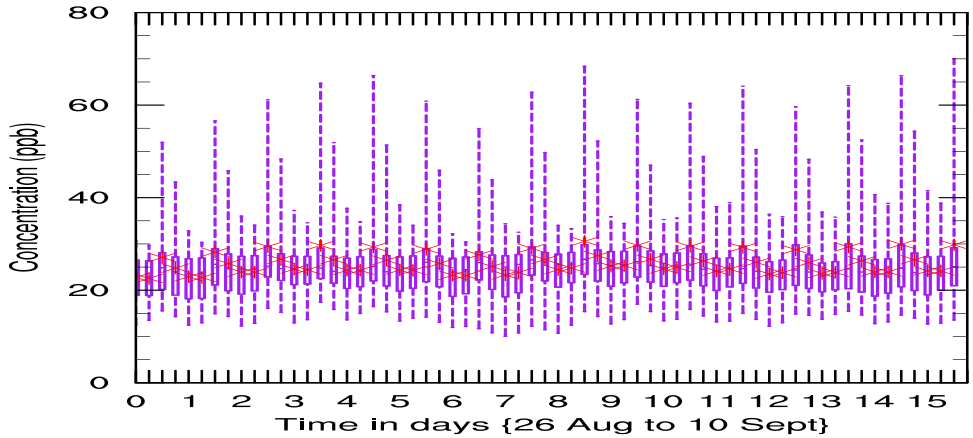

Fig. 4.9: (a) Ozone (O_3) concentrations over southern Africa, plotted at the surface. Concentrations for the sub-domains are plotted at high (4 km) and low (20km) resolutions respectively. Low-resolutions for the nests are plotted by extracting data from the parent grid (d01), considering only

sizes/locations for each grid. Model output at 1200 UTC 30 August 2008. (b) Vertical profile in the east-west direction, fixed at 10°S latitude, and (c) Domain averaged O_3 concentration, averaged over d01.

4.7 Aerosols

Next I present results on the aerosol prediction and cloud processes over southern Africa. I shall discuss effects on AQ and on cloud microphysical properties and dynamics due to aerosol concentrations in the next chapters. I begin this section by presenting primary emitted particulates before secondary particulates.

4.7.1 Primary particulate from biomass burning

Figure 4.10 shows BC aerosol concentration, depicting locations where aerosols are concentrated. The left panel (Fig. 4.10(a)) shows surface concentration whereas the right panel (Fig. 4.10(b)) is latitude–height profile, and the bottom panel (Fig. 4.10(c)) is a domain-averaged concentration. Again, isolated points of high concentrations indicate where BC is concentrated –mainly over Angola, Zambia, parts of Mozambique and eastern South Africa. As highlighted in Chapter 1, organic materials account for a large fraction of atmospheric aerosols; two major components being BC and organic carbon (OC). OC concentration is shown in the supplementary material in the appendix section (Fig. $B3_4$, Appendix B). Majority of primary mass is OC, which also follows a similar temporal and spatial distribution as BC. The distribution is almost similar to that of O_3, except that O_3 is more wide spread whereas BC and OC are isolated. Also, BC and OC are primary particulate products (and concentrated near the source) whereas O_3 is a secondary and gas species, thus O_3 can be transported further than particulates.

The vertical profile also shows that BC is concentrated to the west of the domain and confined within 7 km above the surface. In chapter 6, I investigate the contribution of these aerosols on cloud properties. This will look at how aerosols impact on the clouds. The average BC concentration (Fig. 4.10(c)) shows an increase in concentration between days 7 and 9 and on day 15. I shall also examine the pollution scenario during the study period, as well as contributions by different sources.

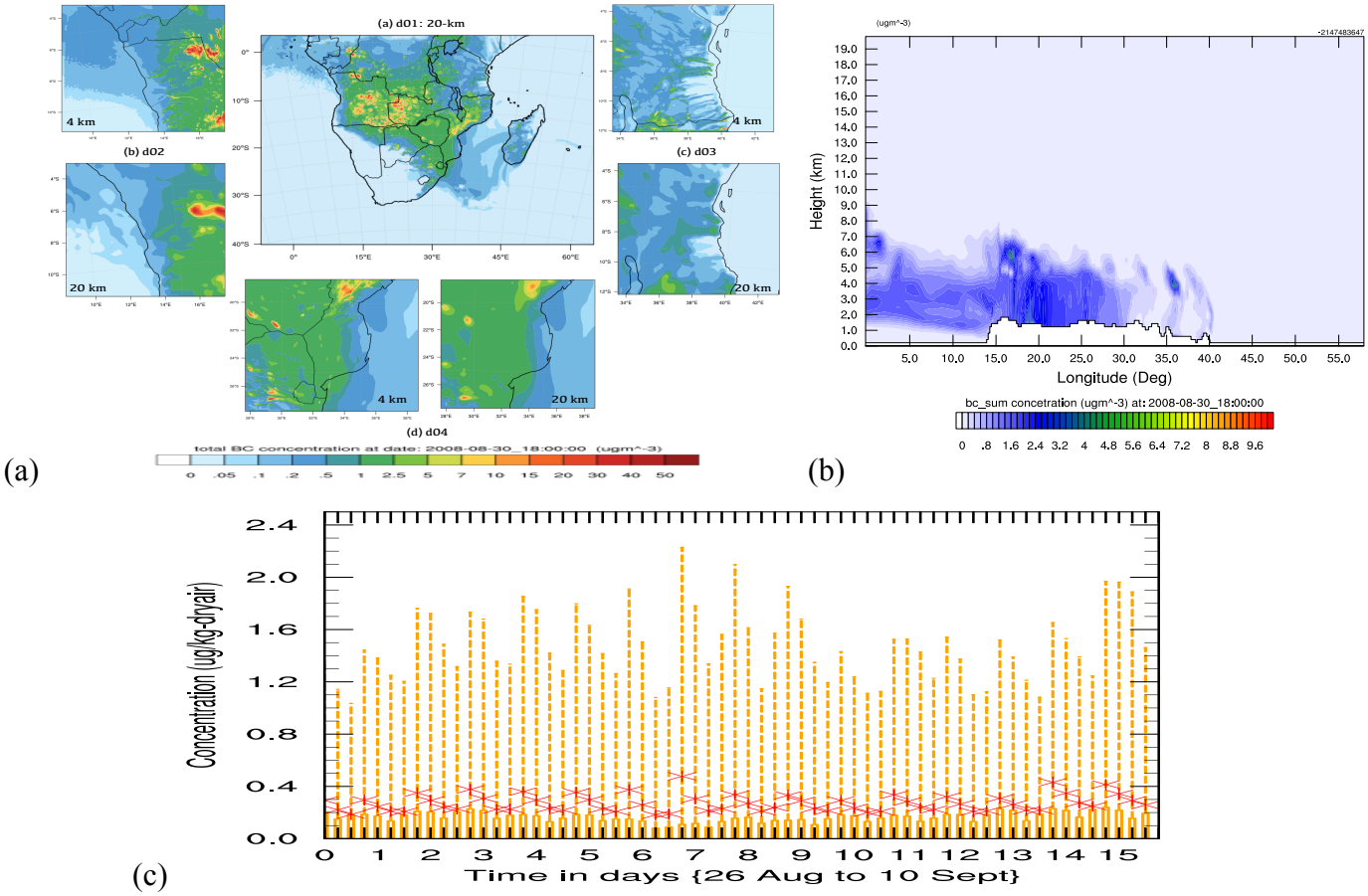

Fig. 4.10: Black carbon (BC) concentrations over southern Africa plotted at the surface. Low-resolutions for the nests are plotted the same way as highlighted above. Model output at 1800 UTC 30 August 2008. (b) Vertical profile for BC in the east-west direction, at 10°S latitude, and (c) Domain averaged BC concentration, averaged over d01.

4.7.2 Secondary aerosol production

After emission of primary pollutants into the atmosphere, secondary aerosols are formed from different chemical reactions/transformations of primary pollutants including gas-to-particle partitioning. The most significant formation of these aerosols depends on the concentration of precursor species (e.g. NO_x, NH_3 and SO_2) as well as meteorological conditions. Figure 4.11 shows sulphate (SO_4^{2-}) aerosol concentration; the top panels show concentrations at the surface and within vertical cross section along 10°S, whereas the panel below is domain-averaged concentration across d01.

There are some differences in spatial distributions of concentrations between the coarse and fine grids for all results presented here. The fine grids have higher concentrations and more isolated maxima of pollution variations than the coarse grid, even when plotted on the 20-km domain (e.g. Fig. 4.7, for CO). Although SO_4^{2-} can be lofted higher into the atmosphere and transported away, high concentrations are also confined within 5 km and to the west of the domain as shown in BC above. Although on average, the SO_4^{2-} concentration lies around 0.3 μg m^{-3}, there was a decline in the

concentration between days 6 and 7 (Fig. 4.11(c)). One difference between the primary and secondary pollutants noticed here is on their distribution patterns. Primary pollutants are locally distributed, with high concentrations near their points of emission whereas secondary pollutants tend to be more regionally distributed.

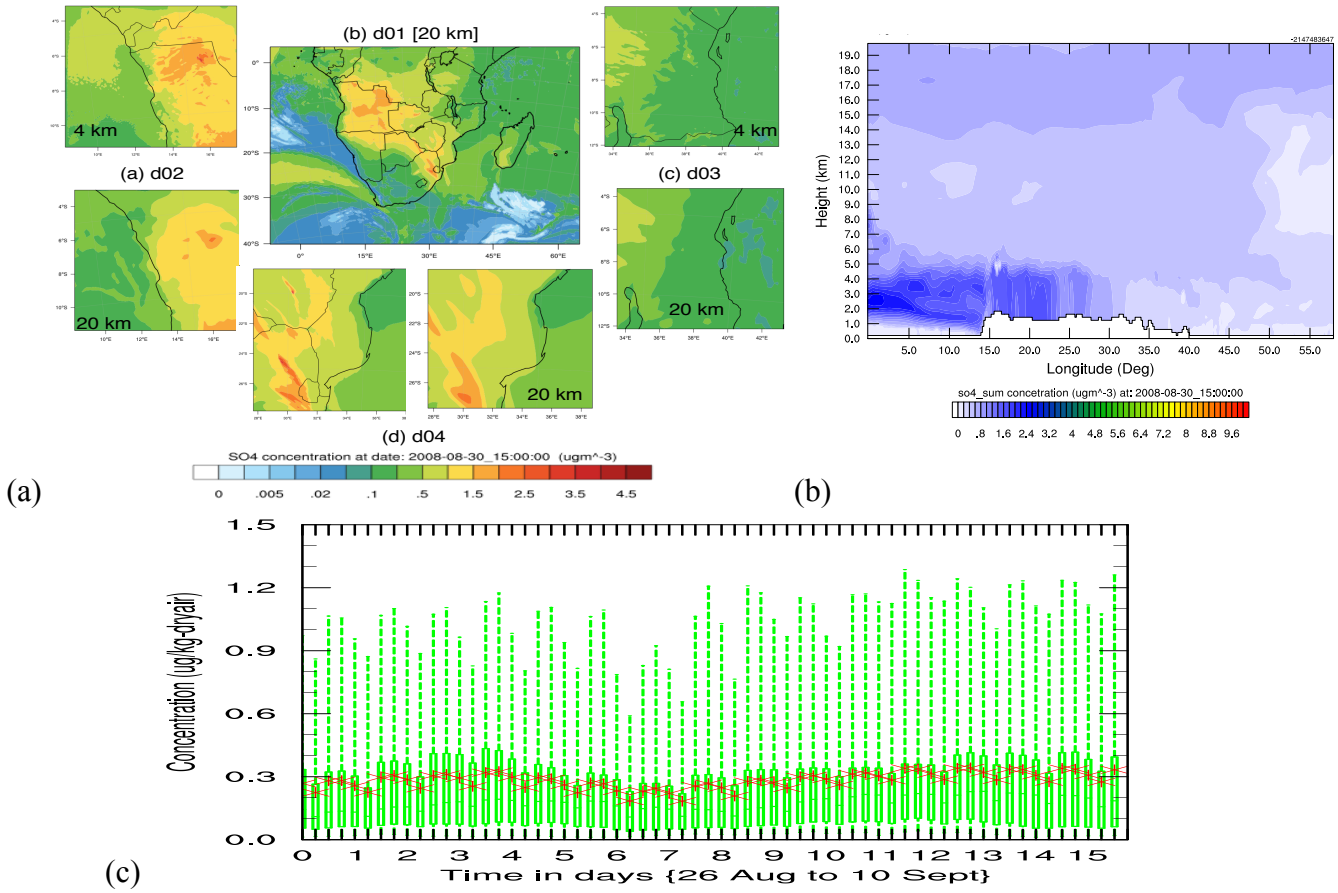

Fig. 4.11: Sulphate SO_4^{2-} concentrations over southern Africa, plotted at the surface. Low-resolutions for the nests are plotted the same way as highlighted above. Model output at 1500 UTC 30 August 2008. (b) Vertical profile for SO_4^{2-} in the east-west direction, at 10°S latitude and (c) Domain averaged SO_4^{2-} concentration, averaged over d01.

The vertical cross sections are plotted at a latitude where there are high concentrations of the pollutants (except for a small variation in NO, Fig. 4.8(b)). Box-and-whisker plots show temporal variation across the whole period, indicating where the distribution is centred (Figs. 4.7c, 4.8c, 4.9c, 4.10c and 4.11c). They show the interquartile range of the calculated statistics, with the median response (shown by the horizontal lines dividing the box), the 25th to 75th percentiles (shown by the box) and 5th and 95th percentiles (shown by the whiskers); the asterisk indicate the mean. In most species shown above, high aerosol concentrations are modelled over the central-southeast of the domain. The position and geographical pattern of the concentrations are characteristic of the evolved 'river of smoke' observed with MODIS instrument onboard the satellite described by Swap et al. (2003). As indicated in section 4.3, the transport pattern was almost sustained throughout the episode, demonstrating that the observed

river of smoke originated from the heartland of southern Africa. But at times, episodes of aerosol transportation occur between periods of otherwise 'clean conditions.' For example, both NASA satellite imagery (http://earthobservatory.nasa.gov/NaturalHazards/view.php?id=9060&eocn=image&eoci=morenh) and a Global Early Warning System for Wildland Fires (http://www.fire.uni-freiburg.de/gwfews/demos.html) indicate vast amount of smoke flowing from the fires over land. On other occasions, background levels of aerosols increase as the entire lower troposphere become laden with aerosols from various sources, including biogenic, dust, sea salt and industrial emissions.

4.7.3 Total particulate matter (PM)

Atmospheric particulate matter, which can be from natural or anthropogenic sources may be emitted by local or regional sources (Pey et al., 2008). Regional and local atmospheric processes play key role in the variability levels and composition of PM, especially in regions where local anthropogenic and natural emissions are considerably high (e.g. Highveld, tropical central- and southwest Africa). Figure 4.12 shows PM (PM_{10}) distribution (high concentrations [order of 1000 μg m^{-3} or more] predicted in the southwest) along the Kalahari–Namib Desert, dominated by dust aerosols. This suggests the presence of other pollutant sources and/or formation of secondary particulates. Meanwhile, high concentrations (over 300 μg m^{-3}) are still observed over Angola and further up northeast.

Average PM concentration during the simulation (Fig. 4.12(b)) was around 30 μg m^{-3}, with high concentrations simulated between days 31 August and 3 September 2008. The period of increase in PM concentration correlates with the time of high pollutant outflow into the southwest Indian Ocean from the mainland captured in the satellite described above, peaking on 1 September 2008. Although high PM_{10} concentrations appear to the southwest of the mainland, the smoke plume was confined mainly to the southeast.

The extremely high PM concentration in the region bounded by 30–40°S and 15–30°E raises a number of first-order questions about the contributing factors to the ambient aerosol loading. It clearly appears that, from the results shown and discussed above, BB is not the dominant source of PM concentration in the south. Considering other emissions in the model as discussed in section 4.4, neither biogenic nor sea salt may be possible causes of this high loading, implying that either anthropogenic or dust emissions are the primary sources. A large part of southwest southern Africa is a desert, from as far as Zambia through Namibia–Botswana and South Africa –the so-called Kalahari Transect (KT) (Shugart et al., 2004).

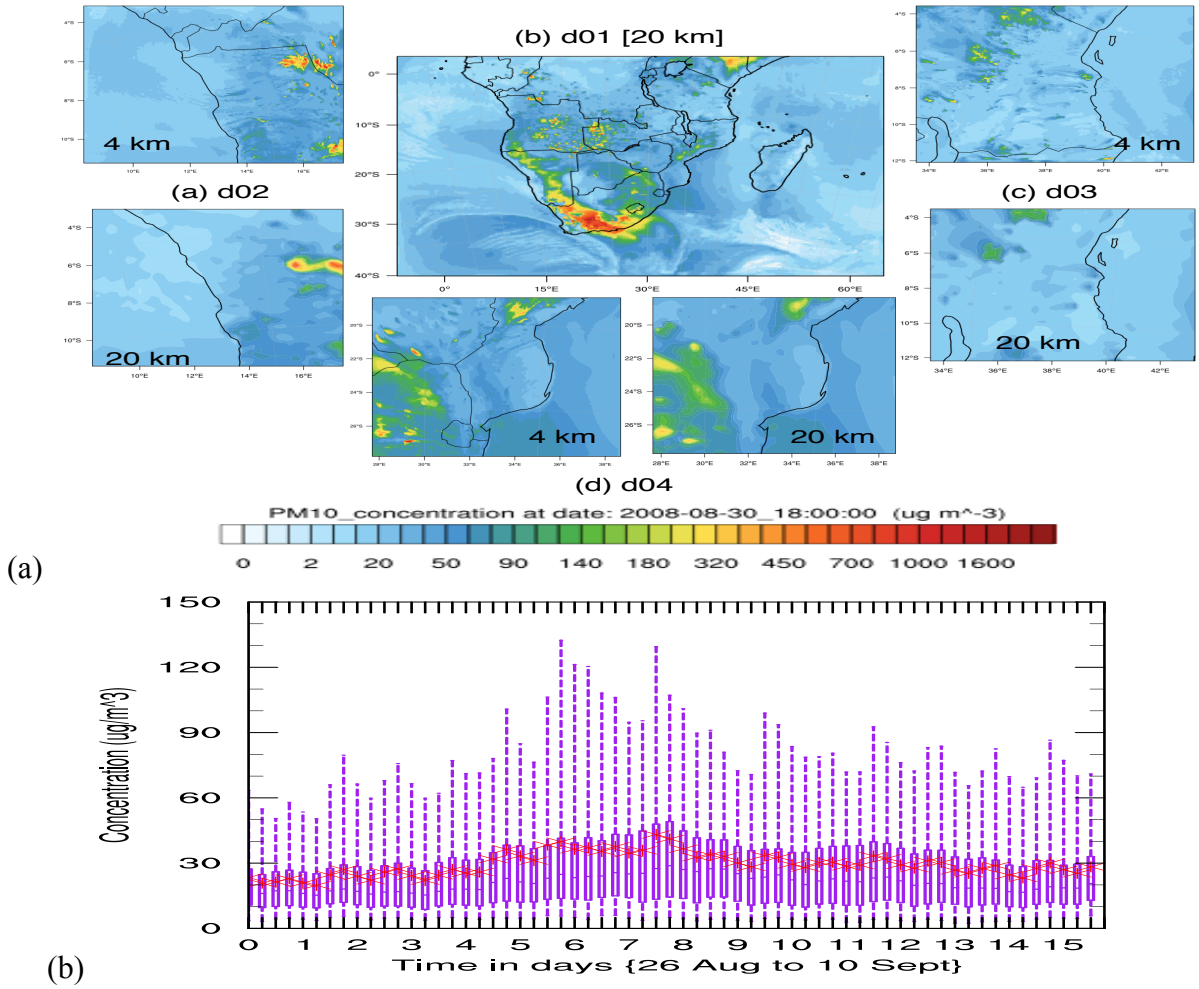

Fig. 4.12: Surface distributions of particulate matter (PM_{10}) concentration. Sub-domains are plotted at high resolution (4 km) and low resolution (20 km) respectively. Model output at 1800 UTC 30 August 2008. (b) Domain averaged PM_{10} concentration, averaged over d01.

Also, South Africa with its major industries and power generation (Piketh and Walton, 2004; Bigala, 2008) as well as its major urban areas, is by far the largest industrialized country in the region (Josipovic et al., 2009). Therefore, both dust and anthropogenic emissions would be expected to be higher in the southern part of the domain than farther north. The emissions budget in the model is closed by attributing the difference between PM_{10} and the sum of all other primary emitted aerosol components to other inorganics (OIN). OIN is the same species used for the transportation of dust aerosol in the model. It is therefore not possible to simply use OIN as a source tracer.

The first treatment would therefore lead to an attribution of a discrepancy in the primary particle mass emission budget from any source to the same species as dust. Although this might be the case, the grid cells with the highest concentrations of PM are not around the major cities in South Africa (e.g. Cape Town, Pretoria or Johannesburg). Inspection of the aerosol concentrations shows that PM concentration along the southwest coast coincides with OIN, which also lie along the Kalahari–Namib Desert. The main area with high OIN concentration is the area bounded by 20–25°E and 30–35°S. In

addition to the MOZART module boundary conditions providing dust, dust is generated online within the domain and hence folded into the emissions driving the model simulations. In order to investigate the cause of the elevated OIN concentration, a short model run was performed without dust emissions. Fig. 4.13 shows PM_{10} and OIN concentration at 1800 UTC 30 August 2008, plotted for the outer domain from the simulation with dust (Fig. 4.13(a) and (c)) and without dust (Fig. 4.14 (b) and (d)) emissions.

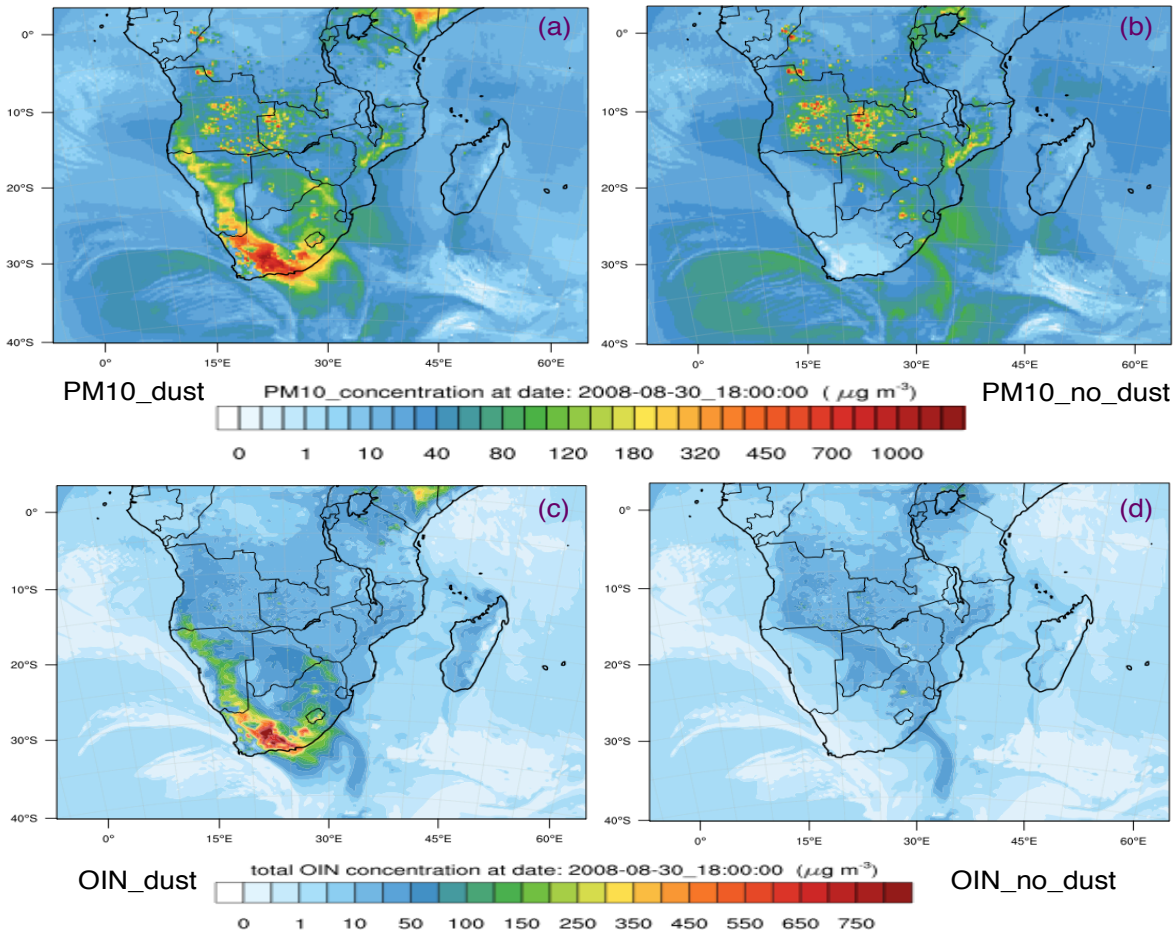

Fig. 4.13: Surface concentration for PM_{10} ((a) and (b)) and OIN ((c) and (d)). Left panels contain dust whereas the right panels have no dust. Model output at 1800 UTC 30 August 2008.

The high predicted PM concentration over South Africa mainly comes from dust emissions, hence the main source of OIN. There are mineral resources around this area (e.g. uranium deposits in the Karoo Uranium Province of the Western Cape and the Langer Henrich plant in Namibia). The two countries are among the top uranium-producing countries in the world (Schartz, 2008). However, fugitive emissions from the mining activities should be included in the anthropogenic emissions from EDGAR, despite there being minimal reported anthropogenic emissions from the region. There will be an element of the emissions implicated in the land-use category, such that uranium-mining emissions are subsumed into the online dust emission calculations. Although PM concentration is significantly lower in the simulation without dust (Fig. 4.14), there is little constraint from in-situ measurements of PM

loading to indicate which is more realistic. Further work should be conducted to investigate the changes in pollutants concentration and impact on AQ from both model simulations and in-situ measurements. AQ is the main focus in chapter 5 and the contribution from dust are briefly described in section 5.7.

4.7.4 Dust emissions and their parameterisation

Dust emissions are mechanically generated as a result of wind blowing over soil or sand devoid of vegetation. The loose particles can easily be blown away by the wind, sometimes resulting in dust storms, with the magnitude and particle-size distribution of the emissions being dependent on the wind speed. Other small particles can result from the disintegration of larger particles during collision. This section briefly describes the dust parameterisation.

Dust parameterisations are based on the soil type, emission source and threshold wind speed (Astitha et al., 2012). When the wind blows (a threshold of about 10 m s^{-1}) over the Earth surface, dust particles are injected into the atmosphere through saltation (Shao et al., 2011; Astitha et al., 2012, and references therein). Particle generation is initiated when the drag near the Earth surface exceeds the gravitational inertia of the sand particles and moves them downwind in horizontal motion. Direct emission of soil particles, referred to as aerodynamic entrainment (Shao et al., 2011), occurs when dust are lifted directly from the surface with free and abundant dust. Dust emissions can also be generated primarily from self-abrasion or disintegration of large soil fragments when they hit the hard surfaces (Shao et al., 2011).

WRF-Chem generates the dust online during the simulation. Dust emission data (e.g. erosion factor, clay fraction, sand fraction) is provided from the information produced by WPS. When compiling the WRF-Chem code and using WPS input data (with the setting in the *namelist.input* file), this adds the dust scheme (WRF-Chem user guide: http://ruc.noaa.gov/wrf/WG11/Users_guide.pdf). However, there are possible alternative dust schemes that can be used in WRF-Chem (such as the GOCART scheme (Zhao et al., 2013)). It is possible that the model overestimates these emissions leading to the high concentrations through dependencies in the online scheme. For example, in wetted areas, temperature and precipitation fields adjust the soil wetness and hence limiting dust production (Astitha et al., 2012). This thesis focuses on the BB contribution to aerosol behavior, but the dust contribution should be the focus of further work.

4.7.4.1 Contribution to aerosol optical properties

One important property for aerosols is their role in radiative forcing. Dust aerosols contribute to the global aerosol burden and play important role in the earth radiative budget and cloud microphysical properties (Zhao et al., 2013, and references therein). The high concentration observed in the model

simulations could make a substantial contribution to the aerosol optical depth (AOD), one of the foci in chapter 6. It is therefore important to determine the magnitude of the online dust emissions influence on AOD. Figure 4.14 shows spatial distribution of column integrated PM_{10} and $PM_{2.5}$ concentrations and AOD at 550 nm wavelength, plotted for the outer domain only.

Figure 4.14(a) shows PM_{10} and $PM_{2.5}$ with- and without dust, whereas Figure 4.14(b) shows AOD also plotted with dust (left panel) and without dust (right panel). A large amount of PM loading is simulated across the domain along a zone of high BB emissions and over the southern-most tip of the subcontinent. $PM_{2.5}$ shows more spatial distribution and hot spots of high PM concentrations. The diagonal AOD concentration gradient coincides with more PM loading mainly along the BB-dominated region, and areas downwind pollution where BBAs are advected. There is still substantial contribution to AOD from dust emissions as shown in the bottom left panel, but not as high as for BB-dominated areas. PM loading also affects remote areas downwind such as over the top right part of the domain. The dust appear to make a minor contribution to AOD compared to BBAs; this could be attributed to particle size distribution (dust particles are coarser than BBAs), because even where PM is highest, AOD is low but higher over BB-dominated regions. On the other hand, fire emissions can be generated in large quantities and can be lofted higher due to buoyancy so would make a significant contribution than dust emissions. This will be discussed again in chapter 6, focusing on ACIs. A further check on this could also be to plot particle size distribution from each bin to determine from which size bins do dust compare with AOD. Chapter 6 shall also discuss the contribution of aerosol concentration to AOD in different parts of the domain. Further analysis will also be done to compare the model simulated AOD with measurements where available, over southern Africa.

Next I discuss cloud properties and the relationships with aerosols. Here, I focus on the model predictions of cloud condensation nuclei (CCN) particles and cloud droplet number concentration (CDNC). See chapters 1 and 2 for further details on aerosol activation, supersaturation and cloud formation. I shall also discuss in the next chapters, ACIs and their influence on the regional pollution in more details, quantifying the contributions due to different emission sources.

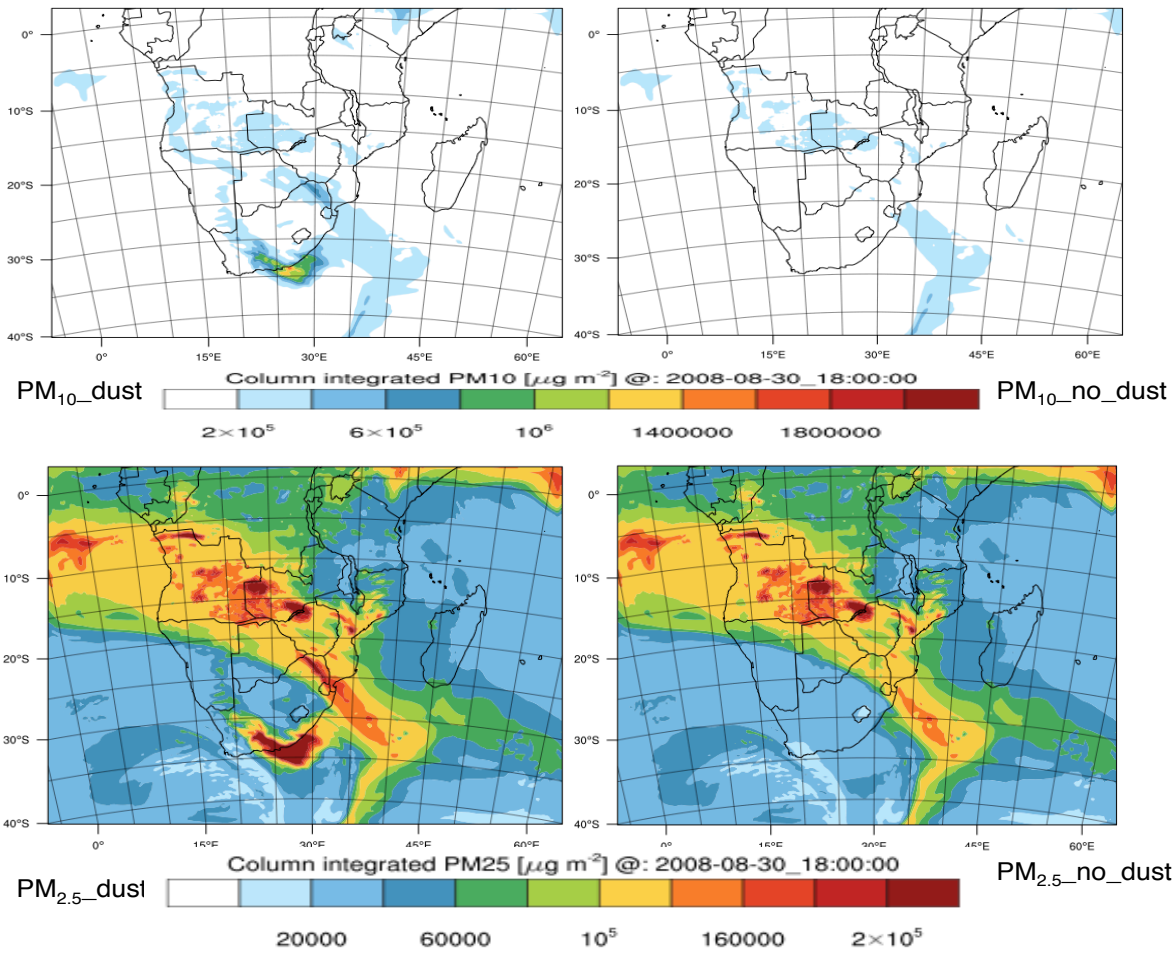

(a) Column integrated PM (PM_{10} –top two panels and $PM_{2.5}$ –bottom two panels).

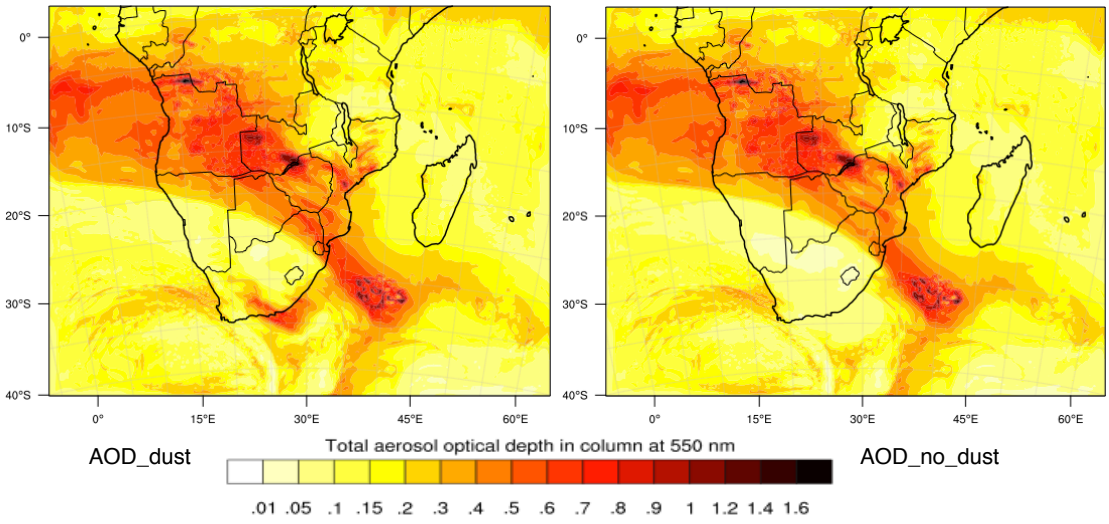

(b) Aerosol optical depth (AOD)

Fig. 4.14: Spatial distribution of PM (a) and AOD (b). Left panels with dust whereas right panels do not have dust. Model output at 1800 UTC 30 August 2008.

4.8 Cloud condensation nuclei (CCN)

Aerosols (particularly water-soluble or those containing water-soluble components) serve as sites upon which water vapour condenses to form clouds. Under suitable conditions, water vapour condenses on

these particles (known as CCN) that nucleate into cloud droplets (Gong et al., 2011). Aerosol activation is a key process in ACI controlling CDNC and has direct implication on cloud microphysical properties and precipitation formation. As highlighted in chapter 3, WRF-Chem carries 6 CCN spectra at different supersaturations corresponding to CCN1, CCN2, CCN3, CCN4, CCN5 and CCN6 respectively. In this section I show (Fig. 4.15) only two variables, CCN2 and CCN6. These are calculated and plotted at layers below cloud base in the grid cells, only where there are clouds. Figure 4.16 shows average CCN concentrations for the entire simulation for all 6 CCN variables.

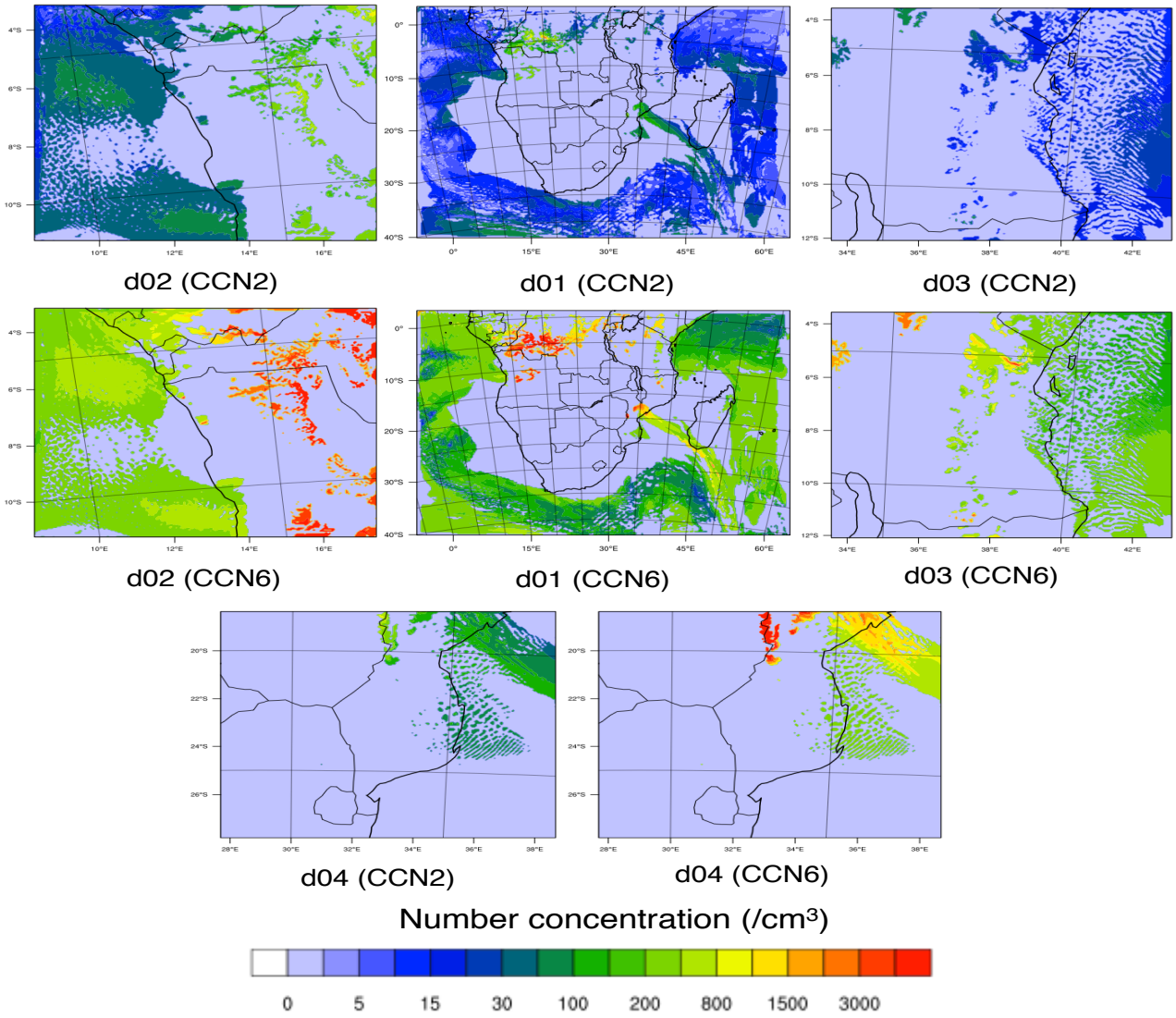

Fig. 4.15: CCN number concentrations at the layer below cloudbase, plotted only where there are clouds in the grid cell. Model output at 1800 UTC 1 September 2008.

Although a small area of the landmass has CCN than over the oceans, high concentrations are observed over northern Angola, western DRC and central Mozambique/eastern Zimbabwe. For example CCN6 concentration over these locations is of the order 3000 cm^{-3}. These results indicate that processes are better resolved at fine grid spacing (4-km), than at a coarser scale (20-km). On the other

hand, it is clear that as supersaturation increases, more particles become activated, as shown in the box-and-whisker plots (Fig. 4.16), for average CCN concentrations. For example, at CCN1 (0.02% supersaturation), the average concentration is about 30 cm^{-3}, whereas at CCN6 (1% supersaturation), the average concentration can be as high as 1000 cm^{-3}.

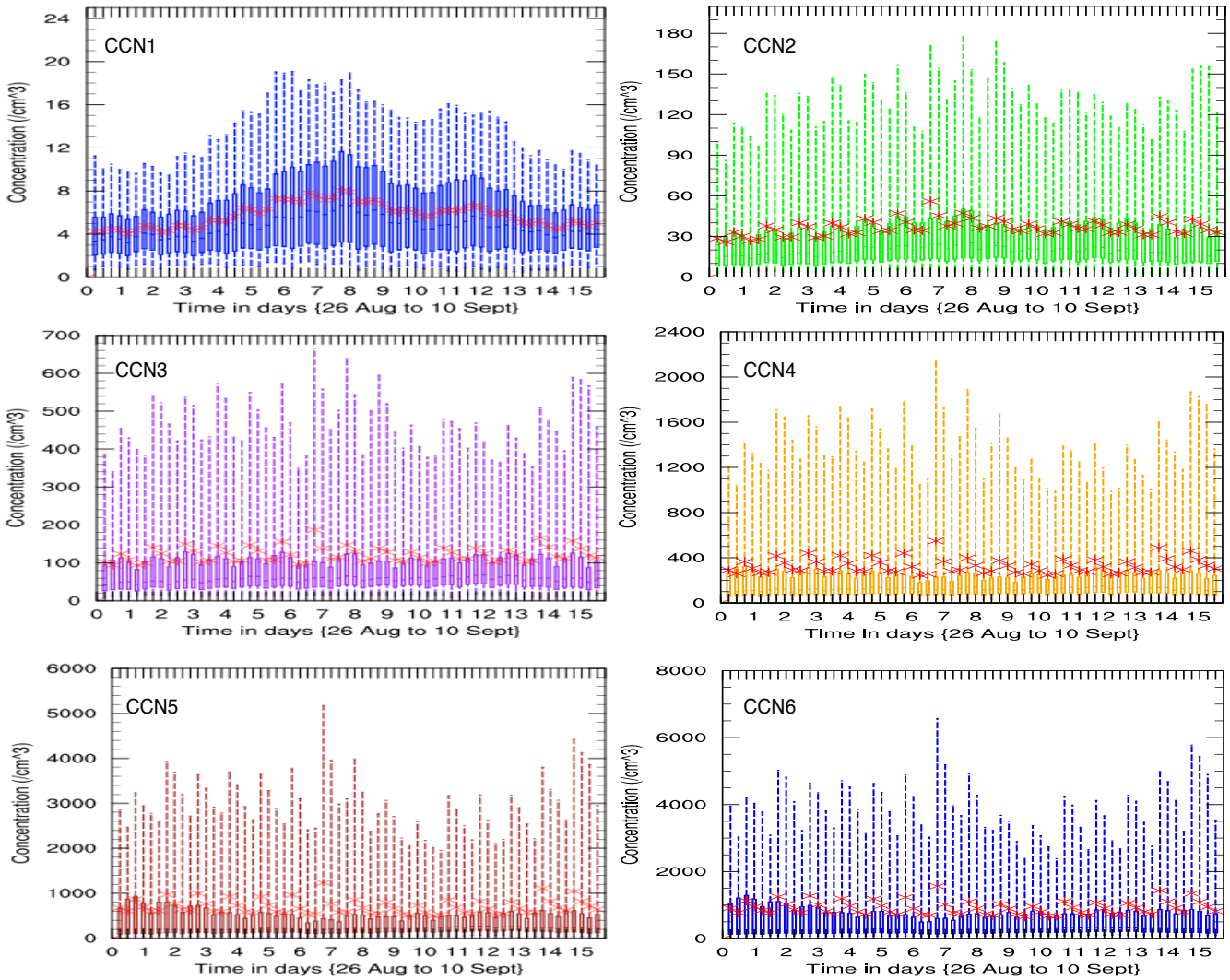

Fig. 4.16: CCN average number concentration. Domain-averaged CCN over d01 for the entire simulation.

4.9 Clouds and supersaturation

Cloud condensation nuclei number is key to CDNC and a key parameter dependent upon particle size, composition and ambient conditions. However, the number and proportion of cloud droplets is a function of concentration and size of CCN particles partaking in cloud formation. The aim of this section is to demonstrate the variability of modelled CDNC due to different aerosols over southern Africa. Detailed analysis will be presented in the next chapters.

Figure 4.17 shows modelled maximum CDNC (Nd_{max}) and effective supersaturation S_{eff} for different domain resolutions. Similarly, high droplet concentrations are observed in the tropics where high CCN

concentration (Fig. 4.15) is predicted. As expected, there are more clouds over the ocean than over the landmass, but high CDNC (order of 2000 cm^{-3}) are observed over land. A band of cloud projects from the southeast into the southwest Indian Ocean via Madagascar. This is along the exit corridor through which pollution often advect into the marine environment (see section 4.2), associated with the so-called "river of smoke." A notable observation in Fig. 4.17 also show that at a low resolution, cellular clouds are correlated with high supersaturation, whereas at high resolution, clouds become more cellular, correlated with low supersaturations. This indicates that changes in clouds driven by aerosols are not simply a function of the aerosol loading itself, but could also be due to environmental and other feedback processes that amplify the initial response.

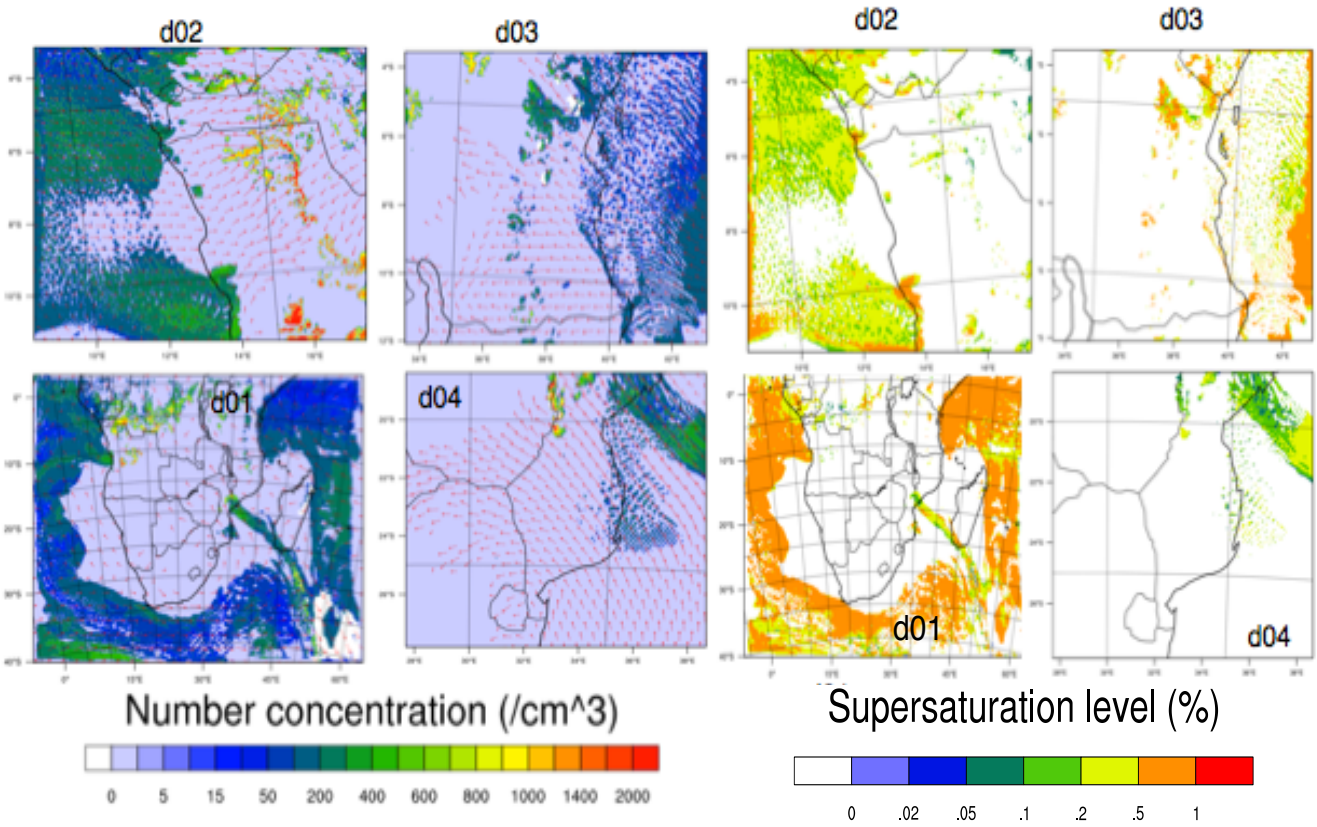

Fig. 4.17: Model predictions for maximum cloud droplet number (Nd_{max}) and effective supersaturation S_{eff}, plotted only where there are clouds in the grid cell. S_{eff} is determined above where CCN concentration is diagnosed. Model output at 1800 UTC 1 September 2008.

Over the oceans, cloud responses are dominated by increase in cloud cover, whereas over land they are dominated by reductions in water content. Low cloud cover over land is very minimal (not shown) where clouds are probably cumuliform, extending to higher levels compared to marine clouds. The analysis (in the next chapters) will examine cases for cloud changes (e.g. due to aerosol concentration and/or model resolution, focusing on regions where most of the oceanic regions aerosols overlay clouds such as western Angola–DRC boarder with the southeast Atlantic.

4.10 Cloud types in southern Africa

To facilitate interpretation of results, I also highlight on some common cloud types and properties over southern Africa. The reason behind this is to identify the cloud field as homogeneous or dominant over the study domain as possible. While the homogeneity of cloud field is the main criterion for the characterization, clouds still succumb to natural variation of their micro- and macro structural characteristics. However, it is understood that clouds adjustments to aerosol perturbations depend on aerosol properties (Sorooshian et al., 2009). Their influence on the radiative balance for example, depends on their occurrence and microphysical properties related to radiative behavior; changes in greenhouse gases, aerosols, large-scale circulations and/or thermodynamic structure of the atmosphere (Diaz et al., 2015, and references therein). Meanwhile, this chapter does not discuss effects of radiative effects.

Diaz et al. (2015) used WRF to represent cloud cover over Africa and their effects on precipitation and radiation. They outline different generations of different cloud types; from deep convective (associated with the intertropical convergence zone [ITCZ]) to marine stratocumulus formed off the coast of Namibia (Klein and Hartman, 1993). Stratus clouds are often observed over southern Africa, especially near oceanic areas. These are the most common of the three main stratiform clouds characterised by large spatial coverage with distinctly organized patterns (Klein and Hartmann, 1993). Other studies (e.g. Skaeda et al., 2011) also indicate that during intense burning over southern Africa, emission layers advect westwards into the southwest Atlantic, where they overlay vast decks of stratocumulus clouds. From our model predictions, three common types are identified: marine stratus, convective and layered clouds. Meanwhile, we do not explore cloud dynamics and characteristic evolution in this chapter.

Tropical central Africa is the global third most extensive region of deep convection after the west Pacific warm pool and Amazonia. Over the Indian Ocean, common clouds appear to be related to thick convective clouds. Depending on their chemical composition and sizes, aerosol effects contribute to convective processes. For example, in some areas, they can lead to cells with more precipitation, whilst other cells can be less intense with less precipitation (Ntelekos et al., 2009). In the simulation with 20-km grid spacing, precipitation was generated mostly by cumulus parameterisation resulting in less reliable prediction of rain and convective mass fluxes. However, with 4-km grid spacing, the processes are more resolved (see Appendix B), hence more predicted processes across a larger area.

4.11 Summary

Owing to different major sources of aerosols and trace gases, southern Africa has experienced a considerable change in recent years and has been recognized as a major source of aerosols in the

southern hemisphere. In addition, shifting populations, land use change and agricultural practices as well as industrial developments, the regional aerosol composition and loading have changed in nature and quantity (Billmark et al., 2003, and references therein). In this chapter, we characterized the regional atmosphere based on the WRF-Chem simulation during a biomass-burning episode in the dry season of 2008. The simulation was performed on a quad nesting to assess the extent to which microphysical data (in the sub-domain) compares with the coarse domain, and how consistent are they with each other. Different emissions (natural and anthropogenic) have been discussed and how they are represented in WRF-Chem. Also considered are meteorological conditions and chemical dynamics in different locations of the domain. In reality, southern Africa has a vast emission content that not only include BB and anthropogenic activities, but also biofuels, trash burning, sea salt, dust and biogenic VOCs. The variability of the simulated aerosols increase with resolution and distribution is resolved better at high-resolutions.

While anthropogenic emissions are clustered over the domain and vary throughout the year, BB emissions are concentrated in the tropics, limited to the dry season (May–August). BB generates large quantities of aerosols that can be lofted to higher altitudes and advected over the southeastern Atlantic where they overlay low-level clouds. During periods when anticyclonic conditions prevail, aerosols are transported over the sub-continent and aerosol concentrations increase in areas initially not in the vicinity of such pollutants. On the other hand, the southeast region is subject to the outflow of pollution from the mainland carrying pollutants into the southwest Indian Ocean. Our results lead us to hypothesize that increase in BB aerosols play a major role in the regional pollution and could limit the horizontal extent of the ITCZ in driving the magnitude of convective processes in the northern hemisphere. Detailed analysis of the sub-grid domains (high resolution) will be done in the succeeding chapters. We shall investigate effects of BB emissions over the domain, with respect to other emission sources; the main objective being to assess how different emission sources contribute to- and/or influence regional pollution, and how changes in aerosol concentration affect cloud microphysical processes.

Chapter 5

Contributions of different emissions and influences on regional pollution

5.1 Introduction

In the past, much emphasis has been placed on industrial activities in the Northern Hemisphere with the assumption that there is less contribution from the Southern Hemisphere to global pollution. However, the understanding has changed nowadays since air pollution has become an important concern both regionally and globally. The Southern Hemisphere –particularly the subcontinent of Africa is strongly affected by sources of aerosol and trace gases from biomass burning (Magi et al., 2009, and references therein), biogenic and industrial processes (Piketh et al., 2002). For example, South Africa alone (considered the largest industrial hub in Africa) is responsible for major subequatorial electrical energy from the coal-powered stations (Tesfaye et al., 2013). Various natural and anthropogenic sources burden the regional atmosphere with all types of aerosol and trace gas pollutants. While some pollutants are continuous throughout the year, some are seasonal and/or dominate in certain regions. For example, biomass burning (BB) is common during the dry season and more prevalent in tropical central Africa. Smoke plumes from BB generally spreads downwind thousand of kilometres away from the fire areas impacting on air quality (AQ), human health and regional climate. In the context of air pollution, in which southern Africa appears quite vulnerable due to arid conditions and increasing pollution levels, it is therefore crucial that the knowledge concerning the mechanisms linking the chemical dynamics, flow regimes and existing pollution sources be improved in order to provide insight into future trends at the regional scale.

BB is a recurring problem in southern Africa with direct impact on the AQ and can have a deleterious effect on human heath. Whilst some BB studies have been done in the past focusing on physical, chemical and thermodynamical properties of BB (for example, the SAFARI campaign (Swap et al., 2002; 2003)), modelling simulations of interaction between weather and pollution still remain limited, as well as information on the contribution of different sources to the regional pollution. There is relatively less research on the regional AQ and pollution impact, despite the existence of high pollution conditions, in some cases humans exposed to pollutants exceeding the set standards. This chapter follows from the characterization of the regional pollution in the previous chapter. We extend this assessment to investigate the contributions of different emission sources and changes in aerosol and trace gas emissions over southern Africa. The main focus is to understand the contribution of different emission sources and their influence on the regional pollution. The investigation is carried out to critically evaluate such pollutants that are major regulated species e.g. nitrogen- and sulphur oxides

(NO_x + SO_x), ozone (O_3), carbon monoxide (CO) and particulate matter (PM). Atmospheric circulation systems responsible for pollution transport are also discussed and transport pathways through which pollutants are transported over and away from the domain. The chapter also gives a quantitative analysis of BB to the regional pollution and a comparison of the model perfomance against measurements. The analysis is conducted through the hypotheses formulated to probe the contribution due to BB emissions over southern Africa.

5.2 Attribution of different sources

As shown in the previous chapter, there is a limited distribution of some emissions in other parts of the subcontinent. Different pollutants are concentrated in some parts of the domain, depending on the emission sources, land use and/or meteorology. For example, fire distribution correlates with biome density (Swap et al., 2003) in areas with good rainfall –fostering vegetative growth (Fig. 5.1), compared to anthropogenic that follow human settlements, industrial or urban locations, including marine operations. The strength of vegetation varies in space and time, with species sensitive to the onset and intensity of the rainy season. This suggests a potential for different atmospheric chemical outcomes, depending on when and where emissions take place (Swap et al., 2003). Although central-west southern Africa experiences more BB, the sparse Namibian vegetation does not support a lot of BB (Swap et al., 2003, and references therein).

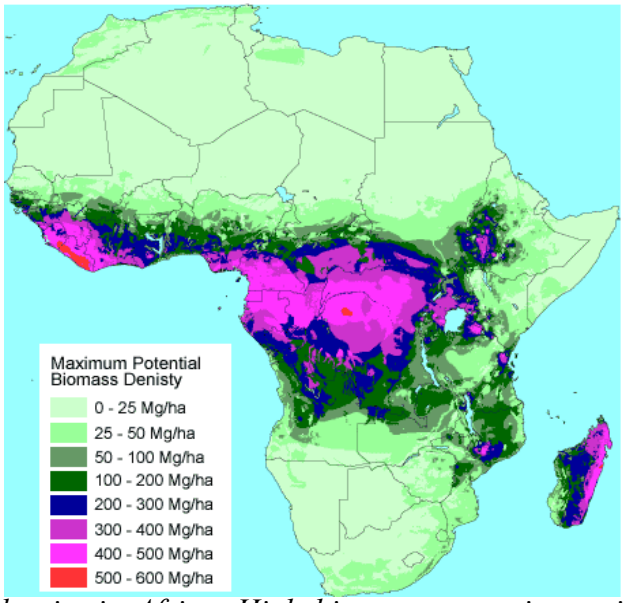

Fig. 5.1: Potential biome density in Africa. High biome appears in tropical central region, where burning is prevalent. (Brown and Gaston, 1996).

BB is a highly seasonal activity over southern Africa (Piketh et al., 2002, and references therein), consistently accounting for 25% of the total global fires annually (Magi, 2009, and references therein). Widespread burning events occur mainly over Angola, Zambia and Democratic Republic of Congo

(DRC) (Wai et al., 2014). In the case of dust aerosols, these are thought to originate from the local soil over surfaces deficient or devoid in vegetation, with higher concentrations in summer (Piketh et al., 2002) related to agricultural activities. Although sea salt is estimated to be the second most abundant global source of aerosols (Blanchard, 1983; Gong et al., 1997a), they are erratic and highly varying aerosols from time to time. They are very common and abundant over southern Africa, along the coastal areas, although typical sea salt particles have been found in some countries over land (e.g. Chimidza and Moloi, 2001). Due to a growing population in Africa and increasing land use demand, the role of BB in atmospheric chemistry, climate and terrestrial ecology is becoming increasingly important. To assess the contribution and influence of BB to the regional pollution, I propose the hypotheses to test (section 5.6). First, I show from the model simulation, pollutant concentrations with respect to different source emissions and discuss source contributions and possible influences on the regional pollution. Below are the hypotheses I propose to test from the simulation:

1. Biomass burning contribution to southern African pollution makes a considerable impact on the air quality to population centers in close-proximity to burning areas. The percentage pollution enhancement is higher in urban locations and active burning areas.

2. Model grid-scale affects the prediction of pollutants; there is a significant reduction in enhancement in pollution concentration in the simulation with BB emissions at lower resolution.

5.3 Transport and distribution of pollutants

This section briefly highlights on the flow patterns controlling the transport and dispersion of pollution over southern Africa. The section focuses on the transport of chemical emissions during the simulation period as predicted in the model. The weather patterns are described in chapter 4. Detailed discussions on the seasonality and inter-annual variability of weather conditions and mean atmospheric circulations is also given by Tyson et al. (1996a,b), Garstang et al. (1996), Freiman and Tyson (2000), Swap et al. (2002; 2003) and Stein et al. (2003). As highlighted in the previous chapter, the sub-continent was influenced by prevailing westerly winds (from the Atlantic) in the subtropics for most of the time, including easterly and northerly winds from the east. These winds provided characteristic flow patterns over the subcontinent, which played important roles in carrying/transporting pollution across the domain, most notably in the southeast, where pollution was channeled along the westerly direction into the marine environment. Similarly, a significant amount of clouds in tropical southeast Atlantic are said to favour pollution transport from the nearby fires into the marine environment. The circulation types in these regions promote direct streaming of pollution across the landmass from the emitting sources into the marine environment. On the other hand, concentration gradient of pollution also depends on the emission flux, chemical reactions as well as particle sizes. Early into the

simulation, pollution was higher in the tropics and lower in the subtropics. An increase in the southeast towards the end of the simulation indicates that the subtropics were affected by tropical burning emissions transported by the frontal systems. While BB is a major source of pollutants over southern Africa during the dry season, some locations tend to be not affected by BB emissions. We shall discuss this in section 5.7.

5.4 Addressing the hypotheses and model simulation

In order to address the hypotheses above, I performed a sensitivity test (in addition to the simulation described in the previous chapter) so as to evaluate the perturbation due to changes in aerosol concentration. For this, I chose to investigate the changes due to BB by switching off BB emission category in the model. I choose these modelling experiments (section 5.5) to focus specifically on changes due to BB since it is the only source controlled in the simulations. Whilst it's important to note that setting an emission source affects the lifetime of other trace species in the troposphere, the approach would nevertheless provide a relatively uncomplicated method to assess the potential impact on different emission types (Aghedo et al., 2007). The method also has the advantage that the combined effect of different species (e.g. CO, NO_x) from the same category can be assessed.

5.5 Model approach

This section describes the simulations performed in this investigation. A full emissions simulation conducted with a quad nesting as described in Chapter 4, consisting of all emission data is used as a base (CNTRL) case. A second sensitivity (TEST) simulation was conducted without BB emissions for a selected period and used as a perturbation case. While the CNTRL was conducted for the entire simulation period (23 August–10 September 2008), the TEST case was conducted only for the second half of the CNTRL period during which there was an increase in aerosol concentration. In this case I use the period 5–10 September to focus on. Both simulations employ the same meteorology to remove the effects of meteorological variability. Effects of changes in emissions are analysed both in terms of spatial distributions and as regionally averaged reduction totals, which are then compared to probe the roles played by BB emissions in influencing regional pollution over southern Africa.

5.6 Results and discussion

I adopt the same procedure used in the previous chapters for the analysis. The first part presents pollution trends and spatial distribution of pollutants predicted from the simulation, starting with primary pollutants (both gases and aerosols) then secondary pollutants, including photochemical species. Next, effects of the changes in different emissions or precursors are analysed and results compared for the simulations (in the perturbation case) to assess the resulting contributions. Lastly, I

examine the hypotheses presented above and discuss the model predictions against measurements, where available. For comparison between the two cases, I focus mainly on the period 5–10 September 2008, considering all model domains.

5.6.1 Primary pollution

5.6.1.1 Primary gases

The period between 5 and 9 September had peak in aerosol and gas concentration over much of the subcontinent as shown in the previous chapter (temporal variations). Peak concentrations for most pollutants occur in the afternoons (coinciding with ignition time of the fires over land). However, concentrations peaking in the mornings indicate such cases where anthropogenic or other emission sources dominate emissions. Figs. 5.2 and 5.3 show primary gas concentrations for carbon monoxide (CO) and nitrogen dioxide (NO_2). The left panels in each pair of the model grid represent the CNTRL whilst the right panels represent the TEST cases respectively. The time series shows daily average of CO for the fine grid averaged to 20 km (CNTRL–TEST: red curves), averaged at 4 km (CNTRL–TEST: blue curves) as well as difference between the coarsened and fine grid average for the CNTRL and TEST (green and purple curves) respectively. This set up is the same for all the figures in this section, aiming to examine whether (and for which model diagnostics) there are any systematic resolution-dependent differences between predictions. I shall focus on domain 2, and highlight on other domains in the discussion (see chapter 3 for grid locations). Spatial distributions and concentrations indicate areas impacted by pollution, also showing how the dynamics change when BB is excluded from the simulation at high resolution (Fig. 5.2 ((a) and (b)). Concentrations change substantially with BB emissions –clearly showing that pollution in these areas (e.g. Angola, DRC, Zambia and Tanzania) is heavily BB-influenced.

Figure 5.2 ((c) and (d)) show the difference in average CO concentration between the same domain at a coarser (20 km) and fine grid averaged to 20 km, with- and without BB (left and right panels) respectively, plotted at the same time as the top panels. Similarly, Fig. 5.3 shows same output for NO_2 as CO; panels on the left represent CNTRL whereas right panels represent TEST. There are significant reductions in species concentrations (e.g. over 2000 ppb in CO and 150 ppb in NO_2) when BB is excluded. Much of this comes from BB. On the other hand, other regions (e.g. subtropics –not shown) tend to be less affected by BB since the magnitude of concentration changes do not vary greatly.

Whilst the average concentrations in both CO and NO_2 do not change much between resolutions, concentrations change across the domains as noticed in areas with high concentrations. NO_x are key species in atmospheric chemistry heavily influenced by anthropogenic emissions. As observed for the subtropics, the relatively minor differences suggest that other parts of the domain (e.g. d04) are less

influenced by local BB sources. The distributions in pollutant concentrations maintained a similar pattern for a couple of days, with concentration gradients decreasing from the north to the south during the course of the simulation. Meanwhile, the west part of the mainland also experienced some concentration changes as some pollutants were advected into the marine environment from the nearby land areas. Plots 5.2 to 5.8 show the differences on results on 6 September for consistency.

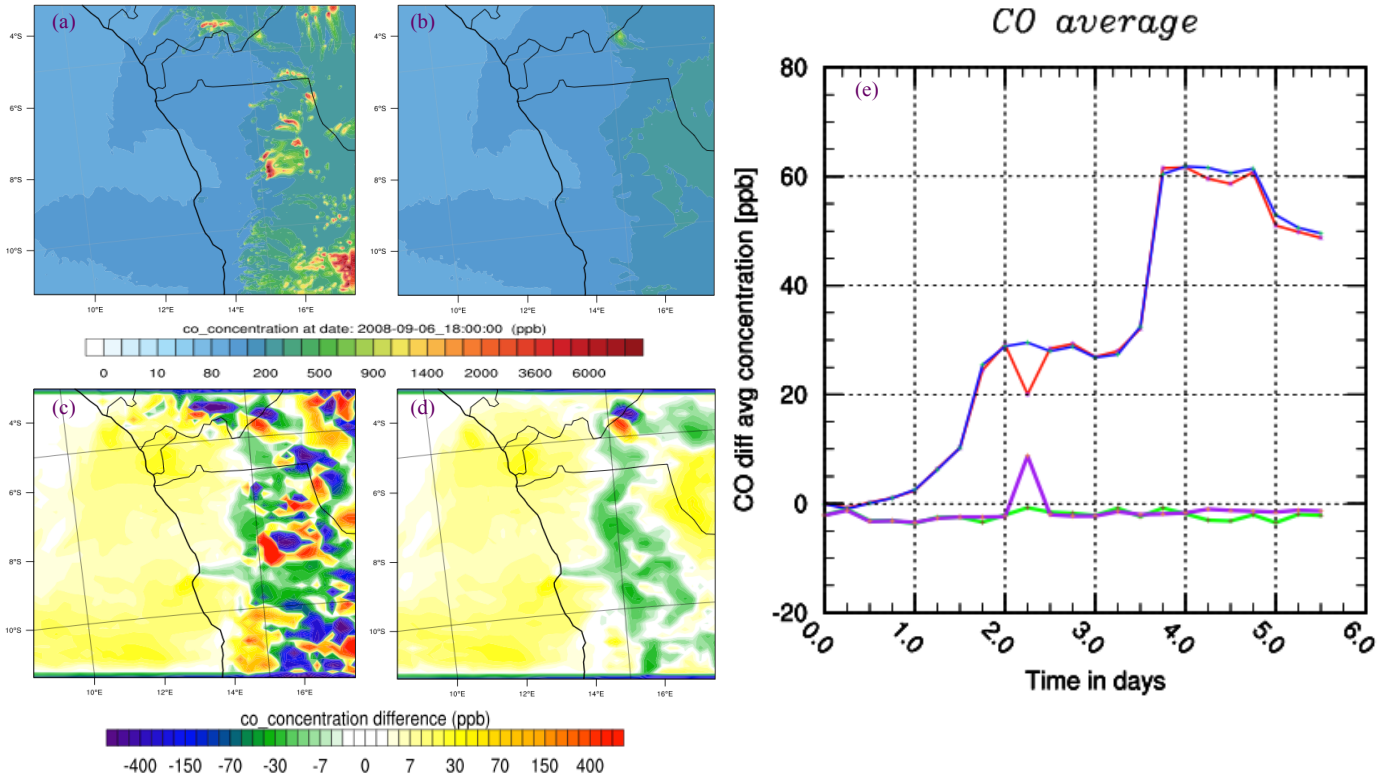

Fig. 5.2: Carbon monoxide (CO). Panel (a) shows surface CO concentration at 18:00 UTC 6 September 2008 at 4 km grid spacing, including BB emissions; (b) shows the same grid without BB emissions. Panel (c) shows the difference between the concentrations simulated at 4 km and 20 km spacing ($[CO]_{coarse} - [CO]_{fine}$) when the fine resolution simulation is degraded to the coarse resolution for the CNTRL simulation and panel (d) is same as (c), but for the TEST case. The right hand panel shows the time series of the differences in average concentrations between the fine and coarse simulations for both cases. Blue line represent $(CNTRL–TEST)_{fine}$; red line represent $CNTRL–TEST)_{coarse}$; purple represent $CNTRL_{coarse} – CNTRL_{fine}$ and green line represent $(TEST_{coarse} – TEST_{fine})$.

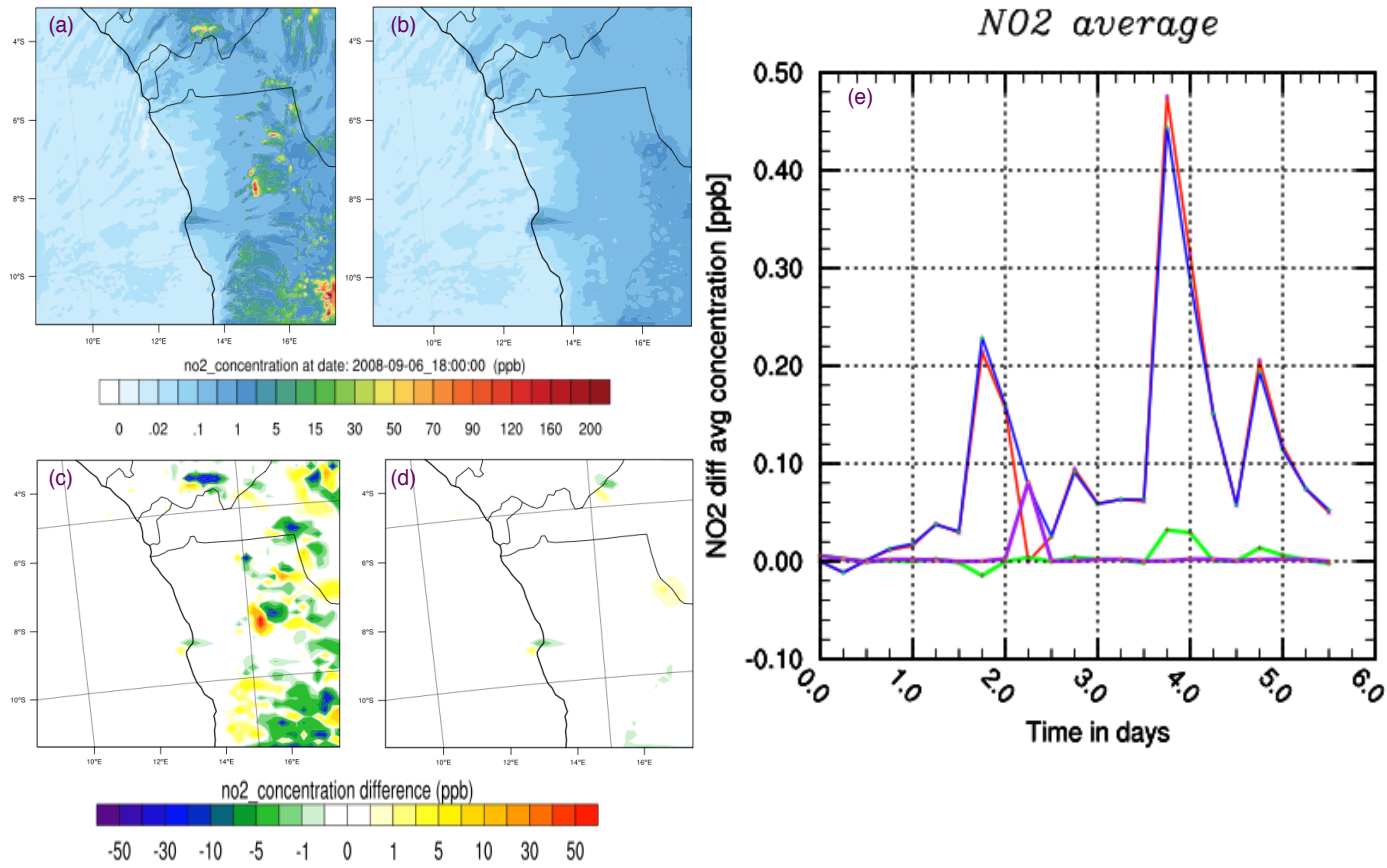

Fig. 5.3: Nitrogen dioxide (NO_2). Panel (a) shows surface NO_2 concentration at 18:00 UTC 6 September 2008 at 4 km grid spacing, including BB emissions; (b) shows the same grid without BB emissions. Panel (c) shows the difference between the concentrations simulated at 4 km and 20 km spacing ($[NO_2]_{coarse} - [NO_2]_{fine}$) when the fine resolution simulation is degraded to the coarse resolution for the CNTRL simulation and panel (d) is same as (c), but for the TEST case. The right hand panel shows the time series of the differences in average concentrations between the fine and coarse simulations for both cases. Blue line represent $(CNTRL - TEST)_{fine}$; red line represent $CNTRL - TEST)_{coarse}$; purple represent $CNTRL_{coarse} - CNTRL_{fine}$ and green line represent $(TEST_{coarse} - TEST_{fine})$.

5.6.1.2 Primary aerosols

Because of their direct emission into the atmosphere, primary aerosols can be quite significant in terms of quantity (generated in large quantities), distribution and atmospheric impacts. Figs. 5.4 and 5.5 show primary aerosol (organic carbon (OC) and particulate matter less than 2.5 μm ($PM_{2.5}$)) concentrations plotted for both model scenarios. Note that OC is mainly from primary BB emissions with little secondary formation in the model configuration used in this study.

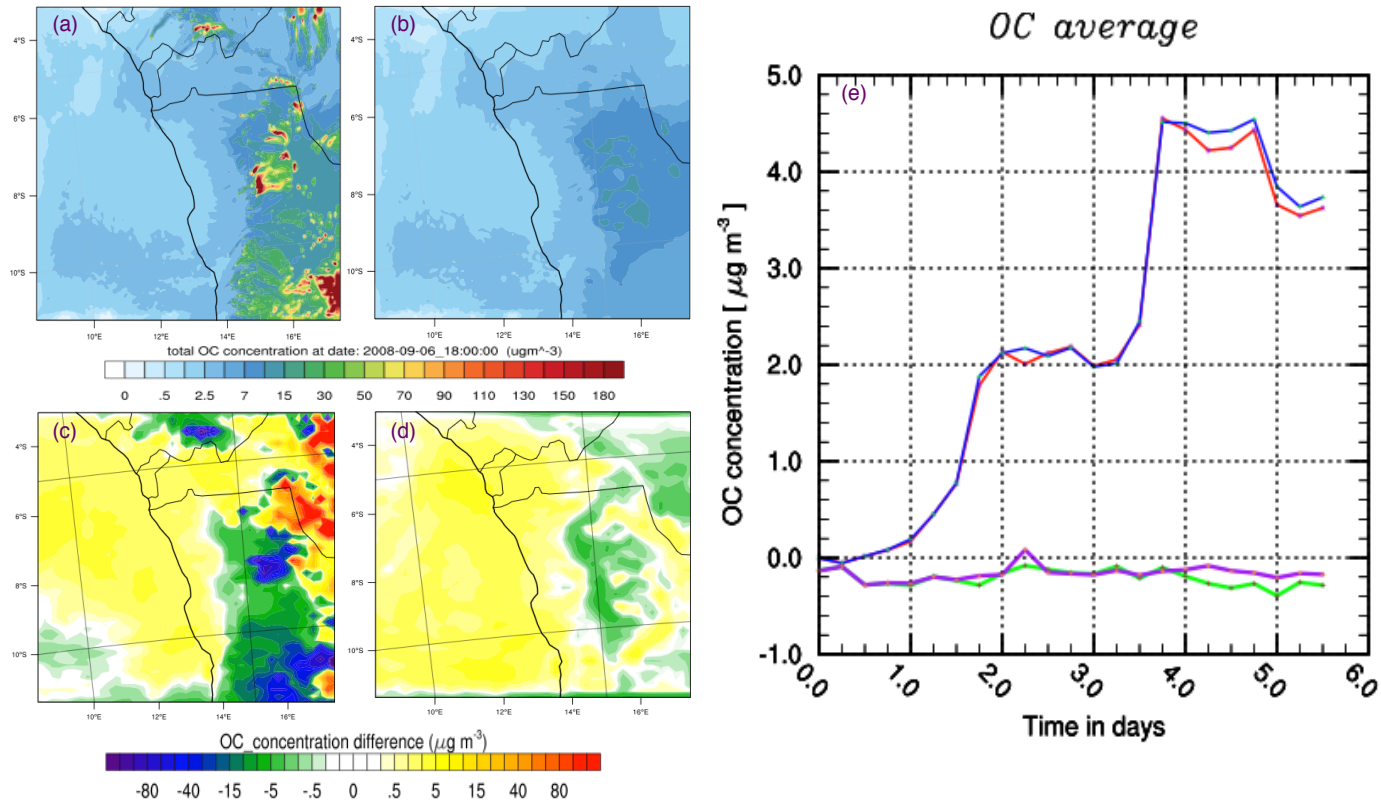

Fig. 5.4: Organic carbon (OC). Panel (a) shows surface OC concentration at 18:00 UTC 6 September 2008 at 4 km grid spacing, including BB emissions; (b) shows the same grid without BB emissions. Panel (c) shows the difference between the concentrations simulated at 4 km and 20 km spacing ($[OC]_{coarse} - [OC]_{fine}$) when the fine resolution simulation is degraded to the coarse resolution for the CNTRL simulation and panel (d) is same as (c), but for the TEST case. The right hand panel shows the time series of the differences in average concentrations between the fine and coarse simulations for both cases. Blue line represent $(CNTRL–TEST)_{fine}$; red line represent $CNTRL–TEST)_{coarse}$; purple represent $CNTRL_{coarse} – CNTRL_{fine}$ and green line represent $(TEST_{coarse} – TEST_{fine})$.

Again the changes in concentrations between the simulations indicate that BB contributes more significantly to pollution over tropical Africa. For example, the dark spots in 5.4 ((a) and (c)) indicate a significant contribution from BB. Also, the time series indicate that concentration increased more from 8–10 September. Meanwhile, $PM_{2.5}$ does not show a lot of variability in space, compared to OC. PM is the sum of all particles (including OC), it is possible that $PM_{2.5}$ concentration (and its spatial distribution) would be less close to that for OC as it is dependent on other emissions (anthropogenic, biogenic, sea salt and dust). Regional and local atmospheric processes play key role in the variability levels and composition of PM, especially in regions where local anthropogenic and natural emissions are considerably high. An interesting point noticed in the time series also, is that the model yields similar results even when averaged to a coarser resolution.

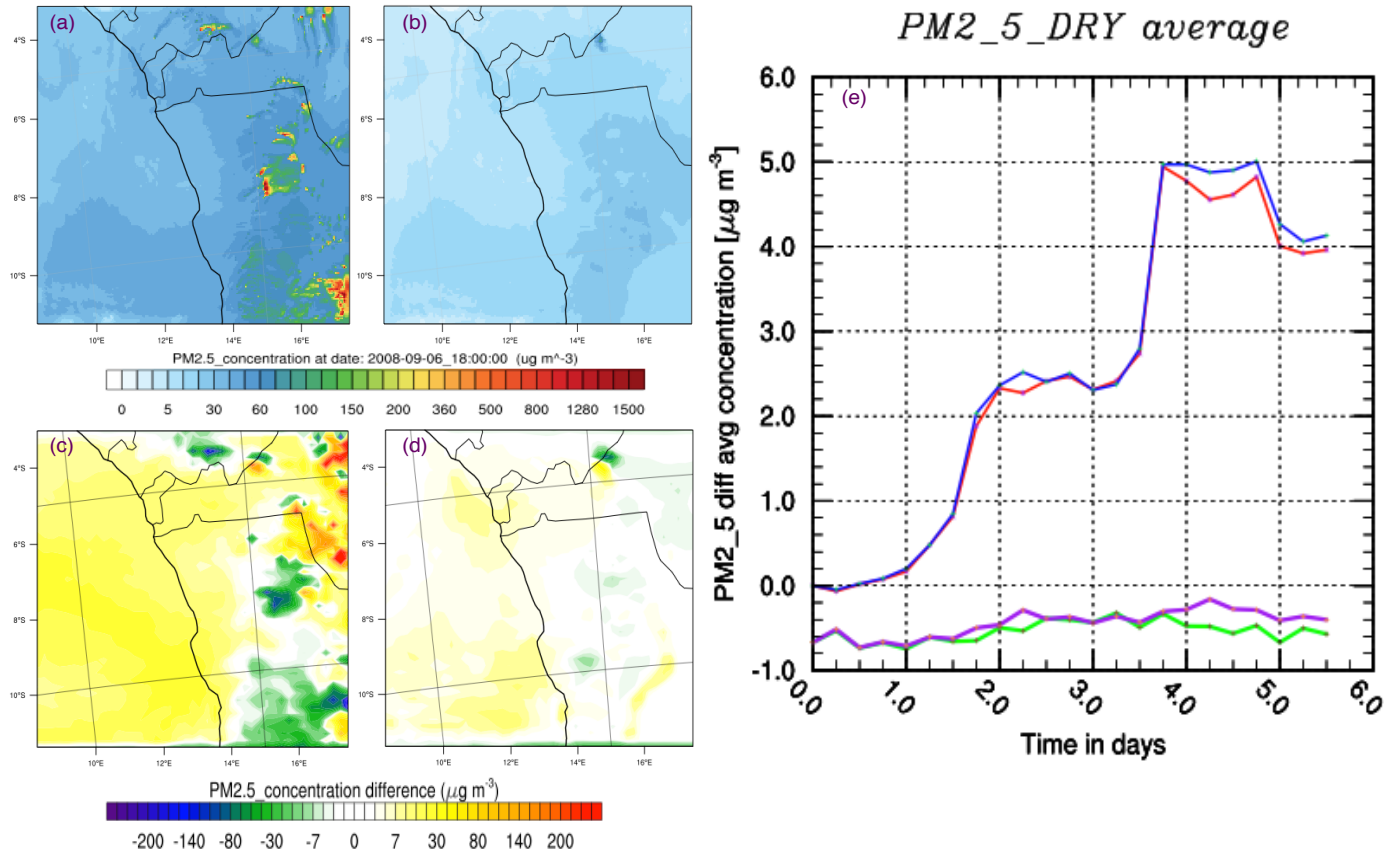

Fig. 5.5: Particulate matter below 2.5 μm. Panel (a) shows surface $PM_{2.5}$ concentration at 18:00 UTC 6 September 2008 at 4 km grid spacing, including BB emissions; (b) shows the same grid without BB emissions. Panel (c) shows the difference between the concentrations simulated at 4 km and 20 km spacing ($[PM_{2.5}]_{coarse} - [PM_{2.5}]_{fine}$) when the fine resolution simulation is degraded to the coarse resolution for the CNTRL simulation and panel (d) is same as (c), but for the TEST case. The right hand panel shows the time series of the differences in average concentrations between the fine and coarse simulations for both cases. Blue line represent $(CNTRL–TEST)_{fine}$; red line represent $CNTRL–TEST)_{coarse}$; purple represent $CNTRL_{coarse} – CNTRL_{fine}$ and green line represent $(TEST_{coarse} – TEST_{fine})$.

Because anthropogenic emissions are clustered in some parts of the domain, the spread and impact in other regions is determined by the meteorology and flux of effluents from the sources. $PM_{2.5}$ mass concentrations are relatively high (above 1000 μg m^{-3}) near BB source regions and urban areas. These high concentrations were also observed for PM_{10} in chapter 4, associated with other inorganic (see Figs. 4.12–4.14). The same pattern is also observed for OC, which reach up to more than 150 μg m^{-3} as a result of BB. These changes clearly indicate that without BB, aerosol concentrations are reduced over much areas of the subcontinent, and hence show the importance of BB contribution to the total aerosol concentration.

5.6.2 Secondary pollution

These pollutants are generated in the atmosphere and depend on the abundance of primary emitted species from the sources. From the results shown above, it implies that secondary aerosols are likely to

be abundant. The key thing to discuss here is that the differences are much more smoothed out for secondary species, without strong and sharp hot and cold spots.

5.6.2.1 Secondary gases and photochemistry

Ozone is one of the important secondary pollutant gases, generated from precursor species including those from BB. Fig. 5.6 illustrates the spatial surface distribution of O_3 concentration and temporal variation. Similarly, I compare the O_3 concentration between CNTRL and TEST, also indicating a notable reduction in concentration in the TEST case. Also, the changes are more defined in the tropics; the reason for this might be as already highlighted above. However, in testing the hypotheses I shall find out if this is the case or not. Although O_3 is more spread over the domain (compared to the primary species), the concentration gradient also decreases from the central (north) to the south, but more towards the west as observed over d01.

In the CNTRL, maximum O_3 concentrations exceed 80 ppb over the central-to-west region (Angola-DRC-Zambia), whereas the TEST concentration only reaches up to 70 ppb (Fig. 5.6 ((a) and (b)). The same is observed for the average concentration differences and time series. On the other hand, due to its long atmospheric lifetime (about a week), O_3 concentrations could be greatly influenced by the airflow of the anticyclone, although predictions can vary depending on other factors such as the rapidly growing urbanization in most southern African countries, causing wide-ranging environmental problems. The focus here is on the contribution due to aerosol concentration from different emission sources and to assess the influence of these pollutants on the regional pollution (section 5.7).

5.6.2.2 Secondary aerosols

Likewise, secondary aerosol generation and concentrations are dependent on primary aerosols, governed by chemical reactions and meteorological conditions in the atmosphere. Although they may not increase particle number, secondary aerosols may increase CCN fraction at a given supersaturation, and are important for atmospheric chemical processes as well.

Figures 5.7 and 5.8 show nitrate (NO_3^-) and sulphate (SO_4^{2-}) aerosol concentrations. There are close similarities (unlike in primary aerosols) in the aerosol concentrations and spatial distributions. High concentrations are predicted over land and spread throughout the landmass. High nitrate concentration (order of 4 $\mu g\ m^{-3}$ and more) is observed over central Angola. Also, higher sulphate concentrations are predicted in the upper half of the domain. Unlike in primary pollutants, the upper half (especially the west) has relatively low aerosol concentrations than the south. But overall (as it was the case with O_3), the magnitudes of the concentration changes (between the simulation cases) are not as large as those observed for primary species.

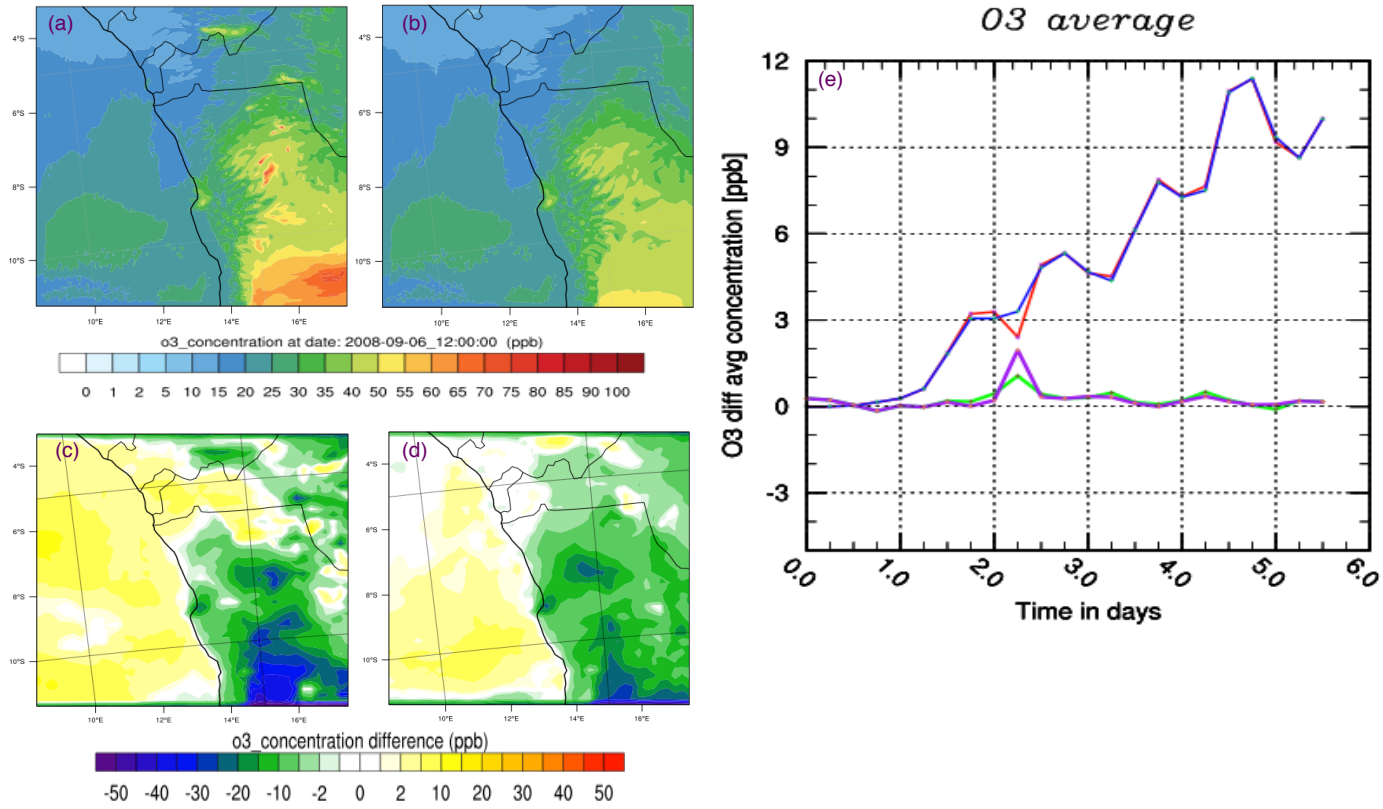

Fig. 5.6: Ozone (O_3). Panel (a) shows surface O_3 concentration at 18:00 UTC 6 September 2008 at 4 km grid spacing, including BB emissions; (b) shows the same grid without BB emissions. Panel (c) shows the difference between the concentrations simulated at 4 km and 20 km spacing ($[O_3]_{coarse} - [O_3]_{fine}$) when the fine resolution simulation is degraded to the coarse resolution for the CNTRL simulation and panel (d) is same as (c), but for the TEST case. The right hand panel shows the time series of the differences in average concentrations between the fine and coarse simulations for both cases. Blue line represent $(CNTRL–TEST)_{fine}$; red line represent $CNTRL–TEST)_{coarse}$; purple represent $CNTRL_{coarse} – CNTRL_{fine}$ and green line represent $(TEST_{coarse} – TEST_{fine})$. O_3 is plotted at midday, considering it as a daytime photochemical species, hence discussing its daytime concentration. However, O_3 still persist at night, but not as high as during daytime.

Figures 5.2–5.8 illustrate changes in pollution concentration between CNTRL and TEST. These changes (concentration gradients) –both in spatial distribution and temporal variation demonstrate the contribution of BB to the total aerosol concentration and show areas that are directly (or indirectly) affected by BB emissions. Tropical central Africa is more affected by BB than the subtropical regions; changes are more reflected in the primary- than secondary pollutants. The first peak in most pollutant concentrations occurred during 28–30 August (not shown), over the regions where BB is most enhanced and downwind of the emissions (particularly Angola, DRC and Zambia) in the west, before extending southwards by end of August. The next largest impact from the total emissions in September covered areas within 0–20°S and 15–40°E. This is evidenced in results from the CNTRL simulation; high concentrations over the central part and nearby regions.

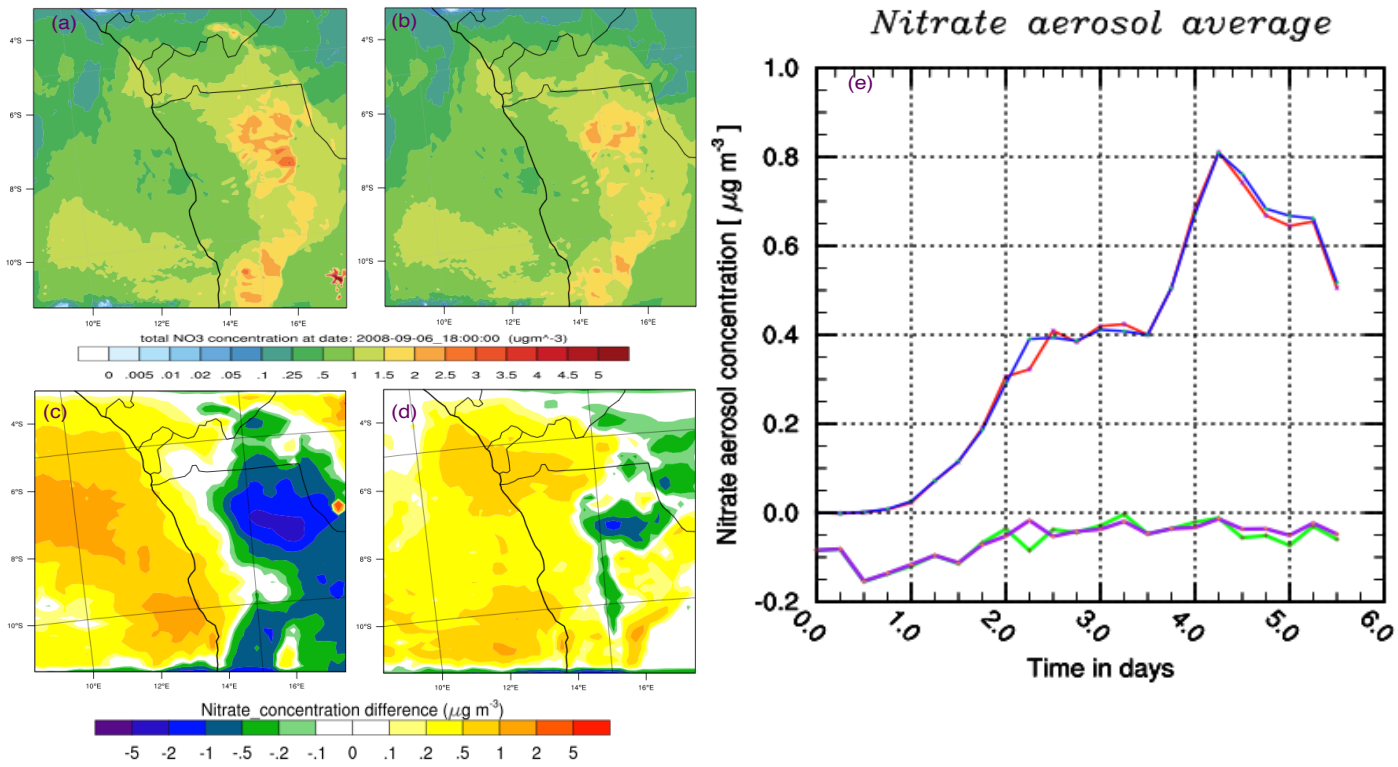

Fig. 5.7: Nitrate aerosol NO_3^-

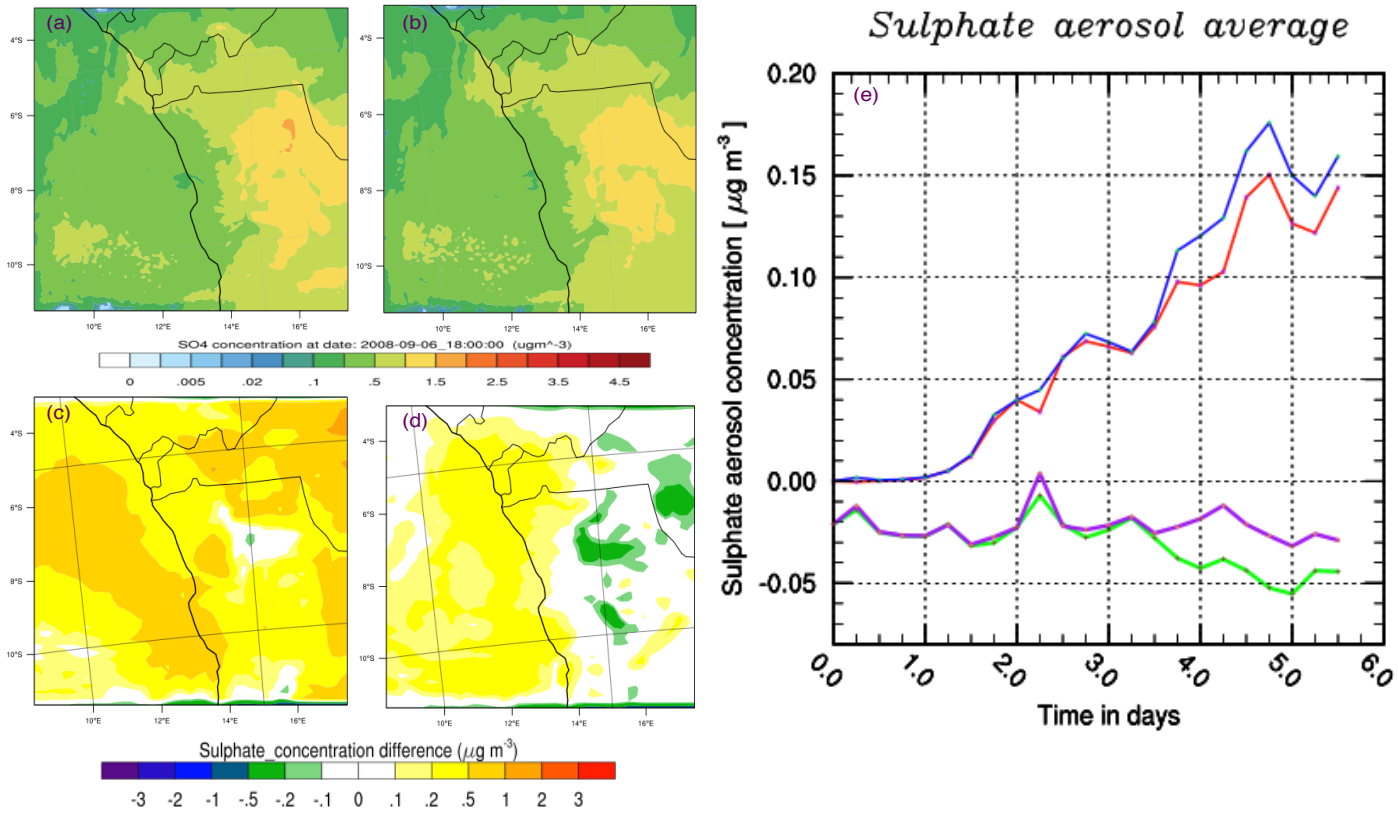

Fig. 5.8: Sulphate aerosol SO_4^{2-}*. In each plot, panel (a) shows surface* SO_4^{2-} and NO_3^- *concentration at 18:00 UTC 6 September 2008 at 4 km grid spacing, including BB emissions; (b) shows the same grid without BB emissions. Panel (c) shows the difference between the concentrations simulated at 4 km and 20 km spacing (*$[SO_4^{2-}]_{coarse} - [SO_4^{2-}]_{fine}$*) (same for* NO_3^-*) when the fine resolution simulation is degraded to the coarse resolution for the CNTRL simulation and panel (d) is same as (c), but for*

the TEST case. The right hand panel shows the time series of the differences in average concentrations between the fine and coarse simulations for both cases. Blue line represent (CNTRL–TEST)$_{fine}$; red line represent CNTRL–TEST)$_{coarse}$; purple represent CNTRL$_{coarse}$ – CNTRL$_{fine}$ and green line represent (TEST$_{coarse}$ – TEST$_{fine}$).

As illustrated in Figs. 5.2–5.6 for example, CO, OC and O_3 concentrations are reduced by as much as 4000 ppb, 160 μg m^{-3} and 20 ppb respectively. With a shorter lifetime than CO, NO_x mixing ratios of 5–200 ppb are more confined to regions close to the NO_x sources. A more notable reduction in concentration gradient occurs in the primary pollutants than secondary pollutants. Time series plots indicate that average concentrations increased mainly between 8 and 10 September, except NO_2 with the first maxima occurring between 6 and 7 September. Similar trends in the curves in both 4- and 20-km grid spacing indicate that results are similar for the same grid averaged to 20 and 4 km. The changes at point locations are quantified and discussed further in section 5.7 below. Although secondary pollutants have the most spatial variation across the domain than primary ones, it appears that changes in concentration for other secondary species (NO_3^- and SO_4^{2-}) are relatively small compared to that of O_3.

Downwind areas are strongly influenced by the long-range transport of pollution as plumes spread over southeastern parts of the mainland, including Madagascar. Pollution from the sub-continent can be transported further away and reach other parts of the world. This has been noted to travel as far as Australia and South America (Crutzen and Andreae, 1990; Tyson and Preston-Whyte, 2000; Piketh and Walton, 2004, and references therein; Kaufman et al., 2005; Edwards et al., 2006) influencing AQ composition, including the global environment. Concentration changes are also likely due to the meteorological conditions, showing how the subcontinent was under the control of westerly winds. Strong winds may have played important roles in the BB episode, both in terms of chemical reactions and carrying pollutants away. The dominant westerly waves (Chapter 4) in the south for example, would likely have pushed the plumes further eastwards. Moreover, pressure systems in the mid-latitude moved eastwards throughout the simulation.

By end of August to mid September 2008, BB mainly affected central-southeastern Africa. The long-range transport had an important impact over countries south of the Congo (e.g. Zambia, Zimbabwe, Mozambique, South Africa and Madagascar), with over 200–600 ppb CO predicted. Concerning O_3, the area influenced was broader than that of CO; considerable burning extended to areas as far as south of Namibia, South Africa, Tanzania and other parts north of central southern Africa. Regions of high O_3 coincide with locations of BB, indicating that MODIS fire emissions are high in these regions. According to Edwards et al. (2006), the fires are widespread across southern Africa by September, and are particularly strong in Angola, DRC, Zambia and Mozambique. For example, a belt of high O_3

concentration appears through Namibia, Angola, Zambia and southern DRC with over 80 ppb. CO was mainly confined over the central, across Angola–Zambia, northern Mozambique and southern Tanzania, while PM show a southward inclination. The difference in terms of area coverage by pollution could also be due to changes in wind patterns. Recall from the previous chapter that winds were prevailingly westerly. However, other secondary aerosol concentrations do not change as much as O_3, indicating that precursors to these species may not be BB-related. Meanwhile, secondary aerosol concentrations do not have a linear relationship with emission levels because they form as a result of chemical reactions or physical transformations in the atmosphere.

In addition to the figures shown here, I also show (see Appendix B) the spatial and temporal variation of gases and particulates over the fine grids. Four species (CO, O_3, $PM_{2.5}$ and SO_4^{2-}) are plotted for the fine grids at 4-km and 20-km respectively. The map plots in each case show output at 4- and 20-km resolutions and the average for the same grid averaged to 20-km. The time series show the difference between CNTRL and TEST at 4-km and 20-km respectively. Also, the variations indicate similarities in the average concentration for the fine grids averaged to 20-km and at 4-km.

In summary, higher resolution simulations clearly and obviously are able to resolve more structure in different atmospheric pollutants. However there is also evidence, from the differences in concentrations for both primary and secondary species, for systematic differences in the spatial distributions of pollutants at different resolutions. For primary pollutants, this shows itself as a localised displacement of pollutant plumes; whereas secondary species have smooth spatial differences in concentrations even though the averages across domains are similar in both CNTRL and TEST simulations.

5.7 Quantification of regional trends and hypotheses testing

This section examines the above-mentioned hypotheses. To address the hypotheses, I quantify changes in pollutant concentrations, focusing mainly on the major regulated species: CO, NO_x, O_3 and PM ($PM_{2.5}$ and PM_{10}). The difference between CNTRL and TEST (from the mean concentrations) is determined, from which the percentage difference is used to investigate the contribution due to BB emissions. For consistency, I also compare the observed trends between fine grid and coarse grid simulations. The time period for this analysis 5–10 September 2008 (132 hours) has 6 midnights and 6 midday data points. First, I selected some cities (Table 5.1) over the domain and determined mean concentrations for the above species at midday, midnight and the entire simulation period. Location of the cities on the map is shown in Fig. 5.9. Before interpreting results I present statistical data (Table 5.2) showing mean concentrations for different pollutants over selected cities.

Table 5.1: selected cities used for analysis

City/town	Location within the coarse grid (d01)			Description
	d02	d03	d04	
Luanda	✓			Angola's largest and national capital; located on the west along the coast adjacent to the SE Atlantic ocean
Marimba	✓			Municipal town in northern Angola
Lubumbashi				Second largest city with vigorous mining activity in DR Congo, located inland, near the border with Zambia
Kinshasa				Largest city and national capital in DR Congo; located in the west near the border with Congo-Brazzaville
Kaoma				District capital located in western Zambia
Dar es Salaam		✓		Largest east African city; Tanzania's old capital and current economic hub, located on the edge of east coast adjacent to the SW Indian ocean
Windhoek				Largest and national city in Namibia; located in the centre most of the country
Francistown				District capital; Botswana's second largest city located in the north east near boarder with Zimbabwe; surrounded by mining areas
Harare				Zimbabwe's capital and largest city; situated in north-east; metropolitan province
Beira			✓	Second largest city in Mozambique, situated in the east along the coast – a sea port place for major commodities
Johannesburg			✓	South Africa's largest and most populated city; also a provincial capital, located in the north-east of the country.
Toliara				Regional capital in southwest Madagascar, along the coast. Also a sea port acting as a major export/import to the international community.

Locations are chosen within environments with background conditions ranging from high BB in the central to more anthropogenic conditions in the south. Table 5.1 also highlights those contained within the fine grids. Since BB is the only source controlled in the simulation, changes in concentration between CNTRL and TEST reflect the contribution due to fire emissions. Thus, the CNTRL is assumed to behave more realistically. Table 5.2 shows the statistics for different pollutants in different cities over the domain. This shows midday and midnight mean concentrations. The entire simulation means is given in Table C1 in the appendix section.

5.7.1 Air quality standards

The first part of the analysis is mainly focused on AQ composition over southern Africa. In this analysis, we shall compare results with the set standards for different pollutants. AQ is assessed through regulating pollutants to protect the environment and ecosystems by providing reasonable measures (i.e. thresholds) for pollution prevention to secure sustainable development through AQ monitoring and waste management control. These standards are set to ensure that the total average concentration of each pollutant does not exceed the amount specified. However, the limits vary for different pollutants and exposure times. Table 5.3 shows threshold limits for SO_2, NO_x, O_3, CO and PM concentrations in hourly, 8-hr, daily and yearly exposure (based on the UK legislation on Air Quality Act).

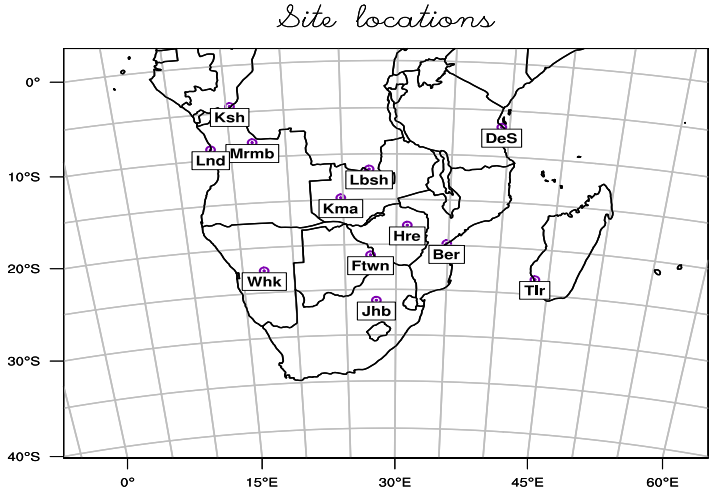

Fig 5.9: Locations of the 12 cities/towns used for evaluation in the investigation.
Key: Lnd = Luanda, Ksh = Kinshasa, Mrmb = Marimba, Lbsh =Lubumbashi, DeS = Dar es Salaam, Kma = Kaoma, Whk = Windhoek, Ftwn = Francistown, Hre = Harare, Ber = Beira, Jhb = Johannesburg, Tlr = Toliara.

Table 5.2: Simulated hourly surface concentrations (averaged at midnight and midday) for BB-inclusive and BB-exclusive simulations. Data in parenthesis indicate results from fine grid for cities contained within high resolution. (Key: BB_on =CNTRL, BB_off =TEST, std dev =standard deviation)

Model scenario		BB_on				BB_off			
Diurnal variation		midnight		midday		midnight		midday	
Location	species	mean	std dev	mean	std dev	mean	std dev	mean	std dev
Luanda	O_3	17 (20)	1.7 (3.8)	29 (32)	6.9 (4.6)	17 (18)	2.0 (2.1)	28 (31)	7.0 (4.4)
	NO	0.09 (0.02)	0.01 (0.01)	1.2 (0.13)	0.53 (0.10)	0.10 (0.02)	0.02 (0.004)	1.1 (0.08)	0.44 (0.05)
	NO_2	1.9 (1.7)	0.20 (1.1)	2.0 (0.36)	1.3 (0.28)	2.0 (2.5)	0.29 (1.2)	1.9 (0.23)	1.2 (0.13)
	CO	116	13 (20)	142	33 (16)	116 (168)	14 (12)	137 (140)	30 (17)

		(149)		(148)					
	PM_{10}	16 (30)	4.7 (11)	20 (27)	11 (8.2)	15 (36)	5.3 (7.3)	19 (24)	10 (7.4)
	$PM_{2.5}$	7.4 (15)	2.5 (4.8)	9.2 (14)	5.6 (4.3)	7.1 (17)	2.7 (3.4)	8.6 (12)	5.4 (4.3)
Marimba	O_3	23 (22)	5.8 (1.0)	44 (42)	5.1 (5.8)	20 (21)	4.0 (1.8)	32 (30)	6.1 (6.6)
	NO	0.01 (0.01)	0.01 (0.02)	0.09 (0.34)	0.06 (0.69)	0.003 (0.00)	0.01 (0.00)	0.03 (0.03)	0.01 (0.01)
	NO_2	4.5 (2.3)	5.0 (2.4)	0.34 (1.1)	0.24 (2.1)	1.3 (0.82)	1.6 (0.70)	0.1 (0.10)	0.04 (0.04)
	CO	642 (381)	569 (197)	252 (302)	37 (113)	251 (220)	126 (67)	184 (190)	31 (31)
	PM_{10}	70 (47)	54 (20)	35 (20)	2.8 (20)	33 (32)	13 (8.2)	28 (28)	5.6 (6.0)
	$PM_{2.5}$	60 (38)	49 (17)	26 (32)	2.5 (13)	26 (25)	11 (6.7)	20 (20)	4.1 (4.5)
Lubumbashi	O_3	25	4.4	68	10	21	2.8	50	9.1
	NO	0.002	0.004	0.09	0.01	0.01	0.01	0.03	0.013
	NO_2	3.3	2.1	0.41	0.12	0.94	0.34	0.11	0.06
	CO	679	277	276	75	338	44	154	36
	PM_{10}	83	27	46	8.8	51	7.7	35	5.8
	$PM_{2.5}$	58	24	28	7.0	29	5.6	18	4.7
Kinshasa	O_3	15	6.0	22	3.01	14	6.7	18	2.3
	NO	0.04	0.01	0.07	0.01	0.05	0.02	0.06	0.01
	NO_2	2.5	2.0	0.15	0.04	2.6	2.0	0.12	0.01
	CO	909	676	186	15	928	675	175	13
	PM_{10}	218	188	32	2.8	225	184	31	3.1
	$PM_{2.5}$	93	77	16	1.8	95	78	15	1.6
Kaoma	O_3	31	3.8	65	11	28	5.7	55	7.5
	NO	0.00	0.00	0.06	0.02	0.00	0.00	0.03	0.01
	NO_2	1.5	0.73	0.26	0.13	0.44	0.11	0.10	0.03
	CO	316	81	193	30	190	26	138	27
	PM_{10}	43	9.2	38	6.1	30	5.1	32	8.3
	$PM_{2.5}$	31	7.5	22	3.8	20	3.0	17	4.8
Dar es Salaam	O_3	12 (16)	5.5 (1.5)	26 (24)	5.3 (5.2)	12 (15)	5.2 (1.7)	25 (23)	5.3 (4.5)
	NO	0.45 (0.00)	0.28 (0.00)	0.17 (0.02)	0.02 (0.02)	0.43 (0.00)	0.23 (0.00)	0.16 (0.01)	0.02 (0.01)
	NO_2	9.5 (1.6)	5.2 (1.3)	0.37 (0.04)	0.1 (0.06)	9.1 (1.4)	5.1 (1.1)	0.34 (0.02)	0.01 (0.01)

	CO	306 (198)	132 (113)	98 (84)	7.0 (9.3)	294 (191)	125 (109)	94 (81)	4.6 (4.9)
	PM_{10}	81 (36)	32 (22)	92 (27)	13 (9.8)	78 (35)	31 (21)	93 (27)	12 (9.9)
	$PM_{2.5}$	34 (20)	15 (13)	15 (8.8)	30 (3.1)	33 (19)	15 (13)	15 (8.5)	2.8 (2.9)
Windhoek	O_3	39	7.8	69	6.3	40	8.6	62	5.4
	NO	0.01	0.01	0.04	0.01	0.003	0.01	0.03	0.01
	NO_2	0.87	0.38	0.15	0.05	0.082	0.38	0.11	0.03
	CO	126	40	193	26	127	40	168	40
	PM_{10}	34	27	87	34	34	27	90	37
	$PM_{2.5}$	16	11	27	9.3	16	11	26	9.2
Francistown	O_3	20	6.4	52	11	19	5.9	49	9.8
	NO	0.003	0.01	0.04	0.01	0.01	0.01	0.03	0.01
	NO_2	1.0	0.44	0.14	0.04	0.89	0.27	0.11	0.03
	CO	208	55	164	22	188	35	152	25
	PM_{10}	52	13	81	52	50	12	80	52
	$PM_{2.5}$	33	6.8	38	21	31	5.9	36	21
Harare	O_3	18	8.3	60	7.1	14	5.5	54	7.7
	NO	0.57	0.38	0.17	0.02	0.72	0.34	0.15	0.02
	NO_2	14	2.8	0.60	0.11	13	3.3	0.50	0.11
	CO	455	169	179	26	327	76	146	26
	PM_{10}	83	19	57	15	69	3.3	52	14
	$PM_{2.5}$	49	15	27	4.9	38	4.2	24	3.8
Beira	O_3	21 (22)	6.2 (6.1)	29 (26)	4.7 (2.6)	21 (22)	6.3 (6.3)	26 (25)	3.0 (3.5)
	NO	0.003 (0.002)	0.01 (0.004)	0.06 (0.02)	0.05 (0.01)	0.002 (0.003)	0.004 (0.01)	0.02 (0.02)	0.01 (0.01)
	NO_2	0.39 (0.30)	0.34 (0.18)	0.14 (0.05)	0.12 (0.02)	0.30 (0.01)	0.23 (0.24)	0.04 (0.15)	0.01 (0.04)
	CO	124 (143)	39 (37)	110 (104)	31 (18)	118 (138)	34 (39)	94 (102)	16 (18)
	PM_{10}	38 (55)	14 (20)	55 (55)	11 (13)	37 (53)	15 (21)	54 (55)	11 (13)
	$PM_{2.5}$	23 (31)	5.9 (9.5)	24 (25)	6.5 (8.2)	22 (31)	7.2 (9.9)	23 (25)	6.3 (8.3)
Johannesburg	O_3	9.6 (15)	6.1 (6.4)	53 (53)	6.8 (9.9)	8.5 (13)	6.2 (6.4)	49 (49)	5.4 (6.9)
	NO	5.1 (0.29)	8.6 (0.35)	0.47 (0.17)	0.13 (0.07)	5.3 (0.38)	8.4 (0.52)	0.43 (0.16)	0.13 (0.07)
	NO_2	29 (18)	13 (2.6)	1.4	0.42	28 (18)	13 (2.8)	1.2 (0.47)	0.31 (0.15)

				(0.56)	(0.25)				
	CO	912 (896)	373 (153)	227 (207)	32 (32)	889 (874)	364 (158)	206 (185)	33 (29)
	PM_{10}	274 (237)	101 (28)	79 (79)	14 (14)	274 (237)	99 (29)	76 (76)	15 (16)
	$PM_{2.5}$	120 (116)	35 (16)	42 (41)	11 (10)	119 (114)	34 (17)	40 (39)	12 (11)
Toliara	O_3	15	6.2	26	3.5	15	6.2	26	3.5
	NO	0.023	0.012	0.04	0.011	0.023	0.01	0.04	0.01
	NO_2	0.85	0.50	0.09	0.03	0.84	0.50	0.08	0.03
	CO	99	15	86	13	98	15	84	12
	PM_{10}	26	6.3	35	5.8	25	6.2	35	5.8
	$PM_{2.5}$	14	2.9	12	1.7	13	2.8	11	1.8

Units: ppb (gases) and μg m^{-3} (aerosols)

Table 5.3: The Air Quality Standard Regulations (revised 2010)

Averaging period	Limit value (threshold) not to exceeded	Concentration in (ppb)
SO_2: 1 hour	350 μg/m^3 more than 24 times per calendar year	134
1 day	125 μg/m^3 more than 3 times per calendar year	48
NO_x (as NO_2): 1 hour	200 μg/m^3 more than 18 times per calendar year	106
1 year	40 μg/m^3	21.3
O_3: Maximum 8-hour daily mean	120 μg/m^3 more than 25 days per calendar year over 3 years	61.2
CO: Maximum 8-hour daily mean	10 mg/m^3 (10000 μg/m^3)	8737
PM_{10} 1 day	50 μg/m^3 more than 35 times per calendar year	
1 year	40 μg/m^3	
$PM_{2.5}$ 1 year	25 μg/m^3	

Maximum daily (24-hr), 8-hr and 1-hr mean concentrations selected by determining/examining running averages, calculated from hourly data per hour.
Source: (http://www.legislation.gov.uk/uksi/2010/1001/contents/made).

5.7.2 Testing the hypotheses

(a) First hypothesis

The first hypothesis states that 'biomass burning contribution to southern African pollution makes a considerable impact on the air quality to population centers in close-proximity to burning areas'. Pollution enhancement is higher in urban locations in active burning areas.

Table 5.2 summarise data used in testing this statement. Different cities and towns were selected within the active fire zones and downwind regions of pollution flow from which average pollutant

concentration were determined. The idea was to assess the change in pollution concentration due to BB. Percentage difference (CNTRL–TEST) is used to describe impact due to BB emissions and compare results with the set standards as shown in Table 5.3. Mean concentrations for the entire 5-day simulation period is given in Table C1 (Appendix C).

Table 5.2 show diurnal variations for different pollutants, computed at 0000 and 1200 UTC across the entire simulation. For example, peak daytime and nighttime concentration decrease in O_3 reflects its photochemical behavior, while variations shown by NO_x and CO is due to the increase in their concentration levels -either due to BB, anthropogenic or biogenic sources. On the other hand, peak/drop in PM also does not necessarily depend on the time of the day but rather regulated by the amount of pollution generated at any given time. Concentrations are higher in CNTRL than in the TEST (see also Table C1). Although BB makes a substantial contribution to pollution across the domain, some of the cities/towns tend to be indirectly affected, except those within the active burning areas or down wind to pollution.

Table 5.4: Percentage concentration differences (%) for selected cities/towns

City/town	Midnight						Midday					
	O_3	NO	NO_2	CO	$PM_{2.5}$	PM_{10}	O_3	NO	NO_2	CO	$PM_{2.5}$	PM_{10}
Marimba	13	70	71	61	57	53	27	67	72	27	23	20
Lubumbashi	16	-80	72	50	50	39	27	67	17	44	36	24
Harare	22	-21	7	28	22	17	10	12	17	18	11	9
Luanda	0	-10	-5	0	4	6	3	8	5	4	7	5
Dar es Salaam	0	4	4	4	3	4	4	6	8	4	0	-1
Johannesburg	1	-4	3	3	1	0	1	-4	3	9	5	4

Units: %

For those cities directly affected by BB, there is significant change in concentrations when BB emissions are included in the simulation. For example Table 5.4 above shows percentage concentration differences over Lubumbashi, Marimba and Harare (more affected) and Luanda, Dar es Salaam and Johannesburg (less affected) at midnight and midday respectively. There is relatively less contribution to primary pollutants in the most populous cities. However, it is worth noting that pollution impact would also depend on other factors such as the relative position of the population/city (i.e. distance away) from the source(s), meteorological conditions (e.g. wind direction, precipitation –to washout pollution), as well as chemical processes leading to secondary pollutants. But it appears that even if

some cities are more/less affected by BB, the situation tend to be slightly complicated. It appears that pollution problem is the burning itself, not necessarily geographical region or relative position of the cities/population to the plumes because the less BB-affected cities also tend to be polluted by their own [anthropogenic] emissions (e.g. Johannesburg), whereas some large/populous cities are both directly affected by BB and/or anthropogenic pollutants (e.g. Harare). The percentage differences over the entire simulation (derived from Table C1), is shown in Table C2, for the more polluted and less polluted cities highlighted above respectively.

5.7.2.1 Comparison with air quality standards

Air quality and pollution problems are some of the major issues of concern to human health, and have gained prominence on the political agenda in the region. Although there might not be national AQ problems (on record) over southern Africa, a number of air pollution conditions (i.e. high emissions) exist (ESA, 2005) where severe AQ problems are likely to occur. Potential examples are those areas mostly impacted by BB and other anthropogenic emissions, including dust. As shown in Tables 5.2 and C1, pollutant concentrations in some cities exceed the limits. As a result, populations in these pollution centers are likely to be at risk to air pollution problems, especially during intense BB events. Consequently, these are some of the most populous cities, some (e.g. Harare) being national capitals. Moreover, since BB is not controlled/regulated over the subcontinent it becomes a persistent problem. Reference can also be made with Torres et al. (2010) study on the satellite observations of the anomalous 2008–2009 Southern Hemisphere BB emissions. The authors indicate that African BB activity exhibited a repetitive and steady annual cycle over the last decade, with an apparent increase in the fire count from 2008 to 2009, while South American fire count declined.

To illustrate these changes, I show mean concentrations at 1-hr rolling average for Marimba, Lubumbashi and Harare (Fig. 5.10). The blue curves represent CNTRL whilst the green curves represent TEST. As shown, concentrations decrease significantly when BB emissions are excluded from the simulation, where some species' (e.g. O_3 and PM_{10}) concentrations drop below the threshold limits (given by the horizontal purple line). Because the TEST was initialized with the same meteorological conditions (on 4 September) as the CNTRL, predictions are identical for most of the species on the first day; deviations become clearer after the second day of the simulation. Marimba shows an increase between days 4 and 5 (i.e. 8–9 September), while Harare peaks nearly a day after. For Lubumbashi, most pollutants peak between the first two days (5–6 September). NO_2 drops (below 2 ppb) when BB emissions are excluded in both Marimba and Lubumbashi, except for Harare that show only a slight decrease. However, this can be expected, considering that Harare is the largest city in Zimbabwe and the nation's capital. Therefore, anthropogenic pollutants are likely to contribute as

well. Marimba is a peri-urban town; more BB-dominated than the other two cities that also experience anthropogenic pollution. Whilst O_3 concentration over Marimba lies below the threshold, it almost exceeds the limit over Lubumbashi and Harare. In all the three cities, PM concentration stays above the threshold in the CNTRL simulation.

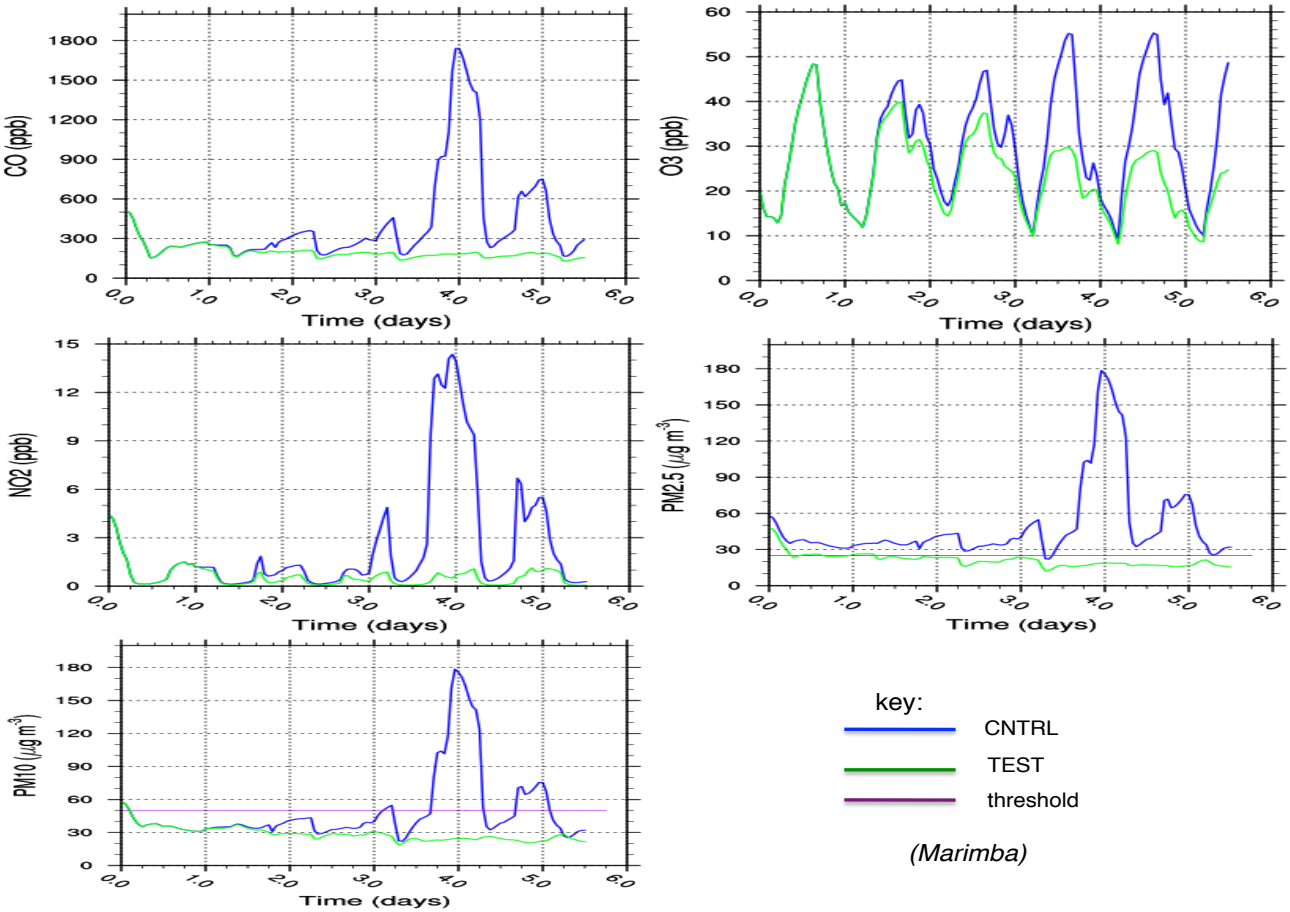

(a) Marimba

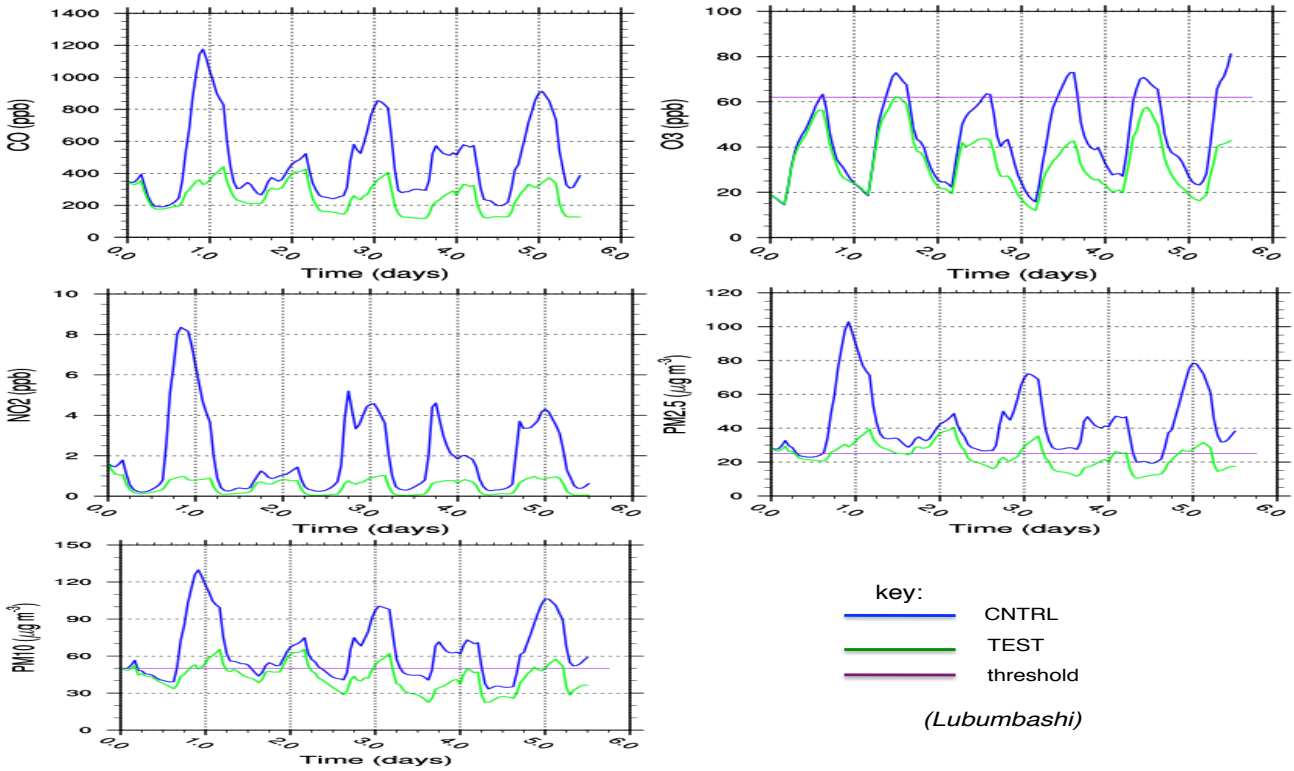

(b) Lubumbashi

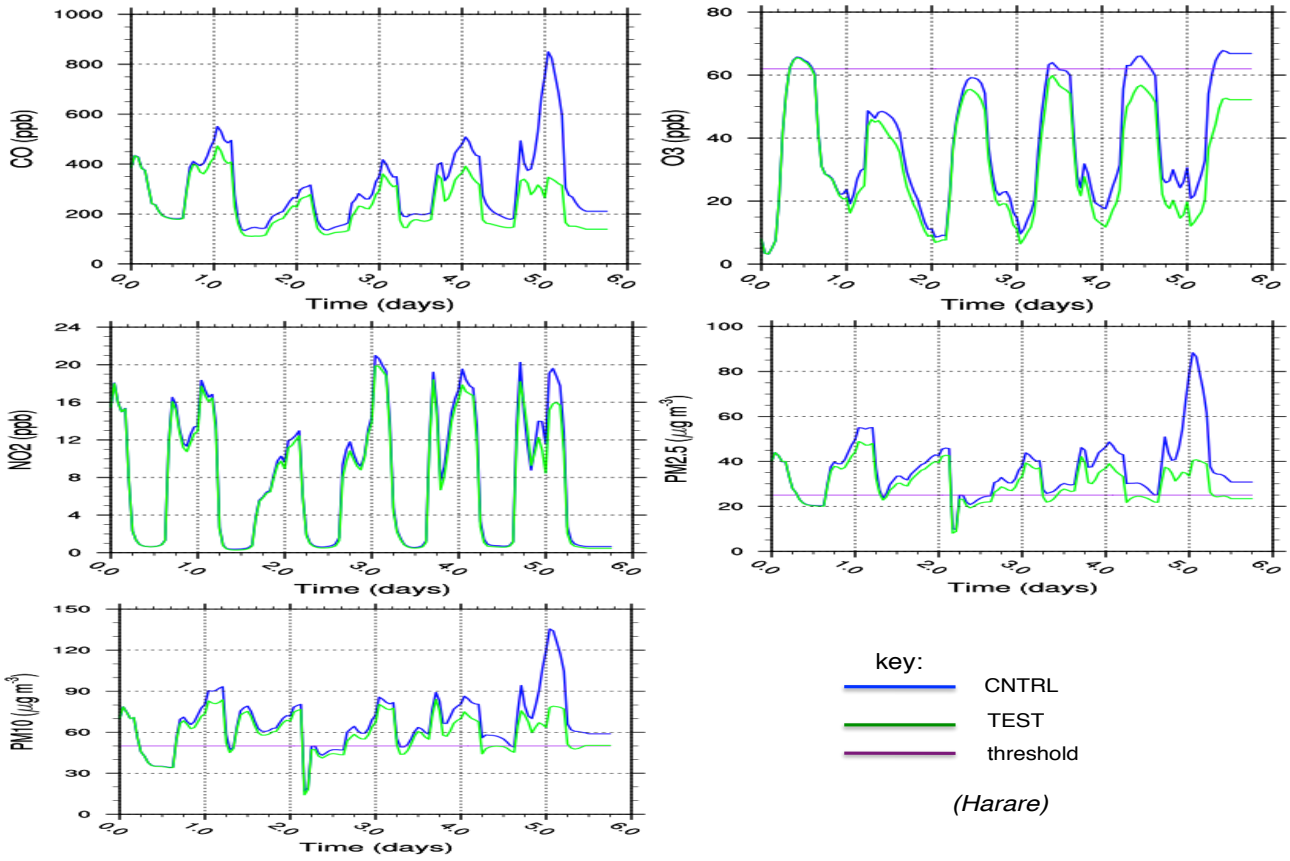

(c) Harare

Fig. 5.10: Mean concentrations (CO, O_3, NO_2, $PM_{2.5}$ and PM_{10}) over (a) Marimba, (b) Lubumbashi, and (c) Harare. The blue and green curved lines show 1-hr rolling average for CNTRL and TEST respectively, whereas the horizontal purple line shows a threshold. All simulations start at 0000 UTC 5 September.

(b) Second hypothesis

The second hypothesis states that model grid-scale affects prediction of pollutants.

In this statement, we assess the change in pollutants' concentrations in order to investigate how grid resolution influence model performance in pollutant prediction. Unlike in the first hypothesis, pollutant concentrations between grid spacing (coarse and fine grids) are compared pair-wise for cities/towns in grid cells where they are contained within high and low resolutions. Metrical analysis is also done to determine percentage difference between the two simulations described above. I focus only on cities/towns contained within high and low resolutions only (see Table 5.1). Fig. 5.11 shows predictions for pollutant average concentrations (CO, O_3, NO_2, and $PM_{2.5}$ and PM_{10}) for Marimba, [d02], Dar es Salaam [d03], and Johannesburg [d04] respectively. Similarly, the plots show the mean concentrations at 1-hr rolling average over the 5-day period. For each pollutant, the left panels show results from the coarse grid whilst the right panels show results from the fine grids.

The model predicts substantial diurnal trends in pollutant concentrations, including the morning/midday and afternoon/evening peak concentrations. The results show the model sensitivity in grid resolution, suggesting that the difference between grids' predictions is probably not dependent upon urban vs. rural, peri-urban or less polluted centers, but reflects how the model performs (at coarse and fine grid spacing) in predicting pollutants. One characteristic difference between the two grid resolutions is that in the coarse grid, multiple pollutants (e.g. fire locations) in one grid cell are aggregated into a single grid box so that they appear to be in one area, whereas in the fine grids pollutants are isolated from one another. Despite similarities in the pattern (i.e. concentrations peaking/dropping at nearly the same times), the magnitudes of the concentrations vary for different species. For example, CO and NO_2 increase (at high resolution) over Marimba, followed by PM, whilst O_3 declines slightly. The pattern is different for Dar es Salaam whereby species concentration change at different times between the grids (e.g., CO, NO_2 and PM decrease substantially in the fine grids after 80 hours). For Johannesburg, concentration levels at high resolution stay relatively below those in the coarse grid, although there are times when the peaks rise above those in the coarse grid.

Meanwhile, O_3 increases slightly above the threshold towards the end of the simulation. Its enhancement generally lies between 40–50 ppb in both grids, reaching up to 50–70 ppb in the last 2 days. Notice also, different pollutant levels/concentrations at 0000 UTC on 5 September, between the coarse and fine grids in all the cities. Percentage difference at midnight and midday are shown in Table 5.5 below for Marimba, Dar es Salaam and Johannesburg respectively. Results in parenthesis indicate

changes in the fine grids. Comparing these plots with averages for the whole domain (e.g. Chapters 3 and 4) shows that deviations can be much greater when data is averaged for a specific location or grid cells. This suggests that average statistics over a large area or whole domain are likely to mask any local differences (Kong et al., 2014).

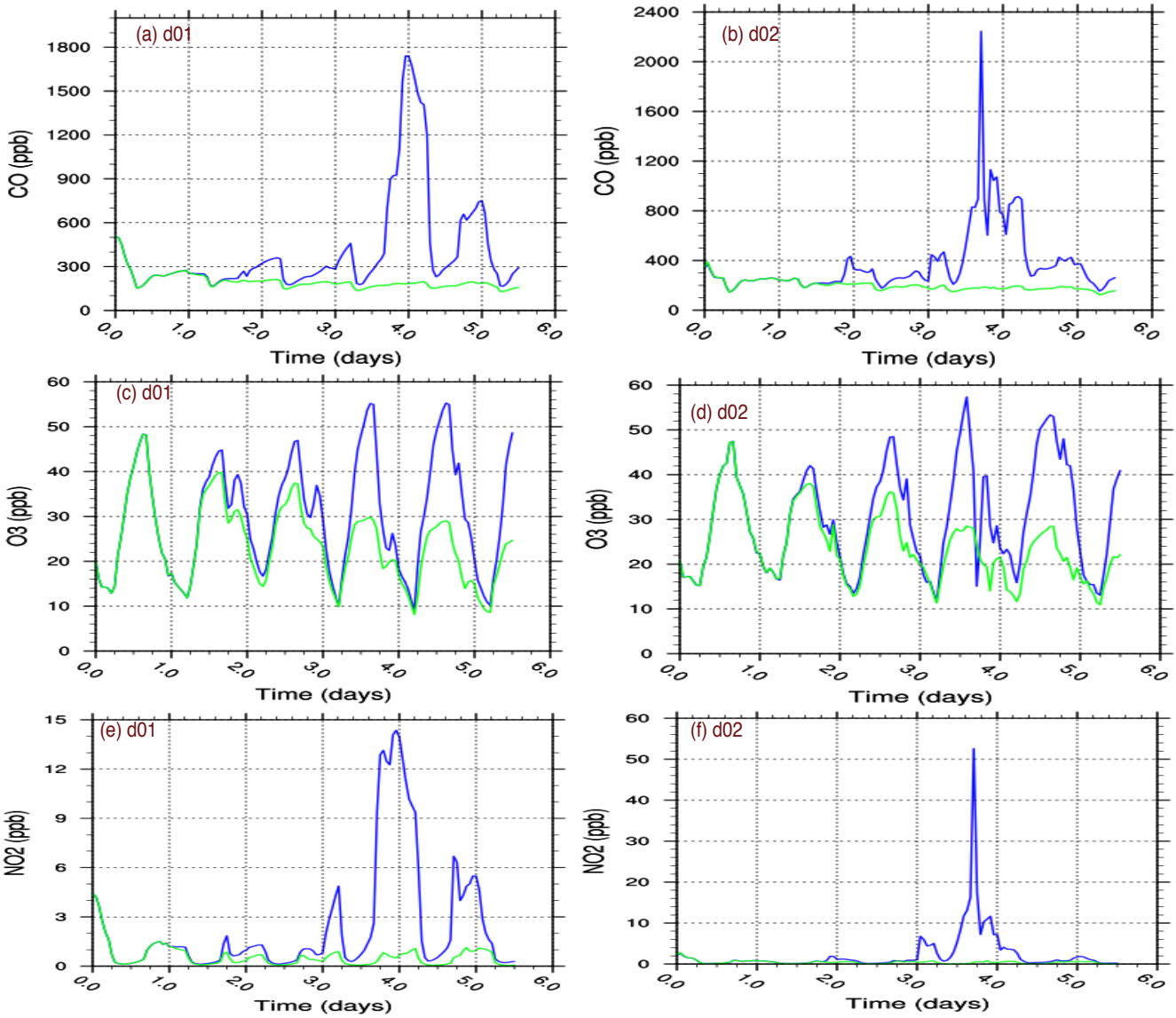

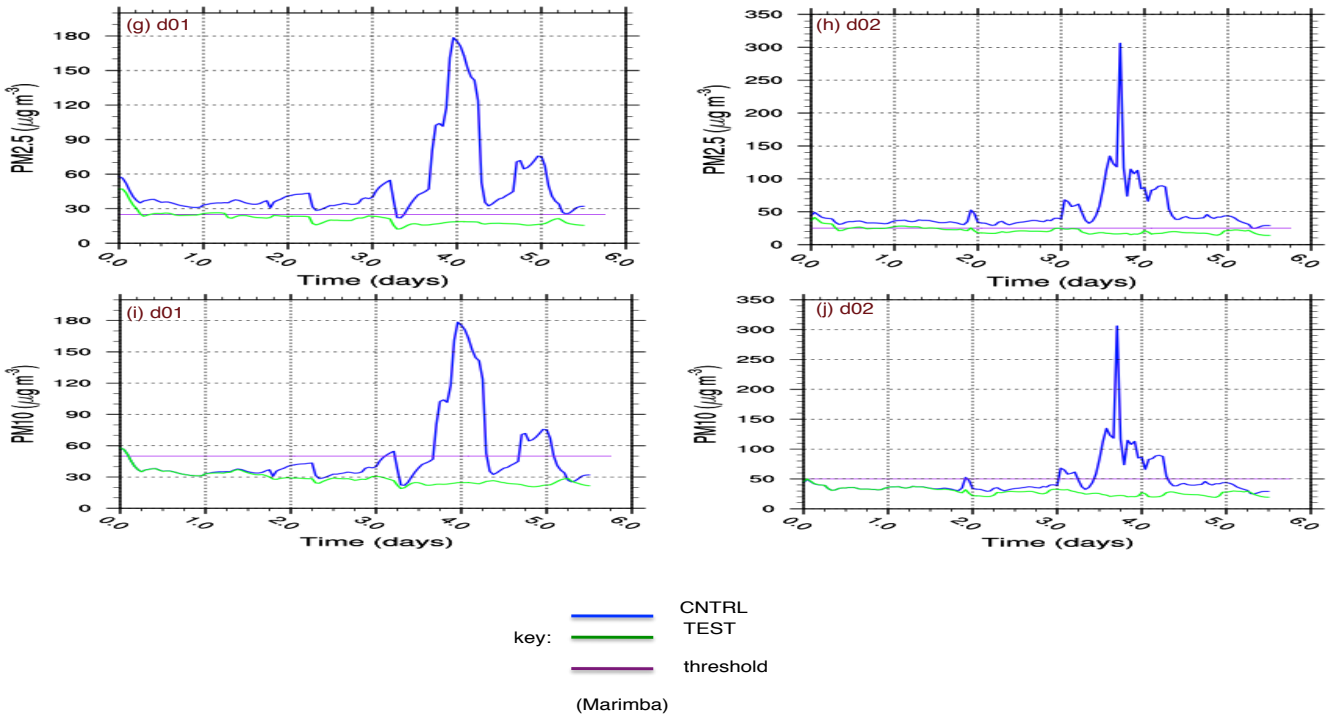
(g) d01
(h) d02
(i) d01
(j) d02
PM2.5 (μg m-3)
PM10 (μg m-3)
Time (days)
key:
CNTRL
TEST
threshold
(Marimba)

(a) Marimba

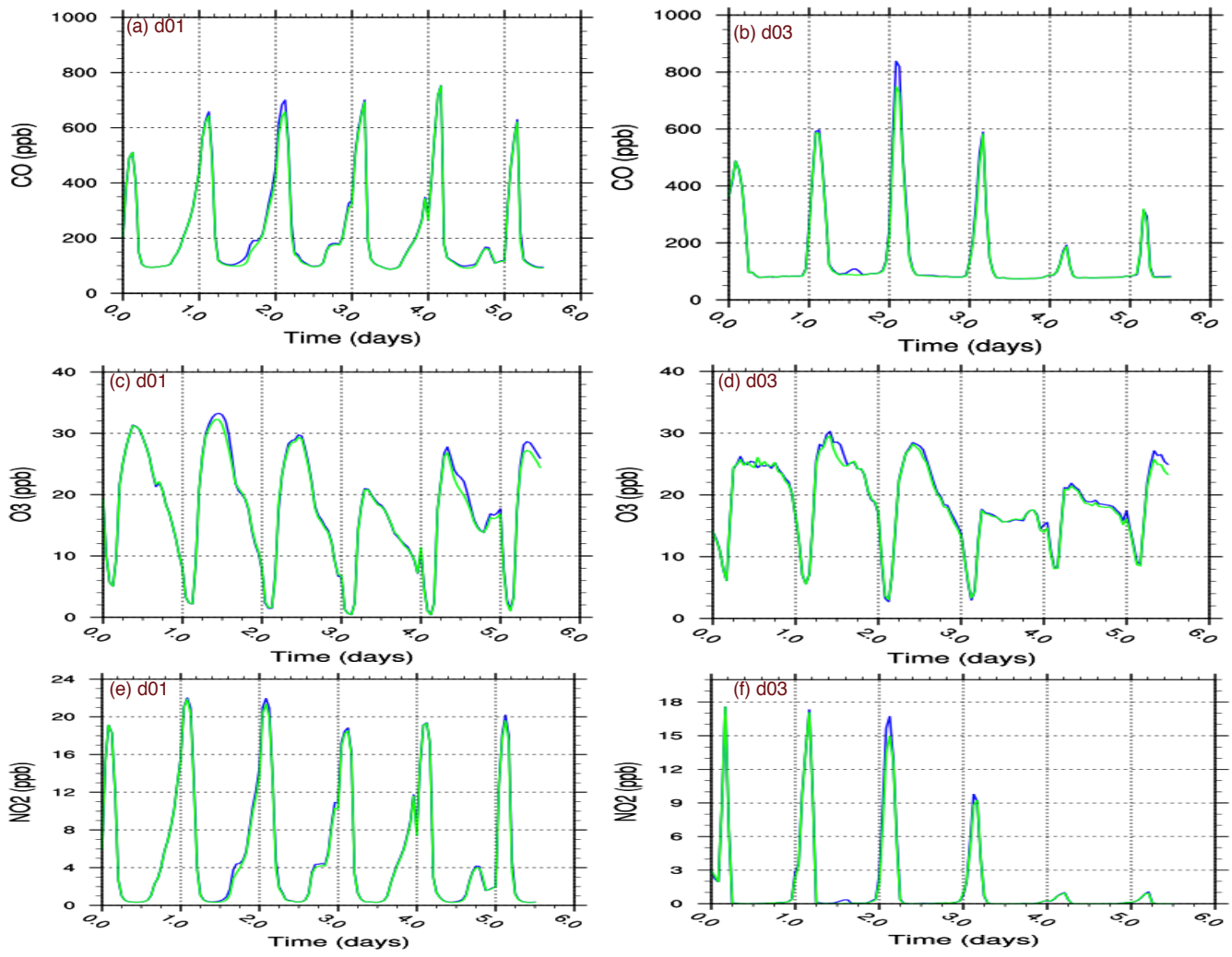
(a) d01
(b) d03
(c) d01
(d) d03
(e) d01
(f) d03
CO (ppb)
O3 (ppb)
NO2 (ppb)
Time (days)

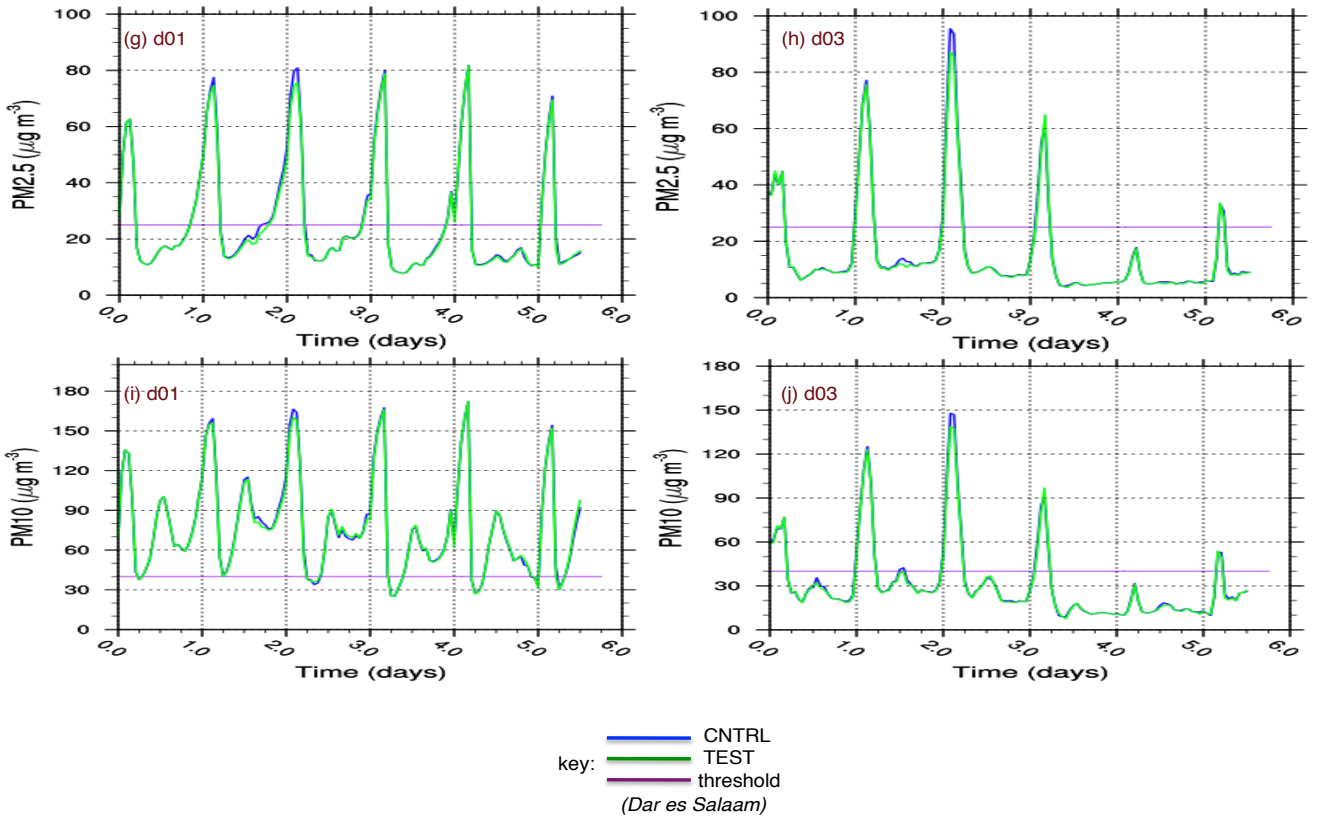

(b) Dar es Salaam

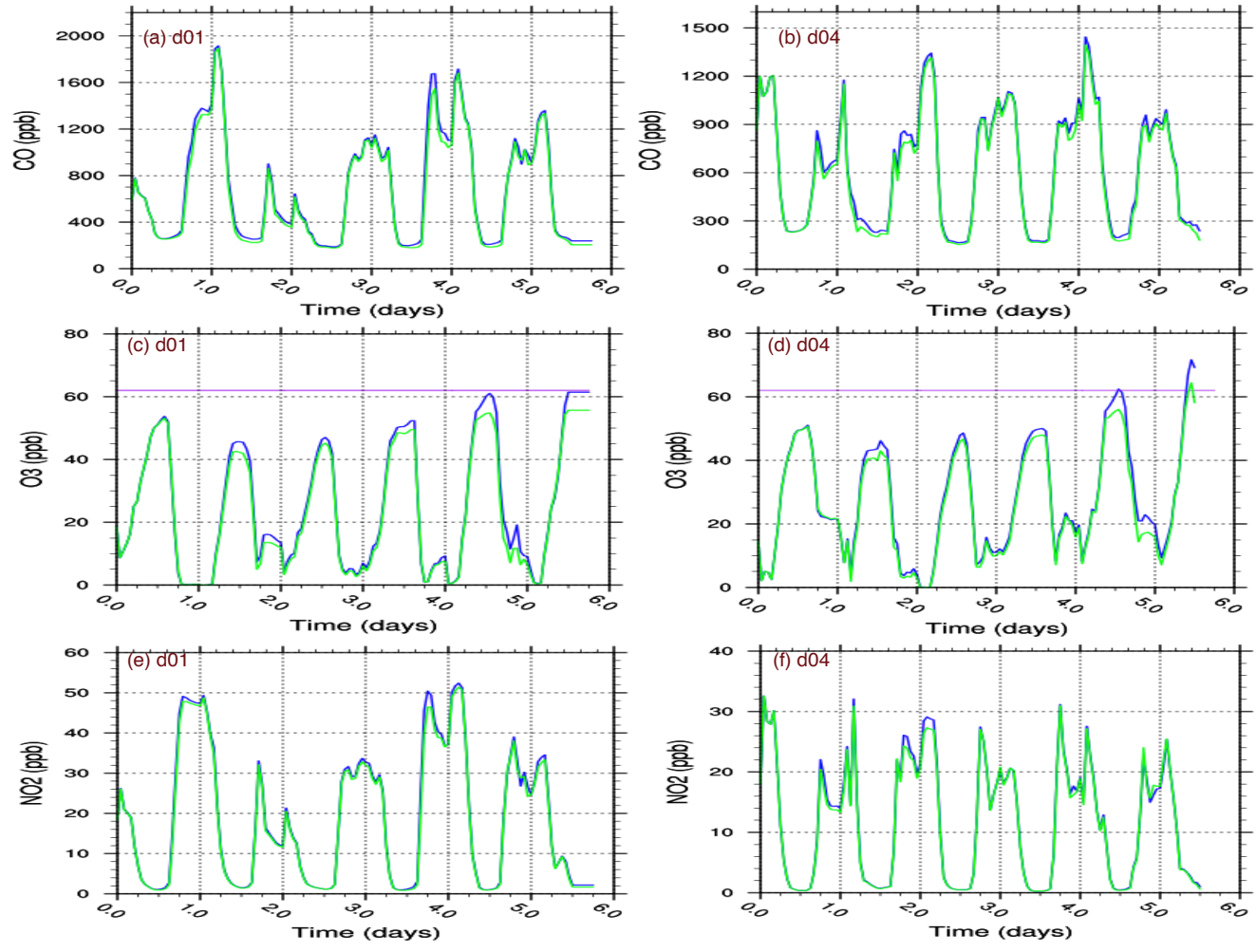

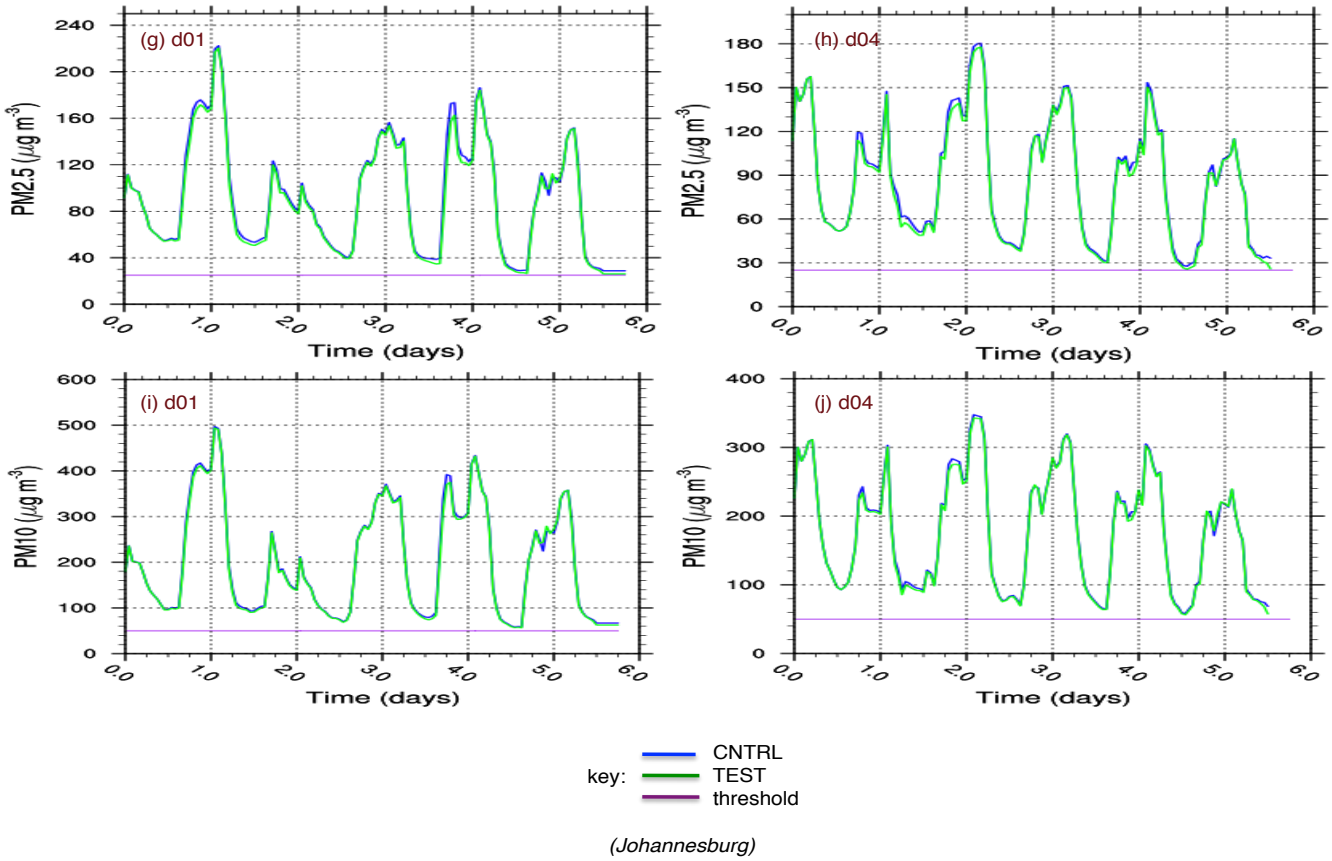

(c) Johannesburg

Fig. 5.11: Mean hourly concentrations (CO, O_3, NO_2, $PM_{2.5}$ and PM_{10}) over (a) Marimba [d02], (b) Dar es Salaam [d03], and (c) Johannesburg [d04]. For each gas/aerosol, left panels represent the coarse grid (20-km) and right panels represent fine grids (4-km). Blue curves represent CNTRL whilst green curves represent TEST. Horizontal line (purple) shows a threshold value. All simulations start at 0000 UTC 5 September.

Table 5.5: Percentage concentration differences for selected cities/towns

City/town	Midnight						Midday					
	O_3	NO	NO_2	CO	$PM_{2.5}$	PM_{10}	O_3	NO	NO_2	CO	$PM_{2.5}$	PM_{10}
Marimba	13 (5)	70 (100)	71 (64)	61 (42)	57 (34)	52 (32)	27 (29)	66 (91)	71 (91)	27 (37)	23 (38)	20 (-29)
Dar es Salaam	0 (6)	4 (0)	4 (13)	4 (4)	3 (5)	4 (3)	4 (4)	6 (50)	8 (50)	4 (4)	0 (3)	-1 (0)
Johannesburg	12 (13)	-4 (24)	3 (0)	3 (3)	1 (2)	0 (0)	8 (8)	9 (6)	14 (16)	9 (11)	5 (7)	4 (4)

Units: %

With reference to Table 5.3, results indicate that although the tropics are subject to more BB than the subtropics, on average, the latter has high pollution. But this can be expected, considering Johannesburg being a megacity (the largest in southern Africa) with more pollution from other sources, especially anthropogenic. PM concentrations over Johannesburg lie above the limit (25 μg m^{-3}

yr^{-1} [$PM_{2.5}$] and 50 μg m^{-3} day^{-1} [PM_{10}]), followed by Dar es Salaam and Marimba. Similarly, O_3 concentration is just below the limit, followed by Marimba and Dar es Salaam (not exceeding 40 ppb). Although the allowed thresholds for PM in table 5.3 are the daily and yearly, comparison with the model prediction give an indication of the pollution scenario during southern African BB event.

As highlighted in the previous chapter, dust emissions over the Kalahari Transect (KT) will have a substantial influence to the high PM loading predicted over Johannesburg and other cities such as Windhoek and Cape Town. Under certain meteorological conditions these emissions will contribute substantially to the total aerosol concentration over southernmost part of Africa. For example a strong gradient in PM_{10} loading observed in Fig. 4.12. Because of these high concentrations, dust emissions will negatively impact on the AQ and also contribute to pollution exceedances of the PM thresholds for cities such as Johannesburg. OIN concentration (not shown) was also found to be relatively higher (over 300 μg m^{-3}), over Johannesburg implying that these particulates are not affected by changes in BB and could probably be from the same source. This also suggests that almost all of the pollution in southwest Africa (and to some extent, Johannesburg and surrounding areas) is influenced by dust emissions. As much as Johannesburg being the largest city regionally (with a lot of anthropogenic sources), these emissions will also contribute substantially to the poor AQ over much of southern Africa. Although it would at least be better for the aerosols to be dust (coarse particulates) than BBAs, they are still bad for human health and AQ; BBAs are smaller and so they can be more harmful than coarse particles. However, coarse particles can still be harmful considering the high concentrations over such populous cities. Thus, there is a strong need to establish that the dust parameterisations in the model are realistic (e.g., making measurements to compare with). Furthermore, work should be done by conducting simulations with- and without dust over the domain, especially over the KT.

5.8 Comparison with in-situ and remotely sensed observations

In this section model results are compared with in-situ measurements and remotely sensed observations of pollutant species over the domain. Measurement data from some point stations, satellites and field studies are compared with predictions from the simulation.

5.8.1 Surface measurements

Surface modelled pollutant concentrations of CO and O_3 are compared with measurements from an observing station (Cape Point) -only one station data available. Daily average concentrations obtained from the World Data Center for Greenhouse Gases [WDCGG]; (http://gaw.empa.ch/gawis/default.asp/), are compared with modelled surface average concentrations to assess its ability to characterise temporal variations. Figure 5.12 shows hourly modelled and

measured CO (a primary combustion tracer) and O_3 (secondary photochemical product of combustion and natural emissions) from the Cape Point station (34.35°S, 18.50°E), South Africa in 2008. These species are selected as they are annually sampled to study the regional haze across a range of environments and meteorological conditions during the campaign. Average modelled CO concentration is about 70 ppb, peaking up to 96 ppb and 160 ppb on 27 August and 6 September (about 1.8 times its background level) respectively. On the other hand, average measured CO concentration in the sampling location was 60 ppb, although there are some days with no data recorded, including the peak concentrations captured in the model.

While the trends shown for O_3 are similar between model and measurement, WRF-Chem predicts low average O_3 concentration (about 26 ppb) than measurement (about 31 ppb). Because the modelled and measured trends are similar, even for secondary species, despite the differences in the average background, this might indicate a bias towards imported pollution from the global MOZART boundary conditions, hence higher predicted primary species. If the model imports higher pollutant concentrations from the boundaries, even if the processes within the model are performed correctly, it would still predict more pollution relative to the background levels.

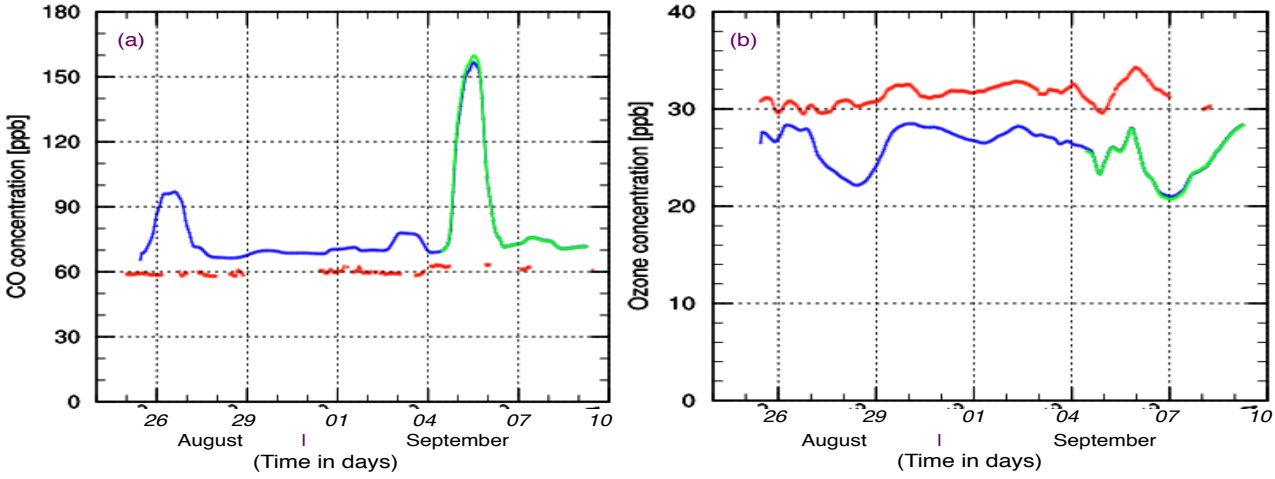

Fig. 5.12: Modelled and measured average for (a) CO and (b) O_3 for the Cape Point station. Source: http://gaw.empa.ch/gawsis/. The red line shows measurement, whereas the blue and green lines show CNTRL and TEST simulations.

Also, for days affected by cloudy conditions, some uncertainties in modelling cloud processes and their interactions with solar radiation could also be some of the reasons for such discrepancies. To check if this is the case or could be other factors within the model (e.g. chemical reactions between species, including biogenic and meteorological influence), likely to be missed in the measurement, I plot (Fig. 5.13) CO output at the initialisation time with MOZART boundary conditions.

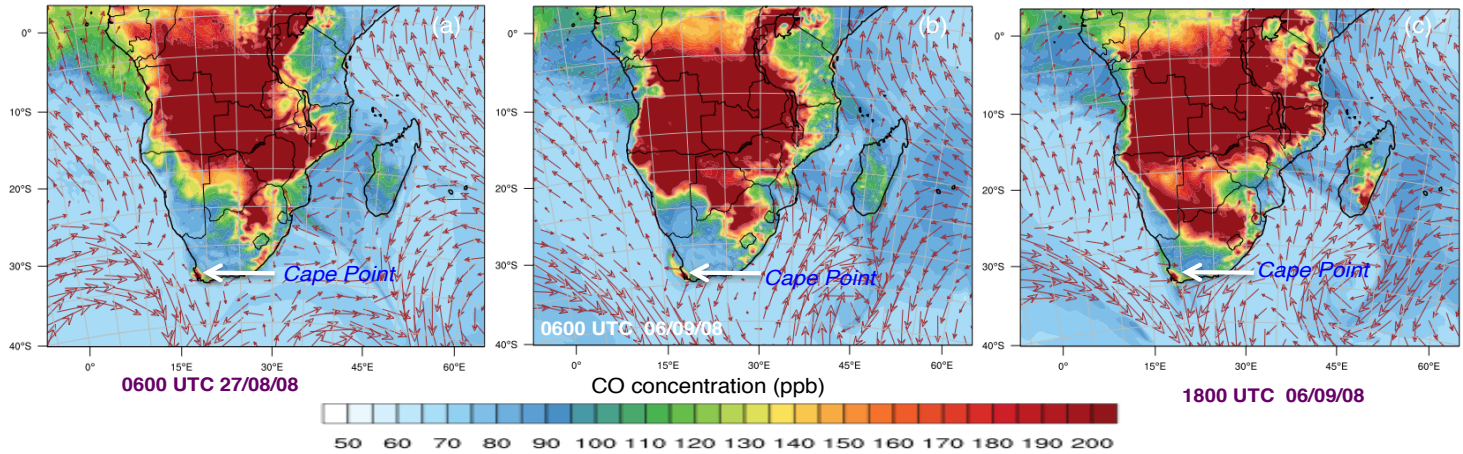

Fig. 5.13: WRF-Chem modelled CO output from MOZART boundary conditions.

Figure 5.13 show surface CO concentration and wind field over southern Africa at (a) 0600 UTC 27 August, (b) 0600 UTC and (c) 1800 UTC 6 September. Vectors show the wind direction. The days plotted correspond to the spikes observed in Fig. 5.12 above, with Cape Point as indicated in Fig. 5.13. As shown, there are hot spots around Cape Point (>100 ppb) suggesting global MOZART conditions could be responsible for the mismatch between the time-dependent trends shown in Fig. 5.12 above. Cape Point experienced westerly wind that provided characteristic flow patterns from the boundaries, thus playing important roles in importing pollution across the domain. The magnitude of the wind speed and vector promote direct streaming of pollution towards Cape Point. This is also consistent with the meteorological field described in chapter 4. Although Cape Point experiences much of marine environment, there would be a considerable influence from urban areas such as Cape Town.

5.8.2 Ozonesondes

Here I discuss simulated vertical profiles of O_3 concentration with measurement from two sonde stations (Lusaka [24°S, 28°E] and Irene [18°S, 26°E]). The ozonesonde sites used are maintained by the Southern Hemisphere Additional Ozonesondes (SHADOZ) project: (http://crock.gsfc.nasa.gov/shadoz/). O_3 profiles for the sondes launched between August and September in Lusaka (2000) and Irene (2007) are compared with model averaged O_3 profiles (there is no data available for 2008). The 2000 Lusaka measurements are obtained from the SAFARI2000 field campaign database (http://www.daac.ornl.gov/S2K/safari.html), whereas the Irene measurements are obtained from the SHADOZ database –collected from different project studies as described in the website. About 6 sondes launched in Lusaka between 6 and 11 September 2000 and 4 sondes launched in Irene between August and September 2007 are averaged and compared with profiles of modelled daily O_3 concentration from the surface up to 10 km above mean sea level (Fig. 5.14). The model and observation show a latitudinal gradient of increasing concentrations with decreasing latitude, although deviations between the model and observation could perhaps result from the spatial resolution of the

model being coarse, relative to that of the spatial coverage of the sondes. The largest discrepancies is observed for Lusaka, where the model underestimates O_3 concentrations in the lower troposphere, despite the location being within region of intense BB. Measured O_3 concentration decreases between 200 and 600 hPa whereas modelled concentrations increases.

For Irene, predictions are fairly similar between the model and the measurement. However, WRF-Chem predicts an enhancement of 5–10 ppb between 500 and 650 hPa, and 10–15 ppb less than the measured data at 300 hPa. Although Irene is not within a region of intense BB, it is most likely to be impacted by the "river of smoke" during the eastwards transport of pollution from the mainland into the Indian Ocean. The deviations observed between the model and sondes could also result from station-to-station variations as well as instrumental precision limits. For example, tropical stations vary in the O_3 data than coastal stations. Thompson et al. (2003) also indicate that higher stratospheric O_3 at Irene can be attributed to higher frequency of midlatitude air.

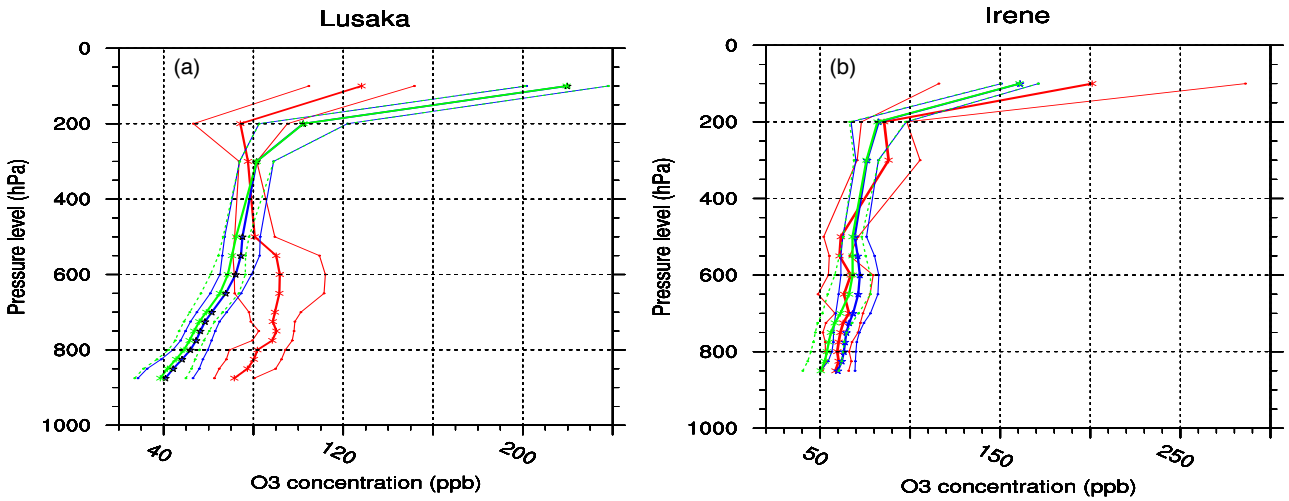

Fig. 5.14: Average comparisons of WRF-Chem modelled and SHADOZ ozonesonde measurements at (a) Lusaka and (b) Irene. Red dashed curve represent measurement whereas green and blue curves represent TEST and CNTRL, whereas thin solid lines represent the standard deviations respectively.

5.9 Summary

This chapter presents an analysis of the contribution of different pollution sources and their influence on the regional pollution from the simulation of a biomass-burning episode. A regional scale online-coupled model system was applied to assess the contributions of different emission sources and feedback processes between chemistry and aerosol pollution. A perturbation (TEST) simulation was conducted during the second half of the base (CNTRL) simulation to assess the contribution due to BB. Both primary and secondary pollutants from natural and anthropogenic sources are accounted for. Statistical analysis for major regulated pollutants is performed (with reference to the standard limits) to investigate pollution enhancement in different locations. Results indicate that BB makes a substantial contribution to the total aerosol concentration over southern Africa, especially in the active burning

regions. For example, tropical central Africa is most affected by BB pollution whereas subtropical southern Africa is relatively more anthropogenically dominated. The high PM loading over the KT indicates a substantial contribution of dust to AQ over the southern part of Africa. These emissions can adversely affect human health from the local centers, leading to pollutant exeedances in some cases. A comparison between the model and measurement was done assess the model and demonstrate its performance in predicting pollutants. The model shows a skill in predicting pollution concentration as well as temporal variations in respective locations of the domain. Although the model show offsets in some cases (e.g. surface O_3 and sondes), the trends are similar to the measurements. However, a severe inavailability of measurement data over southern Africa makes it difficult to adequately assess the model. There is a need for data, especially in a region impacted by high prevalence of BB and growing industrialization such as southern Africa.

The percentage difference in pollutant concentrations was used to describe impact due to BBAs, and it was found that BB emissions are responsible for regional surface enhancement of pollutants close to- or within the burning regions, exceeding the limits in some cases. There is a substantial enhancement of pollution over cities/towns near active burning areas, whilst in the case of the most populous/large cities, the impact is relatively low (see Table C2 in the Appendix). From the CNTRL simulation, most pollutants exceed threshold limits in cities directly impacted by BB emissions. Therefore, populations in such areas with direct impaction by BB can be more at risk, especially during intense BB events. Although secondary pollutants are dependent on primary/precursor species, variations become more regional (because other factors such as meteorology and chemical reactions/processes in the atmosphere play a role) than being localized. It is apparent that BB in southern Africa can be major concern to AQ and human health because even in rural or peri-urban areas pollutant levels are high. Nevertheless, the high concentrations in the tropics appear to be a general condition (because of prevalent BB) than a meteorological condition.

Chapter 6

Influences on aerosol-cloud interactions (ACIs) and radiative forcing

6.1 Introduction

Aerosols play important roles in the earth-atmosphere system and can influence the weather in many ways. For example, they provide the nuclei for cloud droplet formation and ice crystals by serving as cloud condensation nuclei and ice nuclei (CCN and IN) respectively. Whilst aerosols are essential components of cloud formation, they can also influence the atmospheric radiative balance, changes in cloud properties and impact on the atmospheric budget of a wide range of elements and compounds (Pósfai et al., 2003). They affect the atmospheric energy budget directly by scattering and absorbing solar radiation, and contribute to the suppression of evaporation and moisture transport (Salameh et al., 2007). Cloud-nucleating properties from smoke aerosols can perturb cloud microphysics, affecting radiative forcing (RF) and cloud lifetime (indirect effects). On the other hand, absorption of solar radiation can considerably modify atmospheric stability (Salameh et al., 2007).

This chapter focuses on aerosol-cloud interactions (ACIs) and their influence to RF. Here I attempt to use a somewhat more elaborate formulation for ACIs to include more of the physical underpinnings for direct and indirect aerosol effects, and contrast the signatures in RF and responses to pollution. The key area is to explore the feasibility of using WRF-Chem in studying ACIs in the regional domain and the roles aerosol play in weather modification. Specific focus is on the extent to how these interactions are affected by changes in aerosol concentrations due to biomass burning (BB) and various feedback mechanisms such as parameterisation, leading to different cloud responses.

6.2 Aerosols, clouds and radiative interactions

Aerosols can affect or alter the earth-atmosphere system in various ways. Broadly these effects are classified into aerosol radiative-interactions (ARIs) and ACIs. The interactions are commonly described as direct and indirect aerosol effects (or cloud adjustments due to aerosols: IPCC, 2013). Depending on the particle size, abundance, chemical composition and ambient environment, aerosols serve as CCN and facilitate cloud droplet formation, while on the other hand altering cloud properties and hence precipitation formation. Overall, the processes are influenced by the characteristics of CCN population entering clouds at the beginning and during its growth (Teller and Levin, 2006) or those near the clouds. Aerosol-induced change on cloud droplet number and size with resultant impacts on cloud brightness is known as the ‘first indirect’ effect, albedo effect or Twomey effect (Twomey, 1977; Sherwood et al., 2011). The change in cloud droplet number can affect cloud microphysical

properties and ultimately affect cloud lifetime and precipitation formation (Haywood et al., 2003). This is known as the 'second indirect' effect or Albrecht effect (Albrecht, 1989). Clouds that form in polluted environments may be characterised by high concentrations of small-sized droplets (Twohy et al., 2005), and can enhance cloud albedo and suppress precipitation (Yorks et al., 2009).

Absorption of radiation due to absorbing aerosols can contribute to atmospheric radiative heating and the so-called 'semi-direct' effect. Aerosols such as black carbon (BC) can absorb solar radiation; the process is accompanied by increase in emitted thermal energy, leading to increase in atmospheric air temperature. Ultimately, this has implications on the relative humidity (RH) that decreases due to a deficit in ambient vapour pressure. This process facilitates cloud droplet evaporation and contributes to cloud dissipation.

6.3 Knowledge gaps and hypothesis

As well as their importance in the atmosphere, aerosols impact on the global climate. The potential impacts of aerosol feedbacks on clouds and climate are described in four terms: direct, semi-direct, first indirect and second indirect effects. In particular, the indirect effect is subject to large uncertainties so much so that cloud representation is one of the key challenges in climate modelling (Klein et al., 2012; Ma et al., 2014). The main reason is that accurate representation and prediction of clouds and small-scale processes is not easily achieved even with the fine scale models and most cloud processes occur at scales far smaller than can be resolved by climate models. The dynamics, radiation, clouds and trace components interact in numerous ways, making the estimates difficult.

The southern African dry season (May–August) is dominated by BB type-of-pollution, during which there is a clear signal of strong interactions between aerosols and cloud microphysics. Emissions and other by-products from BB are frequently observed over land, and at the same time persistent deck of stratocumulus covers the west coast, influencing long-range transport over the Atlantic Ocean (Peers et al., 2014). During summer, the nocturnal low-level jet carries pollutants from the coastal landmass and interactions with biogenic emissions may lead to formation of secondary aerosols (Knippertz et al., 2015). These species interfere with the radiative budget and affect the amount of solar radiation reflected or scattered back into space and partly absorbed by the atmosphere. To investigate this, I employ the same approach described in chapter 5 (section 6.4). In order to frame the investigation of the influence on ACIs and RF due to BB, I hypothesise that:

1. During periods of enhanced burning or increased pollution, there is a significant change in the intensity of light directly scattered/absorbed across the domain. Aerosol optical depth (AOD) reaches its maxima in areas in close-proximity to the fires and the air quality (AQ) at the ground is worse due to absorbing aerosols confined to a shallow layer not impacting the overall column above.

2. BB contributes a considerable amount of semi-direct effect largely driven by increased lower tropospheric stability due to BC absorbing aerosols in the column, inducing a significant 'burn off' to cloud layers where BC coincides with clouds in the domain.

3. Changes in BB aerosol loading lead to perturbations in cloud droplet size and number concentration, substantially influencing radiative forcing.

In the analysis, I examine the changes in different model domains at high and low resolution. Results are presented and discussed for both simulations, paying attention to regions where the changes are very significant.

6.4 Modelling approach

The approach described in chapter 5 will be used here, comparing the two model scenarios (CNTRL and TEST). All domains (and sizes) are the same as described in chapter 4. Similarly, CNTRL covers the entire simulation period described in chapter 4 (26 August through 10 September 2008), and the TEST simulation was conducted only for the second half of the CNTRL (5–10 September) to assess the impact/changes in aerosol concentration due to BB aerosols (BBAs). The TEST was initialized at 0000 UTC 5 September with the same meteorological conditions, trace gas and aerosol quantities (except BB emissions) to ensure that differences between the two simulations are due to BB emissions only. For analysis (to address the hypotheses above), I focus on the period 5–10 September 2008.

6.5 Results and discussion

The first part of the analysis (sub sections 6.5.1–6.5.2) focuses on the nature of sources of CCN and their interactions with cloud properties, effects of changing aerosol concentration on the RF and cloud parameterisations. The second part (section 6.6) addresses the hypotheses with respect to the implications from the results.

6.5.1 Cloud condensation nuclei (CCN)

While ACIs through the indirect effects depend on a number of environmental factors, the primary aerosol-related quantity is the cloud condensation nuclei (Sihto et al., 2011, and references therein). In this section, I demonstrate the relationship between aerosols and cloud processes via CCN. I shall focus only on model prediction (see Chapters 1 and 2 for details) and discuss model-simulated CCN concentrations over the domain to shed light on CCN spectra corresponding to activated particles and how they are affected by parameterisations in the model. CCN number is key to cloud droplet number concentration (CDNC) dependent on factors such as particle composition and ambient conditions. This can be computed at different supersaturation levels in WRF-Chem (Chapters 3 and 4). Figure 6.1 shows CCN concentration at 1.0% supersaturation (CCN6), calculated at the cloud base, only where

there are clouds in the domain, plotted in each domain at 1800 UTC 6 September 2008. For simplicity, I present CCN at only one supersaturation in the figures, but will account for other supersaturations in the discussion.

The figure shows the potential number of particles that can activate into cloud droplets at 1% supersaturation. This is the highest supersaturation level in WRF-Chem, at which the maximum number of aerosols can be activated. At the lowest supersaturation (CCN1[0.02%]), only a few particles activate into cloud droplets. The figure shows how changes in aerosol concentration affect CCN spectra. Results also show responses to the aerosol changes at different grid spacing, indicating that at dx = 4 km (fine grids) more processes can be explicitly resolved. High concentrations are predicted over land than the marine environment; for example, highest CCN concentration (order of 3000 cm^{-3}) is observed over Angola, Democratic Republic of Congo (DRC) and Tanzania. CCN concentrations increase in the CNTRL simulation. For the TEST simulation, CCN maxima only reach up to 2000 cm^{-3}. Again the concentrations are higher in the tropics than in the subtropics. It is evident that spatial pattern of aerosol number concentrations result in varying CCN number concentrations, and influenced by BB.

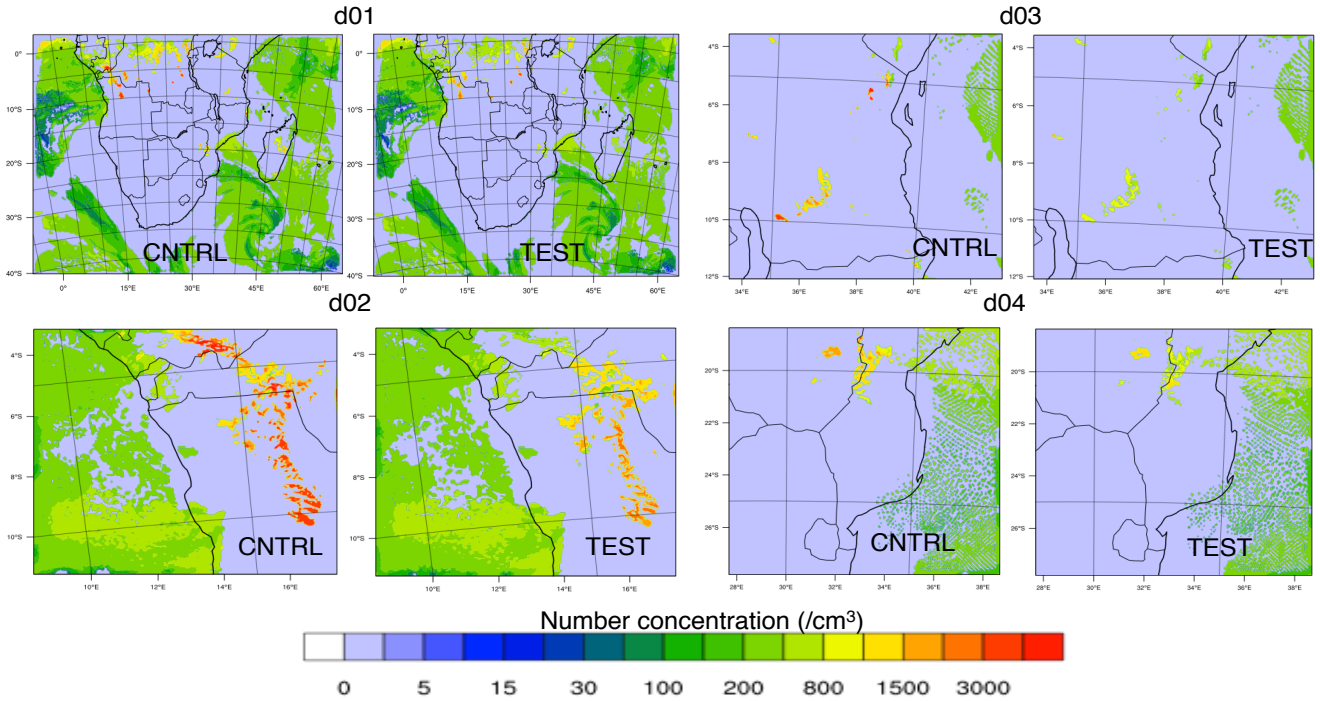

Fig. 6.1: CCN number concentrations, plotted at the layer below cloud base where there are clouds in the grid cell. CCN plotted at 1.0% supersaturation only. Model output at 1800 UTC 6 September 2008.

Figure 6.1 indicate that the number concentration for CCN particles increases in areas dominated by BB emissions. This indicates the contribution by BBAs to cloud formation via CCN, as noticed between CNTRL and TEST simulations. Also, the high CCN number concentrations over land indicate

the difference between continental aerosols and marine aerosols, even when BB emissions are excluded from the simulations. For example, the aerosol number concentration can be higher over the ocean (due to sea salt), yet CCN number concentration is still low. However, calculations for supersaturation (Fig. 6.3) indicate that areas with high CDNC concentrations over land correlate with relatively low supersaturation and vice versa. For example, effective supersaturation $S_{eff} \geq 0.5\%$ is predicted mainly over the ocean than over land, whereas high CCN are predicted over land (see also Figs. 4.15 and 4.17). This indicates the relationship between CCN, CDNC and critical supersaturation S_c. The pattern of the CCN strongly depends on the supersaturation, while the distribution depends on the size distribution and chemical composition of aerosol particles, which determines the shapes of the CCN spectra and therefore distribution of CCN at different supersaturations (Bangert et al., 2011).

To further demonstrate the quantification of CCN, I plot the temporal variation of CCN6 between d01 and d02 (Fig. 6.2) over the entire period. Blue curve represent prediction from d02 whereas the brown curve represent prediction from d01. At low resolution, the model predicts low CCN number –order of 800 cm^{-3} compared to the high resolution, which predicts over 2500 cm^{-3} CCN. Figure 6.1 also shows areas with high CCN number.

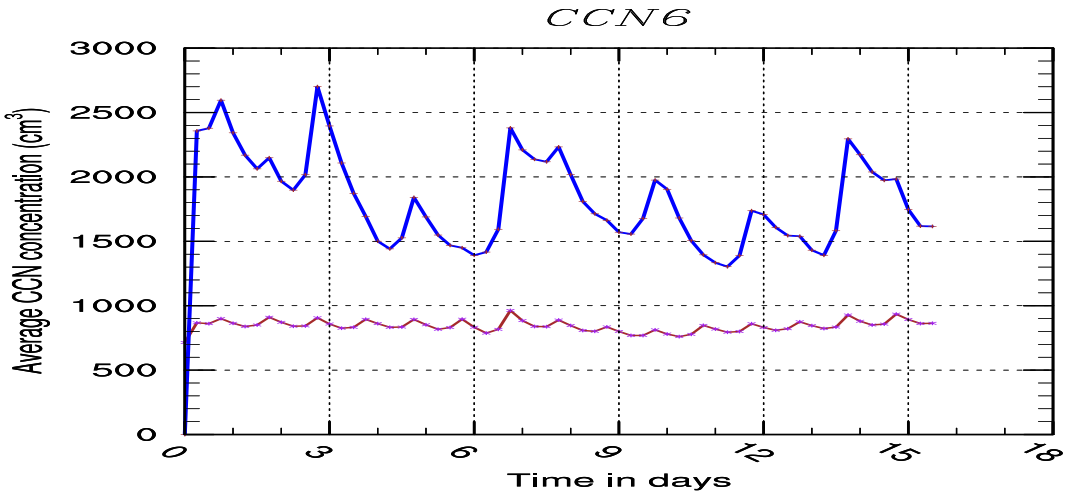

Fig. 6.2: CCN6 temporal variation over the entire simulation period. CCN plotted at 1.0% supersaturation only where there are clouds in the grid cell. Blue and brown curves represent outputs averaged across d02 and d01 respectively.

The process leading to cloud formation start from condensation of supersaturated water vapour onto hygroscopic particles (or those containing water-soluble compounds –referred to as CCN). CDNC is determined by the CCN entering cloud base and from entrainment of particles at cloud boundaries (Flossmann, 1998). Figure 6.3 show maximum CDNC (Nd_{max}) and the corresponding supersaturation S_{eff} at 1800 UTC 6 September 2008, plotted in each domain. Figure 6.3(a) is plotted at the level where maximum CNDC is predicted over the domain, within the lowest cloud bands only, whereas Fig. 6.3(b) is generated by predicting S_{eff} corresponding to the CCN spectra shown in Fig. 6.1 above. The

vectors show the wind direction. CDNC is maximum (order of 2000 cm^{-3}) over the same locations where maximum CCN in Fig. 6.1 is predicted -over Angola, DRC and Congo-Brazzaville. Whilst more clouds are predicted over the ocean, deep convection occurs over land, corresponding to higher aerosol concentrations. Droplet number increases in the CNTRL than in the TEST. Still over the oceans, some areas show a patchy distribution in Nd_{max}.

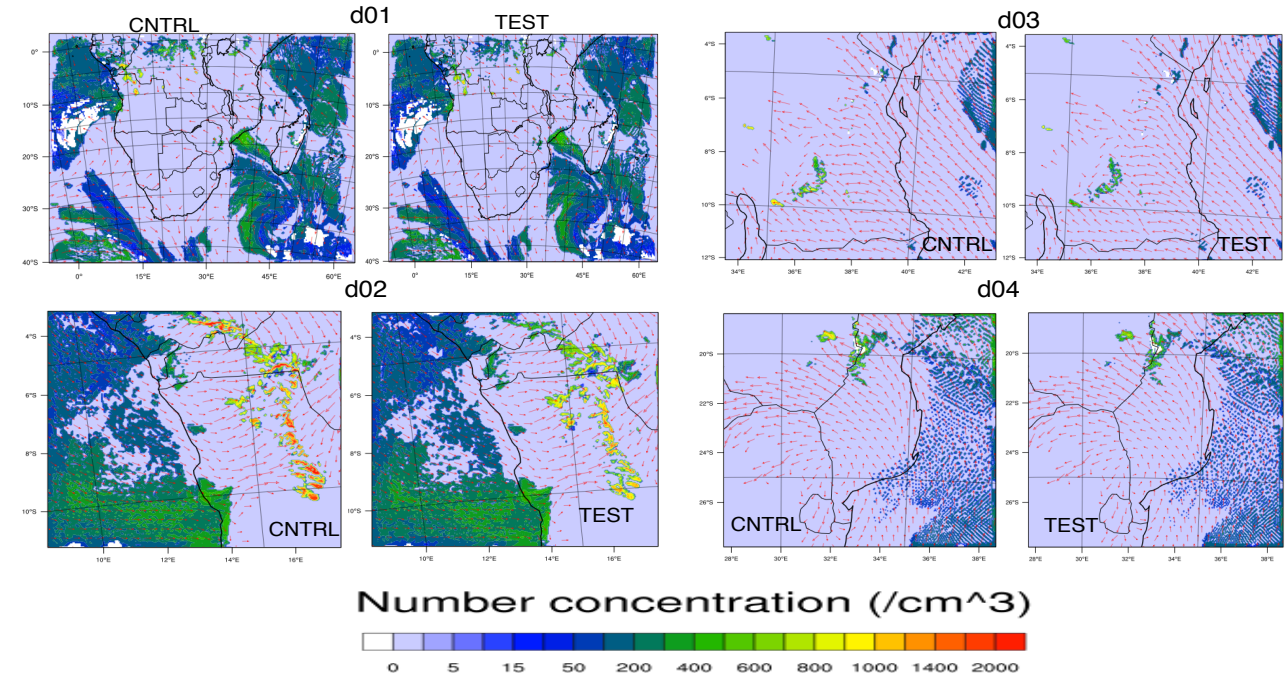

(a) Nd_{max}

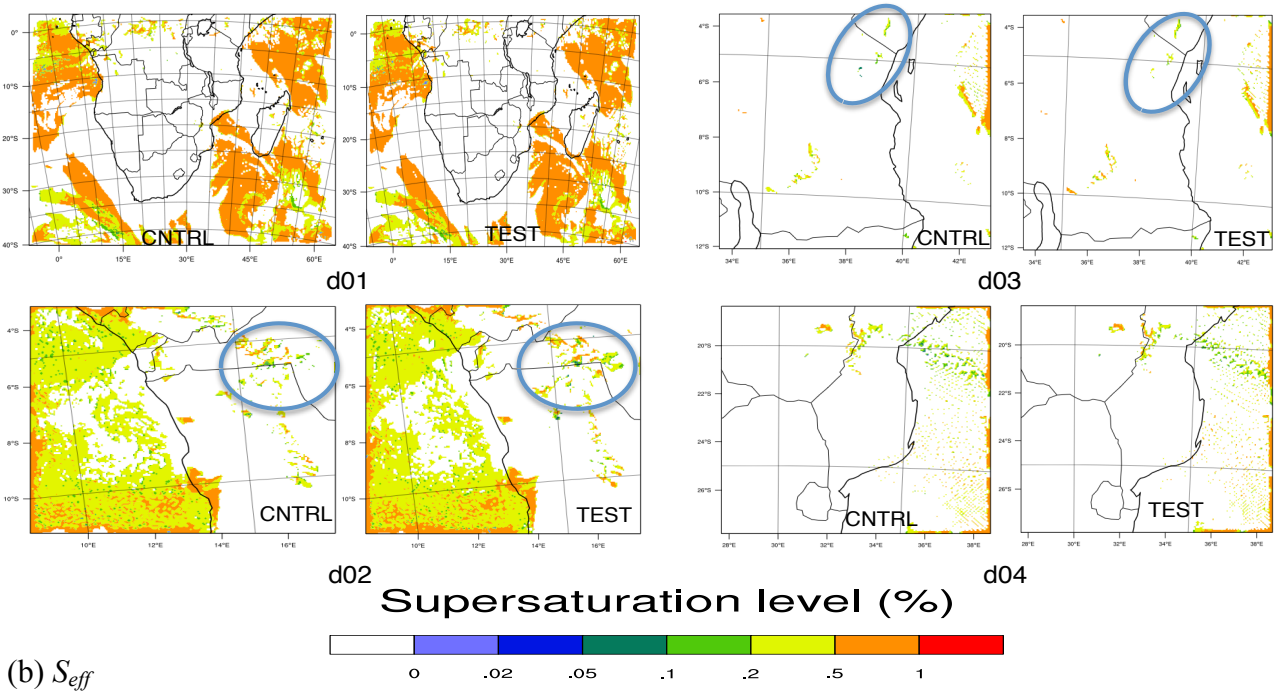

(b) S_{eff}

Fig. 6.3: Model predictions for (a) maximum cloud droplet number, Nd_{max} and (b) effective supersaturation S_{eff}. Nd_{max} is plotted only where there are clouds in the grid cell, whereas S_{eff} is determined just above cloud base where CCN concentration is diagnosed. Model output at 1800 UTC 6 September 2008.

Variations in CDNC between domains and model scenarios indicate cloud responses to aerosol concentrations at different grid resolutions (i.e. parameterised vs. resolved clouds). Comparing the sub-domain regions at high and low resolutions highlights the sensitivity in the model predictions. For example in the coarse grid, locations of high Nd_{max} are characterized by cellular clouds, correlated with high supersaturations, whereas fine grids have diffuse clouds with relatively low supersaturations. A closer look at Fig. 6.3(b), for the fine grids shows that S_{eff} decreases where Nd_{max} increases. Thus for a given saturation level, increase in particle number decreases environmental maximum supersaturation S_{max}. Although there are close similarities in supersaturations between the simulations (compared to CCN and clouds), there are some differences in the fine grids (highlighted in circles) in some parts of the domains. The above section demonstrates how aerosols (serving as CCN) form clouds, as well as cloud properties under different aerosol concentrations and grid resolution. However, although CCN concentrations do not necessarily give the same CDNCs, they are a convenient means of characterizing the cloud nucleating ability (Schwartz and Slingo, 1995).

Next, I show profiles of cloud droplets over the domain (i.e. corresponding height for Nd_{max} and vertical cross section through clouds). Figure 6.4 is a longitude-height profile plotted at 5°S at 1200 UTC and 1800 UTC 6 September. This is a slice across d01 from Fig. 6.3(a) above, through a region of deep convection in the west-east direction. The barbs show wind direction at respective height above the surface. Maximum Nd_{max} values are predicted over land close to the west coast. Although clouds form at the same altitudes (in both simulations), the dynamics vary, depending on changes induced due aerosol input. For example, high concentrations in the CNTRL indicate more elevated aerosols from the fires.

Portions of elevated deep clouds in the west are within the regions of high pollution concentrations as shown in the previous chapters. This is where BB burning is most prevalent, demonstrated by the difference between CNTRL and TEST. However, the response of CDNC to changes in aerosol population and chemical properties can be non-linear and vary from one region to another with time (e.g. Yuzhi et al., 2014). Therefore, estimates of the net ACIs on the radiative balance can be restricted to specific atmospheric conditions, climate regimes and/or cloud types. This will be discussed in section 6.6 below.

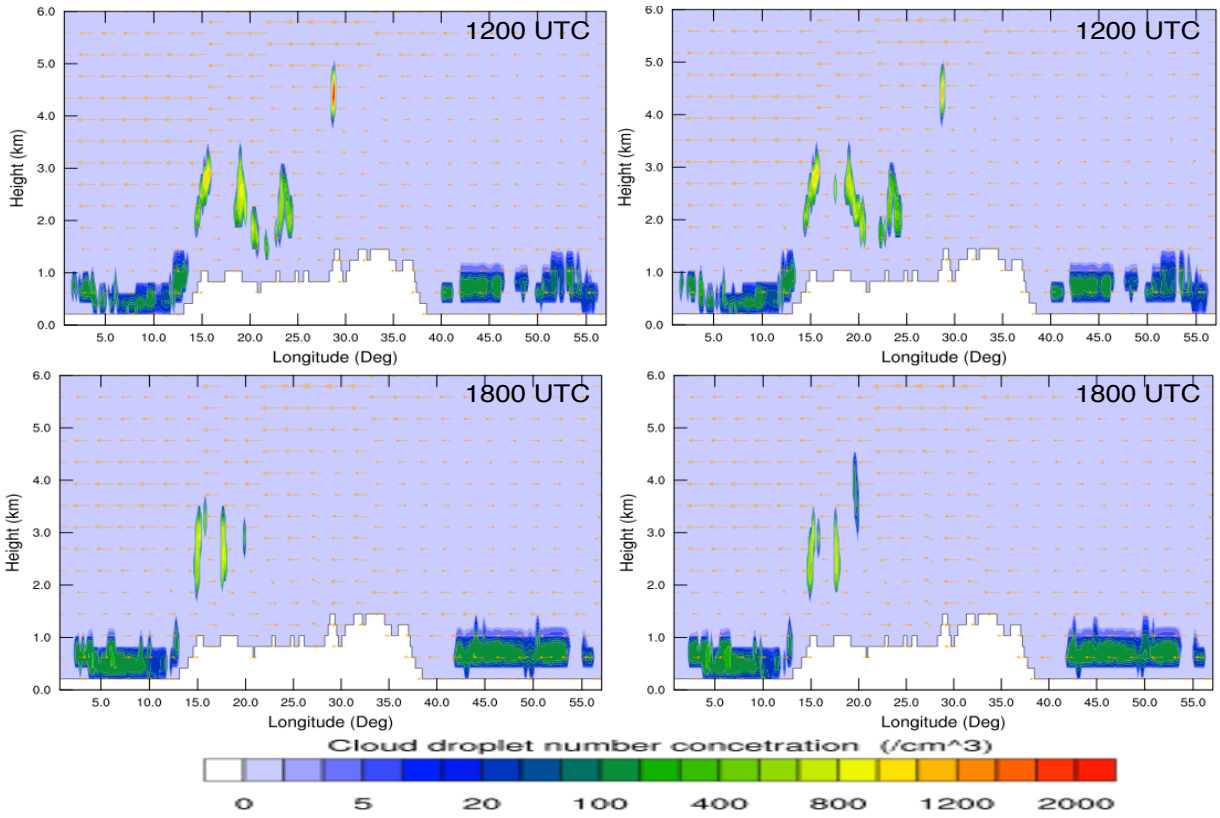

Fig. 6.4: Vertical profiles of Nd_{max}, fixed at 5°S latitude in west-east cross section plotted for the outermost domain. Left panels represent CNTRL and right panels represent TEST. Model output at 1200 UTC and 1800 UTC 6 September 2008.

Similarly, the time series of CDNC plotted in Fig. 6.5 shows the temporal variation during the entire period. CDNC increased in the afternoon towards morning of the next day (minimum at midday). Minimum average droplet number is predicted between 3 and 5 September (days 9–11), while maximum is predicted on 26–27 August and 9 September.

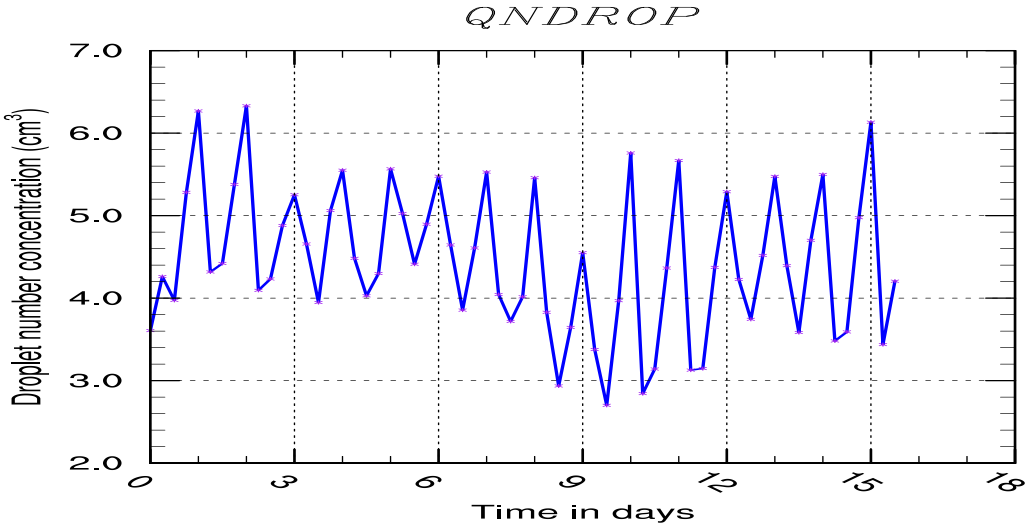

Fig. 6.5: Time series for cloud droplet number variation. Model output from 0000 UTC 26 August to 1200 UTC 10 September over d01.

6.6 Implications of results and hypothesis testing

We have presented results from the simulations showing how the dynamics change with respect to aerosol concentrations –in this case, due to BB. This section focuses on the hypotheses formulated in section 6.3 to investigate effects of changing aerosol concentration and impact due to BB. First, I present statistical data determined for the quantities: CCN, BC aerosol concentration, cloud fraction (CLD FRAC), CDNC (Nd), AOD, single scattering albedo (SSA [ω_o]), QCLOUD and liquid water content (LWC) to test the hypotheses. The metrics (Tables 6.1–6.4) are computed for all grids at vertical levels (pressure altitudes) averaged over the domains for which the simulation was conducted. I compare results domain-wise, unless where the interest is on one/some parts of the domain. The hypotheses are addressed below: section 6.6.1 focus on aerosol direct effects while section 6.6.2 focus on indirect effects.

Results discussed here are for the 5-day simulation period described in section 6.4 above and all the quantities presented are averages over this period. The first part presents metrics from which the percentage differences between CNTRL and TEST are used to describe contribution due to BB emissions. Throughout this section, the symbol Δ represents the difference between the two simulations. Tables 6.2–6.4 show statistics for the fine grids (for each level, I show metrics at 4-km and 20-km grid spacing); brown and orange fonts indicate TEST results at 4 and 20-km grid spacing, while blue font indicates CNTRL at 20-km. For d01, green font indicates TEST. The main focus of this section is to investigate feedbacks between aerosols, clouds and implications on the radiative budget. Whilst some statistical results in the plots are given in terms of days (days 1 to 6), variations for the modelled clouds and aerosols between the two simulations are more pronounced after the first day. The numbered days correspond to 5–10 September respectively. In the analysis, I shall discuss some results for days 8 and 9 September (days fairly away from the initial conditions of the TEST case) during which there were substantial effects due to aerosol concentrations and significant changes in cloud properties.

Table 6.1: Mean concentrations for d01, averaged over the first 8 pressure levels.

Level	BC	CCN1	CCN2	CCN3	CCN4	CCN5	CCN6	Nd	Qcld	Cldfra	Lwc	AoD	SSA
1000	0.03	4.72	16.8	52.6	117	211	277	9.01	0.014	0.13	0.482	0.32	0.93
	0.03	4.72	16.6	51.4	113	200	265	8.76	0.014	0.13	0.478	0.24	0.93
950	0.08	3.92	19.6	65.6	154	310	400	27.5	0.055	0.24			0.93
	0.06	3.89	18.3	59.6	134	259	340	27.1	0.054	0.24			0.93
900	0.19	3.84	28.8	97.3	236	492	617	15.6	0.029	0.13			0.94
	0.15	3.74	25.8	83.9	192	381	489	15.1	0.029	0.13			0.94
850	0.32	4.02	38.6	131	331	686	843	5.46	0.011	0.05			0.95
	0.24	3.83	33.1	107	251	494	621	5.08	0.013	0.05			0.95

800	0.38	3.95	41.5	143	361	739	896	2.58	0.013	0.02			
	0.28	3.72	35.1	116	273	536	663	2.15	0.005	0.02			
700	0.42	3.57	41.7	168	397	801	943	1.16	0.005	0.01			
	0.28	3.20	31.8	115	262	535	655	0.93	0.001	0.01			
600	0.33	2.64	31.7	147	333	699	828	0.74	0.001	0.02			
	0.18	2.25	21.2	84	186	421	527	0.64	0.001	0.02			
500	0.15	1.63	15.1	67.2	156	497	497	0.13	0.000	0.03			
	0.09	1.52	11.8	47.6	105	374	374	0.12	0.000	0.03			

Units: BC [µg m^{-3}]; CCN [cm^{-3}]; Nd [cm^{-3}]; S_{eff} [%]; Qcloud [g kg^{-1}]; Lwc [g m^{-2}]

Table 6.2: Mean concentrations for d02, averaged over the first 8 pressure levels.

Level	BC	CCN1	CCN2	CCN3	CCN4	CCN5	CCN6	Nd	Qcld	Cldfra	Lwc	AoD	SSA
1000	0.22	3.15	36	108	218	343	394	2.38	0.001	0.013	0.643	3.15	0.90
	0.22	3.39	39	118	234	342	412	2.46	0.001	0.020	0.637	3.19	0.90
	0.12	2.14	23	69	150	239	285	20.5	0.008	0.136		0.74	
	0.13	2.17	23	70	151	239	285	21.1	0.008	0.140		0.46	
950	0.29	3.18	40	125	279	510	612	74.0	0.115	0.357			0.90
	0.25	3.39	41	123	256	422	502	73.6	0.115	0.398			0.91
	0.23	2.78	34	104	239	438	540	61.7	0.176	0.485			
	0.20	2.78	32	97	212	360	443	61.6	0.178	0.482			
900	0.67	5.97	79	248	581	1021	1170	23.1	0.051	0.102			0.91
	0.58	5.77	73	219	483	775	878	22.1	0.050	0.140			0.91
	0.64	5.75	75	234	549	969	1115	21.1	0.052	0.141			
	0.56	5.59	69	209	463	746	844	19.8	0.050	0.134			
850	1.1	7.88	111	358	869	1506	1688	3.05	0.004	0.010			0.90
	0.88	7.34	97	300	694	1109	1226	2.30	0.003	0.013			0.92
	0.10	7.59	105	334	807	1398	1569	3.32	0.005	0.018			
	0.83	7.13	93	286	660	1062	1176	2.53	0.004	0.016			
800	1.4	8.06	124	428	1091	1963	2197	3.82	0.002	0.006			
	0.97	6.95	96	316	763	1270	1412	2.56	0.002	0.008			
	1.29	7.88	126	410	1041	1886	2115	6.78	0.004	0.016			
	0.93	6.85	94	307	741	1246	1387	4.75	0.003	0.015			
700	1.5	6.67	117	507	1237	2285	2512	4.31	0.002	0.004			
	0.81	4.88	71	278	662	1201	1356	3.09	0.002	0.006			
	1.44	6.64	115	498	1226	2259	2483	5.37	0.002	0.007			
	0.81	4.94	71	277	669	1223	1381	4.45	0.003	0.007			
600	1.1	4.67	83	437	1001	1873	2055	2.37	0.001	0.002			
	0.46	2.77	39	169	390	783	913	1.91	0.001	0.004			
	1.09	4.52	84	447	1023	1909	2087	1.34	0.001	0.002			
	0.46	2.86	40	176	408	819	950	1.32	0.001	0.003			
500	0.50	2.01	33	182	454	1872	1193	0.25	0.000	0.001			
	0.12	1.37	14	65	154	783	473	0.22	0.000	0.004			
	0.50	2.04	34	186	466	1044	1229	0.30	0.000	0.008			

	0.16	1.41	15	68	163	394	495	0.32	0.000	0.008			

Units: BC [μg m^{-3}]; CCN [cm^{-3}]; Nd [cm^{-3}]; S_{eff} [%]; Qcloud [g kg^{-1}]; Lwc [g m^{-2}]

Table 6.3: Mean concentrations for d03, averaged over the first 8 pressure levels

Level	BC	CCN 1	CCN 2	CCN3	CCN4	CCN5	CCN6	Nd	Qcld	Cldfr	Lwc	AoD	SSA
1000	0.07	3.18	17.7	79.0	148	290	416	0.00	0.000	0.000	0.101	0.26	0.91
	0.06	3.19	17.1	75.2	136	259	378	0.00	0.000	0.000	0.100	0.18	0.91
	0.06	3.01	16.0	69.9	136	272	398	0.01	0.000	0.000		0.26	
	0.05	3.02	15.5	66.2	124	238	356	0.01	0.000	0.000		0.17	
950	0.13	2.90	20.4	87.3	195	420	587	9.20	0.007	0.056			0.91
	0.09	2.83	17.8	74.1	149	296	436	8.90	0.007	0.053			0.92
	0.11	2.64	17.7	74.7	170	376	535	43.2	0.034	0.233			
	0.07	2.60	15.6	64.0	132	269	404	40.9	0.034	0.234			
900	0.19	2.43	21.6	85.6	226	532	726	5.72	0.014	0.047			0.92
	0.11	2.30	17.1	64.5	138	322	469	5.35	0.013	0.029			0.93
	0.18	2.29	20.4	78.5	216	522	714	6.41	0.018	0.051			
	0.10	2.16	16.1	58.4	134	317	460	5.63	0.018	0.050			
850	0.25	2.49	25.3	95.8	273	660	885	1.82	0.003	0.012			0.93
	0.14	2.29	18.7	65.3	160	362	521	1.38	0.003	0.008			0.94
	0.25	2.34	26.7	92.5	268	661	882	2.12	0.002	0.009			
	0.13	2.15	18.1	63.1	158	366	520	1.49	0.002	0.009			
800	0.30	2.42	27.3	105	303	730	945	0.35	0.003	0.003			
	0.16	2.19	19.7	69.3	173	393	537	0.30	0.003	0.002			
	0.30	2.30	26.7	104	303	735	946	0.22	0.000	0.001			
	0.16	2.07	19.2	68.0	173	397	536	0.18	0.000	0.001			
700	0.49	2.90	42.6	201	504	1081	1278	0.32	0.001	0.001			
	0.21	2.27	24.4	92.1	217	459	575	0.18	0.001	0.001			
	0.52	2.92	44.4	212	531	1139	1342	0.28	0.000	0.001			
	0.22	2.26	25.1	96.2	228	482	599	0.16	0.000	0.001			
600	0.40	2.42	34.1	159	380	819	977	0.88	0.002	0.002			
	0.17	1.90	19.5	73	165	369	466	0.43	0.002	0.002			
	0.41	2.48	35.6	167	398	857	1020	0.77	0.001	0.001			
	0.17	1.93	20.3	76.2	172	380	476	0.43	0.001	0.002			
500	0.09	1.48	12.3	47.5	104	263	350	0.00	0.000	0.000			
	0.09	1.48	12.2	46.3	101	255	341	0.00	0.000	0.000			
	0.09	1.48	12.3	47.4	104	263	350	0.00	0.000	0.000			
	0.09	1.48	12.2	46.4	101	255	341	0.00	0.000	0.000			

Units: BC [μg m^{-3}]; CCN [cm^{-3}]; Nd [cm^{-3}]; S_{eff} [%]; Qcloud [g kg^{-1}]; Lwc [g m^{-2}]

Table 6.4: Mean concentrations for d04, averaged over the first 8 pressure levels.

Level	BC	CCN1	CCN2	CCN3	CCN4	CCN5	CCN6	Nd	Qcld	Cldfr	Lwc	AoD	SSA
1000	0.15	8.28	37	114	237	478	643	3.43	0.001	0.016	0.063	0.45	

	0.09	8.21	32.8	94.3	172	310	446	2.74	0.001	0.013	0.062	0.40	0.91
	0.14	7.22	33.0	102	222	456	621	12.0	0.008	0.052		0.44	0.92
	0.08	7.18	29.2	84.0	159	289	422	9.26	0.008	0.052		0.39	
950	0.39	9.95	63.3	196	456	917	1159	5.56	0.003	0.032			0.92
	0.22	9.55	51.1	144	279	481	656	5.28	0.002	0.030			0.92
	0.38	9.29	60.4	187	441	890	1127	15.7	0.018	0.082			
	0.22	8.98	49.4	139	274	472	644	15.3	0.018	0.081			
900	0.55	10.7	79.4	243	566	1102	1375	2.46	0.004	0.019			0.93
	0.34	10.2	65.5	185	371	630	834	2.31	0.007	0.011			0.93
	0.54	10.4	77.7	237	555	1081	1344	2.73	0.007	0.021			
	0.34	9.96	65.0	183	371	630	827	2.53	0.006	0.021			
850	0.63	10.6	86.4	265	609	1143	1421	0.52	0.004	0.002			0.94
	0.45	10.1	74.5	214	444	749	972	0.40	0.004	0.002			0.94
	0.62	10.4	85.1	260	596	1117	1380	0.81	0.001	0.002			
	0.45	9.99	74.5	214	445	748	959	0.54	0.001	0.001			
800	0.65	9.80	84.0	261	592	1091	1344	0.25	0.000	0.003			
	0.51	9.42	74.7	219	459	772	981	0.21	0.001	0.003			
	0.64	9.73	83.3	256	582	1071	1311	0.42	0.000	0.001			
	0.51	9.44	75.3	219	462	774	971	0.34	0.000	0.000			
700	0.52	6.42	60.1	196	430	781	967	0.01	0.000	0.000			
	0.46	6.25	56.1	177	373	648	819	0.00	0.000	0.000			
	0.52	6.37	59.6	193	422	757	919	0.00	0.000	0.000			
	0.56	6.25	56.3	176	373	637	783	0.00	0.000	0.000			
600	0.25	2.78	27.8	109	231	481	619	0.02	0.000	0.000			
	0.21	2.66	25.0	93.5	192	401	531	0.01	0.000	0.000			
	0.24	2.73	27.1	106	223	463	584	0.02	0.000	0.000			
	0.20	2.65	24.6	91.8	189	391	505	0.01	0.000	0.000			
500	0.13	1.62	14.9	65.0	140	330	439	0.00	0.000	0.000			
	0.10	1.56	13.2	65.4	117	282	381	0.00	0.000	0.000			
	0.13	1.63	15.1	65.4	142	334	443	0.00	0.000	0.000			
	0.10	1.58	13.5	56.8	119	286	385	0.00	0.000	0.000			

Units: BC [μg m^{-3}]; CCN [cm^{-3}]; Nd [cm^{-3}]; S_{eff} [%]; Qcloud [g kg^{-1}]; Lwc [g m^{-2}]

6.6.1 direct aerosol effects

(a) First hypothesis

H1. The hypothesis proposes that during periods of enhanced burning or increased pollution, there is a significant change in the intensity of light directly scattered/absorbed across the domain. AOD(τ_λ) reach maxima in areas in close-proximity to the fires and the AQ at the ground is worst due to absorbing aerosols confined to a shallow layer not impacting the overall column above.

Firstly, AOD (defined as reduction of light intensity due to scattering and absorption by particles along the column) is determined from the two model simulations for all grids. Then I compare and discuss

results computed for different model grids between the two simulations. Figure 6.6 shows AOD at 550 nm at 1800 UTC 8 September 2008, plotted for domains d01 and d02. I focus on these two grids because of the predicted high AOD in the west. Panels on the left represent CNTRL whilst panels on the right represent TEST. Tropical central Africa is characterized by an increased build-up in BBAs, forming a regional haze with high AOD (location of greatest fire emissions). AOD becomes stronger around BB-dominated regions, decreasing southward across the landmass. Highest AOD are predicted over Angola, DRC and neighbouring Congo-Brazzaville, and some parts of western Zambia and Botswana.

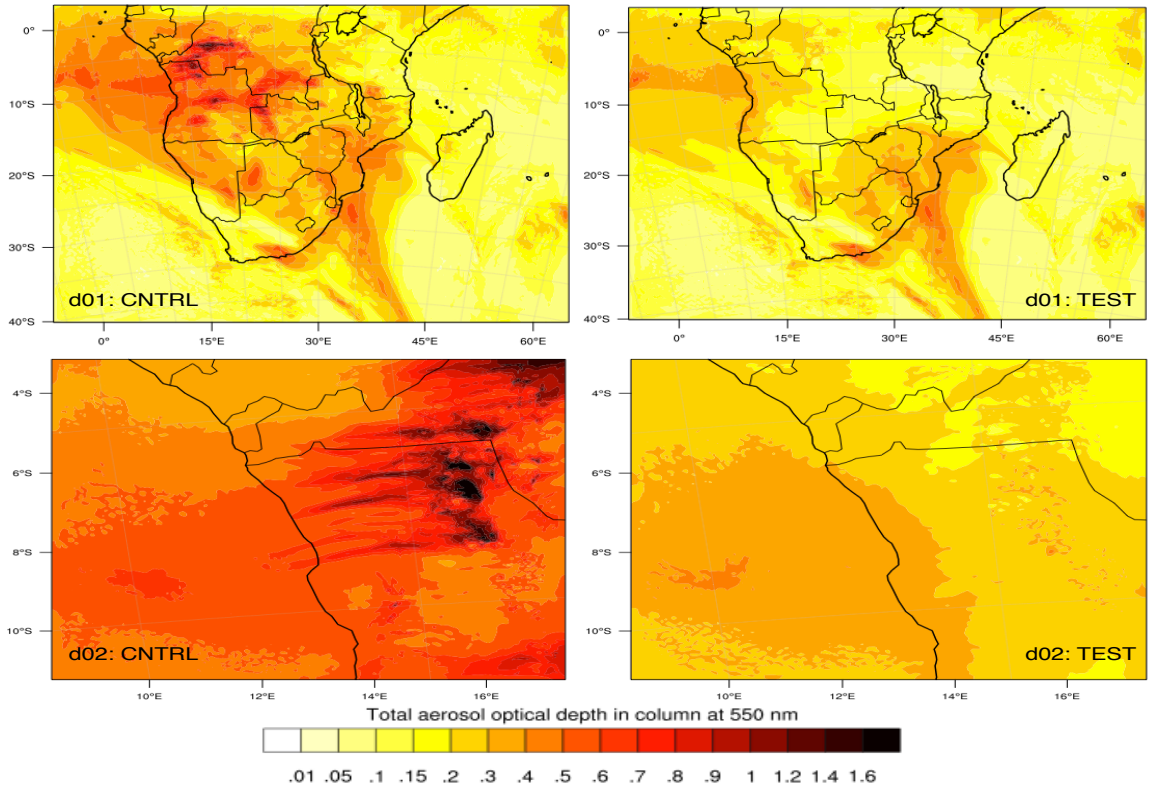

Fig. 6.6: Aerosol optical depth at 550 nm. Left panels represent CNTRL while the right represents TEST simulation. Model output at 1800 UTC 8 September 2008.

In CNTRL, maximum AOD reach up 1.6 over these regions while the southern part reach only up to 0.6. An increase in AOD over the ocean is influenced by carbonaceous aerosols above the cloud layers (Skaeda et al., 2011). The effect of aerosol is very much reduced in the TEST over the domain. For example, some parts of the landmass have AOD less than 0.1. This indicates that BBAs induce a substantial effect over southern Africa. From tables 6.1–6.4, the percentage differences were determined from ΔAOD for all grids. These are found to be: +26%, +38%, +31% and +11% for domains d01, d02, d03 and d04 respectively.

Next, I show temporal profiles to demonstrate AOD variation across the 5-day period over all grids (Fig. 6.7). In all the panels, blue curves (with red asterisks) represent CNTRL whilst brown curves (with green asterisks) represent TEST. For instance, in d01, CNTRL varies between 0.28 and 0.33 whilst TEST drops to 0.19 by the end of the simulation. In d02, both curves drop from 1.05 (at the start) to about 0.6 by the end of day 1 (i.e. evening of 5 September). Thereafter, CNTRL peak to 0.98 after day 4 (8 September); the first peak at mid day on 7 September. TEST decreases like in d01, but to a minimum of 0.33 at the end.

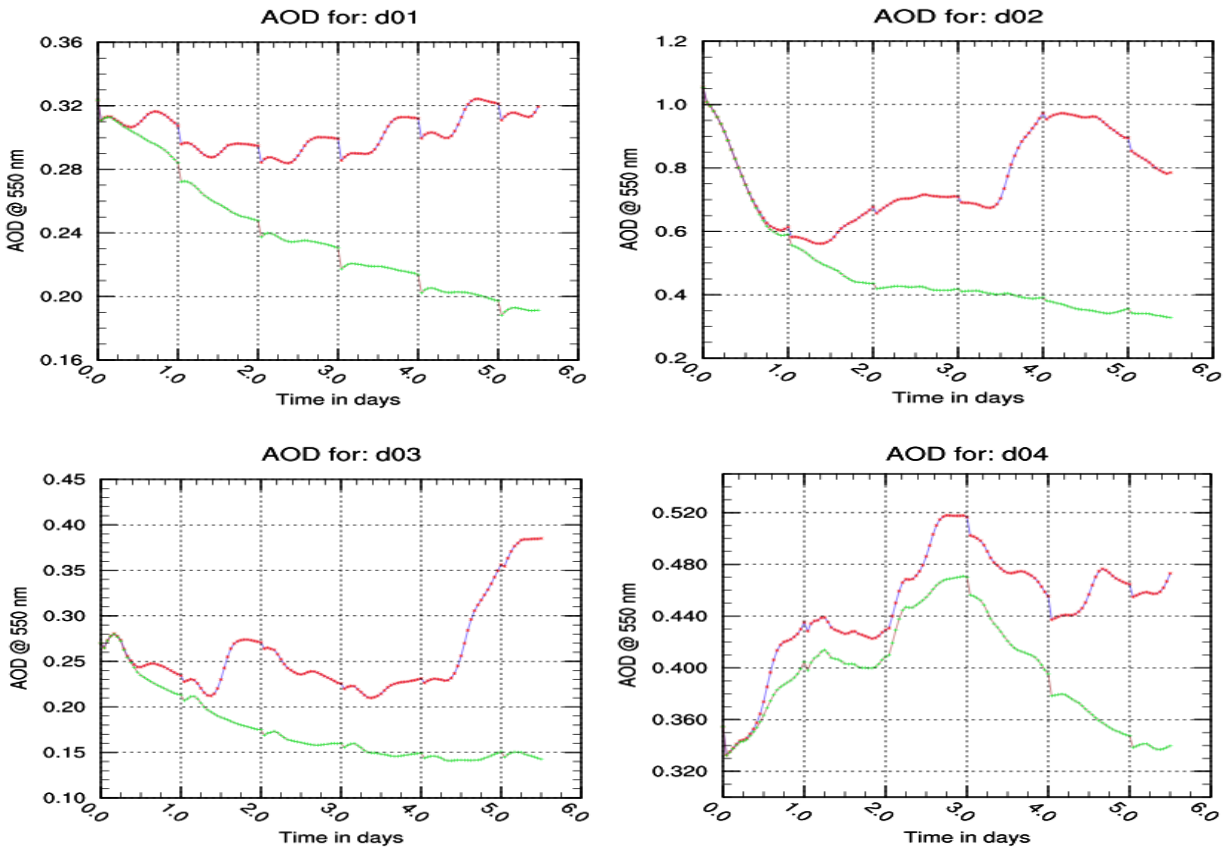

Fig. 6.7: Time series AOD at 550 nm between 5 and 10 September 2008. Curves with red makers represent CNTRL while curves with green markers represent TEST. All simulations start at 0000 UTC 5 September.

For d03, CNTRL varies between 0.22 and 027 within the first 2 days (first peak occurring at 1800 hrs on 6 September), and subsequently increases to 0.38 at the end; TEST maintains a 'near-steady' pattern until reaching a minimum of 0.14 at the end. The pattern shown by d04 is very much different from other domains; AOD increases in both curves (CNTRL peaks to 0.52 whilst TEST reach 0.46) on the evening of day 3 (7 September). By the end of the simulation, both curves drop to 0.47 and 0.34 respectively. This indicate that in the southernmost part, not only BBAs are responsible for AOD variation, although not as much as in d02. This could also be associated with the high PM_{10}

concentration predicted over South Africa (see Figs. 4.12–4.14 in Chapter 4). Conditions under which AOD relates to aerosol effects are such that:

for - AOD = 0: no aerosol effect
- AOD ~ 1: large aerosol effect
- AOD > 1: extremely high aerosol concentrations.

In chapter 4 (section 4.7.5.1) AOD was computed from the simulations with- and without dust to determine the contribution due to PM from dust emissions. As shown here, BBAs make a major contribution across d01 and dominate PM in d02 and d03. Also, there is a substantial contribution to AOD from dust aerosols in d04, although not as much as BB. The coarse dust particles contribute to AOD mostly in the lowest model layers whereas fine particles contribute throughout the column up to higher altitudes. This was shown in $PM_{2.5}$ output, which comprises fine particles. Fine particles can be lofted higher into the atmosphere, and those from the fire emissions can be pumped higher because of buoyancy from the fires. Dust-dominated regions contributed about 0.6 to the AOD in places in the KT, whereas BB-dominated region contributed up to 1.6 at their peaks. Most of the contribution to AOD comes from BBAs as observed in Fig. 6.6 above. It is worth mentioning that in chapter 4, AOD was only plotted from the CNTRL simulation (with- and without dust), whereas in this chapter the AOD is plotted from the CNTRL and the TEST scenarios. Both simulations here have dust switched "ON", hence the difference between Fig. 4.14 and Fig. 6.6.

Single scattering albedo (SSA or ω_o)

Aerosol single scattering albedo (ratio of scattering to the total light extinction) is another critical parameter in determining direct aerosol impacts. BBAs exhibit a much higher variability in optical properties due to different aerosol types and combustion characteristics. For example, BB has a large BC content, which is a good absorber of radiation, a result which leads to a decrease in shortwave radiation near the surface (Grell et al., 2011a). Regions affected by dense BB display a large variability in SSA, depending on the relative contribution of different aerosol types. Aerosol concentration with high absorbing components tend to scatter less radiation energy than aerosol concentration with less absorbing components. The expression for ω_o is given by:

$$\omega_o = \frac{\sigma_{sca}}{\sigma_{ext}} = \frac{\sigma_{sca}}{\sigma_{sca} + \sigma_{abs}} \qquad ; 0 \le \omega_o \le 1 \qquad [6.1]$$

where σ_{sca} is scattering coefficient, σ_{ext} is extinction coefficient and σ_{abs} is absorption coefficient. Like AOD, ω_o is computed at four wavelengths in WRF-Chem: 300 nm, 400 nm, 600 nm and 1000 nm respectively. Figure 6.8 shows ω_o at 600 nm, computed for all grids. Results for the TEST (blue

curves) increase higher than CNTRL (red curves), indicating that without BB, particles are less absorbing (opposite to AOD). For ω_o close to 0, all particle extinction is due to absorption, whilst ω_o close to unity indicates that all particle extinction is due to scattering. Again, the trend in d04 differs markedly to the other domains –a reason that could be alluded as above for AOD.

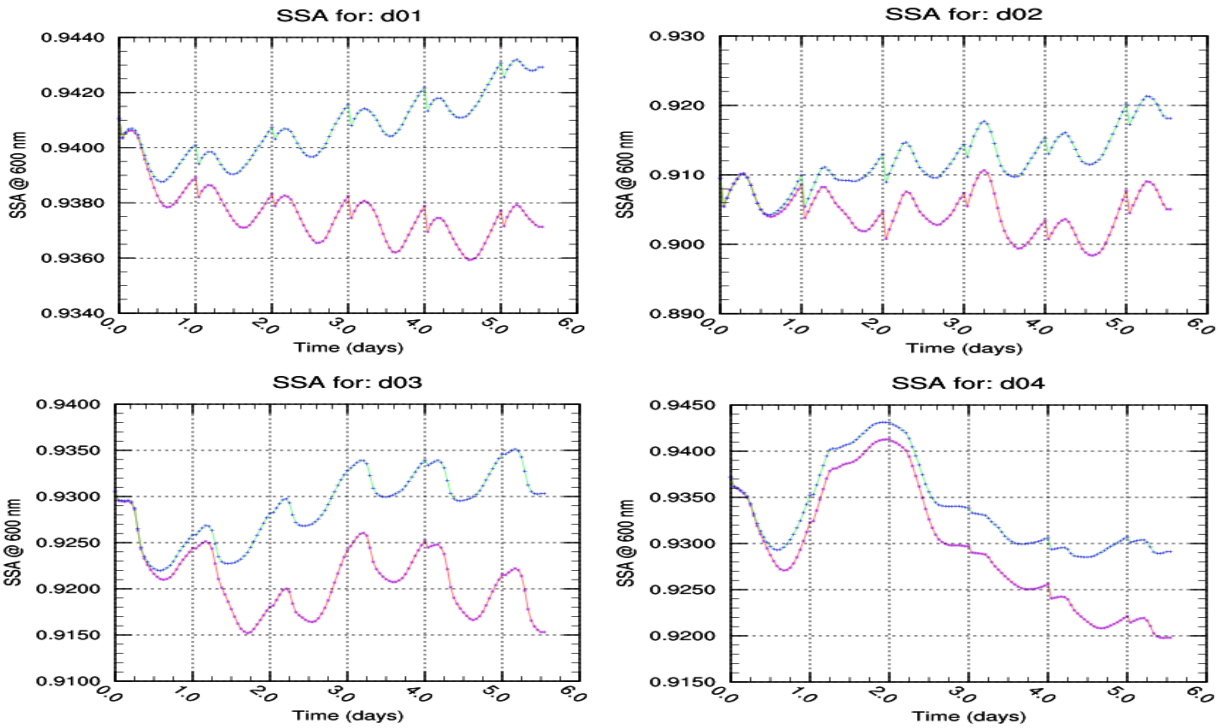

Fig. 6.8: Aerosol SSA (hourly averages) across the 5-day campaign. The red curves (with purple asterisks) represent CNTRL while the green curves (with blue asterisks) represent TEST. Small domains are plotted at 4-km each. All simulations start at 0000 UTC 5 September.

6.6.2 Comparing model predictions against measurements

This section also focuses on comparing the model prediction against measurements to evaluate the representativeness of the column-integrated AOD against measurements in order to assess the sensitivity of the cloud microphysical properties with respect to BBAs. I attempt to quantify ACIs focusing on the high aerosol production by performing the same kind of analysis, comparing model results with statistical data from the measured background values in order to account for the non-linearity in AOD. Although the main goal is not to verify against measurement, it is gratifying to be able to show that the model does a reasonable work in simulating aerosols and weather patterns. Model simulated AOD is compared with the MODIS onboard the Aqua-Terra satellite-retrieved measurements as well as the SAFARI 2000 field measurements.

Figure 6.9 shows time series of the column integrated AOD at 550 nm from WRF-Chem and MODIS measurement (http://giovanni.gfsc.nasa.gov/giovanni/). The measurement data is obtained for the

region during the period over which the model was applied. The red curves represent measurement whereas the blue and green curves respresent the CNTRL and TEST simulations respectively. Dashed lines indicate the standard deviation in each case.

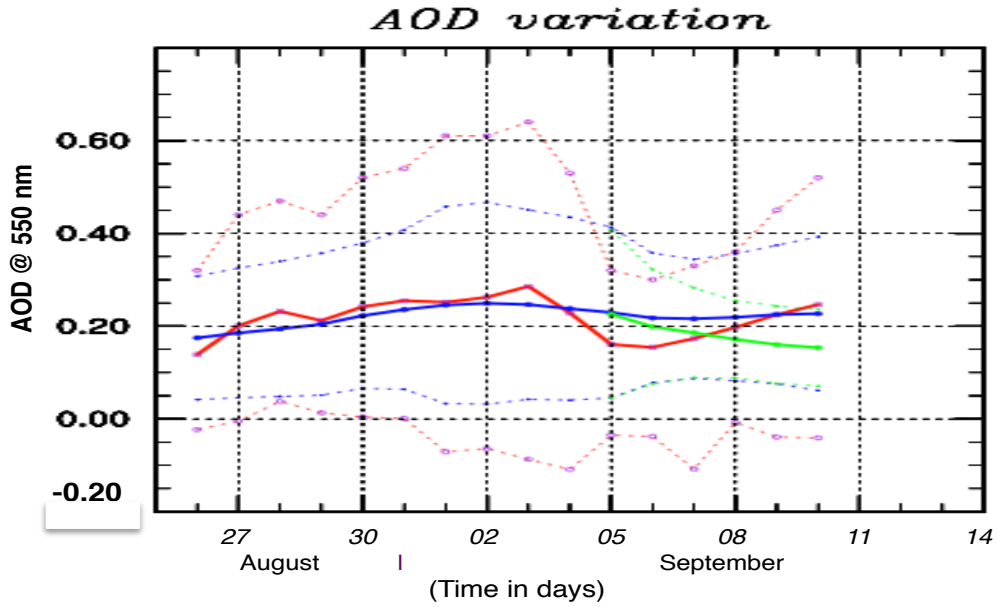

Fig. 6.9: Temporal variation of column integrated of AOD from WRF-Chem and MODIS onboard the Aqua satellite measurement (http://giovanni.gsfc.nasa.gov/giovanni/). Daily output from 26 August to 10 September 2008.

AODs are notably higher in both the MODIS data and WRF-Chem (CNTRL); mainly due to BBAs, noting that other sources also make small contributions during the dry season. The AOD profile in WRF-Chem (CNTRL) roughly follows the distribution in MODIS, except overpredicting between 4 and 9 September. WRF-Chem also captures the spatial variability and a decrease in AOD as shown in the TEST, although some discrepancy may arise from comparing grid-box mean with point observation from the satellite retrievals. Because we attempt to extract the influence of aerosols on observed weather patterns isolated from additional other forcing factors (e.g. GHGs, land-use change and SSTs present in the real climate), their contribution cannot be completely ignored, hence not easy to make direct comparisons to observational data. WRF-Chem shows a small spread (region enclosed between the standard deviation) compared to MODIS, but higher AOD between 4 and 6 September. The negative values in the satellite deviation could suggest that the satellite didn't see much of the clouds. However, it is important to understand the extent to which aerosol-driven clouds and stability changes resemble those driven by other processes (Skaeda et al., 2011).

Likewise, I compare the model simulated AOD with the Aerosol Robotic Network (AERONET) measurements from three locations over the domain obtained from the SAFARI2000 database (http://www.daac.ornl.gov/S2K/safari.html). Figure 6.10 shows daily-modelled AOD against the

AERONET measurements for Kaoma (14.81°S, 24.80°E), Mongu (15.27°S, 23.15°E) and Skukuza (25.0°S, 31.60°E) respectively at 500 nm. The measurement (red curves) and CNTRL simulated (green curves) AOD are plotted from 26 August to 10 September 2008, while the TEST (blue curves) is plotted for 5 days only.

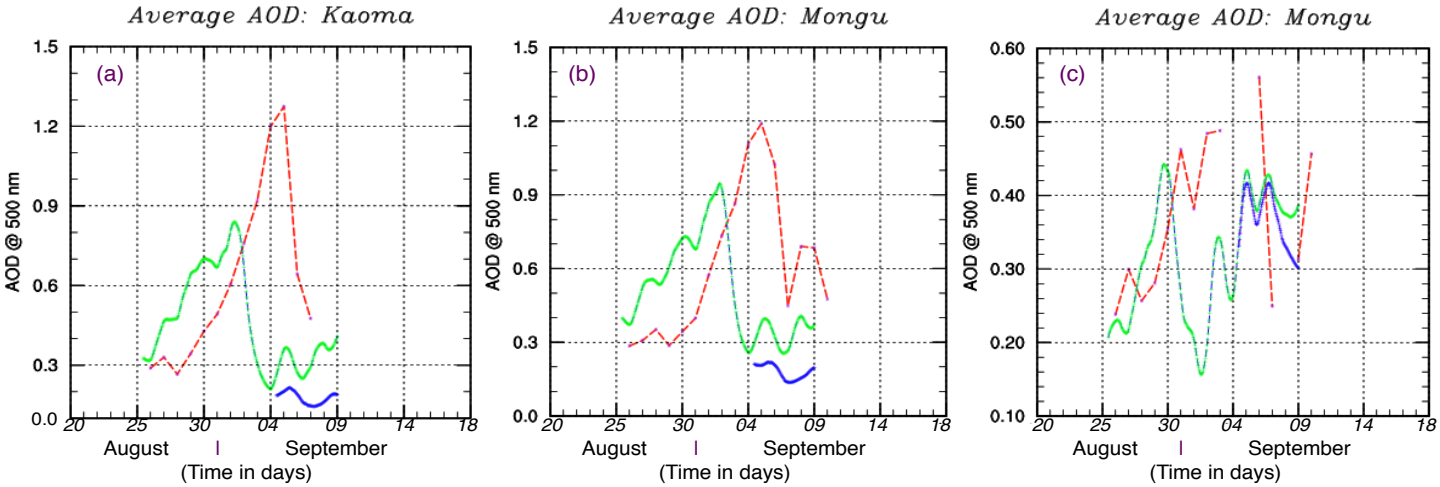

Fig. 6.10: Temporal variation of column integrated of AOD from WRF-Chem and SAFARI measurements (http://www.daac.ornl.gov/S2K/safari.html/). Daily output from 26 August to 10 September 2008. Red lines show measurement, green and blue lines show CNTRL and TEST.

Daily average AERONET (although in some cases, only few data points were recorded per day) and modelled results are similar in the first two towns –maximum on 6 September. Although AOD increases in all the towns between 26 August and 2 September, the model lags behind measurement. Measured AOD continues to increase after 2 September while the model prediction drops after 3 September. Although the model simulated AOD increases again between 4 and 5 September, it is quite lower than the measured AOD. As observed earlier, the TEST simulated AOD is quite low (below 0.30). On the other hand, although Skukuza shows a slight pattern in the variation, AOD is still low (below 0.6) compared to the other two locations. However, the AOD also increases between 26 and 30 August, while the measured AOD continue to increase until 2 September. There was no measurement between 3–6 and 8–9 September respectively.

(b) Second hypothesis

H2. The second hypothesis states that BB contributes a considerable amount of semi-direct effect largely driven by increased lower tropospheric stability due to BC absorbing aerosols at the surface inducing a significant 'burn off' to cloud layers over the domain.

Here I investigate effects of aerosol concentration on clouds. This statement assess changes in cloud profiles across the domain, specifically due to BC aerosols on cloud cover. Specific focus will be on regions with more cloud coverage. Fig. 6.11 show vertical profiles for BC and cloud mixing ratio (QCLOUD), averaged over the 5-day period, plotted for all grids. CNTRL has higher aerosol

concentrations lofted to higher elevations than the TEST; a lot of variability is shown more in d02. Maximum average concentration in TEST (fine grids) is about 1.2, 0.5 and 0.2 μg m^{-3} while in CNTRL is 1.8, 0.8 and 0.5 μg m^{-3} for d02, d03 and d04 respectively. The magnitude of the bulge in each plot shows the aerosol concentration over each grid. Again this is more indicated in domain d02 followed by d03 and d04. Figure 6.11(b) depicts cloud water mixing ratio (Qcloud), showing effects on clouds due to aerosol concentration (especially d02 and d03), and heights at which clouds are predicted. A more 'purplish' colour indicates a shift towards the TEST, whilst a 'brownish' colour indicates dominance from CNTRL.

Although clouds occur at different heights across domains, few clouds are predicted over d02, followed by d03 and d04 respectively. This shows that burn-off occurs more in the tropics (d02 and d03) and least in the subtropics (d04). Majority of aerosol concentration are between 1.5 and 5 km, with a steep drop-off above 6 km. Aerosols would be primarily located above the low level clouds (see Fig. 6.4), therefore maximizing effects of radiation absorption, leading to a strong positive direct effect. Although the profiles in Fig. 6.11(a) are plotted up to 10 km, results indicate that emissions can be elevated up to higher altitudes. Cloud burn-off occurs more from above clouds (due to more aerosols lofted higher) than from below.

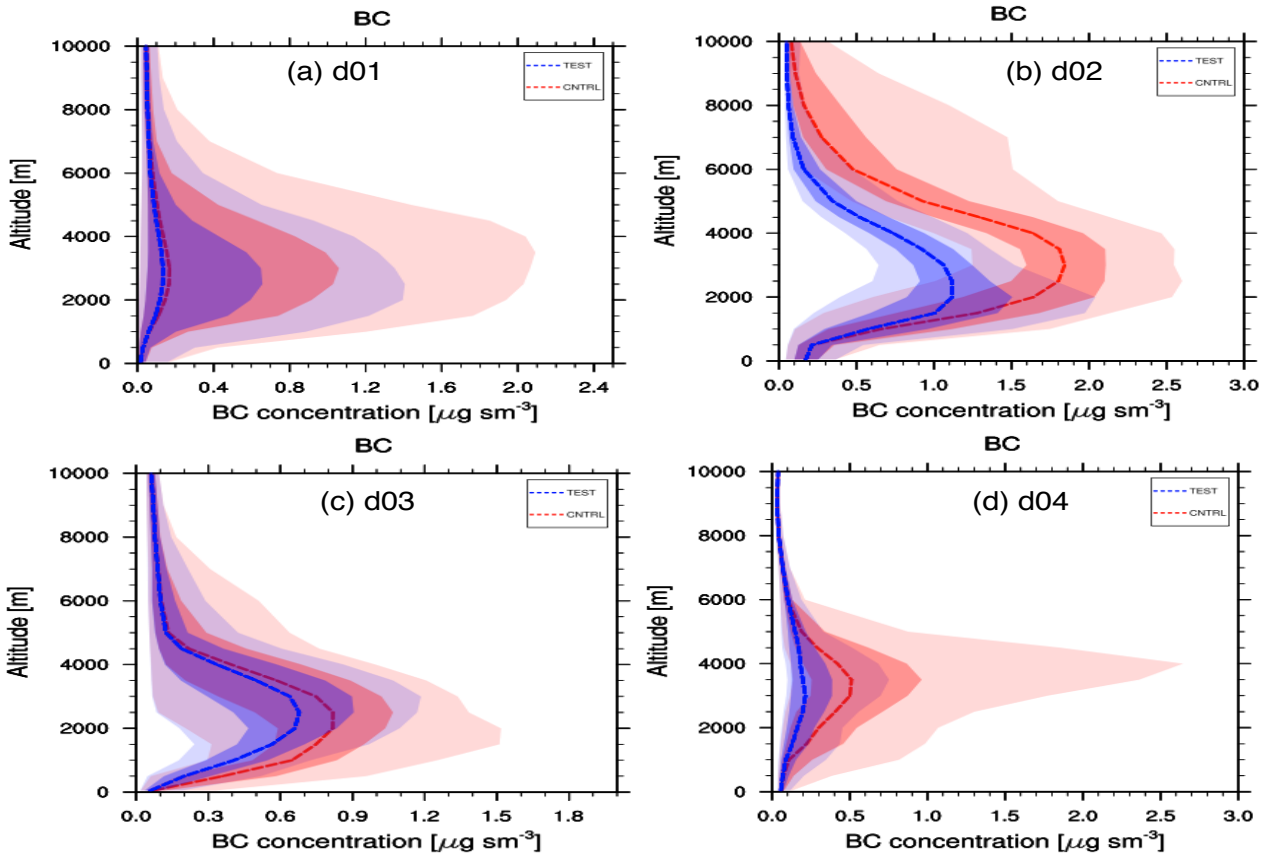

(a) BC profile concentration

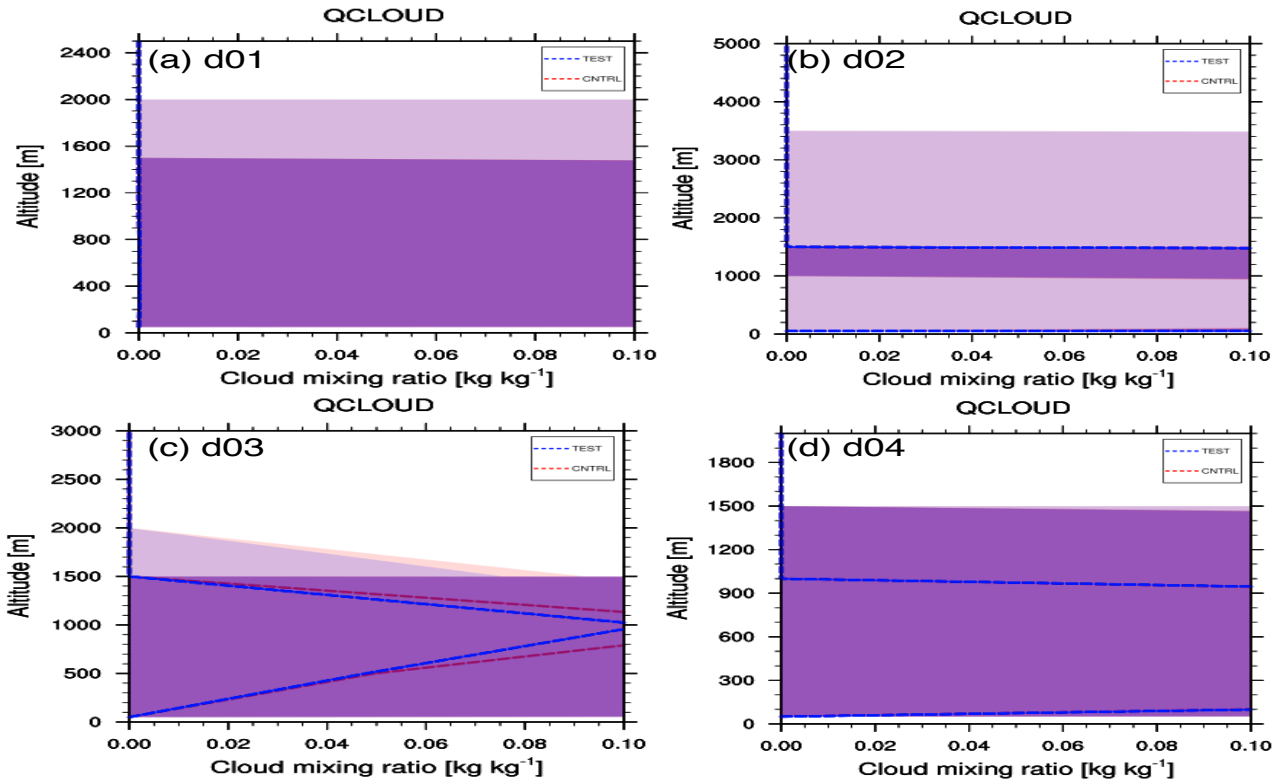

(b) Cloud water mixing ratio

Fig. 6.11: Profiles for (a) BC and (b) QCLOUD, averaged across the 5-day period over all model grids. The red and blue dashed lines show mean concentrations for CNTRL and TEST, whilst the strong shaded red and blue regions indicate the interquartile ranges and the faded regions are the fifth to the ninety-fifth percentile ranges.

In Tables 6.1–6.4, the mean BC concentrations are determined across the domains over different pressure levels. For instance, at 950-hPa, percentage difference from ΔBC are found to be 25%, 14%(13%), 31%(36%), 44%(42%) for d01, d02, d03 and d04 respectively. Results in parenthesis are calculated at low resolution for the fine grids. At 500-hPa, these are found to be 40%, 76%(68%) and (23%)(23%) for d01, d02 and d04, while d03 shows no change between CNTRL and TEST.

6.6.3 indirect aerosol effects

Here, I focus on indirect effects induced by aerosols -mechanisms through which aerosols can modify the microphysical cloud properties, lifetime, cloud morphology and precipitation patterns.

6.6.3.1 CCN and cloud droplet number concentration

The number concentration of cloud droplets is primarily controlled by environmental supersaturation, other than aerosol number concentration. The latter is an important source of CCN.

This statement addresses the relationship between CDNC (or CCN) with supersaturation *S*. In order to accurately simulate ACIs, models should be able to predict CCN concentrations correctly. CCN concentration depends on aerosol number, size distribution, hygroscopicity and ambient supersaturations (Shrivastava et al., 2013). I first look at predictions for CCN and N_d to relate with S_{eff}

and compare results between high and low resolutions (resolved and parameterised). Figure 6.12 shows average CCN at 1.0% supersaturation and CDNC, plotted for all domains. Blue curves (with red markers) represent CNTRL whilst brown curves (with green markers) represent TEST. Both quantities have higher number concentration in the CNTRL than in the TEST; the peaks indicate the contribution from BB. Meanwhile, comparing the trends in the quantities (between CCN and N_d) shows that variations differ markedly in both simulations. For example, in Fig. 6.12(a), TEST remain below CNTRL throughout the simulation period, even where there are some peaks in the curves. On the other hand, the pattern in Fig. 6.12(b) shows close similarities between the two scenarios (except orders of magnitude (ΔNd)), indicating that CDNC is not directly dependent on CCN number concentration. Thus, there is no one-to-one relation between CCN concentration and CDNC (Romakkaniemi et al., 2012).

As highlighted earlier (chapters 2, 3 and 4), supersaturation is one important factor controlling cloud droplet formation. The number of cloud droplets that form after activation of CCN particles depends on S_{max}, as well as updraft velocity (w) through which water vapour is lofted up. As discussed below, increase in aerosol concentration tends to decrease S, influencing the probable number of cloud droplets (some CCN fail to activate because more CCN particles compete for the available water vapour). More CDNC in the fine grids shows explicitly resolved w.

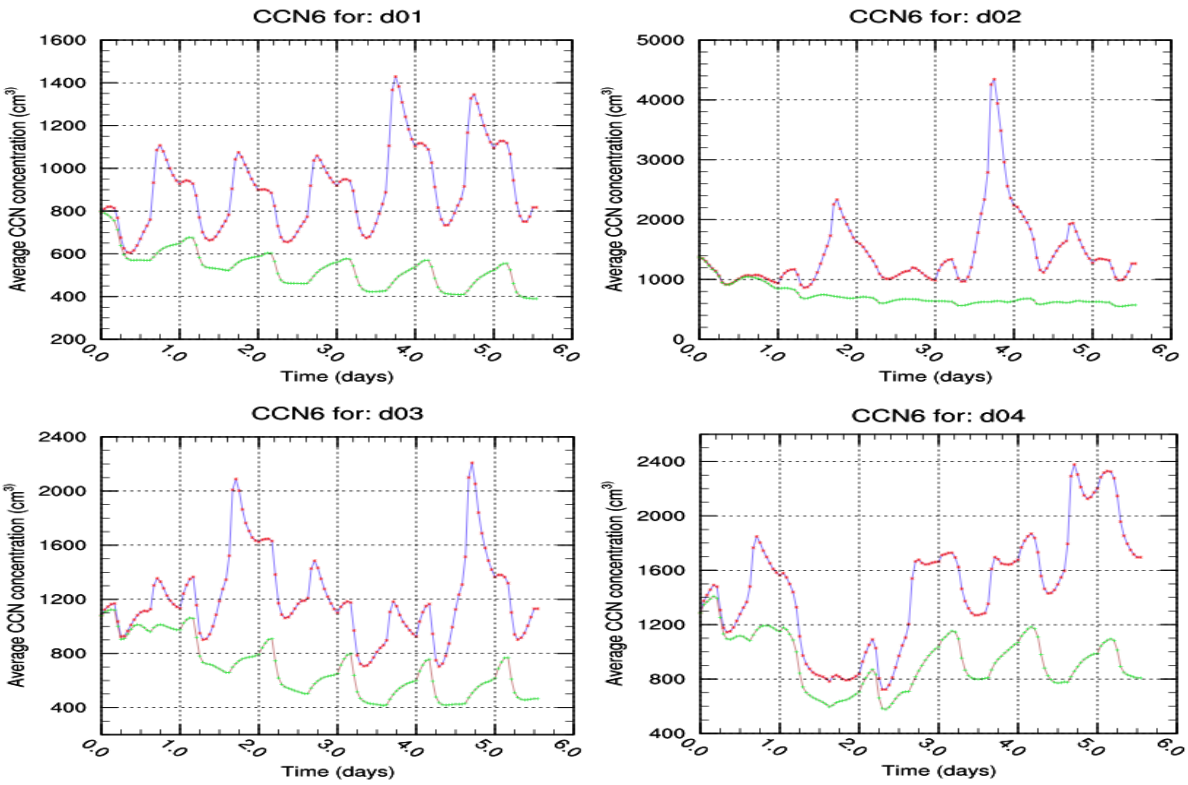

(a) CCN concentration at 1.0% supersaturation

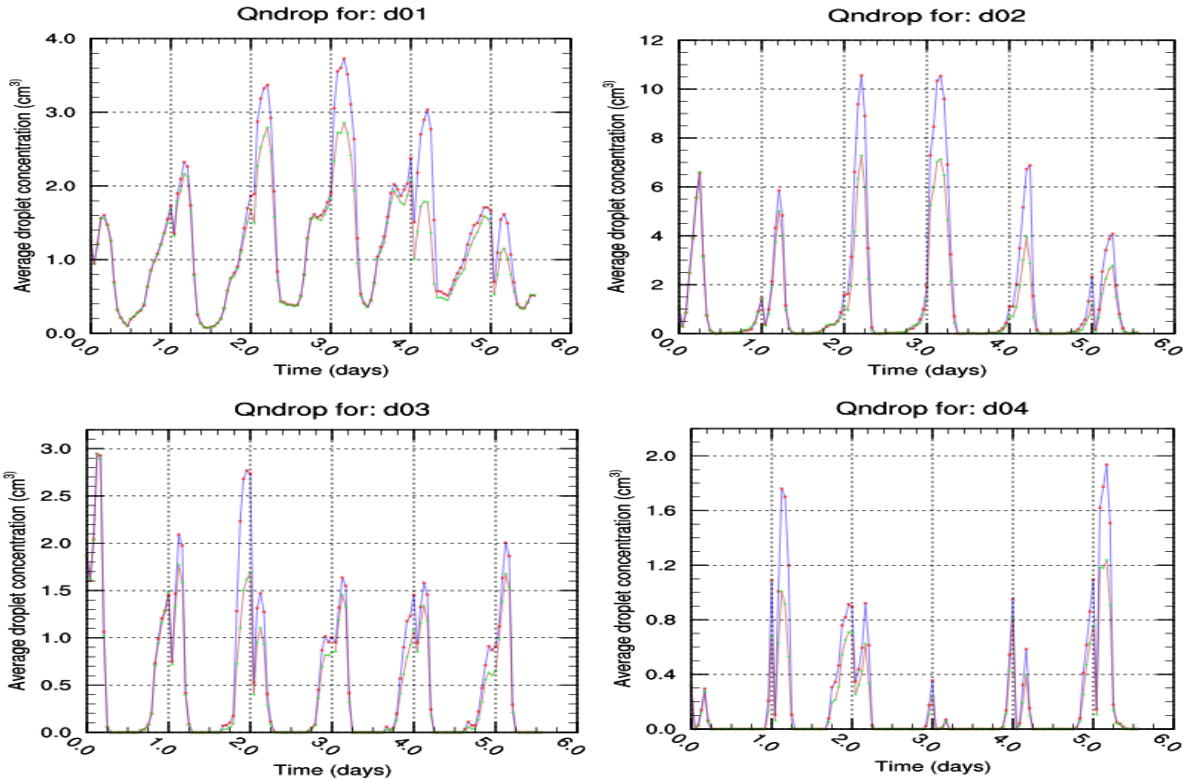

(b) Droplet number concentration

Fig. 6.12: (a) CCN concentration and (b) CDNC averaged across the 5-day period, plotted for all grids. Curves with red markers represent CNTRL while curves green-marked curves represent TEST. Small domains are plotted at 4-km. All simulations start at 0000 UTC 5 September.

To further demonstrate effect of aerosol concentration on supersaturation, I compare the model-predicted supersaturation between the two model scenarios for the small domains. Figure 6.13 shows S_{eff}, plotted for d02, d03 and d04 respectively, averaged over 5 days at 4-km ((a), (b) and (c)) and 20-km ((d), (e) and (f)) grid spacing respectively. Effective supersaturation is not explicitly carried in WRF-Chem, but diagnosed from the model-computed Nd_{max} and CCN (discussed in sections 6.5.2, and 3.7 of chapter 3). To determine the corresponding supersaturation, S_{eff} is determined by comparing maximum droplet number N_d computed with CCN concentration. For example, if $N_d >$ CCN1 and $N_d <$ CCN2, then S_{eff} must be between 0.02 and 0.05%. S_{eff} is determined and plotted at the base of the lowest clouds in the layer immediately above CCN and is plotted only for those grid cells that contain clouds in their columns. The red curves represent domain-averaged S_{eff} in the CNTRL simulation whereas blue curves represent TEST.

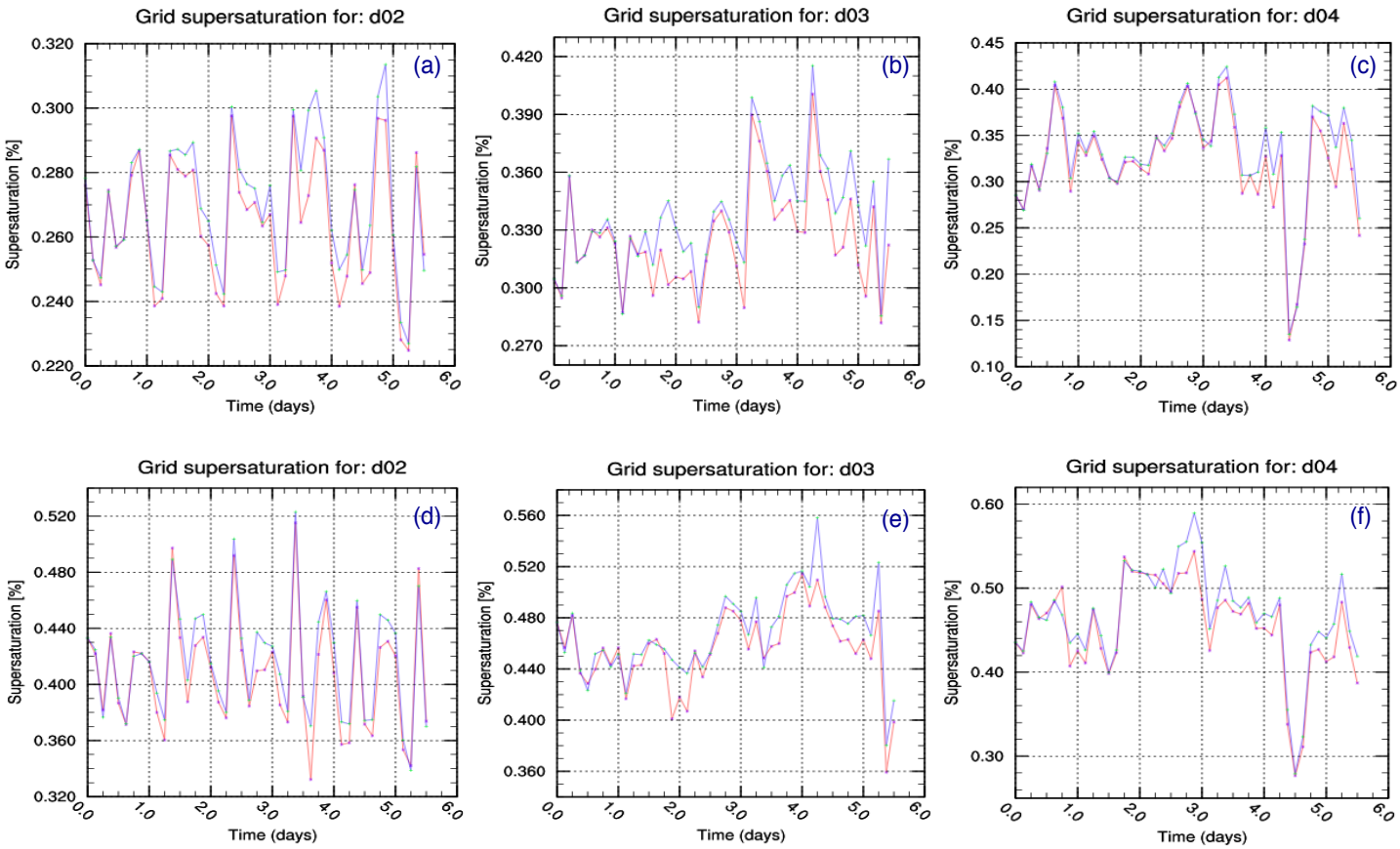

Fig. 6.13: Effective supersaturation: top panels ((a), (b) and (c)) at 4-km grid spacing, and bottom panels ((d), (e) and (f)) at 20-km grid spacing. In both plots, the red curves represent CNTRL whereas the green curves represent TEST.

Irrespective of grid spacing (4-km and 20-km), the TEST is higher on average, than CNTRL showing that predicted S_{eff} is reduced with higher aerosol concentrations (i.e. with BBAs). For example, S_{eff} is lower in d02 compared to d03 and d04, taking into account that this sub-domain had more aerosols due BB emissions as shown in the previous sections and chapters. Therefore, increase in aerosol concentration consequently impacts on the environmental supersaturation (a decrease in S_{eff} in CNTRL) as might expected. The effect is shown in both high and low resolution plots, although the magnitude of S_{eff} differs between the two grid spacings, which I discuss below.

6.6.3.2 Supersaturation and grid resolution dependence

Notwithstanding aerosol concentration discussed above, I also consider model prediction with respect to grid resolution. Here I examine the model sensitivity in parameterised and grid-resolved clouds from predictions for S_{eff} at high and low resolution. Figure 6.14 shows the same data for S_{eff} discussed above, but re-plotted such that the plots show results for the CNTRL and TEST predictions plotted separately to compare effects on resolved and parameterised clouds. Panels on the left represent CNTRL whereas panels on the right represent TEST. The blue curves indicate average S_{eff} at 20-km

grid spacing whereas the red curves indicate S_{eff} at 4-km respectively. As shown, S_{eff} increases at 20-km grid spacing than at 4-km grid spacing.

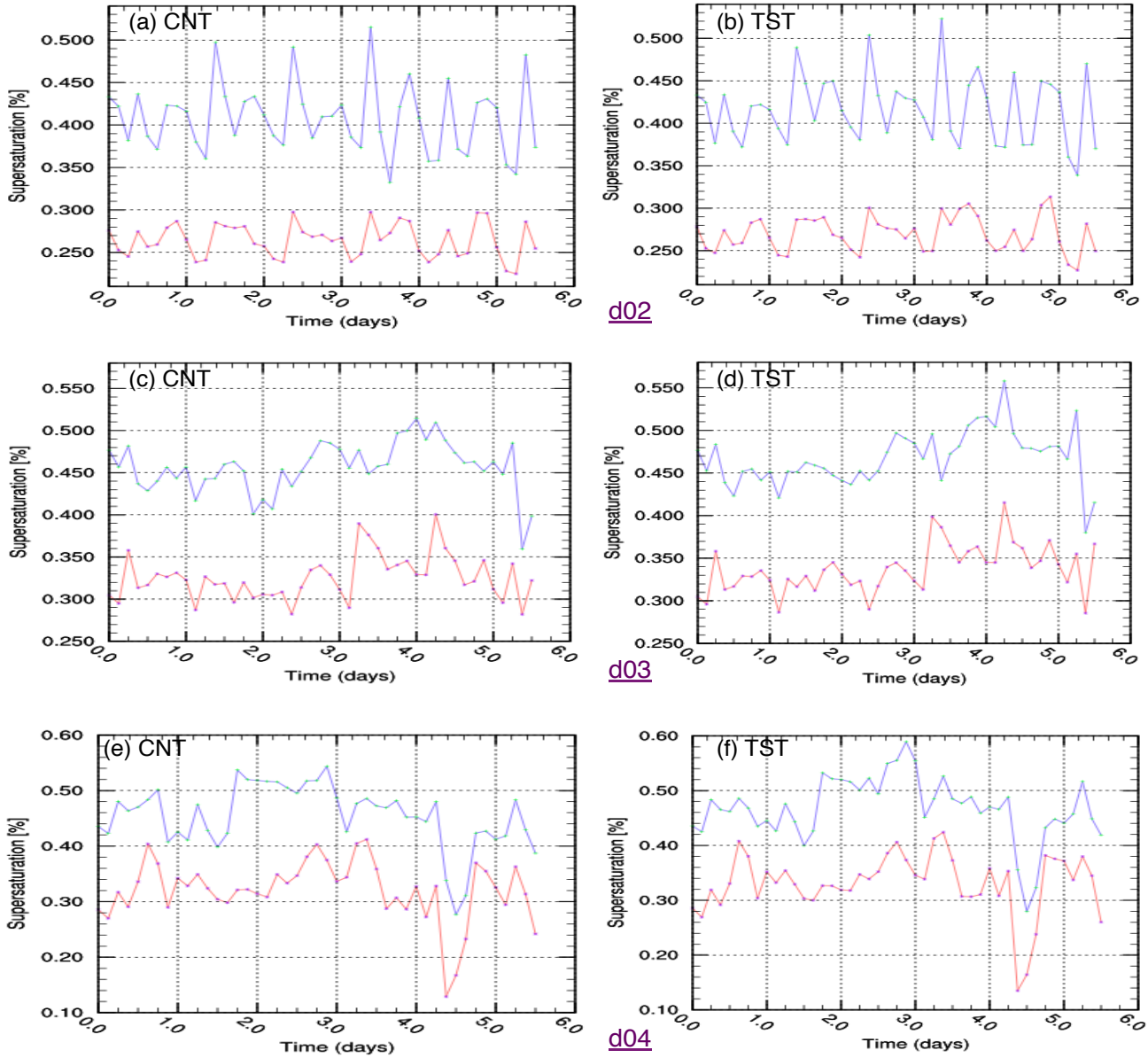

Fig. 6.14: Resolved (red curves) and unresolved (blue curves) S_{eff}. Left panels represent CNTRL and right panels represent TEST. All simulations start at 0000 UTC 5 September.

The predictions exhibit different trends in S_{eff} between the high and low resolution, indicating the model sensitivity in resolved and unresolved clouds. Average S_{eff} predictions at 4-km grid spacing remain lower than those at 20-km grid spacing at all times, (consistent with the results shown in chapter 4 (e.g. Fig. 4.17) and section 6.5.2). Again, domains with low aerosol concentration (d04 and d03) have higher S_{eff} than d02. Even where cloud temporal variation is different, unresolved clouds show higher S_{eff} than in resolved clouds. As shown earlier, d02 had more clouds than the other sub-domains. In contrast, we saw that particle concentrations increased over locations dominated by BBAs. Since at 20-km grid spacing fewer of the clouds are resolved and higher fraction is parameterised using

the cumulus scheme, the high S_{eff} in the lower resolution simulations shows that there is less effective reduction of water vapour, but condensational growth of activating droplets implicit in the parameterisation. This is equivalent to an implied lower concentration of CCN competing for the available water vapour.

In the higher resolution simulations, droplet activation parameterisation in resolved clouds lowers S_{eff} more effectively implied in the cumulus parameterisation at lower resolution (with more CCN particles activating to cloud droplets). In principle, particle fraction of activated CCN at a given supersaturation in the cloud should be similar in both grid spacing, if activated at the same S_{eff}, taking into account the influence of different ambient conditions. Thus, higher resolution and the consequent ability to capture ACIs more realistically leads to better representation of pollution-meteorology feedbacks. Particle activation is however, controlled by the environmental supersaturation which is the main factor determining the size of droplet formation in cloud condensation (Twomey and Squires, 1959), although other mechanisms can affect the dynamics.

6.6.3.3 Liquid water content and precipitation

The first indirect effect (cloud albedo adjustments resulting from increase in aerosols) states that a cloud with smaller droplets will be brighter than that with larger droplets for a given liquid water content (LWC) because of numerous particles activated. Also, the second indirect (lifetime effect) and the semi-direct can both influence the LWC (Chapter 1, section 1.6). LWC is defined as the total liquid water contained in clouds per unit mass of dry air. This is also dependent on the dynamics and hence determined by the type of clouds (Chakraborty and Maitra, 2012). Information about vertical variability in cloud microphysical properties is important in assessing aerosol-cloud properties. For example, LWC profiles partially controls the radiative transfer in cloudy atmospheres and the earth radiation budget (Korolev et al., 2007, and references therein).

Here I focus on the aerosol-changes to assess the response of cloud water content and precipitation. Figure 6.15 shows the temporal profiles for the domain averaged column integrated LWC, plotted for all grids from the two simulations. Both simulations show similar patterns; for example, midday minima and midnight maxima in LWC (Fig. 6.15(a)). As expected, the model predicts high LWC in the tropics than in the subtropics. For example, the maximum LWC for d02 is 1.2 g m^{-2} whereas for d03 it is about 0.21 g m^{-2}. For d04, the maxima is around 0.18 g m^{-2} (except in the morning of 6 September –reaching up to 0.25 g m^{-2}).

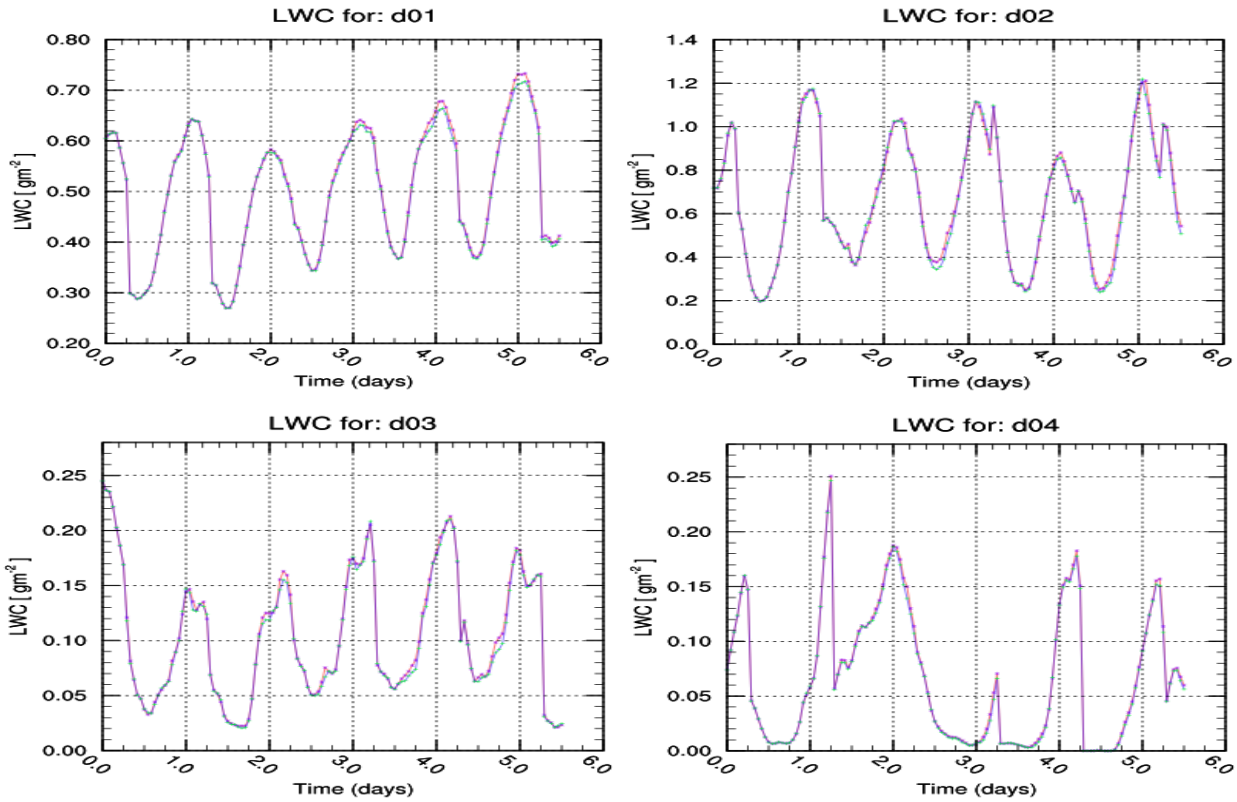

(a) Liquid water content (LWC)

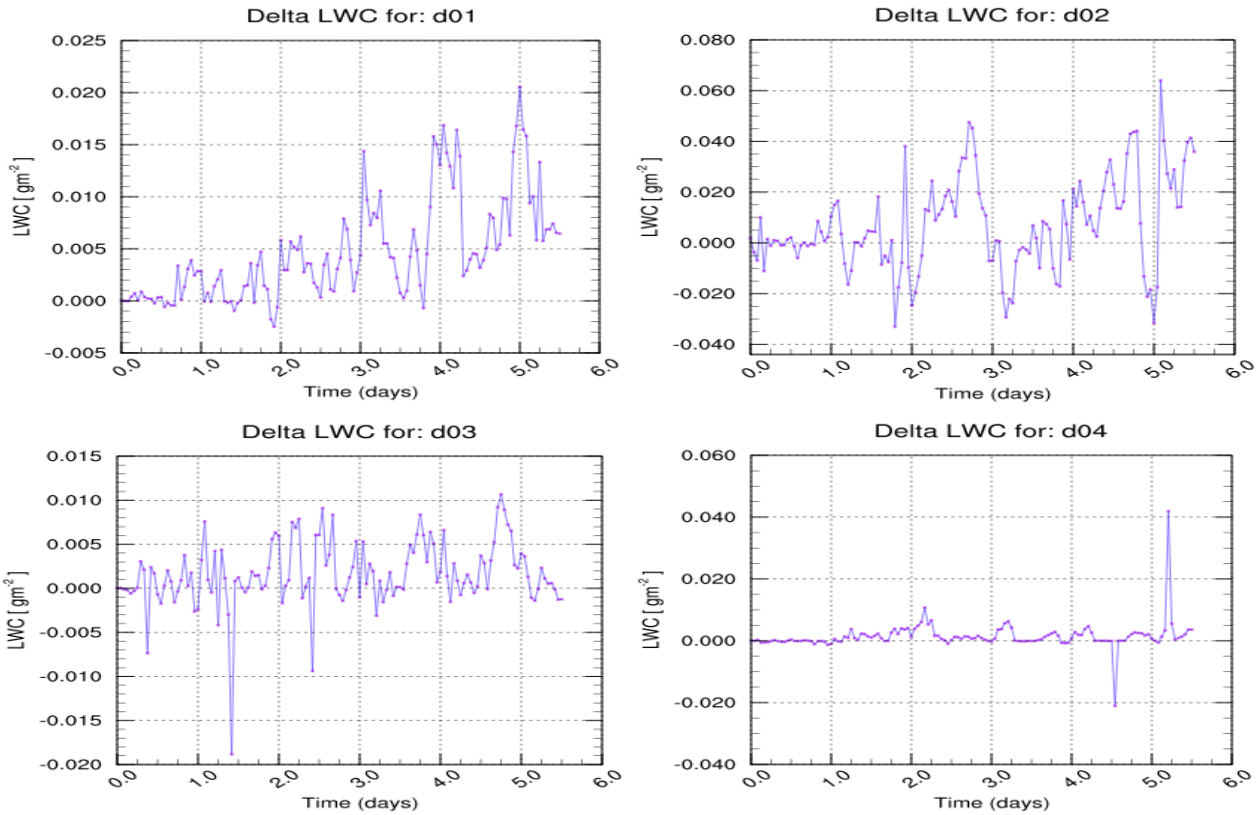

(b) Change in LWC

Fig. 6.15: Time series for column integrated LWC (a): CNTRL (blue curves) and TEST (orange curves), and (b) ΔLWC only. All simulations start at 0000 UTC 5 September.

Also, there are days (e.g. 5, 8, 9 September) when LWC is below 0.02 g m^{-2} or zero in d04. Differences in LWC (ΔLWC) are small and plotted in the four panels of Fig. 6.15(b) for all domains. Cases where ΔLWC is negative is when there is more LWC predicted in the TEST than in the CNTRL. As highlighted earlier, tropical Africa is mostly influenced by BB, and has more rainfall than the subtropical south. Subtropical southern Africa is impacted by anthropogenic pollution and to some extent, dust emissions from the Kalahari. There is a clear signal in ΔLWC over domains d02 and d03 than d04 where there is more cloud cover, though all domains show differences resulting from BB. The peaks in the positive direction correspond to an increase in LWC although following a precipitation event (e.g. spikes in the negative direction) aerosol loading is reduced and hence cloud development (Savane et al., 2015). From Fig. 6.15(b), it is clear that the sum of ΔLWC is positive across all domains, indicating that LWC increases in the simulation with BB. This suggests that the second indirect effect (i.e. increase in cloud lifetime and decrease in precipitation) is stronger than the semi-direct effect.

Whilst there is a reduction of LWC in the east, the amount increases in equatorial west Africa. The reduction of LWC in the BB-dominated area could also be due to a weakened southward moisture transport and a shallower daytime PBL; surface temperature is enhanced above the surface with more fires. Aerosols can heat up the atmosphere stronger at the top of the boundary layer, leading to more stable and shallower PBL (Grell et al., 2011a). The former slows down the build up of lower tropospheric moisture, whereas the latter would reduce the probability for surface air to reach the level of free convection. However, because there is frequent cloud cover over tropical Africa even during the dry season, clouds are often partially embedded in the regional smoky hazes. Again, impact on LWC could also be related to cloud properties (e.g., indicating small clouds or dying stages of large clouds). High aerosol concentrations from the fires and corresponding CCN number lead to an increase in the cloud water mixing ratio, leading to decrease in rainwater mixing ratio, but higher droplet number concentrations. The droplet number increases, while rainwater is decreased. Similarly, precipitation increase can be attributed to both radiative- and the microphysical feedback. As shown in Fig. 6.15, although the overall ΔLWC suggests the second indirect effect being stronger than the semi-direct effect, the effect is more pronounced in the fine grids.

To further assess the model's ability in predicting liquid water, I plot model simulated liquid water path (LWP) against measured LWP from the MODIS satellite (Fig. 6.16) for the coarse domain. The red curves represent measurement whereas blue curves represent model output. Solid red and blue lines are the averages while the thin dashed lines indicate the standard deviations respectively. Although the measured and simulated LWP are not a one-to-one match, the averages are close to one

another –ranging between 70 and 100 gm^{-2}. Meanwhile, the satellite has a wide spread than the model (the same was observed for AOD in Fig. 6.9 above). The overall result however, shows that the model does a reasonable job in simulating LWP on average, as the measurement.

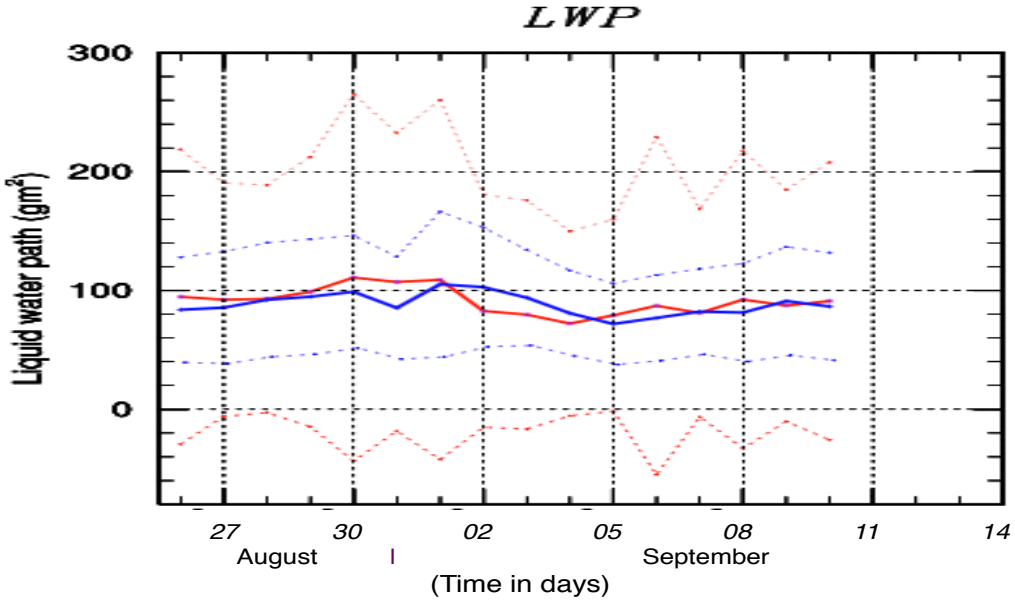

Fig. 6.16: Column integrated liquid water path from WRF-Chem and MODIS onboard the Aqua satellite measurement (http://giovanni.gsfc.nasa.gov/giovanni/). Daily output from 26 August to 10 September 2008. Red lines show measurement, whereas blue lines show CNTRL simulation.

Notwithstanding results discussed above, these signals indicate the aerosol-induced changes on clouds, which can also manifest in precipitation formation as discussed below. Precipitation is another important quantity in ACIs because aerosols and clouds are very linked to one another so much that a change in the other has a direct or indirect effect on the other. This is an important mechanism in the hydrological cycle linking aspects of climate (weather and chemistry). Therefore, change in cloud dynamics will directly affect precipitation. Figure 6.17 shows the column-integrated rainwater mixing ratio (Qrain), plotted for all domains.

The model predicts more precipitation over domains d02 and d03 as in the case with LWC above. For d04, maximum precipitation occurs between 6 and 7 September (days 2 and 3), with other days being almost zero. Although the magnitude of LWC between CNTRL and TEST is almost similar, there is clear indication that precipitation changes when the effect of fires is considered. For example, in domains d02 and d03, the TEST shows increase in Qrain (6–8 and 8–9 September). The pattern in Qrain also does not follow the same trend as LWC. This can be expected because of the non-convective clouds in addition to enhanced aerosol concentrations (air becomes more polluted and the non-precipitating clouds are low level) resulting in high CCN number and CDNC, but diminished particle sizes and less conversion to rain (Grell et al., 2011a).

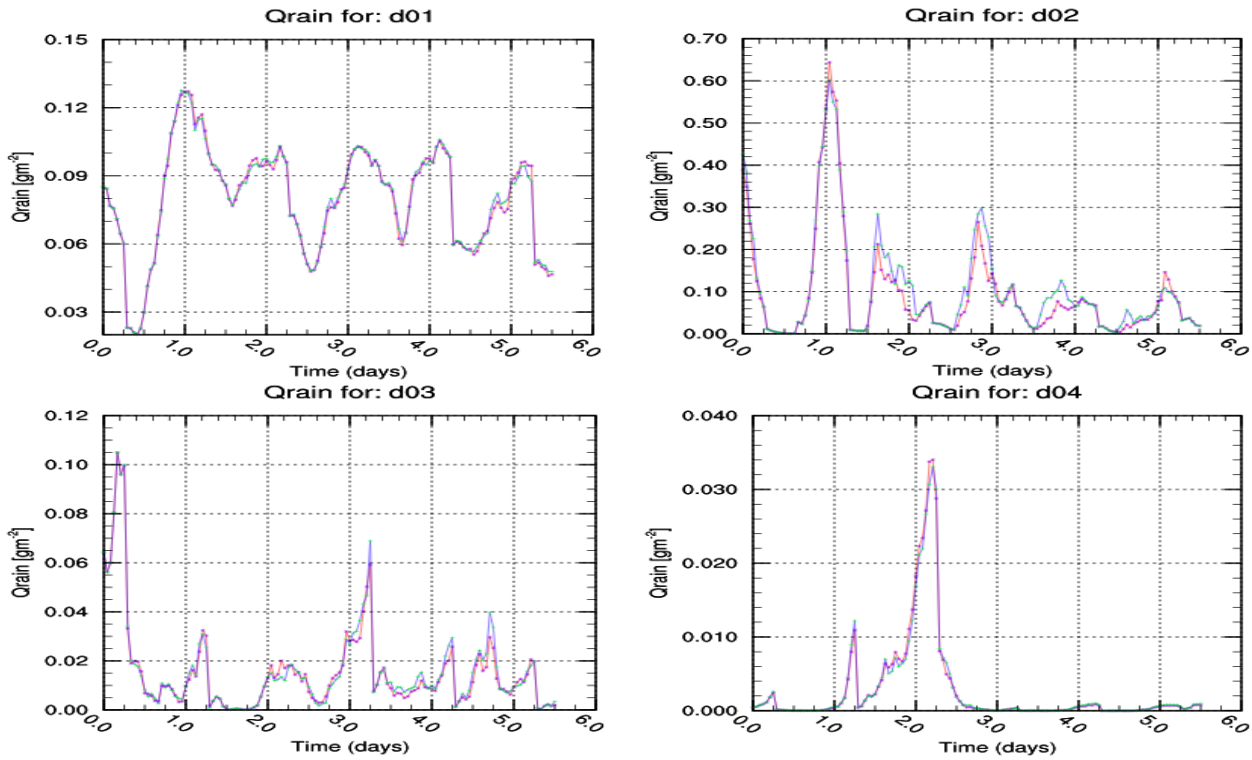

Fig. 6.17: Time series for column-integrated rainwater (Qrain). Blue curves (with green markers) represent CNTRL whilst orange curves with purple markers represent TEST. All simulations start at 0000 UTC 5 September.

As showed in the tables, quantities increase in resolved clouds (i.e. fine grid simulations), where the model becomes more sensitive to the changes and resolves clouds explicitly. Although the changes are not as large across the domains, grid resolution dependence can also be effective for instantaneous precipitation rate over regions where synoptic and/or mesoscale convective features are better resolved at higher resolutions (Ma et al., 2015). According to Ma et al. (2015), increase in LWC in the fine grids is also because of high moisture convergence, therefore resulting in higher liquid condensation. While the deviation in LWC (statistics shown in the tables) could be attributed to either (i) not enough water vapour condensation, (ii) more precipitation formed or (iii) mechanical evolution in clouds, information is still unclear about the variability in these quantities. Whether this could be attributed to averaging scale, cloud life cycle phases or aerosol loading (Savane et al., 2015), some information would be needed to unravel the processes. Although further diagnostics would be needed to assess the possible physical mechanisms for this increase, the work is considered beyond the scope of this study.

(c) Third hypothesis

H3. The third hypothesis proposes that changes in aerosol loading lead to perturbations in cloud droplet size and number concentrations. Radiative forcing varies considerably, with a large variability appearing between clear and cloudy-sky region. I estimate that RF is dominated by cloudy-sky forcing at the surface, implying that aerosol indirect effects can be more important than direct effects.

Analysis of the above results showed that cloud microphysical properties such as CDNC, CCN and S_{eff} are functions of pollutant loading and grid resolution. Here I investigate whether the model predicts similar relationships between aerosol concentration and cloud microphysical properties as discussed above. To test this statement, I examine the changes in the flux energy over the domains between the two model scenarios. First, I determined the statistical data (mean flux) to assess the changes in the radiative balance (RB) due to BBAs. The changes in RB can be calculated either at the top of the atmosphere (TOA) or ground surface (BTM), for 'upwelling' or 'down-welling'. This can be determined for "clear-sky" or "cloudy sky" conditions. It should however, be noted that since the study is performed during winter (when domain is relatively dry with less/low cloud cover), this hypotheses might not be adequately addressed. Derivations for the expressions are given in the supplement (Appendix C). Table 6.5 shows results for absorbed shortwave and RB, computed for clear- and cloudy sky determined over the domains. Fig. 6.18 shows change in absorbed shortwave (SW) radiation plotted over d01 and d02. Red curves represent CNTRL whilst blue curves represent TEST. The change in the total flux (ΔESW) indicates the sum of energy absorbed/scattered due to aerosols, inferred to the contribution due to BBAs.

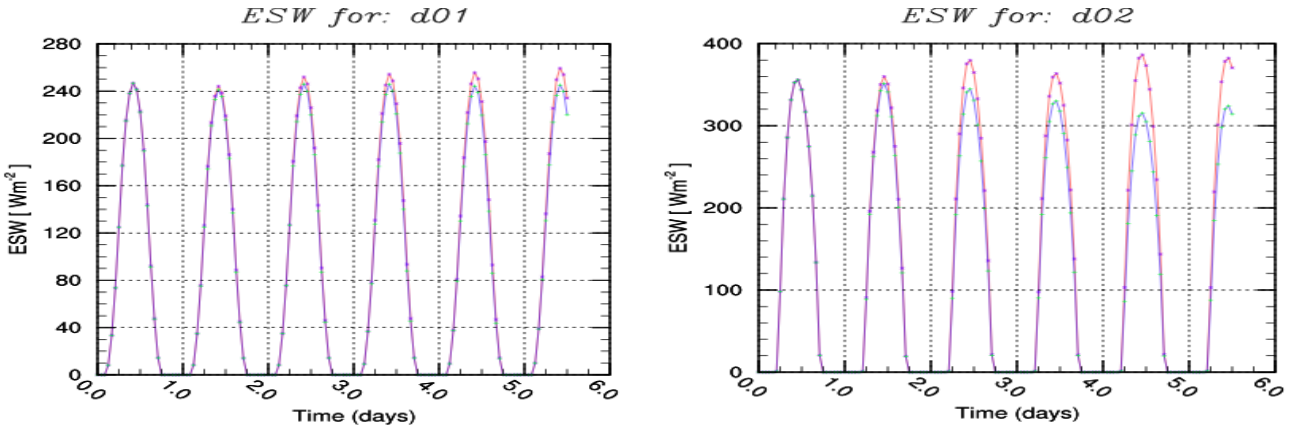

Fig. 6.18: Daily mean time series of absorbed energy (Wm^{-2}) between the CNTRL (blue curves) and TEST (orange curves) simulations. Model output for domains d01 and d02. All simulations start at 0000 UTC 5 September.

Table 6.5: Mean radiative flux over the domains, averaged over 5 days.

grid	RB_{cldy}		RB_{clr}		SW_{btm}		ESW_{abs}	
	CNTRL	TEST	CNTRL	TEST	CNTRL	TEST	CNTRL	TEST
d01	37±92	37±92	235±104	235±104	840±116	860±11	234±73	220±58
d02	70±44	71±49	277±26	278±26	559±93	627±98	370±61	314±53
d03	89±31	89±31	269±29	269±29	805±47	861±47	233±20	210±11
d04	39±25	39±25	218±26	218±26	800±39	821±39	223±26	209±21

Units: W m^{-2}

RB_{cldy} and RB_{clr} = cloudy- and clear-sky radiative balance

SW_{btm} = SW radiation at surface/ground
ESW_{abs} = absorbed SW radiation energy (cloudy sky)

The mean SW flux absorbed at the surface (ESW_{abs}) in the TEST is less than that for CNTRL, indicating that aerosols absorb more solar radiation when BB is included. The changes are greatest between 9 and 10 September as shown in Fig. 6.18 for d02. Increase in absorbed radiation decreases the amount of radiation reaching the Earth surface and evaporates cloud particles located in the upper part of low cloud layers (semi-direct effect) as noticed in Fig. 6.11. The rate of absorption (i.e. effect of semi-direct) depends on the absorbing aerosol concentration, which in this case is higher in tropical west Africa (d02: +56 Wm^{-2}) compared to tropical east (d03: +23 Wm^{-2}) and subtropics (d04: +14 Wm^{-2}). As shown in section 6.6.1, the presence of BBAs decreases the scattering efficiency (SSA), while increasing AOD respectively.

Carbonaceous aerosols can reduce the amount of solar energy reaching the Earth surface while on the other hand the BC component heats up the atmosphere aloft. Therefore, by redistributing the solar heating between the Earth surface and the atmosphere, BC can impact on the atmospheric stability, regional circulation patterns and hydrological cycle (Randles and Ramaswamy, 2010, and references therein). Apart from changes in LWC and the cloud profiles, it could be expected that reduced downwelling solar radiation at cloud top associated with absorbing and scattering aerosols might enhance the net solar energy (LW + SW) cloud top cooling and could drive thicker or more extensive clouds. The amount of downwelling longwave (LW) radiation reaching the Earth surface indicates the strength of the atmospheric aerosol effect and hence a key parameter in climate modelling. However, there could be other aerosol properties affecting how they absorb radiation not being captured in the model, for example, when the model produce fewer or optically thinner clouds (Wu et al., 2011). Also, the mixing rule (herein Maxwell–Garnett) may under-predict the absorption amplification of other aerosol components and/or the organic portion of the aerosol would be slightly absorbing in the visible spectrum.

On the other hand, although ESW_{abs} decrease in the absence of BBAs, the RB appears to be relatively insensitive to BBAs. In both cloudy and clear sky conditions, RB is found to be quantitatively similar in both model scenarios, whereas the SW flux at the ground (SW_{btm}) increases in the TEST. Despite the similarities in the calculated quantities, ΔRB differs slightly in d02 between clear and cloudy sky conditions. Also, d02 has more LWC and precipitation (see Fig. 6.15) across the simulation period. However this can be expected because of BB-dominance over this domain, while other domains have less cloud cover and precipitation. The height profile in Fig. 6.11 also shows aerosol concentration at different levels and changes in cloud water mixing ratio.

6.7 Summary

A pair of simulations was conducted by varying emission concentrations using the regional WRF-Chem model, in which one simulation was conducted without BB emissions to investigate ACIs over southern Africa. Statistical analysis was conducted to assess the changes in aerosol concentration due to BBAs. The model predictions were also compared with measurement to assess the sensitivity of the cloud microphysical properties with respect to BBAs. Although WRF-Chem shows a good skill in quantifying and predicting data comparable to the measurement, more data is still needed to adequately assess the model in order to have more confidence. Results (i.e. differences between CNTRL and TEST) indicate that BB makes a substantial contribution to aerosol effects, and significantly contributes to ACIs over the subcontinent. The changes explain the importance of BB emissions to the overall regional pollution, which is by far the greatest proportion of southern African carbonaceous aerosols. Results also indicate differences dependent to aerosol concentrations, particularly in BB-dominated regions where anthropogenic emissions do not show overlap with other emissions. For example, there are areas where modelled BC concentrations are highest and strongly influenced by BB emissions indicating substantial contribution to cloud burn-off (semi-direct effect), especially over tropical west central Africa. With BB, there is an increase in pollutants and hence more AOD in fire-active areas compared to anthropogenic-dominated regions. AOD increased by +26%, +38%, +31% and +11% over domains d01, d02, d03 and d04 respectively. Although direct effects are shown to be more profound in the tropics, the southeast region indicates that other pollution sources also contribute (e.g., Figs. 6.7–6.9). Also, CDNC is dependent upon environmental supersaturation for a given aerosol population.

Individual aerosol and cloud layers over tropical Africa result in stronger SW radiation absorbed than other regions. The radiative effects can be altered when BB emissions (and other sources) interact with the low level clouds over land and marine environment; most profound in tropical west Africa where BBAs can lead more energy absorption in excess of +56 Wm^{-2} (15%). For d01, d03 and d04, ΔESW was found to be +14 Wm^{-2} (6%), +23 Wm^{-2} (10%) and +14 Wm^{-2} (6%) respectively. Comparing the fine grid regions at high resolution to the same regions in the coarse grid indicates the model sensitivity in predictions. A change in the flux over d02 appears to be a result of elevated absorbing aerosol layers which can inhibit radiation from reaching the clouds and earth surface and evaporate cloud particles. It was also shown that increase in aerosol concentration leads to increases in CCN number concentration, while supersatutration decreases, especially over tropical west Africa. Increasing grid resolution in the model improves model performance in simulating meteorological and chemical variables, feedback patterns and temporal distributions over the domain. Clouds are better resolved in the fine grids, covering a smaller portion of the domain. The mean integrated LWC with-

and without BB is found to be 0.482 gm^{-2} (0.478 gm^{-2}); 0.643 gm^{-2} (0.637 gm^{-2}); 0.101 gm^{-2} (0.100 gm^{-2}) and 0.063 gm^{-2} (0.062 gm^{-2}) for d01, d02, d03 and d04 respectively.

Although clouds are better resolved at high resolutions, supersaturation increases in parameterised cloud and reduces when cloud are resolved, implying less reduction of water vapour in parameterised clouds than there is under resolved conditions. Also there is overall increase in LWC across all domains in the simulation with BB than there is when BB emissions are excluded. This indicates that the second indirect effect is stronger than the semi-direct effect. Model simulated LWP was also compared to measured LWP and was found be to close to one another. Overall, results imply that ACIs over southern Africa become more important as a result of BB emissions. The modelling framework employed in this study can be useful to probe effects of aerosol concentration and cloud responses at different parameterisations. This can also be helpful in guiding the future parameterisation development to improve ACI processes as well as sub-grid variability. The sensitivity model runs conducted with two different resolutions showed an impact on the modelled aerosol and cloud droplet number concentration and the averaged size distribution over the domain.

Chapter 7

Summary, conclusion future directions

7.1 Aerosols, clouds and interactions in the atmosphere

The earth-atmosphere is composed of gases and suspended liquid and solid particles in different sizes, shapes and chemical compositions. Most particles are of very small sizes (order of microns or less) and perceived only when particle concentrations are very high in the atmosphere. Atmospheric trace components are of special interest to humankind because they play critical roles in the atmosphere through their interaction with meteorology and modification to the atmospheric chemistry. They govern the atmospheric branch of the hydrological cycle through clouds and precipitation formation (via CCN), modify radiation budget, changes in ambient AQ, oxidation capacity and have major impacts on human health, vegetation and ecosystems (Zhang et al., 2009). While some species are emitted directly from their sources into the atmosphere, some are formed in the atmosphere from chemical reactions and transformations of other species.

Aerosols interact with clouds through acting as CCN and IN during clouds formation or freezing of ice crystals respectively. Also, increase in aerosol concentration impacts on cloud optical properties due to cloud droplet size distribution and reflection of solar radiation by clouds (Twomey effect). This may also impact on the cooling effect of the global climate. Aerosol perturbation on cloud formation can cause LWC maintained longer, increasing cloud lifetime (Albretcht effect). One other way to address these impacts is construction of models that incorporate various components of the earth system and testing them against observational or measurement data. State of the art-coupled models allows estimates of ACIs. A major challenging factor is to find and understand how clouds respond to perturbations in the aerosol properties (e.g. Koren et al., 2010) from various pollutant sources.

7.2 Contribution of this PhD study

This PhD study utilizes the WRF-Chem model v3.4.1 (a numerical mesoscale model able to simulate gas- and particle-phase and cloud processes) to investigate interactions of atmospheric aerosols with clouds over southern Africa. The study presents one of the major progress in modelling ACIs and aerosol properties, based on the simulation of meteorological and chemical processes from a BB episode during the dry season in 2008. A major part of the work was dedicated to the setup and comprehension of a modelling system able to represent meteorological and chemical processes for a realistic representation and description of the regional atmosphere. The novelty of this study is the combined analysis of ACI sensitivity to aerosol loading and cloud response in a regime-base approach, enabling a profound view into the aerosol-chemistry-meteorology system. To analyse the various

feedback mechanisms related to the cloud microphysical processes and the impact of varying emissions, a comprehensive cloud parameterisation scheme was incorporated in the model framework to simulate aerosol-cloud processes at fine grid scales. The model was set up on a quad grid simulation with coarse scale (20-km grid spacing) and fine scale (4-km grid spacing) simulations. Nested simulation was performed to explicitly resolve convection in the fine grids. Chapter 2 presented the model framework and data processing for the simulation. Methodology and pre-analysis is presented in Chapter 3, whereas Chapter 4 focused on the characterisation of the regional pollution with WRF-Chem.

To investigate impact of pollution on southern African AQ composition and cloud microphysical processes due to aerosol changes in more detail, a perturbation (TEST) simulation was conducted during the second half of the baseline (CNTRL) simulation without BB emissions. The reasonable performance of the model on coarse and fine grid simulations enable us to conduct a series of sensitivity experiments to examine the role of aerosols in changing clouds and weather patterns. Chapter 5 focused on correlating aerosol contribution from different pollution sources and their influence on the regional pollution. Several cities/towns were chosen as point sources to assess how different locations are affected by BB emissions and/or other pollution sources as well as their influence on the regional pollution on different horizontal scales. The study reveals that emissions from major pollution sources (MPSs) are becoming more important for the regional and global air pollutants. Once emitted into the atmosphere, aerosols show differences in their atmospheric dispersion and contribution, depending on the particle sizes and geographical locations of the MPSs. This results in their potential to pollute the surface and locally downwind locations. Through moderating meteorological variables, aerosols exert feedbacks on AQ (Zhang et al., 2015) as evidenced in the report.

Finally, chapter 6 focused on ACIs, changes in cloud processes due to aerosol concentration and radiative balance. This investigated both direct and indirect aerosol effects. Impact of aerosol concentration is shown to be more evident (enhanced) when BB emissions are included in the simulation. The contribution of BBAs on CDNC, RB and LWC was investigated through the hypotheses proposed. It was found that CDNC and LWC were higher in regions with high aerosol concentrations, especially towards the west. Whilst this was evident in the high aerosol concentration, SSA tends to decrease in the same regions, indicating that more particle extinction was due to absorption. This is consistent with particle concentration diagnosed in chapters 4 and 5, indicating that even if BB is a major factor in some areas, other sources also make a significant contribution in other parts of the domain. To further evaluate the model, predictions were compared with measurements to

demonstrate its performance and the relevance of results. Comparison was done for some gases, aerosol properties and cloud variables from remote sensing techniques, field studies and observing stations. The model showed some skill in capturing the patterns/trends and chemical concentrations although in some same cases there is an offset where the model under/over-predicts the variables. However, a severe lack of measurement data over southern Africa makes it very difficult for a thorough assessment of WRF-Chem.

The main conclusions from this study are presented below and potential future work (studies) highlighted under recommendations.

- Southern Africa is burdened by all types of aerosols and trace gas pollutants from both natural and anthropogenic sources. Pollution depends on land use, meteorological conditions and biome density. Rural areas prone to agricultural and other livelihood activities, and those covered by dense forests (e.g. tropics) are the main source of biogenic and fire emissions whereas the more urban and industrial areas are more responsible for anthropogenic emissions.
- BBAs contribute a substantial proportion to the regional pollution and AQ composition, influencing atmospheric aerosol loading, resulting in pollution exceedance of major pollutants in some areas. There is a significant effect on the cloud layers in the vicinity of fires over land, leading to substantial effect due to semi-direct effect. Similarly, dust emissions over the Kalahari Desert contribute substantially to pollution in the southwest, particularly PM. This can impact on the regional AQ and human health over southern Africa.
- The simulation highlighted model sensitivity in grid resolutions. It was found that clouds respond differently to aerosol concentrations at different grid spacing. In the fine grids (cloud resolving scale), clouds are better resolved, covering a small portion of the total area than in the coarse grid (parameterised scale). Also, effective supersaturation (S_{eff}) with respect to water reached during cloud formation is lowered if BBAs are present. There is less reduction in water vapour in parameterised clouds than in resolved clouds. S_{eff} tends to be grid dependent (increases in unresolved clouds), implying less competition of water vapour by CCN than in resolved clouds. The sum of LWC is higher in CNTRL than in TEST across all domains, implying that the second indirect effect is stronger than the semi-direct effect.
- Although BB makes a substantial contribution to pollution, some of the regions tend to be indirectly affected, except when in the vicinity or downwind of pollution. Enhancement to the chemical species occurred more in cities directly affected by BB, whereas the most populous cities appeared to be indirectly affected by BB (see tables 5.4, 5.5 and C2).

  AOD becomes stronger near active burning areas with an enhancement of up to 38% and 31% in tropical west and east regions whilst in the less-active burning areas, AOD increased by

11%. Excess energy absorbed is found to be higher over tropical west (+56 Wm^{-2}), followed by tropical east (+23 Wm^{-2}) and southeast (+14 Wm^{-2}) respectively.

7.3 Recommendations and future work

This study provides a benchmark for a more understanding of the atmospheric AQ composition, and is important to evaluate effects of air pollution over southern Africa. Model evaluation and results analysis presented in this study identified some important possible investigations that can be good candidates for future work. For example, further studies can be done to continue the work primarily focusing on extending the analysis presented in chapters 5 and 6, which in this case are limited to an investigation on a single winter period. Because the model is run for a relatively short time period, it is likely not to fully adjust to the aerosol forcing/evolutions, thus reducing statistical significance of the results. This can be extended in several other ways to improve reliability of results, their validity for various meteorological conditions and pollution scenarios. Extending the simulation period can lead to more understanding of weather patterns under different chemical and meteorological conditions. However, it is worth noting that simulations with regional models (at cloud resolving grid scales) can be computationally expensive, especially for sensitivity studies with several parameters and atmospheric processes such as in WRF-Chem (often referred to as a 'one-atmosphere' model). This is often a limiting factor and time consuming.

Further investigations and contrasts with other pollution scenarios would suffice when extending the period to include or cover the wet season as well, thus increasing the robustness of results. The considerably different meteorological and pollution conditions will have important effects on tropospheric chemistry and aerosols, which cannot be extrapolated from the results of the simulations during wintertime alone. Further more, analysis of the statistical data presented can be improved and more information compared or contrasted with measurement and/or fieldwork dataset (e.g. campaigns) if available. Additionally:

* It would also be necessary to undertake investigation(s) of other case studies similar to that examined in this work (e.g. monsoon onset, dust outbreak), together with a sensitivity analysis of the variations of the microphysical cloud properties under different weather conditions.

* With a significant contribution from dust emission to PM, a similar analysis and/or simulations is worth performing to compare their contribution to the regional pollution and meteorological implications.

* Long-term studies would not only be crucial for improving aerosol chemistry modelling over southern Africa, but also serve for monitoring AQ management plans and further identifying main

pollutant sources within different source categories (Kuik et al., 2015). Also, combining ground-based measurements and satellite remote sensing would make it possible to obtain relatively reliable information regarding aerosol distributions over the domain (Yuzhi et al., 2014).

* There is a severe lack of measurement data over southern Africa; this still makes it very difficult for some model evaluations in order to test the suitability and performance of the models. More data need to be available and/or measurements done so that results can be compared with the real world.

* Work must also be coordinated with initiatives through other bodies and/or research institutions, collaborating with other research scientists and within the regional community to facilitate the awareness and understanding of pollution in the regional environment. Enhancing collaborative work amongst investigators can effectively help transfer the knowledge to the global community (Fast et al., 2009a).

* Implementations of different modelling framework and techniques/approaches (e.g. RegCM and other AQ models) can lead to better estimates of the uncertainties and allow for different processes to be assessed. Lastly, the modelling activity should be operational and not limited to a short-term basis; it should be developed for a long-term process dedicated to local-regional-global model studies including chemistry and aerosol processes coupled to the meteorology.

Appendices

Appendix A: Modelling system and data processing

A1: Introduction

The scope of this section is to describe the pre-processing steps done to prepare and process data used in the study. This section briefly highlights on some of the components and descriptions of computational analyses, details of which have been given in various sections of the report. Investigating the interactions of atmospheric trace components with meteorology, their representation in the model and evolution in the atmosphere requires the treatment of relevant physical, chemical and dynamical processes at a precise level of complexity. To fulfil these, several steps have to be undertaken. Below, I highlight on some of the processes and/or precautions taken in the current study.

A2: The model system

The Weather Research and Forecasting model with chemistry (WRF-Chem) is a community regional meteorological fully coupled "online" atmospheric chemical transport model (Grell et al., 2005a; 2011a,b; Fast et al., 2006). The chemistry component is embedded in the WRF model (Skamarock et al., 2005; 2008), itself also a mesoscale meteorological model. WRF-Chem is designed to integrate meteorology and atmospheric chemistry simultaneously, incorporating several chemical mechanisms (gases and aerosol packages) with biogenic emissions, surface deposition, convective transport, turbulence, photolysis and advective transport (Peckham, 2008). Its unique design enables us to look at the interaction between meteorology and chemistry at the same time, without employing the more 'conventional' method of separate simulations. Interaction between solar radiation with aerosols and the microphysical parameterisations are also accounted for in WRF-Chem, making it capable to handle various processes and allowing for fully interactive feedbacks between the chemistry and meteorology (Grell et al., 2004b; Gustafson Jr. et al., 2007).

WRF-Chem requires meteorological and chemical emissions input data through each grid point to predict concentrations and depositions of different chemical species. Different model aspects (both meteorology and chemistry) are described by Skamarock et al. (2005; 2008), Grell et al. (2005a; 2011a,b), Fast et al. (2006), Gustafson Jr. et al. (2007) and Chapman et al. (2009). The user guides: (http://www2.mmm.ucar.edu/wrf/users/docs/user_guide_V3/ARWUsersGuideV3.pdf); (http://ruc.noaa.gov/wrf/WG11/Users_guide.pdf) also give details on the implementation and running of the model. Physical parameterisations used in the current simulation include the Morrison double-moment microphysics (Morrison et al., 2005; 2009) coupled to model aerosol parameterisation, Rapid Radiative Transfer Model scheme for longwave and shortwave radiation (Mlawer et al., 1997; Iacono

et al., 2008); Grell-Dévényi cumulus parameterisation (Grell and Dévényi, 2002), Yonsei University planetary boundary layer scheme (Hong et al., 2006), Noah land surface model (Chen and Dudhia, 2001) together with the chemical bond mechanism-Z (CBM-Z) and the Fast-J photolysis scheme (Wild et al., 2000; Fast et al., 2006). Various input parameters are defined in the *namelist.input* file. Table A1 shows various configuration options used in the model system.

Process	Model Option
Cloud microphysics	Morrison's-double moment
Cumulus parameterisation	Grell-Dévényi
Land surface model	Noah LSM
Boundary layer scheme	YSU
Surface layer scheme	Monin-Obukov
Shortwave radiation	RRTMG
Longwave radiation	RRTMG
Photolysis	Fast-J
Gas-phase chemistry	CBM-Z
Aerosol scheme	MOSAIC (8-bin)
Chemical boundary conditions	MOZART

Table A1: Physical parameterisations used in WRF-Chem model simulation

A3: PREP-CHEM-SRC

This is a grid-mapping program (developed in Brazil) used to prepare emission fields of trace gases and aerosols for use in atmospheric chemistry transport models (Freitas et al., 2011). The source code called "Prep_Chem_source" can be used to generate both anthropogenic and natural emissions for simulation. PREP-CHEM-SRC is commonly used in most WRF-Chem simulations and is available to model users. Emissions dataset obtained from the databases is used to generate emission files *wrfchemi* (anthropognic) and *wrffirechemi* (biomass burning) as input files to run the model. The desired grid configuration and path directories are set and defined in a FORTRAN *namelist.input* template called *'prep_chem_sources.inp.'* After a successful running of the code, the "raw" data generated (binary intermediate format) is then converted into a netCDF format readable by WRF-Chem. This is done through a program called *"convert_emiss.exe"* in the WRF-Chem directory. Emission data developed would represent emission amounts valid for certain date(s) and species used.

A4: Emissions inventory

Table A2 below shows emission species generated from the databases by PREP-CHEM-SRC, while table A3 shows biogenic species (generated by MEGAN module).

A2: *Anthropogenic emissions*

Emission species	**Notes/name**	Data source
E_SO_2	Sulphur dioxide	EDGAR
E_NO	Nitrous oxide	EDGAR
E_NO_2	Nitrogen dioxide	EDGAR
E_CO	Carbon monoxide	EDGAR
E_ETH	Ethane	EDGAR
E_HC_3	alkane	EDGAR
E_HC_5	alkane	EDGAR
E_HC_8	alkane	EDGAR
E_XYL	xylene (aromatic)	EDGAR
E_OL_2 (E_ETE)	Ethylene/ethelene (alkene)	EDGAR
E_OLT	Terminal olifin (alkene)	EDGAR
E_OLI	Internal olifin (alkene)	EDGAR
E_TOL	Toluene (aromatic)	EDGAR
E_CSL	Cresol (aromatic)	EDGAR
E_HCHO	Formaldehyde (carbonyl)	EDGAR
E_ALD	Aldehyde (carbonyl)	EDGAR
E_KET	Ketone (carbonyl)	EDGAR
E_ORA_2	Acetic and higher org. acids (alkene)	EDGAR
E_NH_3	Ammonia	fwabaw
E_$PM_{2.5}$	Particulate matter (<2.5 μm)	EDGAR
E_PM_{10}	Particulate matter (<10 μm)	EDGAR
E_OC	Organic carbon	GOCART/fwbawb
E_BC	Black carbon	GOCART/fwbawb
E_ISO*	Isoprene	-
E_SULF*	Sulphate	-

(*) Indicate species not available from any of the databases, except where secondary.

A3: *Biogenic emissions*

Emission	**Notes**	Data source
ebio_iso	Isoprene	MEGAN

ebio_oli	Internal olifin	MEGAN
ebio_olt	Terminal olifin	MEGAN
ebio_api	Alpha pinene	MEGAN
ebio_lim	Limonene	MEGAN
ebio_xyl	Xylene	MEGAN
ebio_hc3	Alkane	MEGAN
ebio_ete	Ethylene	MEGAN
ebio_ket	Ketone	MEGAN
ebio_ald	Aldehyde	MEGAN
ebio_hcho	Formaldehyde	MEGAN
ebio_eth	Ethane	MEGAN
ebio_ora$_2$	Acetic and higher organic acids	MEGAN
ebio_co	Carbon monoxide	MEGAN
ebio_nr	Nonreactive VOC	MEGAN
ebio_no	Nitrous oxide	MEGAN
*Nitrogen gases (NO, N_2O, NH_3)		-
*Other monoterpenes		-
Other sesquiterpenes		-
*Other VOCs		-
*MBO	Biogenic 2-methyl-3-buten-2-ol)	-
*Myrcene		-
*Acetone		-
*Sabinene		-

(*) Indicate species not available from the database, except where secondary.

Units: mol km^{-2} hr^{-1}

Appendix B: Supplementary material to results

This section presents additional results to support those already presented in the report. Discussion and evaluation has been done in the corresponding parts/sections of the report.

B1: Meteorology

The figures below are presented to compliment results discussed in chapter 4 (section 4.3).

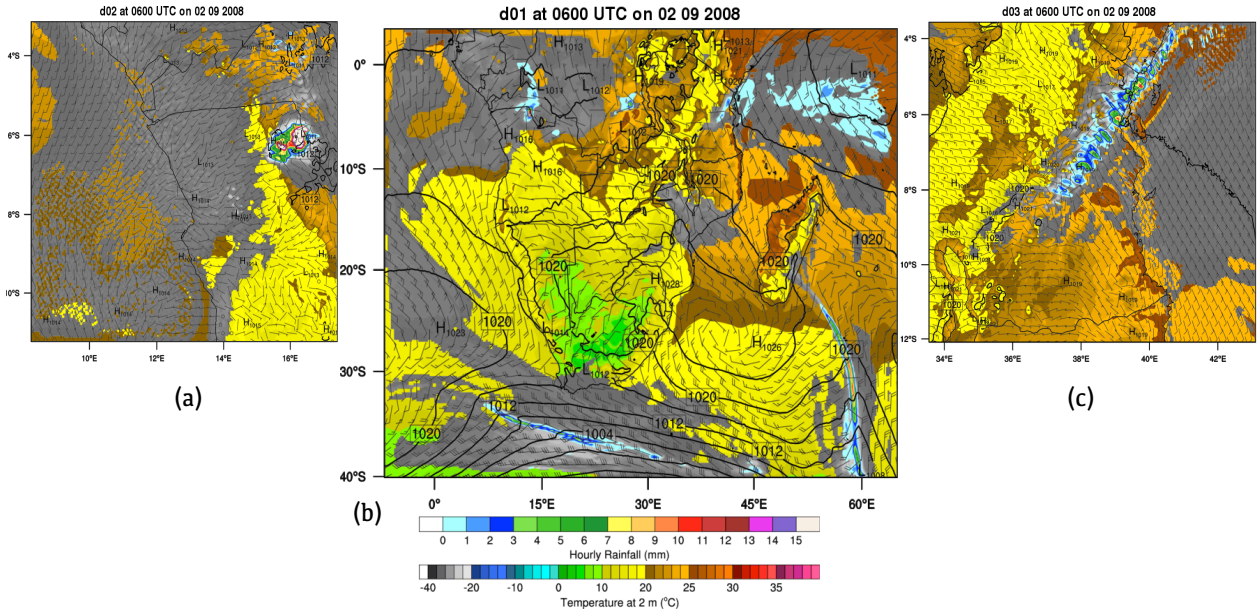

Fig. B1: Composites at coarse (20-km) and fine (4-km) grids. Precipitation band associated with westerly extra-tropical storms in the mid-latitudes. Convective cells over the coarse grid captured over (a) Angola [d02] and (c) Tanzania-Kenya [d03], at high resolutions respectively. Model output at 0600 UTC 02 September 2008.

The figure shows convective cells in the small domains (over Angola [d02] and a band of precipitation along the east coast over Tanzania-Kenya [d03]). Although the coarse domain captures the features, detailed structures are more pronounced in the fine grids. As highlighted in the text, increasing model resolution gives a better resolution of cloud microphysical processes.

B2: Emissions

Spatial distribution of emissions southern Africa, valid at 0000 UTC 30 August 2008.

Figure $B2_1$ show distribution of anthropogenic emissions (BC, OC, NO_2 and total PM (PM_{10}) from EDGAR, whereas as Fig. $B2_2$ show fire emissions (biomass burning) from MODIS (CO, NO, OC and NO_2) respectively. The blue 'lines' in Fig. $B2_1$(c) indicate ship routes over the oceans. Description is given in chapters 3 and 4 in the main text.

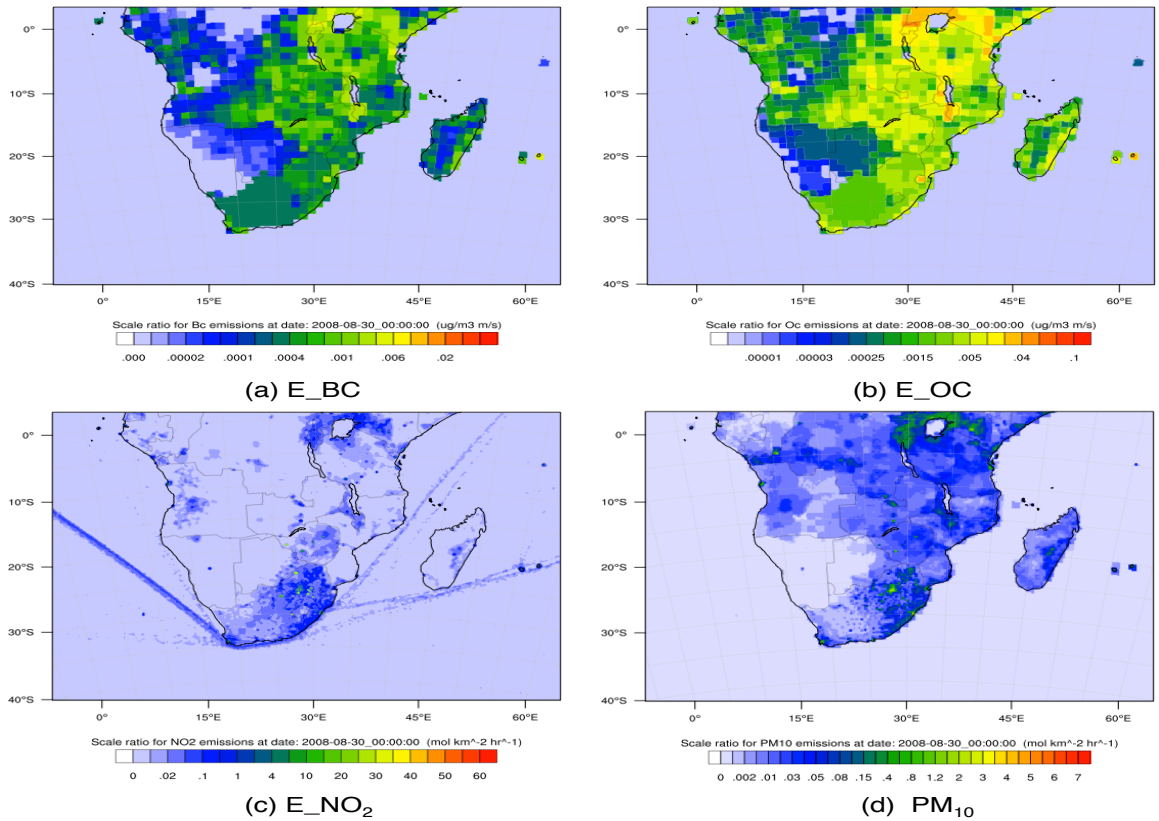

Fig. B2$_1$: Anthropogenic emissions: (a) black carbon, (b) organic carbon, (c) nitrogen dioxide and (d) particulate matter (below 10 μm).

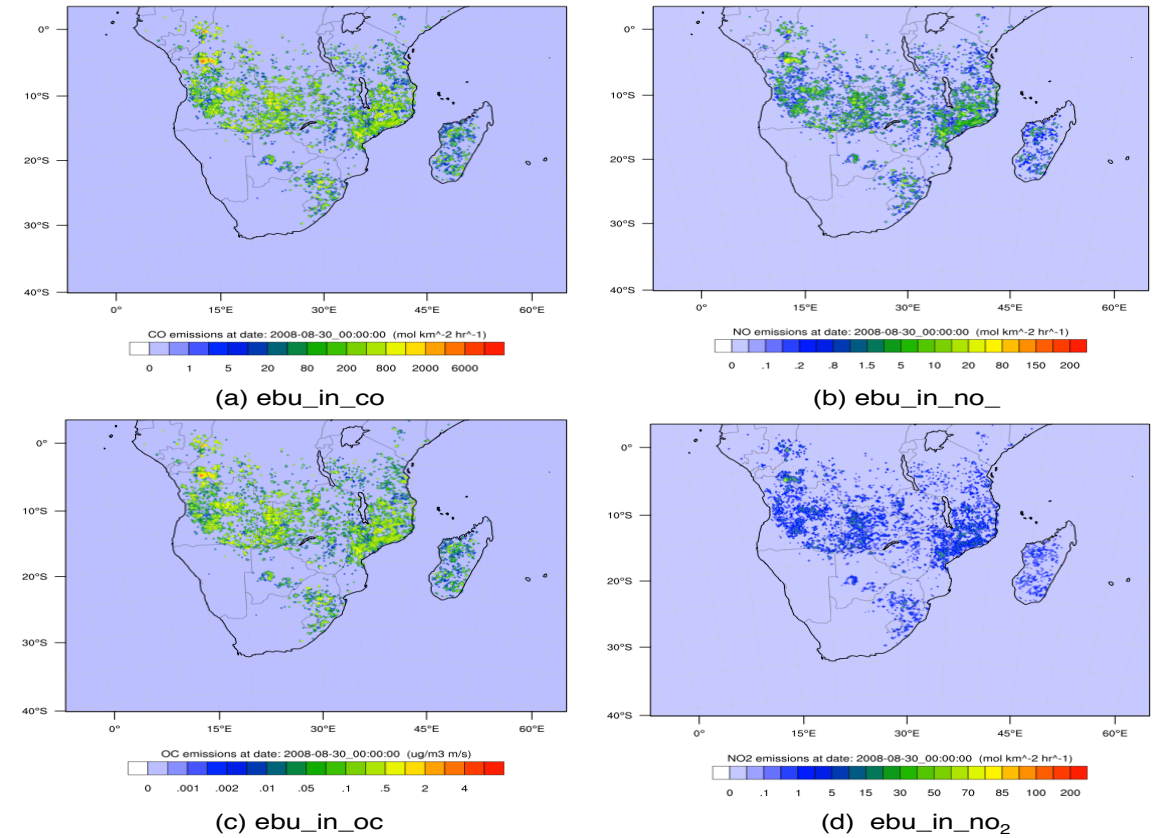

Fig. B2$_2$: Biomass burning (fire) emissions: (a) carbon monoxide, (b) nitric oxide, (c) organic carbon and (d) nitrogen dioxide.

B3: Gases and Aerosols

(a) Spatial and temporal distribution of gases and aerosols over southern Africa (see Chapter 4)

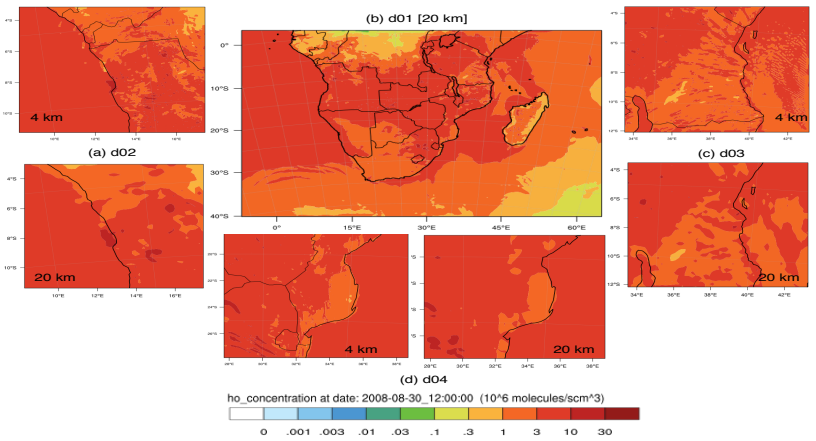

(a) Surface concentration profile

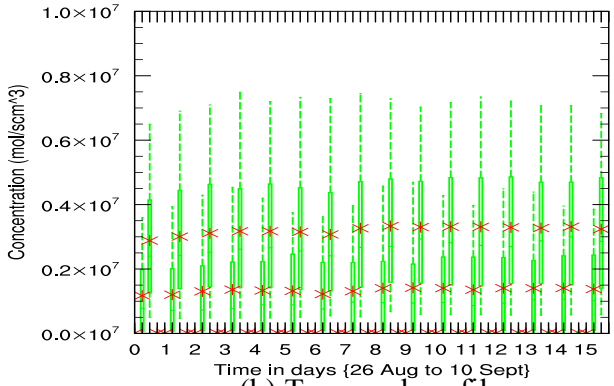

(b) Temporal profile

$B3_1$: Hydroxyl radical (OH), daytime oxidant. (a) Model output at 1200 UTC 30 September 2008. (b) Temporal varation averaged over the coarse domain (d01).

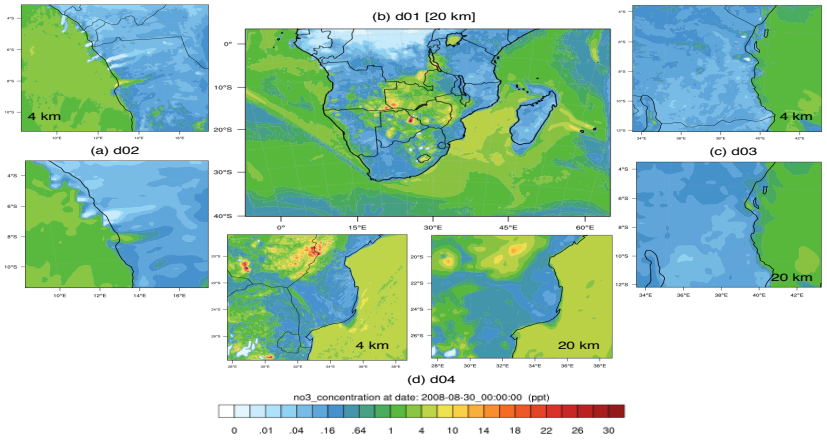

(a) Surface concentration profile

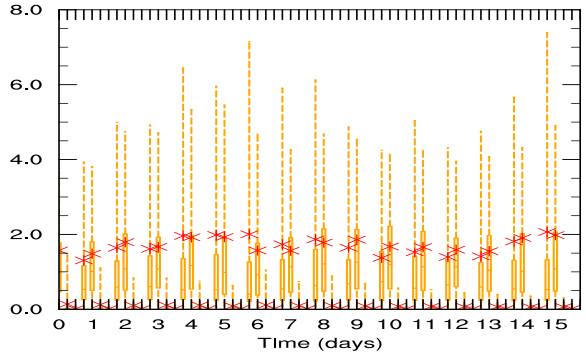

(b) Temporal profile

$B3_2$: Nitrate radical (NO_3), night-time oxidant. (a) Model output at 1800 UTC 30 September 2008. (b) Temporal varation averaged over the coarse domain (d01).

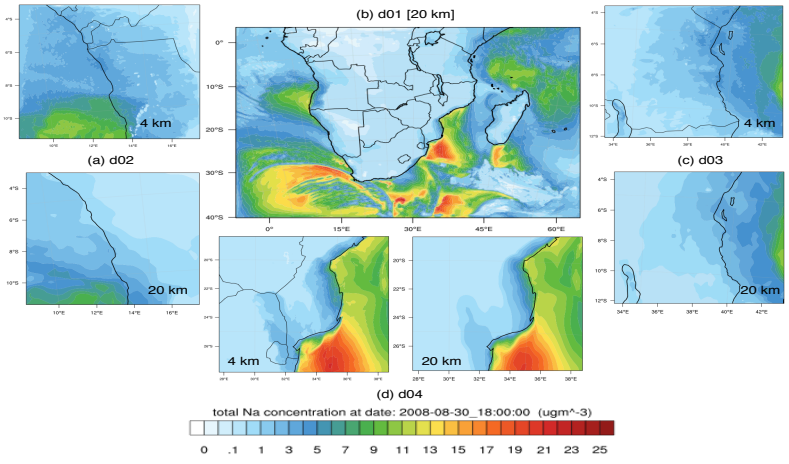

(a) Surface concentration profile

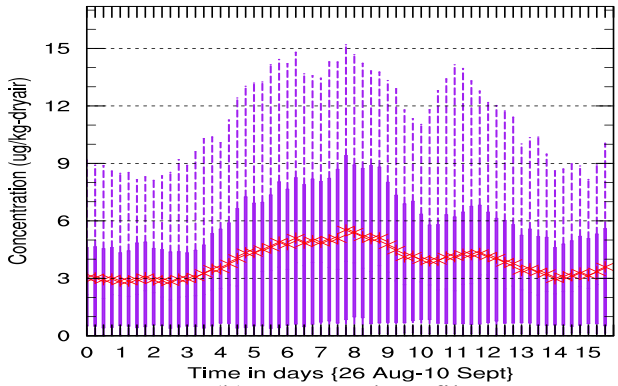

(b) Temporal profile

$B3_3$: Sodium (Na), primary sea salt aerosol. (a) Model output at 1800 UTC 30 September 2008. (b) Temporal varation averaged over the coarse domain (d01).

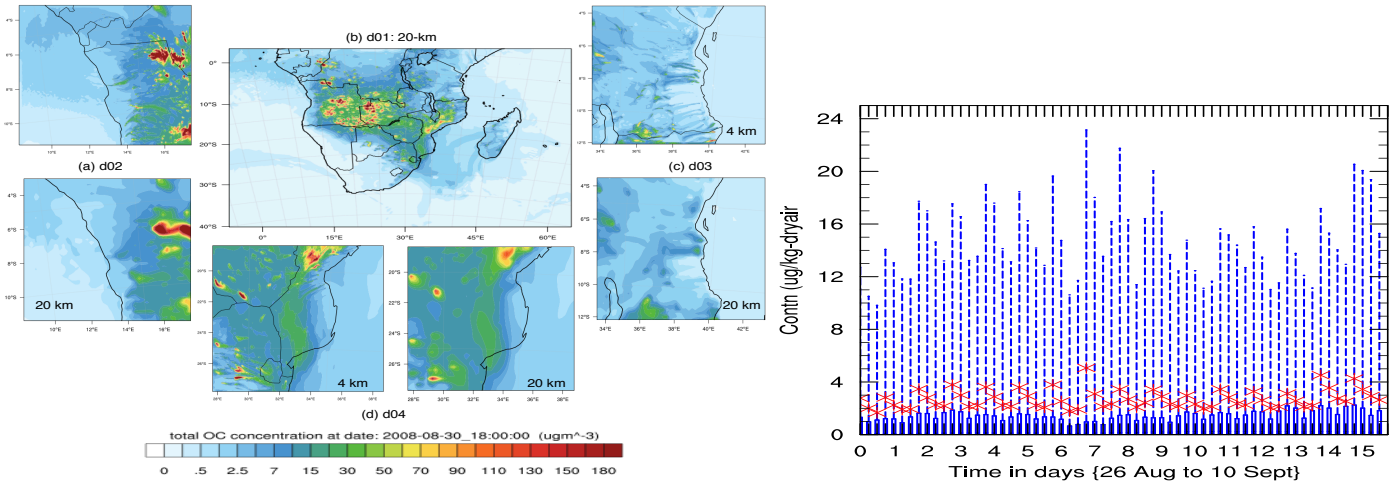

(a) Surface concentration profile (b) Temporal profile

$B3_4$: Organic carbon (OC), primary aerososl. (a) Model output at 1800 UTC 30 September 2008. (b) Temporal varation averaged over the coarse domain (d01).

Fig. B3: Surface and temporal distributions for OH, NO_3, Na and OC species. OH concentration is shown at 1200 UTC. Sub-domains are plotted at fine (4 km) and coarse resolutions (20 km) respectively, whereas the temporal distribution show data averaged over the coarse domain for the entire simulation period (CNTRL).

Figures $B3_1$–$B3_4$ show surface and temporal distributions of gases and aerosols over the domain, plotted at different grid resolutions as described in the text. The first two species are important radicals in tropospheric chemistry. For example, OH is a daytime oxidant whilst NO_3 is a night-time oxidant. OH has maximum concentrations during the day whereas NO_3 has its maximum concentrations during night-time and minimum during daytime. OC is one of the major primary aerosol products of combustion. As shown, concentrations are higher within the BB-dominated regions. Na is a primary sea salt aerosol. Unlike the other chemical species, production and abundance of sea salt depends on their production mechanisms over the ocean surface (e.g. wind speed). Once produced, concentrations depend on reaction properties with other species as well as particle sizes determining their transport away from the sources. The temporal profiles shown against each plot show the diurnal variation from the CNTRL simulation.

(b) Spatial and temporal distribution of gases and aerosols degraded outputs (see Chapter 5)

The figures below show pollutant surface and diurnal variation in the fine grids, in addition to the plots shown in the main text (section 5.6). These are primary- and secondary gases (CO and O_3), secondary aerosol (SO_4^{2-}) and particulate matter less than 2.5 μm ($PM_{2.5}$) –which can be from both primary and secondary pollutants. In each plot, the top panels represent CNTRL and TEST at 4-km grid spacing, whereas the middle panels are at 20-km grid spacing (i.e. same grid plotted at a coarser resolution). The bottom panels show the average concentration for the fine grid averaged to 20-km. In the time series, the red curve is the difference (CNTRL–TEST) from the fine grid; blue curve is the difference

between CNTRL and TEST in the fine grid averaged to 20-km whereas the green curve respresents the difference in the CNTRL for the same grid averaged at 4 and 20-km grid spacing respectively.

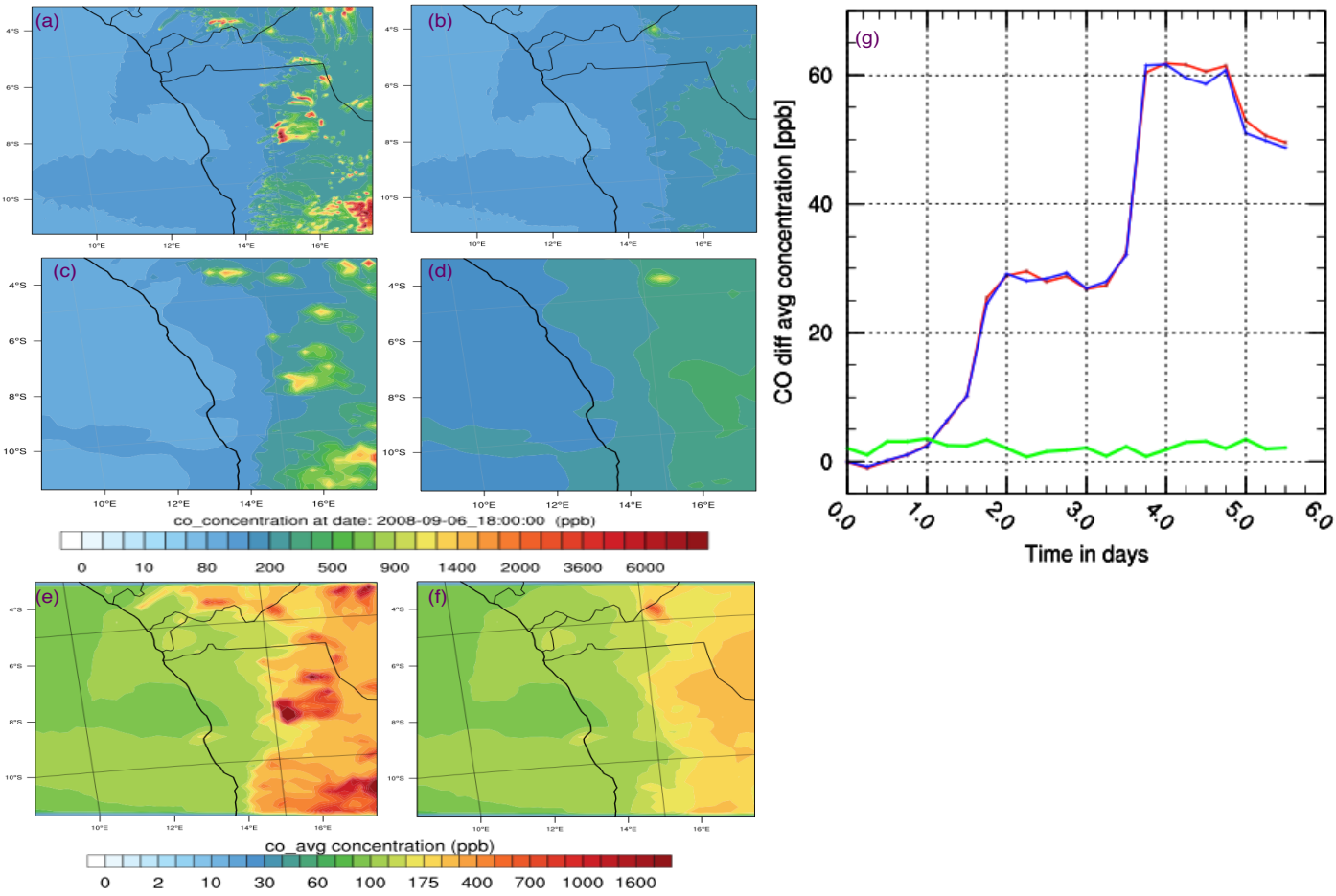

Fig. B4a: CO (d02)

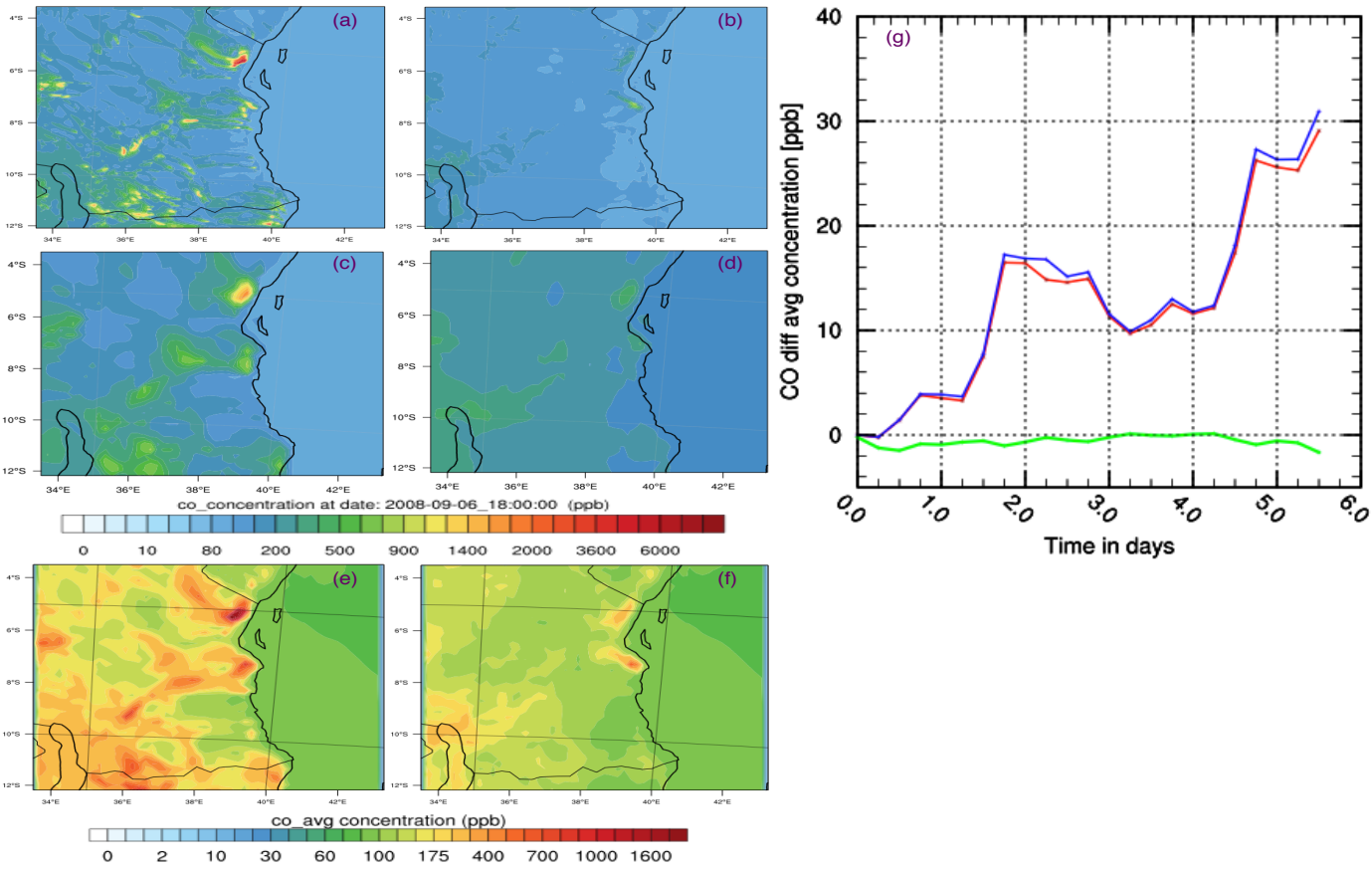

Fig. B4b: CO (d03)

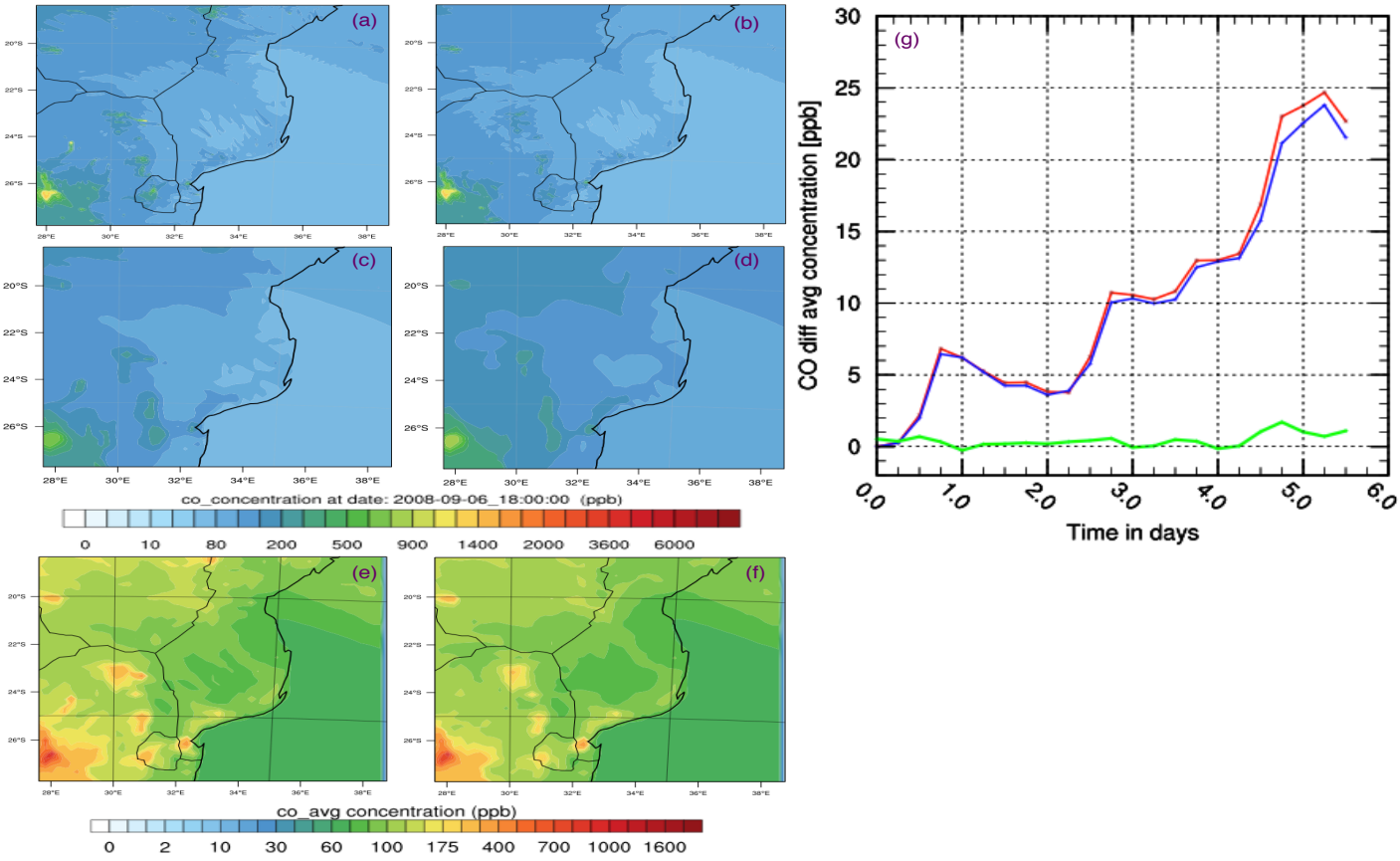

Fig. B4c: CO (d04)

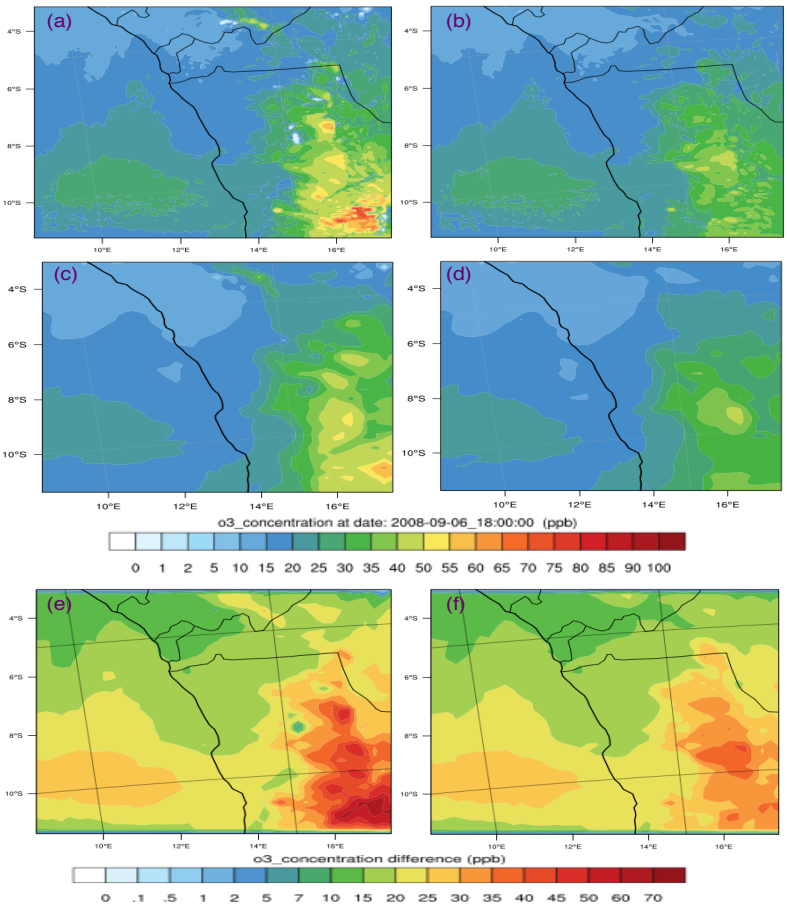

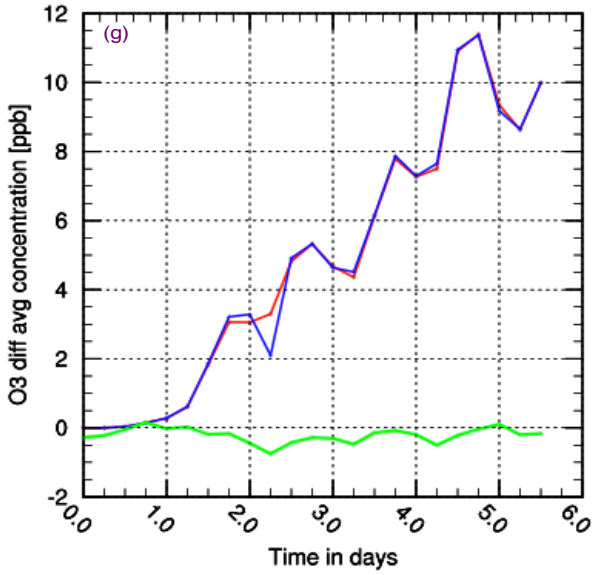

Fig. B4d: O_3 (d02)

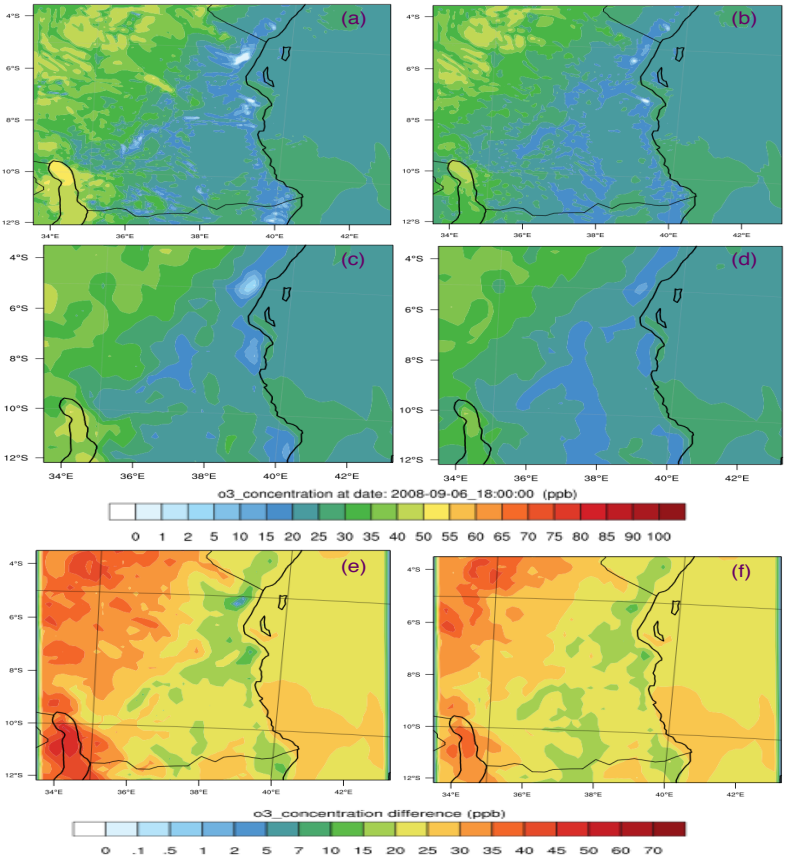

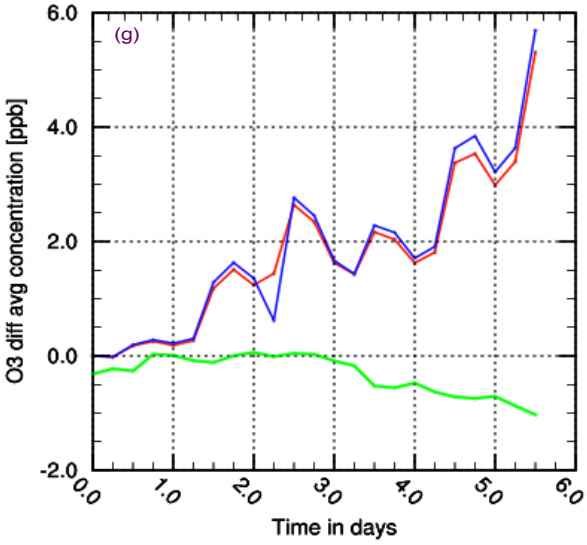

Fig. B4e: O_3 (d03)

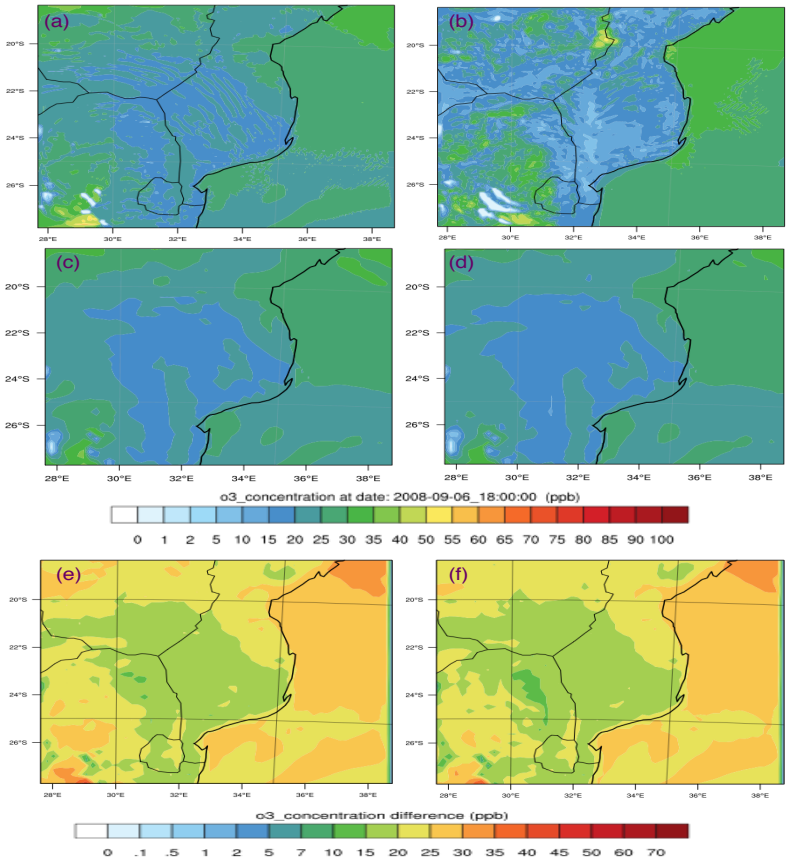

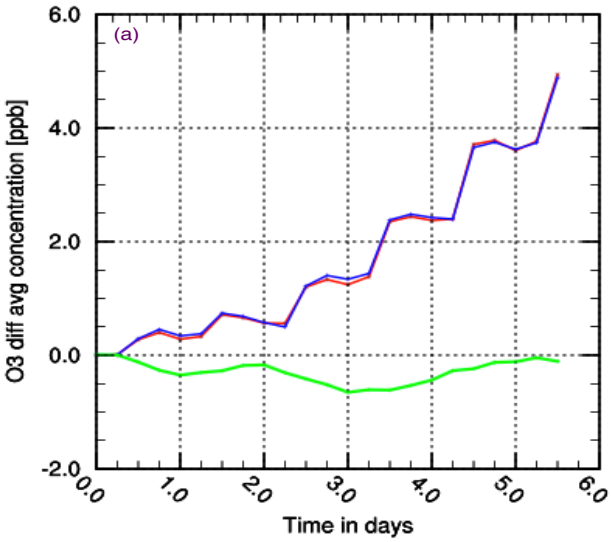

Fig. B4f: O_3 (d04)

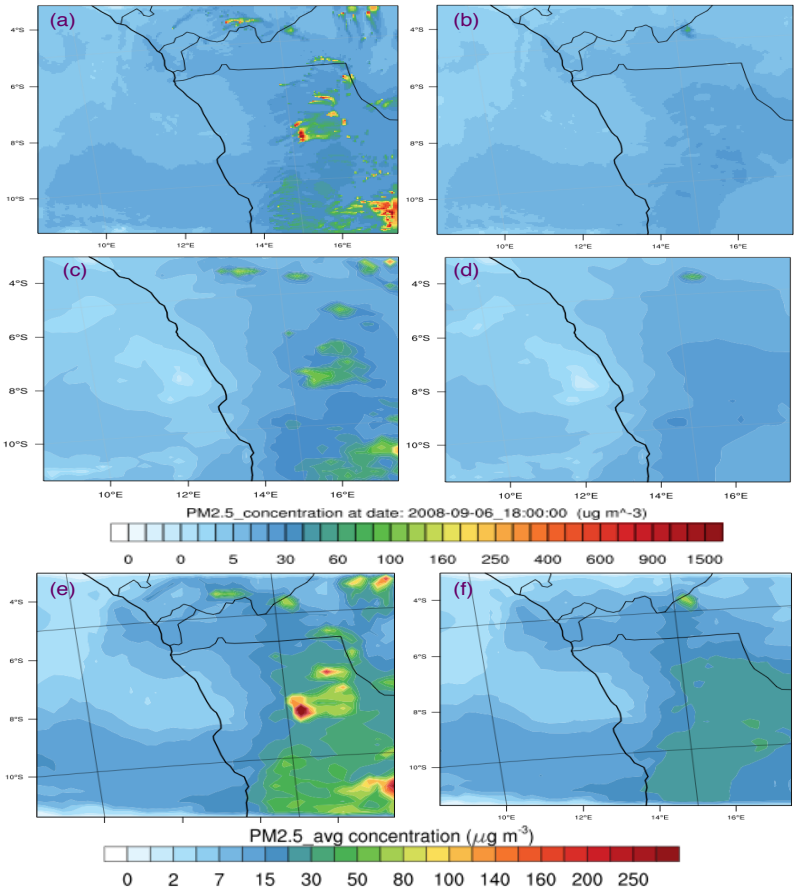

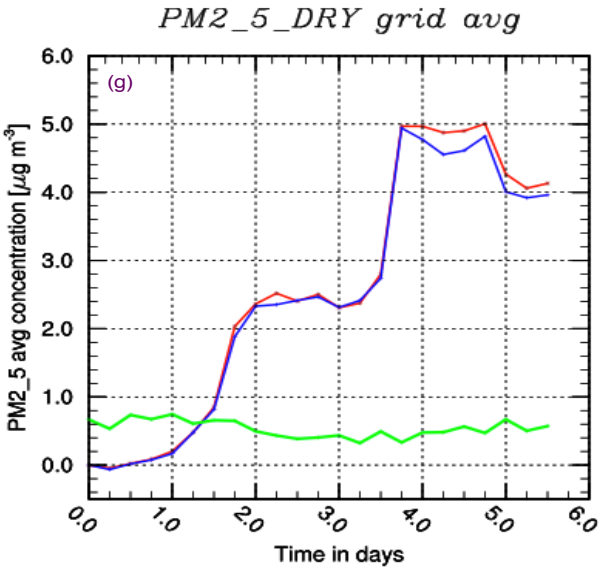

Fig. B4g: $PM_{2.5}$ (d02)

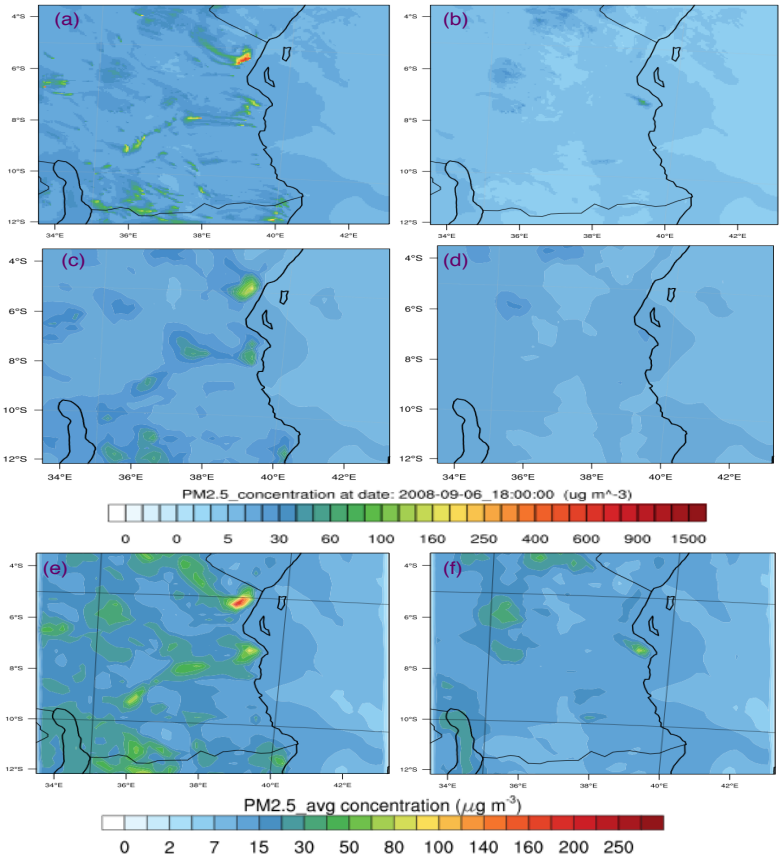

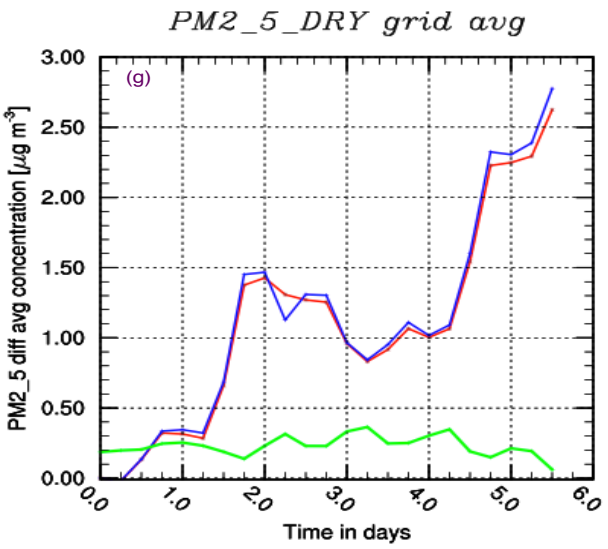

Fig. B4h: $PM_{2.5}$ (d03)

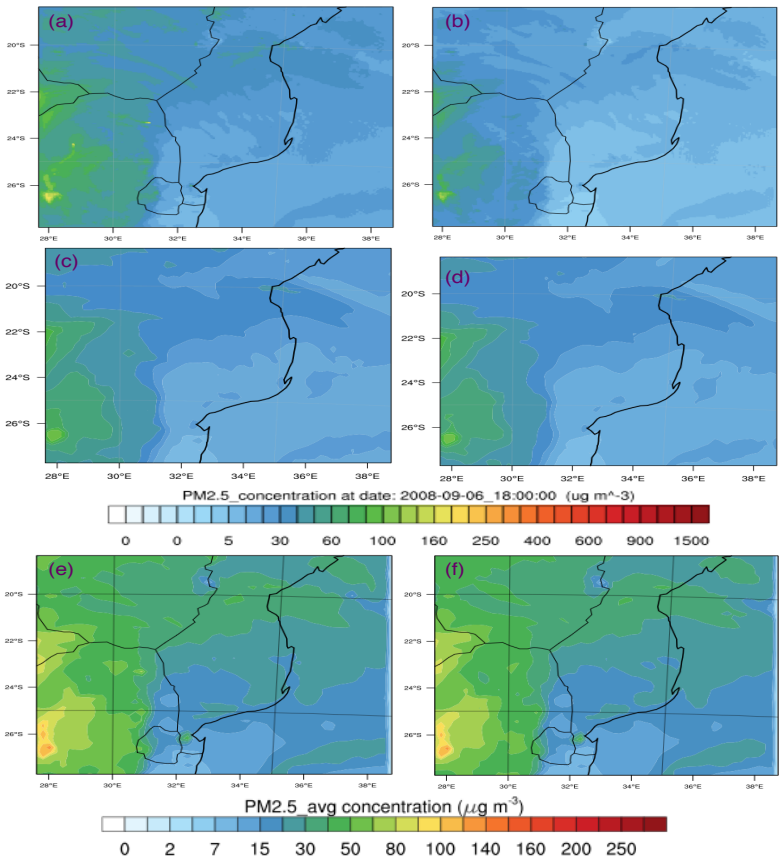

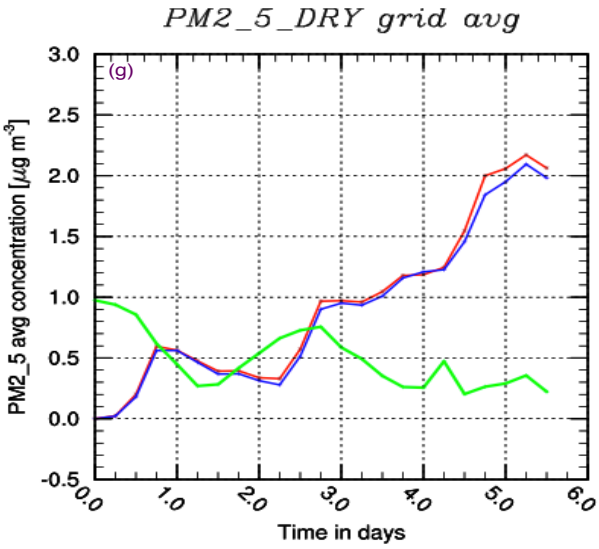

Fig. B4i: $PM_{2.5}$ (d04)

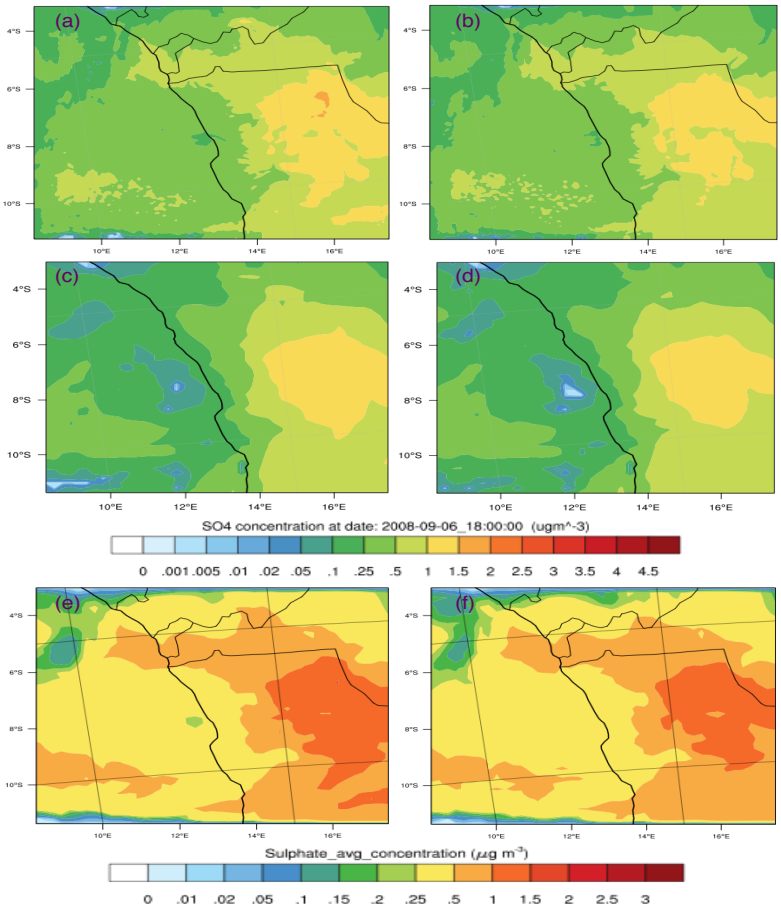

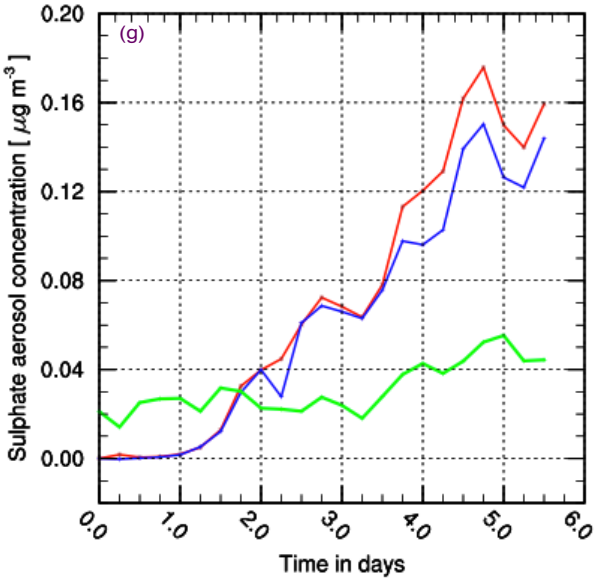

Fig.B4j: SO_4^{2-} *(d02)*

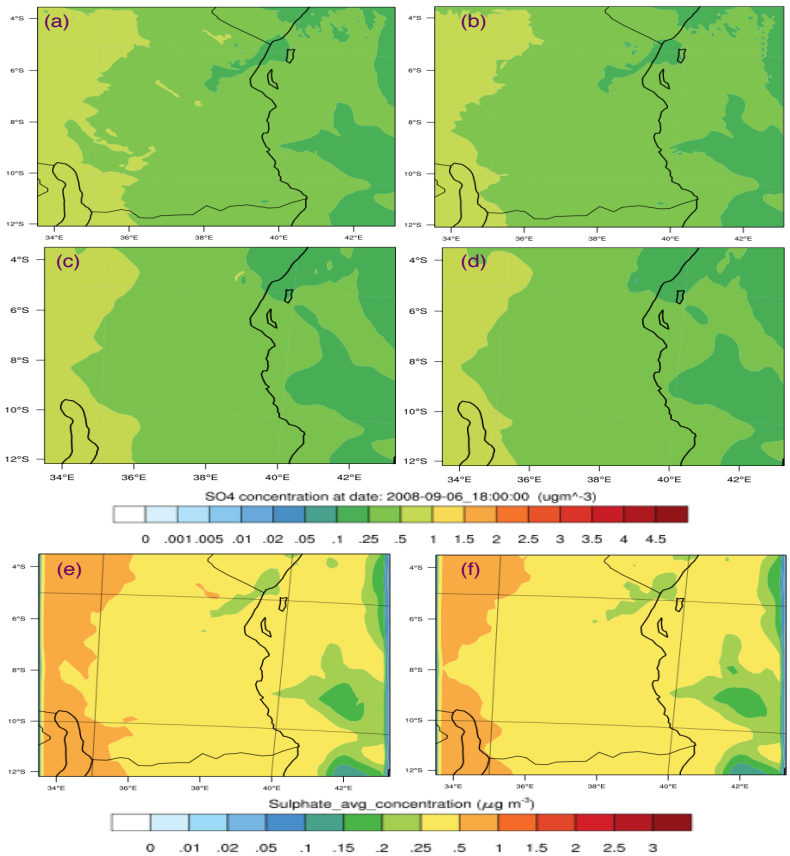

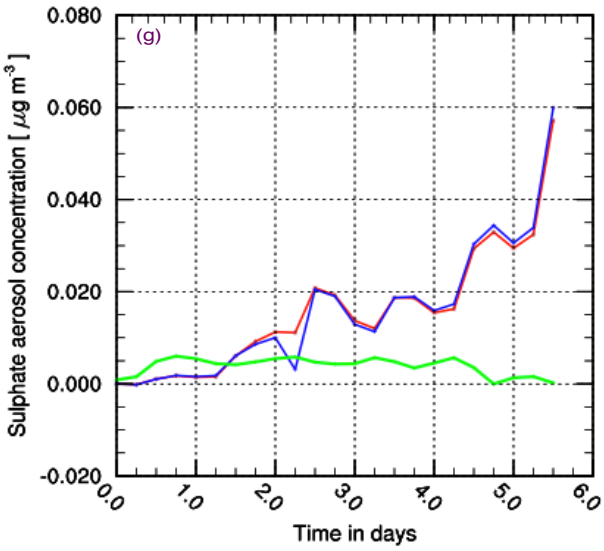

Fig. B4k: SO_4^{2-} *(d03)*

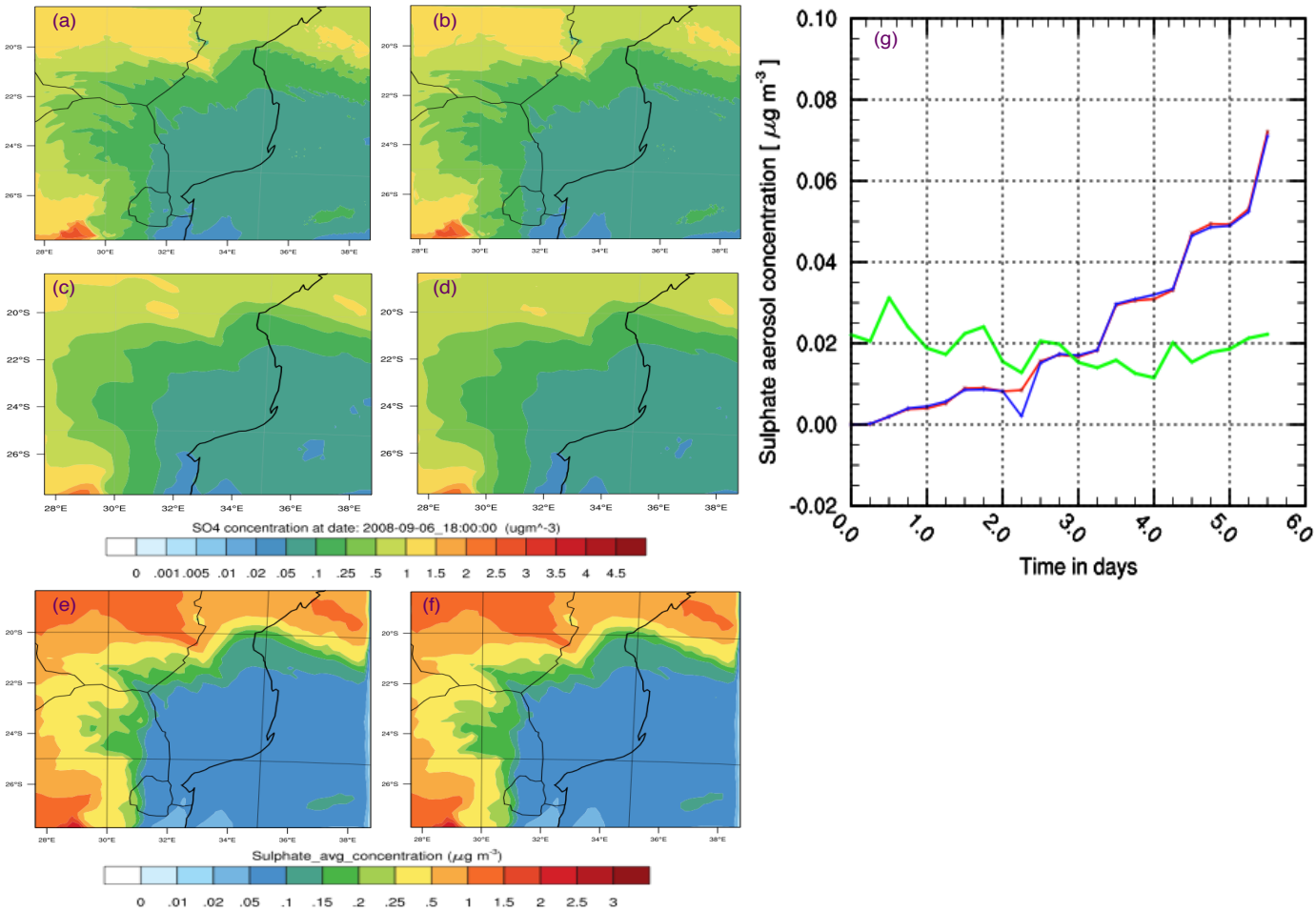

Fig. B4l: SO_4^{2-} (d04)

Appendix C: Statistical data and derivations

Statistical data used for the analysis in chapters 5 and 6. Description for processing these data is given in the main text.

C1: Mean concentrations of major pollutants across the domain

Table C1: Simulated daily surface concentrations for cities over southern Africa, averaged over the entire simulation period. Data in parenthesis indicate results from fine grids.

Model scenario		BB_on		BB_off	
Location	species	mean	std dev	mean	std dev
Luanda	O_3	21 (22)	5.6 (5.5)	20 (22)	5.5 (5.5)
	NO	0.42 (0.07)	0.47 (0.09)	0.42 (0.07)	0.46 (0.09)
	NO_2	2.0 (1.5)	0.92 (1.4)	1.9 (1.5)	0.93 (1.4)
	CO	127 (161)	21 (41)	125 (161)	22 (41)
	PM_{10}	16 (31)	6.2 (13)	16 (31)	6.1 (13)
	$PM_{2.5}$	7.4 (15)	3.0 (6.0)	7.2 (15)	3.0 (6.0)

Marimba	O_3	31 (30)	13 (12)	24 (24)	9.0 (8.0)
	NO	0.08 (0.17)	0.20 (0.44)	0.03 (0.03)	0.04 (0.04)
	NO_2	2.3 (2.3)	3.5 (5.4)	0.57 (0.45)	0.70 (0.42)
	CO	403 (370)	346 (268)	197 (198)	57 (40)
	PM_{10}	49 (48)	33 (32)	29 (29)	6.5 (6.2)
	$PM_{2.5}$	39 (37)	30 (23)	21 (22)	5.6 (4.9)
Lubumbashi	O_3	45	19	34	13
	NO	0.07	0.1	0.02	0.03
	NO_2	2.0	2.0	0.48	0.37
	CO	467	236	246	93
	PM_{10}	64	22	43	10
	$PM_{2.5}$	42	19	24	7.1
Kinshasa	O_3	17	7.3	15	5.9
	NO	0.11	0.16	0.11	0.15
	NO_2	2.1	2.2	2.0	2.2
	CO	804	736	771	720
	PM_{10}	188	188	182	184
	$PM_{2.5}$	83	83	79	81
Kaoma	O_3	45	17	39	14
	NO	0.04	0.04	0.02	0.02
	NO_2	1.1	1.2	0.32	0.22
	CO	271	86	170	39
	PM_{10}	42	7.3	31	7.0
	$PM_{2.5}$	28	6.7	19	4.4
Dar es Salaam	O_3	18 (19)	9.2 (6.6)	18 (19)	8.9 (6.4)
	NO	0.87 (0.17)	1.8 (0.62)	0.88 (0.17)	1.8 (0.62)
	NO_2	5.6 (1.5)	6.6 (3.8)	5.4 (1.5)	6.6 (3.6)
	CO	226 (156)	178 (154)	220 (151)	175 (145)
	PM_{10}	78 (32)	36 (27)	79 (31)	35 (26)

	$PM_{2.5}$	26 (16)	20 (18)	26 (15)	19 (17)
Windhoek	O_3	51	15	49	12
	NO	0.03	0.04	0.03	0.04
	NO_2	0.56	0.4	0.53	0.40
	CO	158	48	149	46
	PM_{10}	57	35	58	37
	$PM_{2.5}$	30	10	21	9.9
Francistown	O_3	35	16	33	15
	NO	0.05	0.09	0.05	0.09
	NO_2	0.58	0.44	0.54	0.39
	CO	186	39	170	32
	PM_{10}	63	31	61	31
	$PM_{2.5}$	35	13	33	13
Harare	O_3	39	20	33	18
	NO	0.55	0.90	0.65	1.02
	NO_2	7.8	7.0	7.3	6.6
	CO	306	150	239	98
	PM_{10}	67	20	59	14
	$PM_{2.5}$	37	13	31	8.2
Beira	O_3	24 (24)	6.2 (4.8)	22 (23)	5.2 (4.8)
	NO	0.03 (0.02)	0.04 (0.03)	0.02 (0.01)	0.02 (0.02)
	NO_2	0.33 (0.24)	0.34 (0.30)	0.22 (0.17)	0.24 (0.19)
	CO	122 (138)	37 (59)	112 (133)	33 (57)
	PM_{10}	42 (54)	15 (19)	41 (54)	15 (19)
	$PM_{2.5}$	22 (28)	7.5 (11)	21 (28)	7.5 (11)
Johannesburg	O_3	25 (28)	20 (18)	24 (26)	19 (17)
	NO	4.7 (1.7)	7.5 (4.2)	4.9 (1.8)	7.6 (4.4)
	NO_2	19 (12)	17 (10)	18 (12)	16 (9.8)
	CO	678 (625)	466 (364)	645 (599)	453 (361)

	PM_{10}	201 (178)	119 (84)	197 (176)	118 (84)
	$PM_{2.5}$	91 (87)	48 (41)	89 (85)	48 (41)
Toliara	O_3	20	6.6	20	6.4
	NO	0.05	0.05	0.04	0.05
	NO_2	0.47	0.44	0.46	0.44
	CO	94	15	92	13
	PM_{10}	26	7.3	26	7.3
	$PM_{2.5}$	12	3.1	11	3.1

Units: ppb (gases) and μg m^{-3} (aerosols)

Table C2: Average percentage concentration differences for the entire run

City/town	Percentage mean concentration differences					
	O_3	NO	NO_2	CO	$PM_{2.5}$	PM_{10}
Marimba	23	63	75	51	46	41
Lubumbashi	24	72	76	47	43	33
Harare	15	-15	6	22	16	12
Luanda	5	0	5	2	3	0
Dar es Salaam	0	-1	4	3	0	-1
Johannesburg	4	-4	5	5	2	2

Units: %

C2: Determining radiative balance due to aerosol effects

The following derivations define the expressions used to determine changes in radiative balance (RB) due to aerosols presented in chapter 6. Following from Skaeda et al. (2011) and Archer-Nicholls et al. (2015) [manuscript in preparation], the expressions are defined and shown below, taking into consideration both the shortwave (SW) and longwave (LW) flux energy going into and out of the system. The energy can be calculated either at the top of the atmosphere (TOA) or ground surface (BTM), in terms of 'upwelling' or 'down-welling' for upward and downward and calculated for "clear-sky" or 'cloudy sky" conditions. Changes to the SW or LW variables can also be determined between model scenarios at different layers in the atmosphere. For example, the change in the downward shortwave radiation at the surface can be determined from:

$$\Delta SW_{BTM}^{\downarrow} = SW_{BTM}^{CNT\downarrow} - SW_{BTM}^{TST\downarrow} \qquad [C1]$$

where; the superscripts 'CNT' and 'TST' denote CNTRL and TEST respectively. In this derivation, the symbol Δ represents the difference between CNTRL and TEST. The RB is determined from the

sum of the energy going into the system minus the sum of the upwelling radiation at the top of the atmosphere, expressed as:

$$RB = \left\{\left(SW_{TOA}^{\downarrow} + LW_{TOA}^{\downarrow}\right) - \left(SW_{TOA}^{\uparrow} + LW_{TOA}^{\uparrow}\right)\right\} \quad [\text{W m}^{-2}] \qquad [C2]$$

where: SW_{TOA} and LW_{TOA} are the shortwave and longwave radiations at the TOA respectively. Arrows "↑" and "↓" indicate the upward and downward direction. The above expression can be determined for clear or cloudy sky conditions:

$$\overline{RB}_{CLR} = \left\{\left(SW_{TOA}^{\downarrow} + LW_{TOA}^{\downarrow}\right) - \left(SW_{TOA}^{\uparrow} + LW_{TOA}^{\uparrow}\right)\right\}_{CLR} \qquad [C3]$$

For example, considering the difference in the net all-sky conditions:

$$\Delta RB = F_{all}^{CNT} - F_{all}^{TST} \qquad [C4]$$

Deriving equation [C4] in terms of the difference between model scenarios at TOA, we obtain:

$$\Delta RB = RB^{CNT} - RB^{TST} = \left\{\left(SW_{TOA}^{CNT\uparrow} + LW_{TOA}^{CNT\uparrow}\right) - \left(SW_{TOA}^{TST\uparrow} + LW_{TOA}^{TST\uparrow}\right)\right\} \qquad [C5]$$

Similar expressions can also be done for cloudy- and clear sky conditions to determine changes in RB or the sum of the direct radiative effect of aerosols:

$$\Delta RB_{CLR} = RB_{CLR}^{CNT} - RB_{CLR}^{TST} \; ; \; \Delta RB_{CLDY} = RB_{CLDY}^{CNT} - RB_{CLDY}^{TST} \qquad [C6]$$

$$2\overline{RB}_{CLR} = \left(RB_{CLR}^{CNT} + RB_{CLR}^{TST}\right) \; ; \; 2\overline{RB}_{CLDY} = \left(RB_{CLDY}^{CNT} + RB_{CLDY}^{TST}\right) \qquad [C7]$$

The total radiative flux absorbed by the atmosphere can be determined from the difference between incoming and outgoing flux over the column:

$$SW_{Abs} = \left\{\left(SW_{TOA}^{\downarrow} + SW_{BTM}^{\uparrow}\right) - \left(SW_{TOA}^{\uparrow} + SW_{BTM}^{\downarrow}\right)\right\} \qquad [C8]$$

Appendix D: Constants

R_v (universal gas contant) = 8.31451 JK^{-1} mol^{-1}

ρ_{air} (air density) = 1.225 kg m^{-3}

ρ_w (water density) = 1000 kg m^{-3}

1 atm (standard atmspheric pressure) = 101325 Pa

References

Abdul-Razzak, H., Ghan, S., Carpio, C. R., 1998. A parameterization of aerosol activation. 1. Single aerosol type. Journal of Geophysical Research, Vol. 103. No. D6., pp. 6123–6131, March, 12, 1998.

Abdul-Razzak, H., Ghan, S. J., 2000. A Parameterization of aerosol activation: 2. Multiple aerosol types. Journal of Geophysical Research, Vol. 105(D5), pp. 6837–6844, March 16, 2000.

Abdul-Razzak, H., Ghan, S. J., 2002. A Parameterization of aerosol activation: 3. Sectional representation. Journal of Geophysical Research, Vol. 107(D3), 4026, 10.1029/2001JD000483, 2002.

Abel, S. J., Highwood, E. J., Haywood, J. M., Stringer, M. A., 2005. The direct radiative effect of biomass burning aerosols over southern Africa. Atmos. Chem. Phys., 5, 1999–2018, 2005. www.atmos-chem-phys.org/acp/5/1999/

Aghedo, A. M., Schultz, M. G., Rast, S., 2007. The influence of African air pollution on regional and global tropospheric ozone. Atmos. Chem. Phys., 7, 1193–1212, 2007. www.atmos-chem-phys.net/7/1193/2007/

Ahmadov, R., 2012. Chemical mechanisms and KPP. WRF-Chem tutorial, NCAR, July 25, 2012. URL: http://ruc.noaa.gov/wrf/WG11/wrf_tutorial_2012/wrfchem_tutorial_gaschem.pdf

Albrecht, B. A., 1989. Aerosols, Cloud microphysics, and Fractional Cloundiness. Science Reports. Vol. 245, pp. 1227–1230.

Allan, B. J., et al., 2000. The nitrate radical in the remote marine boundary layer. Journal of Geophysical Research, Vol. 105, No. D19, pp. 24,191–24,204, October 16, 2000.

Al Razi, K. Md., Hiroshi, M., 2012. Assessment of the Weather Research and Forecasting/Chemistry Model to Simulate Ozone Concentration in March 2008 over Coastal Areas of the Sea of Japan. Atmosphere 2012, 3, 288–319, doi:10.3390/atmos3030288. www.mdpi.com/journal/atmosphere.

Ammuaylojaroen, T., et al., 2014. Effect of direct emissions inventories on modeled ozone and carbon monoxide in Southeast Asia. Atmos. Chem. Phys. Discuss., 14, 12983–13012, 2014. www.atmos-chem-phys.net/14/12983/2014/ doi:10.5194/acp-14-12983-2014.

Andreae, M. O., 1996. Raising dust in the greenhouse effect. Nature 380, 389–390 (04 April 1996). doi:10.1038/380389a0.

Andreae, M. O., Crutzen, P. J., 1997. Atmospheric Aerosol: Biogeochemical Sources and Role in Atmospheric Chemistry. Science. Vol. 276. pp. 1052–1057., www.sciencemag.org.

Andreae, M. O., Merlet, P., 2001. Emission of trace gases and aerosols from biomass burning. Global Biogeochemical Cycles, Vol. 15, No. 4., pp. 955-966.

Andreae, M. O., et al., 2009. Aerosols, Clouds, Precipitation and Climate (ACPC). Science Plan & Implementation Strategy. URL: http://www.ileaps.org/sites/atm.helsinki.fi.ileaps/files/ACPC_SciencePlan_FINAL_Melbourne160809_p3_33.pdf

Andreae, M. O., Rosenfeld, D., 2008. Aerosol-cloud-precipitation interactions. Part 1. The nature and sources of cloud-active aerosols. Earth-Science Reviews, 89 (2008) 13–41, www.elsevier.com/locate/earscirev

Andreas, E. L., Edson, J. B., Monahan, E. C., Rouault, M. P., Smith, S. D., 1994. The Spray contribution to Net Evaporation from the Sea: A Review of Recent Progress. Boundary-Layer Meteorology, 73: 3–52, 1995.

Appraisal, 2013: Integrated assessment for regional and local air quality policies. Layman's report. URL: http://www.appraisal-fp7.eu/site/images/download/Laymansreport_D58.pdf

Archer-Nicholls, S., et al., 2014. Characterising Brazilian biomass burning emissions using WRF-Chem with MOSAIC sectional aerosol, Geosci. Model Dev. Discuss., 7, 6061–6131, doi:10.5194/gmdd-7-6061-2014, 2014.

Archer-Nicholls, S., Lowe, D., Schultz, D. M., McFiggans, G., Aerosol–radiation–cloud interactions in a regional coupled model: the effects of convective parameterisation and resolution (Manusctript prepared for Atmos. Chem. Phys). Version 2014/09/167.15.

Astitha, M., Lelieveld, J., Kader, M. A., Pozzer, A., de Meij, A., 2012. Parameterisation of dust emissions in the global atmospheric chemistry-climate model EMAC: impact of nudging and soil properties. Atmos. Chem. Phys., 12, 11057–11083, 2012. www.atmos-chem-phys.net/12/11057/2012/, doi:10.5194/acp-12-11057-2012.

Atkinson, R., 2000. Atmospheric chemistry of VOCs and NO_x. Atmospheric Environment 34 (2000) 2063–2101. www.elsevier.com/locate/atmosenv

Atkinson, R., Arey, J., 2003. Gas-phase tropospheric chemistry of biogenic volatile organic compounds: a review. Atmospheric Environment. Vol. 37, Supplement 2. pp. 197-219. Elsevier. http://dx.doi.org./10.1016/S1352-2310(03)00391-1.

Atkinson, R., et al., 2004. Evaluated kinetic and photochemical data for atmospheric chemistry: Volume I –gas phase reactions of Ox, HOx, NOx and Sox species. Atmos. Chem. Phys., 4, 146–1738, 2004. www.atmos-chem-phys.org/acp/4/1461/

Atkinson, R., 2008. Our Present Understanding of the Gas-Phase Atmospheric Degradation of VOCs. Book Chapter. Simulation and Assessment of Chemical Processes in a Multiphase Environment NATO Science for Peace and Security Series C: Environmental Security 2008, pp 1–19.

Bailey, R. A., et al., 1978. Chemistry of the Environment. Academic Press, Inc.

Baklanov, A., et al., 2014. Integrated Meteorology Chemistry Models: Challenges, gaps, needs and future directions. White Paper Draft 1. URL: http://wwosc2014.org/documents/PP_AOC_Baklanov_WWOSC_WP_V1.pdf

Baltensperger, U., et al., 2005. Secondary organic aerosols from anthropogenic and biogenic precursors. Vol.130. pp 265–278. The Royal Society of Chemistry.

Bangert, M., Kottmeier, C., Vogel, B., Vogel, H., 2011. Regional scale effects of the aerosol cloud interaction simulated with an online coupled comprehensive chemistry model. Atmos. Chem. Phys., 11, 4411–4423, 2011. www.atmos-chem-phys.net/11/4411/2011/, doi:10.5194/acp-11-4411-2011.

Barmes, B., Mathee, A., Thomas, E., Bruce, N., 2009. Household energy, indoor air pollution and child respiratory health in South Africa. Journal of Enrgy in southern Africa. Vol. 20. No. 1. February 2009.

Barnard, J. C., et al., 2004. An evaluation of the FAST-J photolysis algorithm for predicting nitrogen dioxide photolysis rates under clear and cloudy sky conditions. Atmospheric Environment 38 (2004) 3393–3403. www.elsevier.com/locate/atmosenv

Barnard, J. C., et al., 2010. Technical Note: Evaluation of the WRF-Chem "Aerosol Chemical to Aerosol Optical Properties" Module suing the MILAGRO campaign. Atmos. Chem.. Phys., 10,7325-7340, 2010. www.atmos-chem-phys.net/10/7325/2010/

Baró, R., et al., 2015. Sensitivity analysis of the microphysics scheme in WRF-Chem contribution to the AQMEII phase 2. Atmospheric Environment xxx (2015) 1–10. Elsevier., www.elsevier.com/locate/atmosenv

Ben-Weiss, G. A., Jin, L., Bauer, S. E., Bennartz, R., Liu, X., Zhang, K., Ming, Y., Guo, H., Jiang, J. H., 2014. Evaluating clouds, aerosols, and their interactions in three global climate models using satellite simulations and observations. doi:10.1002/2014JD021722.

Berg, L. K., Shrivastava, M., Easter, R. C., Fast, J. D., Chapman, E. G., Liu, Y., 2014. A new WRF-Chem treatment for studying regional scale impacts of cloud-aerosol interactions in parameterized cumuli. Geoscientific Model Development. Geosci. Model Dev. Discuss., 7, 2651–2704, 2014. www.geoscie-model-dev-discuss.net/72651/2014/, doi:10.5194/gmdd-7-2651-2014.

Bigala, T. A., 2008. Aerosol Loading over the South African Highveld. M.Sc. Dissertation. University of Witwatersrand, South Africa. (wiredspace.wits.ac.za).

Billmark, K. A., Swap, R. J., Macko, S. A., 2003. Characterization of sources for southern African aerosols through fatty acid and trajectory analyses. J. Geophys. Res., 108(D13), 8503, doi:10.1029/2002JD002762, 2003.

Binkowski, F. S., Roselle, S. J., 2003. Models-3 Community Multiscale Air Quality (CMAQ) model aerosol component. J. Geophys. Res., 108(D6), 4183, doi:10.1029/2001JD004109, 2003.

Blanchard, D. C., 1983. Air–Sea Exchange of Gases and Particles, NATO ASI
Ser. Vol. 108, pp. 407–454, D. Reidel, Norwell, Mass.

Blanchard, D. C., 1989. The Ejection of Drops from the Sea and Their Enrichment with Bacteria and Other Materials: A Review. Estuaries. Vol. 12. pp. 127–137.

Brown, R. G., 1999. Chapter 2: Emission and Flash Technique in Environmental Photochemistry. Environmental Photochemistry, Volume 2. The Handbook of Environmental Chemistry, pp. 27–61.

Brown, S., Gaston, G. 1996. Tropical Africa: Land Use, Biomass, and Carbon Estimates for 1980. NDP-055, Carbon Dioxide Information Center, Oak Ridge National Laboratory, Oak Ridge, Tennessee. doi:10.3334/CDIAC/lue.ndp055.

Brown, S. S., et al., 2003. Applicability of the steady state approximation to the interpretation of atmospheric observations of NO_3 and N_2O_5. Journal of Geophysical Research, Vol. 108, No. D17, 4539, doi:10.1029/2003JD003407, 2003.

Brown, S. S., et al., 2007. High resolution vertical distribution of NO_3 and N_2O_5 through the nocturnal boundary layer. Atmos. Chem. Phys., 7, 139–149, 2007. www.atmos-chem-phys.net/7/139/2007/

Brown, S. S., and Stutz, J., 2012. Nighttime radical observations and chemistry. CRITICAL REVIEW. Chem. Soc. Rev., 2012, 41, 6405–6447 www.rsc.org/csr
doi:10.1039/c2cs35181a.

Cater, W. P. L., 2000. Implementation of the SAPRC99 Chemical Mechanism into the Models-3 Framework. A Report to the United States Environmental Protection Agency. URL: www.cert.ucr.edu/~carter/SAPRC99.htm

Chakraborty, S., Maitra, A., 2012. A Comparative Study of Cloud Liquid Water Content from Radiosonde Data at a Tropical Location. International Journal of Geosciences, 2012, 3, 44-49. http://dx.doi.org/10.4236/ijg.2012.31006/

Chang, F., 2007. The Noah Land Surface Model in WRF. A short tutorial. Research Application Laboratory (RAL) LSM group meeting, 17 April 2007. NCAR. www.atmos.illinois.edu/~snesbitt/ATMS597R/.../noahLSM-tutorial.pdf

Chang, W. L., et al., 2011. Heterogeneous Atmospheric Chemistry, Ambient Measurements, and Model Calculations of N_2O_5: A Review. Aerosol Science and Technology. 45:6, 665-695, doi:10.1080/02786826.2010.551672, http://dx.doi.org/10.1080/02786826.2010.551672

Chapman, E. G., Gustafson Jr., W. I., Easter, R. C., Barnard, J. C., Ghan, S. J., Pekour, M. S., Fast, J. D., 2009. Coupling aerosol-cloud-radiative processes in the WRF-Chem model: Investigating the radiative impact of elevated point sources. Atmos. Chem. Phys., 9, 945–964, 2009. www.atmos-chem-phys.net/9/945/2009/

Chatfield, R. B., Guan, H., Thompson, A. M., Witte, J. C., 2004. Convective lofting links Indian Ocean air pollution to paradoxical South Atlantic ozone maxima, Geophys. Res. Lett., 31, L06103, doi:10.1029/2003GL018866.

Cheng, F., Dudhia, J., 2001. Coupling an Advanced Land Surface-Hydrology Model with the Penn State-NCAR MM5 Modeling System. Part I: Model Implementation and Sensitivity. Mon. Weather Rev., 129, pp. 569–585.

Chimidza, S., Moloi, K., 2001. Identification of aerosol particles in three locations in eastern Botswana. J. Geophys. Res., 105(D14), pp. 17,811–17,818.

Chin, M., Ginoux, P., Kinne, S., Torres O., Holben, B. N., Duncan, B. N., Martin, R. V., Logan, J. A., Higurashi, A., Nakajima, T., 2002. Tropospheric Aerosols Thickness from the GOCART Model and Comparisons with Satellite and Sun Photometer Measurements. A.M.S.

Collins, W. J., Stevenson, D. S., Johnson, C. E., Derwent, R. G., 1997. Tropospheric Ozone in a Global-Scale Three-Dimensional Lagrangian Model and Its Response to NOx Emission Controls. Journal of Atmospheric Chemistry 26: 223–274, 1997.

Constantino, L., Bréon, F. M., 2010. Analysis of aerosol-cloud interaction from multi-sensor satellites. Geophys. Res. Lett., 37, L11801, doi:10.1029/2009GL041828.

Constantino, L., Bréon, F. M., 2013. Aerosol indirect effect on warm clouds over South-East Atlantic, from co-located MODIS and CALIPSO observations. Atmos. Chem. Phys. Discuss., 13, 69–88, 2013. www.atmos-chem-phys.net/13/69/2013/, doi:10.5194/acp-13-69-2013.

Cosgrove, T., 2010. Colloidal Science. Principles, Methods and Applications. John Wiley & Sons Ltd.

Cotton, W. R., et al., 2010. Parameterisation or Modeling of Microysical Processes in Clouds. Chpater 4.

Crétat, J. Pohl, B., Richard, Y., Drobinski, P., 2012. Uncertainties in simulating regional climate of southern Africa: sensitivity to physical parameterizations using WRF. Clim. Dyn (2012) 38:613–634, doi:10.1007/s00382-011-1055-8.

Crippa, M., et al., 2013. Primary and secondary organic aerosol origin by combined gas- particle phase source apportionment. Atmos. Chem. Phys. Discuss. 13, 8537–8583. www.atmos-chem-phys-discuss.net/13/8537/2013/. doi:10.5194/acpd-13-8537-2013.

Cristofanelli, P., et al., 2009. Significant variations of trace gas composition and aerosl properties at Mt. Cimone during air mass transport from North Africa –contributions from wildfire emissions and mineral dust. Atmos. Chem. Phys., 9,4603–4619, 2009., www.atmos-chem-phys.net/9/4603/2009/

Crutzen, P. J., Andreae, M. O., 1990. Biomass Burning in the Tropics: Impact on Atmospheric Chemistry and Biogeochemical Cycles. Science. Vol. 250. No. 4988. pp. 1669–1678. doi:10.1126/science/250.4988.1669.

Damian, V., Sandu, A., Damian, M., Potra, F., Carmichael, G. R., 2002. The kinetic preprocessor KPP –a software environment for solving chemical kinetics. Computer and Chemical Engineering 26 (2002) 1567–f1579. Elsevier., www.elsevier.com/locate/compchemeng

Dentener, F. J., Crutzen, P. J., 1993. Reaction of N_2O_5 on Troposheric Aerosols: Impact on the Global Distributions of NOx, O_3 and OH. J. Geophys. Res., 98(D4), 7149–7163.

Diaz, J. P., et al., 2015. WRF-multi-physics simulation of clouds in the African region. Q. J. R. Meteorol. Soc. (2015), doi:10.1002/qg.2560.

de Graaf, M., Tilstra, L. G., Stammes, P., 2012. CLARIFI: Clouds and Aerosol Radiative Interaction Forcing Investigation. Scientific Report; WR 2012-01. Royal Netherlands Meteorological Institute. Ministry of Infrastructure and the Environment. www.knmi/nl/~tilstra/Reports/WR-2012-01.pdf.

Draft SADC Regional Policy Framework on Air Pollution, 2008. URL: https://www.sei-international.org/gapforum/regions/Southern_Africa/Final_circulated_Lusaka_Agreement.pdf.

ESA, 2005. Department of Environmental Affairs and Tourism. South Africa (Country Report). URL: http://www.un.org/esa/agenda21/natlinfo/countr/safrica/atmosphere.pdf.

Edwards, D. P., et al., 2004. Observations of carbon monoxide and aerosols from the Terra satellite: Northern Hemisphere variability. J. Geophys. Res., 109, D24202, doi:10.1029/2004JD004277, 2004.

Edwards, D. P., et al., 2006. Satellite-observed pollution from Southern Hemisphere biomass burning. J. Geophys. Res., 111, D14312, doi:10.1029/2005JD00655.

Emmons, L. K., et al., 2010. Description and evaluation of the Model for Ozone and Related Chemical Tracers, version 4 (MOZART-4). Geoscientific Model Development. www.geosci-model-dev.net/3/43/2010/

Fast, J., et al., 2006: Evolution of ozone, particulates, and aerosol direct radiative forcing in the vicinity of Houston using a fully coupled meteorology-chemistry-aerosol model. Journal of Geophysical Research. Vol., 111, D21305, doi:10.1029/2005JD006721, 2006.

Fast, J. D., Ghan, S. J., Schwartz, S. E., 2009a. Modelling Activities in the Department of Energy's Atmospheric Sciences Programm. Pacific Northwest National Laboratory (PNNL). PNNL-18752. URL: http://www.pnl.gov/main/publications/external/technical_reports/PNNL-18752.pdf

Fast, J., et al, 2009b. Evaluating simulated primary anthropogenic and biomass burning organic aerosols during MILAGRO: implications for assessing treatment of secondary organic aerosols. Atmos. Chem. Phys., 9,6191–6215,2009, www.atmos-chem-phys.net/9/6191/2009/.

Ferreira, J., Marques, C., Rocha, A., Gonçalves, P., 2005. WRF Modelling System Experiements With Different Land Surface Options. URL: 04_Ferreira_Juan_JuanFerreira_Contribution.pdf.

Flaounas, E., Bastin, S., Janicot, S., 2010. Regional climate modelling of the 2006 West African Monsoon: Sensitivity to convetion and planetary boundary layer parameterisation using WRF. Climate Dynamics. March 2010. Vol. 36, Issue 5, pp. 1083–1105, doi:10.1007/s00382-101-0785-3.

Flossmann, A. I., 1998. Interaction of Aerosol Particles and Clouds. *J. Atmos. Sci.,* 55 (5), 879–887.

Forkel, R., et al., 2006. Trace gas exchange and gas phase chemistry in a Norway spruce forest: A study with a coupled 1-dimensional canopy atmospheric chemistry emission model. Atmospheric Environment 40 (2006) S28–42. Elsevier. www.elsevier.com.locate/atmosenv

Forkel, R., et al., 2014. Analysis of the WRF-Chem contributions to AQMEII phase2 with respect to aerosol radiative feedbacks on meteorology and pollutant distributions. Atmospheric Environment. http://dx.doi:org/10.1016/j.atmosenv.2014.10.056.

Formenti, P., Elbert, W., Maenhaut, W., Haywood, J., Osborne, S., Andreae, M. O., 2003. Inorganic and carbonaceous aerosols during the Southern African Regional Science Initiative (SAFARI 2000) experiment: Chemical characteristics, physical properties, and emissions data for smoke from African biomass burning. J. Geophys. Res., 108(D13), 8488, doi:10.1029/2002JD002408, 2003.

Freiman, M. T., Tysosn, P. D., 2000. The thermodynamic structure of the atmosphere over South Africa: Implications for water vapour transport. Water SA. Vol. 26. No. 2. pp. 153–158. http://www.wrc.org.za

Freiman, M. T., Piketh, S. J., 2003. Air Transport into and out of the Industrial Highveld Region of South Africa. Journal of Applied Meteorology. A.M.S. Vol. 42. pp. 994–1002.

Freitas, S. R., et al., 2005. Monitoring the Transport of Biomass Burning Emissions in South America. Environmental Fluid Mechanics (2005) 5: 135–167.

Freitas, S. R., et al., 2007. Including the sub-grid scale plume rise of vegetation fires in low resolution atmospheric transport models, Atmos. Chem. Phys., 7, 3385–3398, doi:10.5194/acp-7-3385-2007, 2007.

Freitas, S. R., Longo, K. M., Dias, M. A. F. S., Chatfield, R., Dias, P. S., Artaxo, P., Andreae, M. O., Grell, G. G., Rodrigues, L. F., Fazenda, A., Panetta, J., 2009. The Coupled Aerosol and Tracer Transport model to the Brazilian development on the Regional Atmospheric Modeling System (CATT-BRAMS) –Part 1: Model description and evaluation. Atmos. Chem. Phys., 9, 2843–2861, 2009. www.atmos-chem-phys.net/9/2843/2009/

Freitas, S. R., Longo, K.M., Alonso, M.F., Pirre, M., Marecal, V., Grell, G., Stockler, R., Mello, R.F., Sa´nchez Ga´cita, M., 2011. PREP-CHEM-SRC –1.0: a preprocessor of trace gas and aerosol emission fields for regional and global atmospheric chemistry models. Geoscientific Model Development. Geosci. Model Dev., 4, 419–433, 2011. www.geosci-model-dev.net/4/419/2011/ doi:10.5194/gmd-4-419-2011.

Fuentes, J. D., et al., 2000. Biogenic Hydrocarbons in the Atmospheric Boundary Layer: A Review. Bull. Amer. Meteor. Soc., 81, 137–1575., doi: http://dx.doi.org/10.1175/1520-0477(2000)081<1537:BHITAB>2.3.CO:2

Gacek, Z. K., 2014. Modeling nighttime chemistry with WRF-Chem: Sensitivity to vertical resolution and boundary layer parameterization. MSc. Thesis, Urbana, Illinois.

Gao, S., Hegg, D. A., Hobbs, P. V., Kirchstter, T. W., Magi, B. I., Sadilek, M., 2003. Water-soluble organic components in aerosol associated with savanna fires in southern Africa: Identification, evolution, and distribution. J. Geophys. Res., 108(D13), 8491, doi:10.1029/2002JD002324, 2003.

Gao, Y., Zhang, Mei-Gen., Liu, X. H., Zhao, C., 2012. Model Analysis of the Anthropogenic Aerosol Effect on Clouds over East Asia. Atmospheric and Oceanic Science Letters, 2012, Vol. 5, No. 1,1–7.

Garcia, V., Fann, N., Haeuber, R., Lonrangs, P., 2008. Assessing the Public Health Impact of Regional-Scale Air Quality Regulations. Air and Waste Management Association. URL: http://pubs.awma.org/gsearch/em/2008/7/garcia.pdf.

Garstang, M., Tyson, P. D., Swap, R., Edwards, M., Kallberg, P., Lindesay, J. A., 1996. Horizontal and vertical transport of air over southern Africa. Journal of Geophysical Research. Vol. 101. No. D19. pp. 23,721–23,736. American Geophysical Union.

Gery, M. W., et al., 1989. A photochemical kinetics mechanism for urban and regional scale computer modelling. J. Geophys. Res., 94, 12, 925–12, 956.

Geyer, A., et al., 2001. Chemistry and oxidation capacity of the nitrate radical in the continental boundary layer near Berlin. Journal of Geophysical Research, Vol. 106, No. D8, pp. 8013–8025.

Ghan, S. J., et al., 1997. Prediction of cloud droplet number in a general circulation model. J. Geophys. Res., Vol. 102, No. D18, pp 21,777–21,794.

Ghan, S. J., et al., 2011. Droplet nucleation: Physicalli-based parameterizations and comparative evaluation. J. Adv. Model. Earth Syst., Vol. 3, M10001, 33 pp. doi:10.1029/2011MS000074.

Giglio, L., Descloitres, J., Justice, C. O., Kaufmann, Y., 2003. An Enhanced Contextual Fire Detection Algorithm for MODIS. Remote Sensing of Enviroment, 87 (2003) 273–282. www.elsevier.com/locate/sre

Giglio, L., et al., 2006. Global estimation of burnt area using MODIS active fire observations. Atmos. Chem. Phys., 6, 957–974, 2006. www.atmos-chem-phys.net/6/957/2006/

Giorgi, F., 2006. Regional Climate modelling: Status and perspectives. J. Phys. IV France 139. pp. 101–118.

Goldstein, A. H., Galbally, I. E., 2007. Known and Unexplored Organic Constituents in the Earth's Atmosphere. Environ. Sci. Technol., 2007, 41(5), pp 1514–1521., doi:10.1021/es072476p

Gong, W., Stroud, C., Zhang, L., 2011. Cloud Processing of Gases and Aerosols in Air Quality Modeling. Atmosphere 2011, 2, 567–616, doi: 10.3390/atmos2040567. ISSN 2073-4433. www.mdpi.com/journal/atmosphere.

Government Gazette, 2005. Republic of South Africa. Vol. 476, No. 27318. 24 February 2005. *https://www.environment.gov.za/sites/default/files/legislations/nema_amendment_act39.pdf*.

Grell, G. A., Dévényi, D., 2002. A generalized approach to parameterizing convection combining ensemble and data assimilation techniques. Geophysical Research Letters, Vol. 29, No. 14, 1693, 10.1029/2002GL015311, 2002.

Grell, G. A., Peckham, S. E., Schmitz, R., McKeen, S. A., 2004a. Fully coupled "online" chemistry within the WRF model: Description and Applications. Presented at 5th WRF Users Workshop, NCAR, June 2004. www.mmm.ucar.edu/mm5/workshop/ws04/Session4/Grell.Georg.pdf

Grell, G. A., Knoche, R., Peckham, S. E., McKeen, S. A., 2004b. Online versus offline air quality modeling on cloud-resolving scales. Geophys. Res. Lett., 31, L16117, doi:10.1029/2004GL020175.

Grell, G. A., Peckham, S. E., Schmitz , R., McKeen, S. A., Frost, G., Skamarock, W. C., Eder, B., 2005a. Fully coupled ''online'' chemistry within the WRF model. Atmospheric Environment. Vol. 39 (37) 6957–6975. www.esrl.noaa.gov/search/publications/1276/

Grell, G. A., et al., 2005b. The WRF-chemistry air quality model: updates, improvements and evaluation. Atmospheric Sciences and Air Quality Conferences, Boulder, CO.

Grell, G. A., et al., 2006. Research-community Priorities for WRF-System Development, Prepared by the WRF Research Applications Board, December 2006. URL: http://www.wrf-model.org/development/wrab/docs/RAB-plan-final.pdf

Grell, G. A., et al., 2011a: Inclusion of biomass burning in WRF-Chem: impact of wildfires on weather forecasts. Atmos. Chem. Phys., 11, 5289–5303, 2011. www.atmos-chem-phys.net/11/5289/2011/, doi:10.5194/acp-11-5289-2011.

Grell, G. A., et al., 2011b. Chapter 3: On-Line Chemistry Within WRF: Description and Evaluation of a Sate-of-the-Art Multiscale Air Quality and Weather Prediction Model. Integrated Systems of Meso-Meteorological and Chemical Transport Models, 2011, pp 41–54, doi:10.1007/978-3-642-13980-2_3.

Gu, Y., Liou, K. N., Ou, S. C., Fovell, R., 2011. Cirrus Cloud in Simulations using WRF with improved Radiation Parameterization and increased vertical Resolution. Journal of Geographical Research. Vol. 116.

Guan, H., Chatfield, R. B., Freitas, S. R., Bergstrom, R. W., Longo, K. M., 2007. Modeling the effect of plume-rise on the transport of carbon monoxide over Africa and its exports with NCAR CAM. Atmos. Chem. Phys. Discuss., 7, 18145–18177, 2007. www.atmos-chem-phys-discuss.net/7/18145/2007/

Guenther, A., Geron, C., Pierce, T., Lamb, B., Harley, P., Fall, R., 2000. Natural emissions of a non-methane volatile organic compounds, carbon monoxide, and oxides of nitrogen from North America. Atmospheric Environment, 34 (2000) 2205–2230. www.elsevier.com/locate/atmosenv

Guenther, A., Karl, T., Harley, P., Wiedinmyer, C., Palmer, P. I., and Geron, C., 2006. Estimates of global terrestrial isoprene emissions using MEGAN (Model of Emissions of Gases and Aerosols from Nature), Atmos. Chem. Phys., 6, 3181–3210, doi:10.5194/acp-6- 3181-2006, 2006.

Guenther, A., Jiang, X., Heald, C. L., Sakulyanontvittaya, T., Duhl, T., Emmons, L. K., Wang, X., 2012. The Model of Emissions of Gases and Aersols from Nature version 2.1 (MEGAN2.1): an extended and updated framework for modeling biogenic emissions. Geosci. Model Dev., 5, 1471-1491. www.geoscie-model-dev.net/5/1471/2012/ doi:10.5194/gmd-5-1471-2012.

Gullikson, E. M., 2001. X-Ray Data Booklet. Section 1.6, edited by A. C. Thompson and D. Vaughan (University of California Press, Berkeley, CA). URL: xdb.lbl.gov/Section1/Sec_1.6.pdf.

Gustafson Jr., W. I., Fast, J. D., Easter, R. C., Ghan, S. J., 2005. Triumphs and Tribulations of WRF-Chem Development and Use. http://www2.mmm.ucar.edu/wrf/users/workshops/WS2005/abstracts/Session8/4-Gustafson.pdf.

Gustafson Jr., W. I., Chapman, E. G., Ghan, S. J., Easter, R. C., Fast, J. D., 2007. Impact on modeled cloud characteristics due to simplified treatment of uniform cloud condensation nuclei during NEAQS 2004. Geophys. Res. Lett., 34, L19809, doi:10.1029/2007GL030021.

Hallquist, M., et al., 2009. The formation, properties and impact of secondary organic aerosol: current and emerging issues. Atmos. Chem. Phys., 9(14), 5155–5236. www.atmos-chem-phys.net/9/5155/2009/

Haywood, J. M., Boucher, O. 2000. Estimates the direct and indirect radiative forcing due to tropospheric aerosols: A Review. Review of Geophysics, 38, 4 November 2000., pp. 513–543. Paper No. 1999RG000078.

Haywood, J. M., Francis, P., Dubovik, O., Glew, M., Holben, B., 2003. Comparison of aerosol size distributions, radiative properties, and optical depths determined by aircraft observations and Sun photometers during SAFARI 2000. J. Geophys. Res., 108(D13), 8471, doi:10.1029/2009JD002250, 2003.

Haywood, J. M., Osborne, S. R., Abel, S. J., 2004. The effect of overlying absorbing aerosol layers on remote sensing retrievals of cloud effective radius and cloud optical depth. Q. J. Meteorol. Soc. (2004), 130, pp.779–800., doi:10.1256/qj.03.100.

Haywood J. M., et al., 2014. Cloud-Aerosol-Radiation Interactions and Forcing: 2016 (CLARIFY-2016). URL: gtr.ruck.ac.uk/project/6B2C2A2C-955F-44EF-9DA8-2D9FF9F7724. NERC-funded project.

Heintzenberg, J., 2003. Physics and Chemistry of Aerosols. URL: http://curry.eas.gatech.edu/Courses/6140/ency/Chapter5/Ency_Atmos/Aerosols_Physics_Chem_Aerosols.pdf

Heintzenberg, J., Charlson, R. J., 2009. Clouds in the Perturbed Climate System: Their Relationship to Energy Balance, Atmospheric Dynamics, and Precipitation. URL: https://mitpress.mit.edu/sites/default/files/titles/content/9780262012874_sch_0001.pdf

Helas, G., Andreae, M. O., Schebeske, G., Le Canut, P., 1995. SA'ARI-94: A preliminary view on results. South African Journal of Science 91, 360-362.

Hersey, S. P., et al., 2015. An overview of regional and local characteristics of aerosols in South Africa using satellite, ground, and modelling data. Atmos. Chem. Phys., 15, 4259–4278, 2015. www.atmos-chem-phys.net15/4259/2015/, doi:10.5194/acp-15-4259/2015/

Hinds, W. C., 1999. Aerosol Technology: Properties, Behaviour, and Measurement of Airbone Particles. 2nd Ed. John Wiley and Sons Inc. URL: ftp://ftp.cdc.gov/pub/Documents/OEL/02.%20Kuempel/References/Hinds_1999-Aerosol%20technology.pdf.

Hobbs, P. V., 2000. Introduction to Atmospheric Chemistry. Cambridge University Press.

Hodzic, A., et al., 2013. Aerosol Direct and Indirect Effects. WRF-Chem Tutorial, July, 22, 2013, Boulder CO. National Center for Atmospheric Research. *ruc.noaa.gov/wrf/WG11/wrf_tutorial.../WRF_CHEM_feedbacks.pdf*.

Holland, M., et al., 2001. The cost of reducing PM_{10} and NO_2 emissions and concentrations in the UK: Part 1. PM_{10}. A report produced for DEFRA and DT1. *uk-airdefra.gov.uk/reports/empire/aeat-env-r-0342.pdf.*

Hong, S. Y., Noh, Y., Dudhia, J., 2006: A New Vertical Diffusion Package with Explicit Treatment of Entrainment Processes. Mon. Wea. Rev., 134, 2318–2341.

Hoose, C., Lohman, U., Erdin, R., Tegen, I., 2008. The global influence of dust mineral composition in mixed-phase clouds. Environ. Res. Lett. 3 (April–June 2008) 025003., doi:10.1088/1748-9326/3/025003.

Hoose, C., et al., 2010. Parameterization of in-cloud vertical velocities for cloud droplet activation in coarse-grid models: analysis of observations and cloud resolving model results. 13th Conference on Atmospheric Radiation. https://ams.confex.com/ams/13CldPhy13AtRad/techprogram/paper_170866.htm

Horowitz, L. W., 2006. Past, present and, future concentrations of tropospheric ozone and aerosol: Methodology, ozone evaliuation, and sensitivity to arosol wet removal. J. Geophys. Res., 111, D22211, doi:10.1029/2005JD006937.

Hu, X. M., Gammon, J. W. N., Zhang, F., 2010. Evaluation of ThreePlanetary Boundary Layer Schemes in the WRF Model. Journal of Applied Meteorology and Climatology, 49, pp. 1831–1844, doi:10.1175/2010JAMC2432.1.

Hu, X. M., Klein, P. M., Xue, M., 2013. Evaluation of the updated YSU Planetary Boundary Layer Scheme within WRF for Wind Resource and Air Quality Assessments. J. Geo. Res., Atmospheres.

Hudson, D. A., Jones, R. G., 2002. Regional Climate Model Simulations of Present-day and future climate of southern Africa. Met Office.

Husar, R. B., Husar, J. D., 1997. Air Pollution Emissions, Atmospheric Processes and Effects on visibility. (Lecture notes material). Washington University.

Hussein, T., Puustinen, A., Aalto, P. P., Makela, J. M., Hameri, K., Kulmala, M., 2004. Urban aerosol number and size distributions. Atmospheric chemistry and Physics. Vol. 4. pp. 391–411. European Geosciences Union. (www.atmos-chem-phys.org/acp/4/391/).

Iacono et al., 2008. Radiative forcing by long-lived greenhouse gases: Calculations with the AER radiative transfer models. J. Geophys. Res., 113, D13103, doi:10.1029/2008JD009944.

Ichoku, C., 2008. Satellite Characterization of Biomass Burning and Smoke Emissions in Africa. *www.aag.org/galleries/gdest/ichokupaper.pdf*

IPCC, Fourth Assessment Report, 2007: Climate Change. Working Group I: The Physical Science Basis. URL: http://www.ipcc.ch/publications_and_data/publications_ipcc_fourth_assessment_report_wg1_report_the_physical_science_basis.htm.

IPCC, Fifth Assessment Report of 2013: Chapter 7: Aerosols and Clouds. (Working Group I). http://www.ipcc.ch/pdf/assessment-report/ar5/wg1/WG1AR5_Chapter7_FINAL.pdf

Ivertfeldt, A., 2002. Air Pollution in Asia and Africa: The Approach of the Rapid Programme. Proceedings of the First Open Seminar on Regional Air Pollution in Developing Countries, held at Stora Hörsalen, Sida (Sveavägen 20, Stockholm), June 4, 2002. www.rapid.org

Jacobson, M. Z., 2002. Atmospheric Pollution. Cambridge University Press.

Jacobson, M. Z., 2005. Fundamentals of Atmospheric Modeling. Cambridge University Press.

Jenkin, M. E., Clemitshaw, K. C., 2000. Ozone and other secondary photochemical pollutants: chemical processes governing their formation in the planetary boundary layer. Atmospheric Environment 34 (2000) 2499–2527. www.elsevier.com/locate/atmosenv

Jiang, X., et al., 2012. MEGAN version 2.10 User's Guide. URL: http://acd.ucar.edu/~guenther/MEGAN/MEGANv2.10_beta/MEGAN2.1_User_Guide_05-07-2012.pdf

Johnson, B. T., Shine, K. P., Forster, P. M., 2004. The Semi-direct aerosol effect: Impact of absorbing aerosols on marine stratocumulus. Q. J. R. Meteorol. Soc. (2004), 130, pp. 1407–1422., doi:10.1256/qj.03.61.

Jolleys et al., 2012. Characterizing the Aging of Biomass Burning Organic Aerosol by the Use of Mixing Ratios: A Meta-analysis of Four Regions. Environron. Sci.Technol., 2012, 46(24), pp 13093–13102., doi: 10.1021.es302386v.

Josipovic, M., Annegarn, H., Kneen, M. A., Pienaar, J. J., Piketh, S. J., 2009. Concentration, distributions and critical level exceedence assessment of SO_2, NO_2 and O_3 in South Africa. Environ Monit. Assess. Springer Science + Business Media B. V.

Kaufmann, Y. J., Justice, C. O., Flynn, L., Kendall, J., Prins, E., Ward, D. E., 1998. Potential global fire monitoring from the EOS_MODIS. Journal of Geophysical Research. 103, 32215–32238.

Kaufman, Y. J., Loren, I., Remer, L.A., Rosenfeld, D., Rudich, Y., 2005. The Effect of Smoke, Dust and Pollution Aerosol on Shallow Cloud Development Over the Atlantic Ocean. modis-atmos.gsfc.nasa.gov/_docs/Kaufman-aerosol-clouds.pdf.

Kazil, J., 2012. Aerosols in WRF/Chem. Wrf tutorial., University of Colorado/NOAA Earth System Research Laboratory. URL: http://ruc.noaa.gov/wrf/WG11/wrf_tutorial_2012/wrfchem_tutorial_aerosols.pdf.

Kgabi, N. A., 2012. Air Quality policy and scientific research in southernAfrica. WIT Transactions on Ecology and Environemnt. 01/2012; 157:151–163., doi:10.2495/AIR120141.

Kirkman, G. A., Piketh, S. J., Andreae, M. O., Annegarn, H. J., Helas, G., 2000. Distribution of aerosols, ozone and carbon monoxide over southern Africa. South African Journal of Science 96, 2000. pp. 423–431.

Kivekäs, N., Kerminen, V. M., Anttila, T., Korhonen, H., Lihavainen, H., Komppula, M., Kulmala, M., 2008. Parameterization of cloud droplet activation using a simplified treatment of the aerosol number size distribution, J. Geophys. Res., 113, D15207, doi:10.1029/2007JD009485.

Klein, S. A., Hartman, D. L., 1993. The Seasonal Cycle of Low Stratiform Clouds. Journal of Climate. Vol. 6., pp. 1587–1606.

Klein, S. A., Zhang, Y.M Zelinka, M. D., Pincus, R., Boyle, J., Glecker, P. J., 2012. Are climate model simulations of clouds improving? An evaluation using the ISCCP simulator. J. Geophys. Res. Atmos., 118, 1329–1342, doi:10.1002/jgrd.50141.

Klüser, L., Kleiber, P., Holzer-Popp, T., Grassian, V. H., 2012. Desert dust observation from space – Application of measured mineral component infrared extinction spectra. Atmospheric Environment 54 (2012) 419-427. Elsevier. www.lsevier.com/locate/atmosenv

Knippertz, P., Evans, M. J., Field, P. R., Fink, A. H., Liousse, C., Marsham, J. H., 2015. The possible role local air pollution in climate change in West Africa. Nature Climate Change. Insight Perspectives, doi:10.1038/NCLIMATE2727.

Köhler, H., 1936. The nucleus in and the growth of hygroscopic droplets. Trans. Faraday Soc., 1936, 32., 1152–1161. doi:10.1039/TF9363201152.

Kokkola, H., Hommel, R., Kazil, J., Niemier, U., Patarnen, A. I., Feichter, J., Timmreck, C. T., 2009. Aerosol microphysics modules in the framework of the ECHAM5 Climate model –intercomparisons under stratospheric conditions. Geosci. Model Dev., 2, 97–112, 2009. www.geosci-model-dev.net/2/97/2009/

Kong, X., et al., 2014. Analysis of meteorology-chemistry interactions during air pollution episode suing online coupled models with AQMEII phase-2. Atmospheric Environment xxx (2014) 1–14, www.elsevier.com/locate/atmosnv, doi:10.1016/jatmosenv.2014.09.02.

Koren I., Feingold, G., Remer, L. A., 2010. The invigoration of deep convective clouds over the Atlantic: aerosol effect, meteorology or retrieval artifact? Atmos. Chem. Phys., 10,8855–8872,2010. www.atmos-chem-phys.net/10/8855/2010/, doi:10.5194/acp-10-8855-2010.

Korolev, A. V., Isaac, G. A., Strapp, J. W., Cober, S. G., Barker, H. W., 2007. In situ measurements of liquid water content profiles in midlatitude stratiform clouds. Q. J. R. Meteorol. Soc. 133: 1693–1699 (2007). www.interscience.wiley.com/, doi:10.1002/qj.147

Kroll, J. H., Seinfeld, J. H, 2008. Chemistry of secondary organic aerosol: Formation and evolution of low-volatility organics in the atmosphere. Atmospheric Environemnt 42 (2008) 3593–3624. www.elsevier.com/locate/atmosenv/

Kuhns, H., Vukovich, J. M., 1997. The emissions Inventories and SMOKE modelling efforts used to support the BRAVO study. 12th Annual US EPA International conference. www.epa.gov/ttnchie1/conference/ei12/mexico/kuhns.pdf.

Kukkonenen, J., et al., 2012. A review of operational, regional-scale, chemical weather forecasting models in Europe. Atmospheric Chemistry & Physics. www.atmos-chem-phys.net/12/1/2012/.

Kuik, F., Lauer, A., Beukes, J. P., Van Zyl, P. G., Josipovich, M., Vakkari, V., Laakso, L., Feig, G. T., 2015. The anthropogenic contribution to atmospheric black carbon concentrations in southern Africa: a WRF-Chem modelling study. Atmos. Chem. Phys. Discuss., 15, 7309–7363, 2015. www.atmos-chem-phys-discuss.net/15/7309/2015/ doi:10.5194/acpd-15-7309-2015.

Kumar, R., Naja, M., Pfister, G. G., Barth, M. C.M Brasseur, G. P., 2012. Simulations over South Asia using the Weather Research and Forecasting model with Chemistry (WRF-Chem): set-up and meteorological evaluation, Geosci. Model Dev., 5, 321–343, doi:10.5194/gmd-5-321-2012, 2012.

Labonne, M., Bréon, F., Chevallier, F., 2007. Injection height of biomass burning aerosols as seen from a spaceborne lidar. Geophys. Res. Lett., 34, L11806, doi:10.1029/2007GL029311.

Lahsen, M., et al., 2013. TheContributions of Regional Knowledge Networks Researching Environmental Changes in Latin America and Africa: a Synthesis of what they can do and why they can be policy relevant. Ecology and Society 18(3): 14, http://dx.doi.org/10.5751/ES-05614-180314.

Lance, S., Nenes, A., Rissman, T. A., 2004. Chemical and dynamical effects of cloud droplet number; implications for estimates of aerosols indirect effect. J. Geophys. Res.

Le Canut, P., et al., 1996. Airborne studies of emissions from savanna fires in southern Africa. 1. Aerosol emissions measured with a laser optical particle counter. Journal of Geophysical Research. Vol. 101, No. D19, pp. 615–630.

Li, J., Pósfai, M., Hobbs, P. V., Busek, P. R., 2003. Individual aerosol particles from biomass burning in southern Africa: 2. Compositions and aging of inorganic particles. J. Geophys. Res., 108(D13), 8484, doi:10.1029/2002JD002310, 2003.

Lin, J. C., T. Matsui, R. A. Pielke Sr., and C. Kummerow (2006), Effects of biomass-burning-derived aerosols on precipitation and clouds in the Amazon Basin: a satellite-based empirical study, J. Geophys. Res., 111, D19204, doi:10.1029/2005JD006884.

Lin, C. Y., et al., 2014. Modelling of long-rang transport of Southeast Asia biomass-burning aerosols to Taiwan and their radiative forcings over East Asia. Chemical and Physical Meteorology, Tellus B, 2014, 66, 23733 http://dx.doi.org/10.3402/tellusb.v66.23733

Lindesay, J. A., et al., 1997. International Geosphere-Biosphere Program/International Global Atmospheric Chemistry SAFARI-92 field experiment: Background and overview. J. Geophys. Res., 101(D19), 23, 521–23,530, doi:10.1029/96JD01512.

Liousse, C., et al., 2010. Western African aerosols modelling with updated biomass burning emission inventories in the frame of the AMMA-IDAF program. Atmos. Chem. Phys. Discuss., 10, 7347–7382, 2010. www.atmos-chem-phys-discuss.net/10/7347/2010/

Liu, X., van Espen, P., Adams, F., Cafmeyer, J., Maenhaut, W., 2000. Biomass Burning in Southern Africa: Individual Particle Characterisation of Atmospheric Aerosols and Savanna Fire Samples. Journal of Atmospheric Chemistry 36: 135–155, 2000.

Lo, K. C., Hung, C. H., 2012. The Development and Application of Weather Research Forecast Chemistry model. International Journal of Advancements in Computing Technology (IJACT) Vol. 4, No. 22, December 2012., doi:10.4156/ijact.vol4. Issue 22.16.

Lohmann, U., Feichter, J., 2005. Global indirect aerosol effects: a review. Atmospheric Chemistry and Physics. Vol. 5. pp. 715–737.

Longo, K. M., et al., 2010. The Coupled Aerosol and Tracer Transport model to the Brazilian developments on the Regional Atmospheric Modeling System (CATT-BRAMS) –Part 2: Model sensitivity to the biomass burning inventories. Atmos. Chem. Phys., 10,5785–5795, 2010. www.atmos-chem-phys.net/10/5785/2010/ doi:10.5194/acp-10-5785-2010.

Lowe, D., et al., 2015. WRF-Chem model predictions of the regional impacts of N_2O_5 heterogeneous processes on night-time chemistry over north-western Europe. Atmos. Chem. Phys., 15,1385–1409, 2015. www.atmos-chem-phys.net/15/1385/2015/ doi:10.5194/acp-15-1385-2015.

Ma, P. L., et al., 2014. Assessing the CAM5 physics suite in the WRF-Chem model: implementation, resolution sensitivity, and a first evaluation for a regional case study.
Geosci. Model Dev., 7, 755–778, 2014. www.geosci-model-dev.net/7/775/2014/, doi:10.5194/gmd-7-755-2014.

Madronich, S., 1987. Photodissociation in the atmosphere, 1. Actinic Flux and the Effects of Ground Reflections and Clouds. Journal of Geophysical Research, Vol. 92. No. D8, pp. 9740–9752, August 20, 1987.

Magi, B. I., 2009. Chemical apportionment of southern African aerosol mass and optical depth. Atmos. Chem. Phys., 9, 7643–7655, 2009. www.atmos-chem-phys.net/9/7643/2009/

Magi, B. I., Ginoux, P., Ming, Y., Ramaswamy, V., 2009. Evaluation of tropical and extratropical Southern Hemisphere African aerosol properties simulated by a climate model. J. Geophys. Res., 114, D14204, doi:10.1029/2008JD011128.

Mann, G. W., et al., 2012. Intercomparison of modal and sectional aerosol microphysics representations within the same 3-D global chemical transport model. Atmos. Chem. Phys., 12, 4449–4476, 2012. www.atmo-schem-phys.net/12/4449/2012/, doi:10.5194/acp-12-4449-2012.

Martins, J. V., et al., 2010. Remote sensing the vertical profile of cloud droplet effective radius, thermodynamic phase, and temperature. Atmos. Chem. Phys., 11, 9485–9501, 2011. www.atmos-chem-phys.net/11/9485/2011/, doi:10.5194/acp-11-9485-2011.

McFiggans, G., et al., 2006. The effect of physical and chemical aerosol properties on warm cloud droplet activation. Vol. 6. pp. 2593–2649. Atmospheric Chemistry and Physics. www.atmos-chem-phys.net/6/2593/2006/

McFiggans, G., 2010. Clouds and aerosols, Lecture Notes. (Unpublished material).

Mearns, L. O., Giorgi, F., Whetton, P., Pabon, D., Hulme, M., Lal, M., 2003. Guidelines for Use of Scenarios Developed from Regional Climate Models Experiments.

Mensink, C., de Ridder, K., 2000. Multiblock dispersion modelling for urban and regional scale interactions. In Air Pollution Modelling and Its Application XIII. Edited by Sven-Erik Gryning and Ekaterina Batchvanova.

Meskhidze, N. A., Nenes, A., Conant, W. C., Seinfeld, J. H., 2005. Evaluation of a new cloud droplet activation parameterization with in situ from CRYSTAL-FACE and CSTRIPE. J. Geophys. Res., 110, D16202., doi:10.1029/2004JD005703.

Miyazaki, K., Eskes, H. J., Sudo, K., 2012. Global NOx emission estimates derived from an assimilation of OMI tropospheric NO2 columns. Journal of Atmospheric Chemistry and Physics. www.atmos-chem-phys.net/12/2263/2012/. doi:10.5194/acp-12-2263-2012.

Mlawer, E. J., Taubman, S. T., Brown, P. D., Iacono, M. J., 1997. Radiative transfer for inhomogeneous atmospheres: RRTM, a validated correlated-k model for the longwave. Journal of Geophysical Research, Vol. 102, No. D14, pp 16,663–16,682, July 27, 1997.

Monks, P. S., 2005. Gas-phase radical chemistry in the troposphere. Chemical Sociery Review, doi: 10.1039/b307982c. URL: web.gps.caltech.edu/classes/get148c/Monks2005_CSR.pdf.

Monks, P. S., et al., 2014. Tropospheric ozone and its precursors from the urban to the global scale from air quality to short-lived climate forcer. Atmos. Chem. Phys. Discuss., 14, 32709–32933, 2014. www.atmos-chem-phys-discuss.net/14/32709/2014/. doi:10.5194/acpd-14-32709-2014.

Morrison, H., Curry, J. A., Khvorostyanov, V. I., 2005. A New Double-Moment Microphysics Parameterization for Application in Cloud and Climate Models. Part I: Description. Vol. 62. Journal of the Atmospheric Sciences.

Morrison, H., Pinto, J. O., Curry, J. A., 2006. Intercomparison of Bulk Cloud Microphysics Schemes in Mesoscale Simulation of Springtime Arctic Mixed-Phase Stratiform Clouds. Monthly Weather Review., Vol. 134, pp. 1880–1900.

Morrison, H., Thompson, G., Tatarskii, V., 2009. Impact of Cloud Microphysics on the Development of Trailing Stratiform Precipitation in a Simulated Squall Line: Comparison of One- and Two-Moment Schemes. Mon. Wea. Rev., 137, 991–1007. doi:http://dx.doi.org/10.1175/2008MWR2556.1

Moxim, W. J., Levy II, H., 2000. A model analysis of the tropical South Atlantic Ocean tropospheric ozone maximum: The interaction of transport and chemistry. Journal of Geophysical Research. Vol. 105, No. D13, pp. 17,393–17,415. Paper No. 2000JD900175.

Nenes, A., Seinfeld, J. H., 2003. Parameterization of cloud droplet formation in global climate models. J. Geophys. Res., 108(D14), 4415, doi:10.1029/2002JD002911, 2003.

Nicholson, S. E., Entekhabi, D., 1987. Rainfall variability in equatorial southern Africa: Relationship with sea surface temperature along the southwest coast of Africa. J. Climate Appl. Meteor., 26, 561–578.

Nicholson, S. E., 1996. A review of climate dynamics and climate variability in eastern Africa, in The Limnology, Climatology and Paleoclimatology of the East African Lakes, *edited by* T. C. Johnson, and E. O. Odada, pp. 25–56, Gordon and Breach, Amsterdam.

Niu, G. Y., et al., 2011. The community Noah land surface model with multiparameterisation options (Noah-MP): 1. Model description and evaluation with local-scale measurements. J. Geophys. Res., 116, D12109, doi: 10.1029/2010JD015139.

Ntelekos, A. A., et al., 2009. The effects of aerosols on intense convective precipitation in the northern United States. Q. J. R. Meteorol. Soc. **135:** 1367–1391 (2009). www.interscience.wiley.com)., doi:10.1002/qj.476. R.M.S.

Nyanganyura, D., Marakau, A., Mathuthu, M., Meixner, F. X., 2008. A five-day back trajectory climatology for Rukomechi Research station (northern Zimbabwe) an the impact of large-scale atmospheric flows on concentrations of airborne coarse and fine particulate mass. Research Articles. South African Journal of Science 104, pp. 43–52.

Obasi, O. P. G., 2001. The Impacts of ENSO in Africa. World Meteorological Organization. Geneva, Switzerland.

Okoola, R., 2000. A Diagnostic study of the eastern African monsoon circulation during the northern hemisphere spring season. Int. J. Climatol., 19:143–168 (1999).

Park, S., Park, S. K., 2015. Representation of vegetation effects on the snow-covered albedo in the Noah land surface model with multiple physics options. Geosci. Model Dev. Discuss., 8, 3197–3218, 2015. www.geosci-model-dev-discuss.net/8/3197/2015., doi:10.5194/gmdd-8-3197-2015.

Pattanayak, S., Mohanty, U. C., Osuri, K. K., 2012. Impact of Parameterization of Physical Processes on Simulation of Track and Intensity of Tropical Cyclone Nargis (2008) with WRF-NMM Model. The Scientific World Journal. Vol. 2012 (2012), Article ID 671437. http://dx.doi.org/10.1100/2012/671437

Peckham, S., 2008. Applications of Numerical Models to Planned and Inadvertent Weather Modification Topics.

Peckham, S., et al., 2012. WRF/Chem Version 3.4 User's Guide. *ruc.noaa.gov/wrf/WG11/**Users_guide**.pdf.*

Peers, F., et al., 2014. Absorption of aerosols above clouds from POLDER/PARASOL measurements and estimation of their Direct Radiative Effect. Atmos. Chem. Phys. Discuss., 14, 25533–25579, 2014. www.atmos-chem-phys-discuss.net/14/25533/2014/ doi:10.5194/acpd-14-25533-2014.

Pei, L., et al., 2014. WRF Model Sensitivity to Land Surface Model and Cumulus Parameterization under Short-Term Climate Extremes over the Southern Great Plains of the United States. Journal of Climate. Vol. 27, pp. 7703–7724, doi:10.1175/JCLI-D-14-00015.1.

Pey, J., et al., 2008. Characterization of a long range transport pollution episode affecting PM in SW Spain. Journal of Environmental Monitoring. www.rc.org/jem, doi:10.1039/b809001g

Pfister, G. G., et al., 2011. Characterizing summertime chemical boundary conditions for airmasses entering the US West Coast. Atmos. Chem. Phys., 11,1769–1790, 2011. www.atmos-chem-phys.net/11/1769/2011/, doi:10.5194/acp-11-1769-2011.

Phadnis, M. J., Carmichael, G. R., 2000. Forest fire in the Boreal Region of China and its impact on the photochemical oxidant cycle of East Asia. Atmospheric Environment 34 (2000) 483–498. www.elsevier.com/locate/atmosenv/

Piketh, S. J., Formenti, P., Annegarm, H. J., Tyson, P. D. 1999. Industrial Aerosol characterisation at a remote site in South Africa. Nuclear Instruments and Methods in Physical Research Section B: Beam interactions with Materials and Atoms. Vol. 150, Issue 1–4. http://dx.doi.org/10.1016/SO168-583X(98)00985-9.

Piketh, S. J., Swap, R. J., Maenhaut, W., Annegarn, H. J., Formenti, P., 2002. Chemical evidence of long-range atmospheric transport over southern Africa. Journal of Geophysical Research. Vol. 107. No. D24, 4817. doi:10.1029/2002JD002056, 2002.

Piketh, S. J., Walton, N. M., 2004. Characteristics of Atmospheric Transport of Air Pollution for Africa. The handbook of Environmental Chemistry. Vol. 4, Part G (2004): 173–195, doi:10.1007/b94527.

Pio, C. A., et al., 2007. Climatology of aerosol composition (organic versus inorganic) at nonurban sites on a west-east transect across Europe. J. Geophys. Res., 112, D23S02, doi:10.1029/2006JD008038.

Pöschl, U., 2005. Atmospheric Aerosols: Composition, Transformation, Climates and Health Effects. Angewandte Chemie. Int. Ed. 44, 7520–7540. www.angewandte.org.

Pöschl, U., et al., 2010. Rainforest Aerosols as Biogenic Nuclei of Clouds and Precipitation in the Amazon. Science, Vol. 329. www.sciencemag.org.

Pósfai, M., Simonics, R., Li, J., Hobbs, P. V., Buseck, P. R., 2003. Individual aerosol particles from biomass burning in southern Africa: 1. Compositions and size distributions of carbonaceous particles. Journal of Geophysical Research, Vol. 108 No. D13. 8483, doi:10.1029/2002JD002291.

Prein, A. F., et al., 2015. A review on regional convection-permitting climate modelling: Demonstration, prospects, and challenges. Review of Geophysics. URL: http://onlinelibrary.wiley.com/doi/10.1002/2014RG000475/pdf

Pruppacher, H. R., Klett, J. D., 1998. Microphysics of Clouds and Precipitation. 2nd Revised edition. Kluwer Academic Publishers. Vol. 18.

Qian, Y., et al., 2009. A Contextual Fire Detection Algorithm for Simulated HJ-1B Imagery. Sensors 2009, *9,* 961-979; doi:10.3390/s90200961. www.mdpi.com/journal/sensors.

Querol, X., et al., 2004. Speciation and Origin of PM_{10} and $PM_{2.5}$ in selected European cities. Atmospheric Environment. Vol. 30, Issue 38. December 2004. 6547–6555. Elsevier. http://dx.doi.org/10/1016/j.atmosenv.2004.08.037

Ragab, R., Prudhomme, C., 2002. Climate Change nad Water Resources Management in Arid and Semi-arid Regions: Prospective and Challenges for the 21st Century. Biosystems Engineering 81(1), 3–34. http://www.idealibrary.com, doi:10.1006/bioe.2001.0013.

Ram, K., Sarin, M. M., Sudheer, A. K., Renjarajan, R., 2012. Carbonaceous and Secondary Inorganic Aerosols during wintertime Fog and Haze over Urban Sites in Indo-Gangetic Plain. Aerosol and Air Quality Research. Vol. 12. pp. 359–370.

Ramaswamy, V., Boucher, O., Haigh, J., Hauglustaine, D., Haywood, J., Myhre, G., Nakajima, T., Shi, G. Y., Solomon, S., 2001. Chapter 6: Radiative forcing of climate change. Contribution of working group I to the Third Assessment Report of the Intergovernmental Panel on Climate Change. http://www.grida.no/climate/ipcc_tar/wg1/pdf/tar-06.pdf

Ramanathan, V., et al., 2001. Aerosols, Climate, and the Hydrological Cycle. Science 294, 2119 (2001); doi:10.1126/science.1064034.

Randles, C. A., Ramaswamy, V., 2010. Impacts of absorbing biomass burning aerosol on the climate of southern Africa: a Geophysical Fluid Dynamic Laboratory GCM sensitivity study. Atmos. Chem. Phys. Discuss., 10, 9731–9752, 2010. www.atmos-chem-phys-discuss.net/10/9731/2010/.

Reff, A., et al., 2009. Emissions Inventory of $PM_{2.5}$ Trace Elements across the United States. Environ. Sci. Technol. 2009, 43,5790–5796, doi:10.1021/es802930x.

Riemer, N. H., Vogel, B., Vogel, T., Anttila, A., Kiendler-Scharr, Mentel, T. F., 2009. Relative importance of organic coatings for the heterogeneous hydrolysis of N_2O_5 during summer in Europe, J. Geophys. Res., 114, D17307, doi:10.1029/2008JD011369.

Rind, D., et al, 2009. Chapter 3: Modelling the Effectes of Aerosols on Climate. Atmospheric Aerosol Properties and Climate Impacts. U.S. Climate Change Science Program. Synthesis and Assessment Product 2.3.

Rio, C., Hourdin, F., Chedin, A., 2009. Numerical simulation of tropospheric injection of biomass burning products by pyro-thermal plumes. Atmos. Chem. Phys. Discuss., 9, 18659–18705, 2009. www.atmos-chem-phys-discuss.net/9/18659/2009/

Roberts, G. C., Artaxo, P., Zhou, J., Swietlicki, E., 2002. Sensitivity of CCN spectra on chemical and physical properties of aerosol: A case study from the Amazon Basin. J. Geophys. Res., 107 (D20), 8070, doi:10.1029/2001JD000 583, 2002.

Roberts, G. C., Nenes, A., Seinfeld, J. H., Andreae, M. O., 2003 Impact of biomass burning on cloud properties in the Amazon Basin, J. Geophys. Res., 108, doi:10.1029/2001JD000 985, 2003.

Robinson, A. L., et al., 2007. Rethinking Organic Aerosols: Semivolatile Emissions and Photochemical Aging. Science 315, 1259 (2007). doi:10.1126/science.1133061.

Romakkaniemi, S., et al., 2012. Effects of aerosol size distribution changes on AOD, CCN and cloud droplet concentration: Case studies from Erfurt and Melpitz, Germany. J. Geophys. Res., 117, D07202, doi:10.1029/2011JD017091.

Rosenfeld, D., Wood, R., Donner, L., Sherwood, S., 2011. Aerosol cloud-mediated radiative forcing: highly uncertain and opposite effects from shallow and deep clouds. Position paper prepared for the WCRP Open Science Conference in Denver, Oct 24–28, 2011.

Rosenfeld, D., Sherwood, S., Wood, R., Donner, L., 2014. Climate effects of aerosol-cloud interactions. Science, 343 (6169), 373–380., doi:10.1126/science.1247490.

SACOS Report, 2003. Report of the CLIVAR/OOPC/IAI WORKSHOP on the South Atlantic Climate Observing System (SACOS). February 6-8, 2003, Hotel Portogalo, Angra dos Reis –Brazil. URL: http://ioc-goos-oopc.org/meetings/oopc-9/SACOS_report.pdf.

Salam, A., et al., 2008. Characteristics of atmospheric trace gases, particulate matter, and heavy metal pollution in Dhaka, Bangladesh. Air Qual Atmos Health (2008) 1:101–109., doi:10.1007/s11869-008-0017-8.

Salameh, T., et al., 2007. Aerosol distributio over the western Mediterranean during a Tramontane/Mistral event. Ann. Geophys., 25, 2271–2291, 2007. www.ann-geophys.net/25/2271/2007/.

Saud, T., et al., 2011. Emission estimates of particulate matter (PM) and trace gases (SO_2, NO and NO_2) from biomass fuels used in rural sector of Indo-Gangetic Plain, India. Atmospheric Environment 45 (2011) 5913–5923. www.elsevier.com/locate/atmosenv

Savane, O. S., Vant-Hull, B., Mahani, S., Khanbilvardi, R., 2015. Effects of Aerosol on Cloud Liquid Water Path: Statistical Method a Potential Source for Divergence in Past Observation Based

Correlative Studies. Atmosphere 2015, 6, 273–298, www.mdpi.com/journal/atmosphere/, doi:10.3390/atmos6030273.

Schartz, O., 2008. A Brief Review of Uranium Mining in Africa. URL: http://www.infomine.com/publications/docs/Mining.com/Sep2008f.pdf

Schefub, E., Schouten, S., Schneider, R., 2005. Climatic controls on central African hydrology during the past 200, 000 years. Nature Publishing Group. Vol. 437. doi:10.1038/nature03945.

Schere, K., Bouchet, V., Grell, G. A., McHenry, J., McKeen, S., 2006. The Emmergence of Numerical Air Quality Forecasting Models and Their Applications. Presentationa at The AMS Forum on monitoring Our Physical and Natural Resources, February 2, Atlanta, GA.

Scholes, R. J., Kendall, J., Justice, C. O., 1996. The quantity of biomass burned in southern Africa. J. Geophys. Res., 101 (D19), pp. 23,667–23,676, October 1996.

Shugart, H. H., Macko, S. A., Lesolle, P., Szuba, T. A., Mukelabai, M. M., Dowty, P., Swap, R. J., 2004. The SAFARI 2000 –Kalahari Transect Wet Season Campaign of year 2000. Global Change Biology. Vol. 10. pp. 273–280.

Schwartz, S. E., Slingo, A., 1995. Enhanced shortwave cloud radiative forcing due to anthropogenic aerosols. NATO advanced research workshop on clouds, chemistry and climate, Heidelberg (Germany), 1995. http://www.science.gov/topicpages/r/radiative+forcing+cloud.html

Seinfeld, J. H., Pandis, S. N., 2006. Atmospheric Chemistry and Physics: From Air Pollution to Climate Change. 2nd ed. John Wiley & Sons Inc.

Sen, R. N., Roos, H., 1994. Is Microphysics Incomplete? Vol. 2. (3). Open systems and Dynamics. Nicholas Copernicus University Press.

Sessions, W. R., Fuelberg, H. E., Kahn, R. A., Winker, D. M., 2011. An investigation of methods for injecting emissions from boreal wildfires using WRF-Chem during ARCTAS. Atmos. Chem. Phys., 11, 5719-5744, 2011. www.atmos-chem-phys.net/11/5719/2011/ doi:10.5194/acp-11-5719-2011.

Shao, Y., Ishizuka, M., Mikami, M., Leys, J. F., 2011. Parameterization of of size-resolved dust emissions and validation with measurements. J. Geophys. Res., 116, D08203, doi:10.1029/2010jg14527.

Sherwood, S. C., Alexander, M J., Brown, A. R., McFarlane, N. A., Gerber, E. P., Feingold, G., Scaife, A. A., Grabowski, W. W., 2011. Climate Processes: Clouds, Aerosols and Dynamics. (B6).

Sherwood, S. C., Alexander, M J., Brown, A. R., McFarlane, N. A., Gerber, E. P., Tuccella, P., Curci, G., Visconti, G., Bessagnet, B., Menut, L., 2012. Modelling of gas and aerosol with WRF/Chem over Europe: Evaluation and sensitivity study. Journal of Geophysical Research, Vol. 117. doi:10.1029/2011JD016302, 2012.

Shrivastava, M., et al., 2013. Modelling aerosols and their interactions with shallow cumuli during the 2007 CHAPS field study. J. Geophys. Res. Atmos., 118, 1343–1360, doi:10.1029/2012JD018218.

Sihto, S. L., et al., 2011. Seasonal variation of CCN concentrations and aerosol activation properties in boreal forest. Atmos. Chem. Phys., 11, 13269–13285, 2011. www.atmos-chem-phys.net/11/13269/2011/., doi:10.5194/acp-11-13269-2011.

Simpson, E., Connoly, P., McFiggans, G., 2014. An investigation into the performance of four cloud droplet activation parameterisations. Geosci. Model Dev., 7, 1535–1542, 2014. www.geosci-model-dev.net/7/1535/2014/

Simukanga, S., Hicks W.K., Feresu S., Kuylenstierna, J. C. I., 2003. The Air Pollution Information Network For Africa (Apina): Activities Promoting Regional Co-Operation On Air Pollution Issues In Southern Africa.

Sinha., P., Jaeglé, P. L., Hobbs, P. V., Liang, Q., 2004. Transport of biomass burning emissions from southern Africa. J. Geophys. Res., 109, D20204, doi:10.1029/2004JD005044.

Skaeda, N., Wood, R., Rasch, P. J., 2011. Direct and semidirect aerosol effects of southern African biomass burning aerosol, J. Geophys. Res., 116, D12205, doi:10.1029/2010JD015540.

Skamarock, W. C., Klemp, J. B., Dudhia, J., Gill, D. O., Barker, D. M., Wang, W., Powers, J. G., 2005. A Description of the Advanced Research WRF Version 2. Boulder, Colorado, National Center for Atmospheric Research (NCAR). Technical note: NCAR/TN-468+STR. URL: http://www2.mmm.ucar.edu/wrf/users/docs/arw_v2.pdf

Skamarock, W. C., Klemp, J. B., Dudhia, J., Gill, D. O., Barker, D. M., Duda, M. G., Huang, X. Y., Wang, W., Powers, J. G., 2008. A Description of the Advanced Research WRF Version 3. Boulder, Colorado. National Center for Atmospheric Research (NCAR). Technical note: NCAR/TN-475+STR. URL: http://www2.mmm.ucar.edu/wrf/users/docs/arw_v3.pdf

Soja, A. J., et al., 2011. Biomass Burning Plume Injection Height Using CALIOP, MODIS and the NASA Langley Trajectory Model. 34th International Symposium on Remote Sensing of Environment – The GEOS Era: Towards Operational Environmental Monitoring.

Southern Africa Sub-Regional Framework on Climate Change Programmes Report, 2010. 1st Draft (Working Document). Southern Africa Development Community (SADC).

Sorooshian, A., et al., 2009. On the precipitation susceptibility of clouds to aerosol perturbations. Geophys. Res. Lett., 36, L13803, doi:10.1029/2009GL038993.

Spichtinger, P., Cziczo, D., 2008. Aerosol–cloud interactions –a challenge for measurements and modelling at the cutting edge of cloud–climate interactions. Environ. Res. Lett. 3 (2008) 025002 (1pp), doi:10.1088/1748-9326/3/2/025002.

Spyrou, C., Kallos, G., Mitsakou, C., Athanasiadis, P., Kalogeri, C., Jacono, M. J., 2013. Modeling the radiative effects of desert dust on weather and regional climate. Atmos. Chem. Phys., 13, 5489–5504, 2013. www.atmos-chem-phys.net/13/5489/2013/, doi:10.5194/acp-13-5489-2013.

State of the Environemnt Report, 2008. (Mpumalanga Province). Atmosphere and Climate Specialist Report. Prepared by T. N. Mdluli.

Stensrud, D. J., 2007. Parameterization Schemes: Keys to Understanding numerical weather prediction models. Cambridge University Press.

Stevens, B., Feingold, G., 2009. Untangling aerosol effects on clouds and precipitation in a buffered system. Nature. Vol 461 (1). doi:10.1038/nature08281.

Stockwell, W. R., Middleton, P., Chang, J. S., 1990. The second generation Regional Acid Deposition Model chemical mechanism for regional air quality modeling. J. Geophys. Res., 95, 16 343–16 367.

Stockwell, W. R., 1994. The Effect of Gas-Phase Chemistry on Aqueous-Phase Sulphur dioxide Oxidation Rates. Journal of Atmospheric Chemistry, 19: 317–327, 1994.

Stockwell, W. R., Kirchner, F., Kuhn, M., Seefeld, S., 1997. A new mechanism for regional atmospheric chemistry modeling. J. Geophys. Res., 102, 25 847–25 879.

Stutz, J., et al., 2004. Vertical profiles of NO_3, N_2O_5, O_3, and NO_x in the nocturnal boundary layer: 1. Observations during the Texas Air Quality Study 2000. J. Geophys. Res., 109, D12306, doi:10.1029/2003JD004209.

Stutz, J., Wong, K. W., Lawrence, L., Ziemba, L., Flynn, J. H., Rappengluck, B., Lefer, L, 2009. Nocturnal NO_3 radical chemistry in Houston, TX. Journal of Atmospheric Environment. Elservier. www.elservier.com/locate/atmosenv. doi:10.1016/j.atmosenv.2009.03.004.

Stein, D. C., Swap, R. J., Greco, S., Piketh, S. J., Macko, S. A., Doddridge, B. G., Elias, T., Bruintjes, R. T., 2003. Haze layer characterization and associated meteorological controls along the eastern coastal region of southern Africa, J. Geophys. Res., 108(D13), 8506, doi:10.1029/2002JD003237, 2003.

Stroud, C. A., et al., 2011. Impact of model grid spacing on regional- and urban- scale air quality predictions of organic aerosol. Atmos. Chem. Phys., 11, 3107-3118, 2011. www.atmos-chem-phys.net/11/3107/2011/., doi:10.5194/acp-11-3107-2011.

Sulzmann, M., Lawrence, M. G., 2006. Automatic coding of chemistry solvers in WRF-Chem using KPP. In 7th WRF Users Workshop, Boulder, Colorado. USA. URL: http://www2.mmm.ucar.edu/wrf/users/workshops/WS2006/presentations/Session6/6_4.pdf

Swap, R. J., et al., 2002. The Southern African Regional Science Initiative (SAFARI 2000): overview of the dry season field campaign. South African Journal of Science 98, March/April 2002.

Swap, R. J., et al., 2003. Africa burning: A thematic analysis of the southern African Regional Science Initiative (SAFARI 2000). Journal of Geophysical Research.Vol. 108. No. D13. 8465. doi:10.1029/2003JD003747.

Teller, A., Levin, Z., 2006. The effects of aerosols on precipitation and dimensions of subtropical clouds: a sensitivity study using a numerical cloud model. Atmos. Chem. Phys., 6, 67–80, 2006. www.atmos-chem-phys.org/acp/6/67/, SRef-ID:1680–7324/acp/2006-6-67.

Tesfaye, M., Botai, J., Sivakumar, V., Tsidu, G. M., 2013. Evaluation of Regional Climatic Model Simulated Aerosol Optical Properties over South Africa Using Ground-Based and Satellite Observations. Atmospheric Sciences, Volume 2013, ID 237483, pp. 1–17. http://dx.doi.org/10.1155/2013/237483.

Terblance, D. E., Mittermaier, M. P., Burger, R. P., Piketh, S. J., 2000. The Aerosol Rercirculation and Rainfall Experiment (ARREX): An initial study on aerosol-cloud. South African Journal of Science. Vol. 96. Issue 1.

Thompson, A. M., et al., 2003. Southern Hemisphere Additional Ozonesondes (SHADOZ) 1998–2000 tropical ozone climatology, 1, Comparison with Total Ozone Mapping Spectrometer (TOMS) and ground-based measurements, J. Geophys. Res., 108(D2), 8238, doi:10.1029/2001JD000967, 2003.

Tie, X., F. Geng, L. Peng, W. Gao, Zhao, C., 2009. Measurement and modeling of O_3 variability in Shanghai, China: Application of the WRF/Chem model, Atmos. Environ., 43, 4289–4302, doi:10.1016/j.atmosenv.2009.06.008.

Tie, X., Madronich, S., Walters, S., Zhang, R., Rasch, P., Collins, W., 2003. Effects of clouds on photolysis and oxidants in the troposphere. J. Geophys. Res., 108 (D20), doi:10.1029/2003JD003659, 2003.

Tong et al., 2013. Investigation of surface layer parameterisation of the WRF model and its impact on the observed nocturnal wind speed bias: Period of investigation focuses on the Second Texas Air Quality Study (TexAQS II) in 2006. URL: aqrp.ceer.texas.edu/projectinfoFY12_13\12–TN1\12–TN1 Final Report.pdf.

Torres, O., Bhartia, P. K., Herman, J. R., Ahmad, Z., Gleason, J., 1998. Derivation of aerosol properties from satellite measurements of backscattered ultraviolet radiation: Theoretical basis. Journal of Geophysical Research. Vol. 103. No. D14. pp. 099–110.

Torres, O., Bartia, P. K., Herma, J. R., Ahmad, Z., Gleason, J., 2002. Derivation of aerosol optcal depth from TOMS observations and comparison to AERONET measurements. Journal of Atmospheric Sciences. Vol. 59, pp. 398–413. doi:http://dx.doi.org/10.1175/1520-0469(2002)059<0398:ALTROA>2.0.C0;2

Torres, O., Chen, Z., Jethva, H., Ahn, C., Freitas, S. R., Bhartia, P. K., 2010. OMI and MODIS observations of the anomalous 2008-2009 Southern Hemisphere biomass seasons. Atmos. Chem. Phys., 10, 3505–3513, 2010. www.atmos-chem-phys.net/10/3505/2010/

Tuccella, P., et al., 2012. Modeling of a gas and aerosol with WRF/Chem over Europe: evaluation and sensitivity study. J. Geophys. Res., 117, D03303, doi:10.1029/2011JD016302, 2012.

Tuccella, P., et al., 2015. A new chemistry option in WRF-Chem v. 3.4 for the simulation of direct and indirect aerosol effects using VBS: evaluation against IMPACT–EUCAARI data. Geosci. Model Dev., 8, 2749–2776, www.geosci-model-dev.net/8/2749/2015/ doi:10.5194/gmd-8-2749-2015.

Tummon, F., Solomon, F., Liousse, C., Tadros, M., 2010. Simulation of the direct and semidirect aerosol effects on the southern Africa regional climate during the biomass burning season. Journal of Geophysical Research. Vol. 115. D1906. doi:10.1029/2009JD013738.

Twohy, C. H., Petters, M. D., Snider, J. R., Stevens, B., Tahnk, W., Wetzel, M., Russell, L., Burnet, F., 2005. Evaluation of the aerosol indirect effect in marine stratocumulus clouds: Droplet number, size, liquid water path, and radiative impact. J. Geophys. Res., 110,. D08203, doi:10.1029/2004JD005116.

Twomey, S., Squires, P., 1959. The Influence of Cloud Nucleus Population on the Microstructure of Convective Clouds. Tellus XI (1959), 4., pp. 409–411.

Twomey, S., 1974. Pollution and the Planetary Albedo. Environ., 8, 1251–1256, 1974.

Twomey, S., 1977. The Influence of Pollution on the Shrotwave Albedo of Clouds. J. Atmos. Sci., 34, 1149–1152., doi:http://dx.doi.org/10.1175/1520-0469(1977)034<1149:TIOPT>2.0.CO;2

Tyson, P. D., 1986. Climatic Change in and Variability in Southern Africa. Oxford University Press. Cape Town.

Tyson, P. D., Garstang, M., Swap, R., Kallberg, P., Edwards, M., 1996a. An Air Transport Climatology for Subtropical Southern Africa. International Journal of Climatology. Vol. 16. pp. 265–291. A. M. S.

Tyson, P. D., Garstang, M., Swap, R., 1996b. Large-Scale recirculation of Air over Southern Africa. Journal of Applied Meteorology. Vol. 35. pp. 2218–2236. A. M. S.

Tyson, P. D., D'Abreton, P. C., 1998. Transport and Recirculation of Aerosols off southern Africa-Macroscale Plume Structure. Atmospheric Environment. Vol. 32, No. 9, pp. 1511–1524.

Tyson, P. D., Preston-Whyte, R. A., 2000. The Weather and Climate of Southern Africa. Oxford University Press.

UNEP, 2004. Sustainable Consumption and Procution Activities in Africa: Regional Status Report (2002–2004). https://sustainabledevelopment.un.org/content/…/ecaRIM_bp2.pdf

van der Werf, G. R., et al., 2006. Interannual variability in global biomass burning emissions from 1997 to 2004. Atmos. Chem. Phys., 6, 3423–3441, 2006. www.atmos-chem-phys.net/6/3423/2006/

Wai, K. M., Wu, S., Kumar, A., Liao, H., 2014. Seasonal variability and long-term evolution of tropospheric composition in the tropics and Southern Hemisphere. Atmos. Chem. Phys., 14, 4859–4874, 2014. www.atmos-chem-phys.net/14/4859/2014/, doi:10.5194/acp-14-4859-2014.

Ward, D. S., et al., 2012. The changing radiative forcing of fires: global model estimates for past, present and future. Atmos. Chem. Phys., 12, 10857–10886, 2012. www.atmos-chem-phys.net/12/10857/2012/., doi:10.5194/acp-12-10857-2012.

Westervelt, D. M., et al., 2015. Radiative forcing and climate change response to projected 21st century aerosol decreases. Atmos. Chem. Phys. Discuss., 15, 9293–9353, 2015. www.atmos-chem-phys-discuss.net/15/9293/2015/

Wiedinmyer, C., et al., 2011. The Fire Inventory from NCAR (FINN) – a high resolution global model to estimate the emissions from open burning. Geosci. Model Dev. Discuss., 3, 2439–2476, 2010. www.geoscie-model-dev-discuss.net/3/2439/2010/

Wild, O., Zhu, X., Prather, M., 2000. Fast-J: Accurate Simulation of In- and Below-Cloud Photolysis in Tropospheric Chemical Models. Journal of Atmospheric Chemistry 37: 245–282, 2000.

Williams, J., 2004. Organic Trace Gases in the Atmosphere: An Overview. Environ. Chem. 2004, 1, 125–136., www.publish.csiro.au/journals/env, doi:10.1071/EN04057.

Williams, P. I., Baltensperger, U., 2009. Chapter 7: Particulate matter in the atmosphere. (Atmospheric Science for Environmental Scientists. Willey-Blackwell Publishing Ltd).

Winkler, H., et al., 2008. Evidence for large-scale biomass burning aerosols from sunphotometry at a remote South African site. Atmospheric Environment 42 (2008) 5569–5578. www.elsevier.com/locate/atmosenv, doi:10.1016/j.atmosenv.2008.03.031.

Woods, J., Hall, D. O., 1994. Bioenergy for development - Technical and environmental dimensions - FAO Environment and Energy Paper 13. Rome, Italy.

Wu, L., Su, H., Jiang, J. H., 2011. Regional simulations of deep convection and biomass burning over South America. 1. Model evlauations using multiple satellite data sets. J. Geophys. Res., 116, D17208, doi:10.1029/2011JD016105.

Yang, Z., Wang, J., Ichoku, C., Hyer, E., Zeng, J., 2013. Mesoscale modeling and satellite observation of transport and mixing of smoke and dust particles over northern sub-Saharan African region. J. Geophys. Res. Atmos. 118, 12,139–12,157, doi:10.1002/2013JD020644.

Yerramilli, A., et al., 2010. Simulation of Surface Ozone Pollution in the Central Gulf Coast Region Using WRF/Chem Model: Sensitivity to PBL and Land Surface Physics. Advances in Meteorology. Vol. 2010 (2010), Article ID 319138, 24 pages. http://dx.doi.org/10.1155/2010/319138.

Yevich, R., Logan, J. A., 2003. An assessment of biofuel use and burning of agricultural waste in the developing world. Global Biogeochem. Cycles, 17(4), 1095, doi:10.1029/2002GB001952.

Yi, B., Yang, P., Bowman, K. P., Liu, X., 2012. Aerosol-cloud-precipitation relationships from satellite observations and global climate model simulations. http://remotesensing.spiedigitallibrary.org, doi:10.1117/1.JRS.6.063505.

Yorks, J. E., McGill, M., Rodier, S., Vaughan, M., Hu, Y., Hlavka, D., 2009. African dust and smoke influences on radiative effects in the tropical Atlantic using CERES and CALIPSO data. https://ams.confex.com/ams/pdfpapers/144743.pdf.

Yurteri, C. U., 2010. A Brief on Aerosol Mechanics. TUDelft. URL: http://www2.msm.ctw.utwente.nl/sluding/TEACHING/ParticleTechnology/Yurteri_Aerosols_PT2010_v4.pdf

Yuzhi., L., Rui, J., Tie, D., Yonkun, X., Guangu, S., 2014. A Review of Aerosol Optical Properties and Radiative Effects. Journal of Meteorological Research. Vol. 28 Issue 6, pp. 1003–1028.

Zakey, A., Solmon, F., Giorgi, F., 2006: Implementation and testing of a desert dust module in a regional implementation and testing of a desert dust module in a regional climate model. *Atmos. Chem. Phys.*, **6**, 4687–4704.

Zaveri, R. A., Peters, L. K., 1999. A new lumped structure photochemical mechanism for large-scale applications. Journal of Geophysical Research. Vol. 104. No. D23. pp. 30,387–30,415.

Zaveri, R. A., Easter, C., Fast, J. D., Peters, L. K., 2008. Model for Simulating Aerosol Interactions and Chemistry (MOSAIC). Journal of Geophysical Research. Vol. 113, D13204, doi:10.1029/2007JD008782, 2008.

Zaveri, R. A., 2008. Modal and Sectional Aerosol Modules. PNNL., 2008 WRF-chem Tutorial, July 23, Boulder, Co. URL: http://www2.mmm.ucar.edu/wrf/users/tutorial/200807/CHEM/Zaveri-Modal-and-Sectional-Aerosol-Modules.WRF-chem%20tutorial.pdf

Zaveri, R. A., Barnard, J. C., Ester, R. C., Riemer, N., West, M., 2010. Participle-resolved simulation of aerosol size, composition, mixing state, and the associated optical and cloud condensation nuclei activation properties in an evolving urban plume. Journal of Geophysical Research. Vol. 115., D17210., doi:10.1029/2009JD013616.

Zhang, Y., Seigner, C. Seinfeld, J. H., Jacobson, M., Clegg, S. L., Binkowski, S., 2000. A comparative review of inorganic aerosol thermodynamic equilibrium modules: similarities, differences, and their likely causes. Atmospheric Environment. Vol. 34, Issue 1., pp.177–137., doi:http://dx.doi.org/10.1016/S1352-2310(99)00236-8.

Zhang, Y., Dubey, M. K., Olsen, S. C., Zheng, J., Zhang, R., 2009. Comparisons of WRF/Chem simulations in Mexico City with groud-based RAMA measurements during the 2006-MILAGRO. Atmos. Chem. Phys., 9, 3777–3798, 2009. www.atmos-chem-phys.net/93777/2009/

Zhang, Y., Pan, Y., Wang, K., Fast, J. D., Grell, G. A., 2010. WRF/Chem-MADRID: Incorporation of an aerosol module into WRF/Chem and its initial application to the TaxAQS2000 episode. J. Geophys. Res., 115, D18202, doi:10.1029/2009JD013443.

Zhang, F., et al., 2014. Sensitivity of mesocale modeling of smoke direct radiative effect to the emission inventory: a case study in northern sub-Saharan African region. IOP Publishing. Environ. Res. Let. 9 (2104) 075002, doi:10.1088/1748-9326/9/7/075002.

Zhang, B., Wang, Y., Hao, J., 2015. Simulating aerosol-radiation-cloud feedbacks on meteorology and air quality over China under severe haze conditions in winter. Atmos. Chem. Phys., 15,2387-2404, 2015. www.atmos-chem-phys.net/15/2387/2015/., doi:10.5194/acp-15-2387-2015.

Zhao, C., Cheng, S., Leung, L. R., Qian, Y., Kok, J. F., Zaveri, R. A., Huang, J., 2013. Uncertainties in modelling dust mass balance and radiative forcing from size parameterisation. Atmos. Chem. Phys., 13,10733–10753, 2013. www.atmos-chem-phys.net/13/10733/2013/, doi:10.5194/acp-13-10733-2013.

Zieger, P., et al., 2011. Comparison of ambient aerosol extinction coefficients obtained from in-situ, MAX-DOAS and LIDAR measurements at Cabauw. Atmos. Chem. Phys., 11,2603–2624, 2011. www.atmos-chem-phys.net/11/2603/2011/, doi:10.5194/acp-11-2603-2011.

Zunckel, M., et al., 2007. Air Quality Modelling Activities in Southern Africa and the Feasibility of a Regional Modelling Centre. APINA Report. URL: www1.eis.bov.bw/EIS/Reoprts/Air Quality Modelling Activities in Southern Africa.pdf.

Zunckel, M., Cairncross, E., Marx, E., Singh, V., Reddy, V., 2010. A Dynamic Air Pollution Prediction System for Cape Town, South Africa. www.umad.de/infos/cleanair13/pdf/full_266.pdf.

"I do not know what I may appear to the world, but to myself I seem to have been only like a boy playing on the seashore, and diverting myself in now and then finding of a smoother pebble or a prettier shell than ordinary, whilst the great ocean of truth lay all undiscovered before me."

(Sir Isaac Newton)